Investigation of OFDM as a Modulation Technique for Broadband Fixed Wireless Access Systems

A dissertation submitted for the degree
of Doctor of Philosophy

V. S. Abhayawardhana, Churchill College May 2003

Laboratory for Communications Engineering
Department of Engineering
University of Cambridge

To my parents .....

... for being the pillars of strength in my life.

Abstract

Broadband Fixed Wireless Access (BFWA) systems offer an effective way to overcome the 'last mile problem' associated with offering pervasive broadband Internet coverage to households and business users. Orthogonal Frequency Division Multiplexing (OFDM) meanwhile is being widely promoted for adoption as the physical layer standard for BFWA systems owing to its unprecedented success in other systems, particularly in digital broadcasting and Wireless LANs. BFWA systems are characterised by burst transmission from the Access Points (APs) to one or more Subscriber Units (SUs) and vice-versa. Owing to latency and throughput considerations, it is desirable that the OFDM system can operate effectively with a relatively low number of subchannels (typically in the order of 64-256). In order to maximise throughput it is important to optimise the use of these subchannels. An additional difficulty is that the system is required to function effectively with the use of inexpensive and low quality oscillators at the SUs. These issues pose fresh challenges that need to be addressed if successful operation of BFWA networks is to be achieved from both a technical and a commercial perspective. This dissertation presents research conducted with the specific aim of applying OFDM effectively and efficiently to the BFWA scenario.

Although OFDM is robust in the presence of multipath channels, its susceptibility to Phase Noise (PN) is widely known. An investigation conducted as part of this work has demonstrated that the effect of PN is two-fold. The first effect is that of phase rotation which is evident on the demodulated constellations of all the subchannels and is known as Common Phase Error (CPE). The second effect is owing to the loss of orthogonality between the subchannels and gives rise to Inter Carrier Interference (ICI) between the subchannels. A simple yet effective algorithm to counter the effects of CPE is presented in this thesis. Simulation re-

sults show that algorithm provides gains of up to 6 dB in terms of Signal to Phase Noise Ratio (SPNR) when applied to a 64 subchannel OFDM system with a PN Power Spectral Density (PSD) bandwidth of 100 kHz in the presence of a typical BFWA channel.

Accurate symbol (frame) and frequency offset synchronisation are also critical in an OFDM system. This is often accomplished by sending one or more training symbols at the start of each frame. The Schmidl and Cox Algorithm (SCA), although very robust in OFDM systems which use a large number of subchannels, fails badly in the BFWA scenario. This dissertation proposes the Iterative Symbol Offset Correction Algorithm (ISOCA) that complements the SCA and achieves perfect symbol synchronisation in the presence of BFWA channels at reasonable SNR levels. The SCA alone by contrast has a probability of only 0.48 of achieving perfect symbol synchronisation for a 64 subchannel OFDM system in a BFWA channel. In addition the SCA has a finite probability of yielding very damaging positive symbol offset estimations. A novel algorithm which complements the frequency offset correction function of the SCA is also proposed. This algorithm, known as the Residual Frequency Offset Correction Algorithm (RFOCA), mitigates the residual frequency offset errors remaining after the application of the SCA. The simulations show that the RFOCA is capable of reducing the residual frequency offset error variance by several orders of magnitude compared with that achieved by the SCA alone.

The use of a Time Domain Equaliser (TEQ) for OFDM systems in wireless channels is also addressed in this work. The TEQ reduces the apparent length of the multipath channel, thus reducing the length of the Cyclic Prefix (CP) that is required and so improving the transmission efficiency. An existing algorithm, which is termed the Dual Optimising Time Domain Equaliser (DOTEQ) is introduced and its limitations are identified. To overcome these problems a novel TEQ training algorithm, namely the Frequency Scaled Time Domain Equaliser (FSTEQ) is proposed. The FSTEQ is designed specifically for use in BFWA channels and it optimises its function in both the time and the frequency domains. It shows a 10-100 fold BER improvement as compared to the DOTEQ while maintaining a superior rate of convergence.

Time Domain Windowing (TDW) can be used to shape the spectra of the

OFDM subchannels, thus reducing side lobe levels. The dissertation investigates the use of an adaptive TDW scheme, which is applied separately to both the transmitter and the receiver in a BFWA system. The results show that TDW should be used if and only if there are uncorrupted samples that can be utilised as part of the windowing function within the CP. Otherwise, performance improvements are negligible. The dissertation also presents some preliminary results based on the concept of using a Maximum Likelihood Sequence Estimator (MLSE) instead of a Decision Feedback Equaliser (DFE), for the purpose of per-subchannel equalisation. The initial results appear to hold some promise though at the cost of very high complexity.

In summary, this dissertation presents novel algorithms that address several problems that arise when OFDM is used as the physical layer in a BFWA system. The solutions in general are not computationally demanding and offer cost effective and substantial improvements in system performance for the BFWA scenario.

Declaration

Except where noted in the text, this dissertation is the result of my own work and includes nothing which is done by someone else or in collaboration.

I hereby declare that this dissertation is not substantially the same as any that I have submitted for a degree or diploma or other qualification at any other University. I further state that no part of my dissertation has already been or is being concurrently submitted for any such degree, diploma or qualification.

This dissertation comprises approximately 42,000 words, 112 figures and 3 tables.

V. S. Abhayawardhana
May 28, 2003

Acknowledgements

First and foremost I would like to thank my supervisor, Dr. I. J. Wassell for his guidance, encouragement and support both in academic work and otherwise. I especially enjoyed the discussions we had over coffee, first thing in the morning while accommodating the bizarre times I used to work at.

My most sincere appreciation is extended to the Cambridge Commonwealth Trust (CCT) and the Overseas Research Students Award Scheme (ORS) for sponsoring my research and thus giving me an opportunity to study at probably the best place in the world. I also thank the Adaptive Broadband Limited (ABL) for providing me with industrial support during the second year of my research.

I would like to thank my adviser, Dr. N. G. Kingsbury, Dr. M. D. Macleod and Dr. M. Sellars for providing me with valuable feedback from time to time.

I am grateful for the efforts of my College tutor Dr. N. Morrison in helping me to secure funding during my final year. I would also like to thank Mrs. Les Dixon of Churchill College and Mrs. M. Cossnett at the Cambridge University Engineering Department (CUED) library for being so patient with my numerous requests.

Special thanks to all the members at the Laboratory for Communications Engineering (LCE) for making it such an enjoyable yet stimulating place to work.

Last, but certainly not least, to Prof. A. Hopper for providing me with such an excellent environment for research.

Publications

Some of the work discussed in this dissertation has been presented in the following publications;

1. V. S. Abhayawardhana, I. J. Wassell, "Common phase error correction with feedback for OFDM in wireless communication", *IEEE Global Telecommunications Conference (IEEE GLOBECOM)*, Volume: 1, Page(s): 651-655, November 2002.

2. V. S. Abhayawardhana, I. J. Wassell, "Iterative symbol offset correction algorithm for coherently modulated OFDM systems in wireless communication", *IEEE International Symposium on Personal, Indoor and Mobile Radio Communications (IEEE PIMRC)*, Volume: 2, Page(s): 545-549, September 2002.

3. V. S. Abhayawardhana, I. J. Wassell, "Common phase error correction for OFDM in wireless communication", *International Conference on Communication Systems, Networking and Digital Signal Processing (CSNDSP)*, Volume: 1, Page(s): 224-227, July 2002.

4. V. S. Abhayawardhana, I. J. Wassell, "Residual frequency offset correction for coherently modulated OFDM systems in wireless communication", *IEEE Vehicular Technology Conference (IEEE VTC), Spring*, Volume: 2, Page(s): 777-781, May 2002.

5. V. S. Abhayawardhana, I. J. Wassell, "Frequency scaled time domain equalisation for OFDM in broadband fixed wireless access channels", *IEEE Wireless Communications and Networking Conference (IEEE WCNC)*, Volume: 1, Page(s): 17-21, March 2002.

6. V. S. Abhayawardhana, I. J. Wassell, “Frequency Scaled Time Domain Equalisation for OFDM in Wireless Communication”, *European Wireless Conference*, Volume: 2, Page(s): 776-780, February 2002.

Contents

List of Figures

List of Tables

Glossary

ABR Achievable Bit rate

ADSL Asymmetric Digital Subscriber Line

AWGN Additive White Gaussian Noise

BER Bit Error Rate

BFWA Broadband Fixed Wireless Access

CIR Channel Impulse Response

CP Cyclic Prefix

CPE Common Phase Error

CPEC Common Phase Error Correction

CPESE Common Phase Error Symbol Estimate

CTF Channel Transfer Function

DFE Decision Feedback Equaliser

DMT Digital Multitone

DOTEQ Dual Optimising Time Domain Equaliser

DROT Dynamic Residual Offset Tracking

EIR Effective Impulse Response

ETF Effective Transfer Function

FBCF Feedback Correction Factor

FEQ Frequency Domain Equaliser

FFT Fast Fourier Transform

FIR Finite Impulse Response

FMT Filtered Multitone

FSTEQ Frequency Scaled Time Domain Equaliser

IBI Inter Block Interference

ICI Inter Carrier Interference

IEE Institute of Electrical Engineers

IEEE Institute of Electrical and Electronic Engineers

IFFT Inverse Fast Frequency Transform

ISI Inter Symbol Interference

ISOCA Iterative Symbol Offset Correction Algorithm

LMS Least Mean Square

LOS Line of Sight

MAF Moving Average Filter

MLSE Maximum Likelihood Sequence Estimator

MMDS Multichannel Multipoint Distribution Service

MMSE Minimum Mean Squared Error

OFDM Orthogonal Frequency Division Multiplexing

OSIR Overall Subchannel Impulse Response

PDF Probability Density Function

PN Phase Noise

PSD Power Spectral Density

QPSK Quaternary Phase Shift Keying

RC Raised Cosine

RFO Residual Frequency Offset

RFOCA Residual Frequency Offset Correction Algorithm

RLS Recursive Least Square

SC Single Carrier

SCA Schmidl and Cox Algorithm

SNR Signal to Noise Ratio

SOF Start of Frame

SPNR Signal to Phase Noise Ratio

SUI Stanford University Interim

TEQ Time Domain Equaliser

TIR Target Impulse Response

TPW Trapezoidal Windowing

TTF Target Transfer Function

VC Virtual Carrier

Chapter 1

Introduction

The tremendous success and exponential growth of the Internet encouraged by the development of novel applications has resulted in requirements for significantly higher network access data rates. The novel broadband applications that are foreseen range from e-commerce, telemedicine, teleteaching and large file transfer to multimedia. These applications are about to revolutionise both the economies of the world and our lifestyles. Any country that ignores broadband communication is going to suffer a severe economic impact. The UK government has identified the provision of broadband as a major objective and has developed strategies to deliver the most extensive and competitive broadband market in the G7 by 2005. As a consequence, the Broadband Stakeholder Group (BSG) has been appointed as the UK government's key advisory group with the aim of achieving this target [1].

The demand for broadband places huge requirements on both the access and the backbone networks of communication systems. The problems of the backbone networks have been addressed by sustained development of switching and transmission technology. However the major bottleneck lies in the access network, known in the industry as the 'last (or first) mile problem'.

There are two possible approaches for delivering broadband. The first approach is by the use of wired technology, represented by optical fibres, Digital Subscriber Lines (xDSL) and cable modems. The second approach is by the use of wireless technology, represented by satellite systems, stratospheric platforms

and Broadband Fixed Wireless Access (BFWA) systems. Among the many xDSL standards, the most commonly used is known as Asymmetric Digital Subscriber Line (ADSL). Currently only cable modems, ADSL systems and BFWA systems have been practically implemented owing to issues of cost and effectiveness. As at November 2002, terrestrial broadband (ADSL, cable modems and BFWA but not satellite) only has the potential to provide service to 67% of UK's households and coverage remains concentrated around areas of high population density. On the other hand, the number of broadband subscribers has grown by 300% in 2002 to reach approximately 4% of all households in UK. This surge in demand is predicted to continue in the near future. In terms of geographical coverage by each technology, ADSL, cable modems and BFWA systems had reached 61%, 40% and 12%, respectively by November 2002 [2]. It is proposed by the BSG that BFWA systems be extensively implemented, particularly in suburban and rural areas to obtain full broadband coverage in the UK and to avoid a 'broadband divide' among the population. One of the key recommendations is to encourage more operators to use BFWA by allocating more spectrum to such systems [3].

BFWA systems can be broadly categorised into Point to Point (PTP) and Point to Multipoint (PMP) terminal radio systems. The PTP and PMP systems usually operate in different frequency bands. For example the Local Multipoint Distribution Systems (LMDS) are in the 28 GHz band, the Multichannel Multipoint Distribution Service (MMDS) is in the 2.5 GHz band and the Unlicensed National Information Infrastructure (UNII) is in the 5 GHz band. Spectrum at 3.5 GHz has also been allocated for PMP systems in Europe. These systems are implemented by placing one or more Subscriber Units (SUs) at the customer premises which has access to a base station, also known as the Access Point (AP). Usually, the downlink from the AP is shared among the several SUs. The uplinks from the SUs usually have a random access element since more than one SU may wish to transmit to an AP at any one time [4].

ADSL modems are designed to use the voice-grade copper telephone channel. The main advantage of this approach is the availability of an extensive existing infrastructure and relatively low installation costs. However the main challenges are the interference due to Near End Crosstalk (NEXT), the restricted bandwidth and the moderate Signal to Noise Ratio (SNR) on the channels. The available

bit rate and hence the applications are limited by the quality of the copper loops already in place. ADSL offers a maximum bandwidth of 6-8 Mb/s downstream and up to 768 kb/s upstream [5].

Cable modems offer downstream data rates of up to 10Mb/s and upstream rates of up to 200 kb/s [6]. Even though there is a large subscriber base, the technology suffers from security issues since the cable link is shared by many users. Cable modems also offer a limited bandwidth for upstream traffic and consequently the implementation of high bandwidth interactive applications will be difficult.

Satellite access offers extremely high rates, offering data rates of up to the order of 10 Mb/s [7]. Satellite access has the advantage of total coverage independent of local population density. However it will be mainly used by the Internet Service Providers (ISP) who lack access to a wide bandwidth backbone rather than individual subscribers owing to the high cost of terminals.

Another area generating interest is the support for relatively broadband applications targeted to mobile devices. These standards are broadly known as International Telecommunication Union's (ITU) IMT-2000, popularly known as 'third-generation' (3G) mobile communication systems. Standards such as the Universal Mobile Telecommunication Systems (UMTS) in Europe will offer data rates up to 384 kb/s for high-mobility users and 2 Mb/s for low mobility users with local coverage, which will enable high value broadband information, commerce and entertainment to be made available to mobile users [8]. While 3G systems are designed to provide 'full mobility', another dimension that is gaining popularity are Wireless Local Area Networks (WLANs) that provide limited mobility with superior data rates [9]. They are commonly known by their standardisation group names or identifiers, for example, the 802.11 suite proposed by the U.S. based Institute of Electrical and Electronics Engineers (IEEE) [10], HIPERLAN1 and 2 proposed by the Broadband Wireless Access Networks (BRAN) project of the European Telecommunication Standard Institute (ETSI) [11] and HiSWAN proposed by the Japanese based Association of Radio Industries and Broadcasting (ARIB). These standards were initially designed to extend the coverage of wired LANs and offer a similar level of functionality. However issues concerning security, mobility, network management, ease of use and scalability remain to be addressed [12, 13].

With the deregulation of the telecommunication industry, massive growth in mobile communication, the emergence of multimedia applications and advanced information services has led to an increase in demand for the telecommunication services resulting in the roll-out of radio based broadband access. The advantages of wireless technology are that it is flexible, supports any traffic mix, has an open-ended uplink-downlink ratio and is suitable for incremental installation and rapid deployment. In developed economies it offers an economic entry into the market enabling effective competition with incumbent operators. In developing economies it permits them to jump a complete technological generation in terms of access technologies. However broadband terrestrial radio transmission has its own problems which need to be addressed, e.g. Inter Symbol Interference (ISI) owing to dispersive channels and Inter Carrier Interference (ICI) and Co channel Interference (CCI) owing to other users. In this dissertation the use of Orthogonal Frequency Division Multiplexing (OFDM) is investigated as a solution to the problems encountered when implementing BFWA systems.

1.1 Use of OFDM for BFWA systems

A modulation technique known as OFDM is gaining popularity among wireless network operators and is actively used in many standards owing to its efficiency and robustness in channels exhibiting multipath delay spread. OFDM involves splitting the original high bit rate data stream into a large number of parallel lower rate data streams which are transmitted in closely spaced subchannels in the frequency domain. The characteristics of OFDM will be discussed in more detail in the chapters that follow. One of the first examples of the widespread use of OFDM is within the Digital Audio Broadcasting (DAB) [14] and the Digital Video Broadcasting - Terrestrial (DVB-T) standards [15]. Here, its use allows terrestrial transmitters placed at different geographical locations to transmit at the same time using the same frequency bands. Hence they are known as Single Frequency Networks (SFNs). Later OFDM was adopted as the physical layer for WLAN standards such as IEEE 802.11a and HIPERLAN2 [16].

It has been apparent for some time that OFDM was going to be a major contender when it came to standardising BFWA systems following its widespread

use in WLANs. The IEEE set up the 802.16 working group to define standard specifications for the Metropolitan Area Networks (MANs) based on broadband wireless access. The air interface is known as WirelessMAN. This group's initial interest lay in the 10-66 GHz band where a Line of Sight (LOS) path between the terminals is deemed an absolute necessity and consequently the propagation distances remain relatively short. A Single Carrier (SC) based air interface has been selected. Later the work was extended in the guise of the 802.16a project to cover the 2-11 GHz range that includes both licenced and unlicensed bands. In this case the physical layer specification has been driven by the requirement for Non-Line-of-Sight (NLOS) operation and hence significant multipath propagation is expected. Hence two out of the three air interfaces proposed are based on OFDM [17, 18]. The work carried out in parallel by the ETSI-BRAN project has resulted in the standard known as HIPERACCESS, which specifies an outdoor, fixed wireless network providing access to a wired infrastructure [19]. It is a SC system which operates in the frequency range from 26 to 28 GHz and also at 40 GHz and provides bit rates of up to 25 Mb/s. It has been extended to cover lower frequency bands from 2 to 11 GHz in the guise of the HIPERMAN standard. HIPERMAN enables both PMP and Mesh network configurations. Another standard that is proposed by the ETSI-BRAN project is HIPERLINK that allows very hight speed (up to 155 Mb/s) indoor, static interconnections between the HIPERACCESS and the HIPERLAN systems. However, HIPERMAN and HIPERLINK are yet to be finalised but are expected to be OFDM based when ratified. Hence it is evident that OFDM will have widespread use in the future, particularly in BFWA systems.

1.2 Overview of the Thesis

This thesis presents research which investigates various problems that arise when using OFDM as the physical layer in a BFWA system. Consequently the performance of OFDM systems in the BFWA scenario has been investigated via extensive and representative computer simulations. The investigation concentrates primarily on coherent, Grey coded Quaternary Phase Shift Keying (QPSK) modulated OFDM systems although some initial work concerning Filtered Multi-

tone (FMT) modulation is also presented in appendix C. The measure of performance, unless stated otherwise, is the Bit Error Rate (BER) as a function of the received SNR.

In typical OFDM based wireless LAN systems, the number of subchannels, N is kept relatively low, typically less than 512. This is done for a number of reasons. The transmitted OFDM signal is generated by adding together randomly varying complex sinusoids, which gives rise to a transmitted signal with a very high dynamic range. An accepted measure of this is the Peak-to-Average Power Ratio (PAPR). A high value of N leads to a high PAPR, demanding the use of highly linear and consequently inefficient power amplifiers [20]. Also note that for typical wireless data transmission systems, for example HIPERLAN-2, short data bursts employing a low number of subchannels (e.g. 64) are used owing to latency and protocol efficiency considerations [21]. Also a high value of N will reduce the inter-carrier spacing of the OFDM signal which renders the system more susceptible to frequency offset and oscillator phase noise. These issues will be discussed in detail in later chapters. For these reasons the OFDM systems that are considered in this thesis have between 64 and 256 subchannels.

In practical OFDM systems, the subchannels at the edges of the multiplex cannot be used to transmit data since their use gives rise to high sidelobe levels yielding unacceptable levels of adjacent channel interference. Besides, the IF filters at the receiver requires a finite roll off bandwidth. The unused subchannels at either end of the OFDM multiplex are known as Virtual Carriers (VCs). The number of VCs required is determined by the standard that is applicable for the particular system and will clearly affect the throughput of the system. However in this work, the number of VCs is assumed to be zero since throughput will not be used as a measure of performance.

In OFDM based systems that are subject to channels with severe frequency selective attenuation, for example in xDSL systems, different subchannels are mapped using different modulation constellations depending upon the subchannel SNR. This is known as ‘bit loading’. Although the channels that are relevant to BFWA systems show a certain degree of frequency selectivity, they are not as hostile as those experienced in xDSL, consequently this operation will not yield a significant gain. A bit loading algorithm will require feedback from the receiver

and also owing to the variation of the channel between transmission bursts, it is not usually employed in fixed wireless systems [22]. Consequently, the OFDM systems investigated in this thesis will be mapped using QPSK for all subchannels and as mentioned previously, all of them will be used for data transmission.

It is assumed that the transmission is performed in relatively short bursts at a sampling frequency of 20 MHz unless stated otherwise. Channel models for BFWA systems were being developed while the research was being carried out. The Stanford University Interim (SUI) models [23] were selected for use owing to their widespread acceptance and have been used throughout the thesis. The transmission burst length selected for use is less than or equal to 2500 symbols with two or more training symbols at the beginning of each burst. At the chosen sample rate of 20 MHz the transmission of a burst takes less than 10 ms. Appendix B introduces the SUI channel models that are extensively used in the following simulations, giving their associated parameter values. The temporal characteristics of the channel model are significantly static during a time period of 10 ms. Hence it has been assumed that the channel remains stationary throughout the transmission burst for all the simulations.

Conventional OFDM systems, such as WLANs, require high quality Radio Frequency (RF) oscillators to generate stable frequencies and thus avoid the effects of frequency offset and phase noise. The RF oscillators form a significant component of the cost of the Subscriber Units (SUs). A lower quality oscillator will reduce the overall cost of the SU and consequently will make BFWA systems more competitive with other broadband systems available in the market. One of the key aims of this research is to mitigate the performance degradation caused by the use of low quality oscillators via the use of novel Digital Signal Processing (DSP) algorithms. Another aim is to improve the performance of both timing and frequency synchronisation.

The performance of OFDM systems employing the DSP algorithms proposed in this work are compared against those of conventional OFDM systems, either employing existing algorithms or in the absence of correction algorithms.

The structure and contents of the thesis will now be briefly introduced. Chapter 2 presents the various components of a digital communication system and also outlines the advantages of using multitone modulation schemes such as OFDM.

It is shown that the subchannel spectra of an OFDM signal overlap and orthogonality is maintained only if timing and frequency synchronisation are preserved. The sidelobe levels of the subchannel spectra are quite high, which also leads to susceptibility to oscillator phase noise [24].

The effects of phase noise on the system performance is investigated in detail in chapter 3. It is found that phase noise introduces two distinct effects. The first effect rotates the subchannel phase and is known as Common Phase Error (CPE) while the second effect gives rise to ICI. The chapter also proposes a novel and effective Common Phase Error Correction (CPEC) algorithm to counter the effects of CPE in a coherently modulated OFDM system. The algorithm shows significant performance gains as compared to conventional OFDM systems in BFWA channels, at only a moderate cost in terms of computational complexity.

Coherently modulated OFDM systems, such as in WLANs, generally employ training symbols usually placed at the beginning of the transmitted burst to achieve frame (symbol) and frequency synchronisation. One of the more robust schemes is the Schmidl and Cox Algorithm (SCA) [25]. Although the SCA performs well for OFDM systems with a large number of subchannels (i.e. N of the order of 1000 or more), its performance degrades for systems with lower values of N. In chapter 4 the symbol synchronisation function of the SCA is examined in more detail. It also proposes the novel Iterative Symbol Offset Correction Algorithm (ISOCA) which complements the SCA and is shown to achieve virtually perfect symbol synchronisation.

Chapter 5 analyses the effects of frequency offset on the performance of an OFDM system. It also investigates the frequency offset correction function of the SCA. It is found that when the SCA is applied to OFDM systems with lower values of N, a residual frequency offset remains that rotates the demodulated constellations at a reduced rate (compared with not using the SCA), but one that is significant enough to induce bit errors. One method that could be employed to mitigate this effect is to embed pilot symbols into the OFDM symbols by placing them in predefined OFDM subchannels. However, this method reduces the transmission efficiency, particularly when the number of subchannels, N is kept low. Since the policy of this work is to use all the subchannels to transmit data, this method will not be adopted. Instead this chapter proposes the data driven

Residual Frequency Offset Correction Algorithm (RFOCA) that complements the frequency offset correction function of the SCA and is shown to provide significant performance gains.

An elegant method of equalising the effects of a channel exhibiting multipath delay spread is to prepend each transmitted OFDM symbol with samples taken from the end of the OFDM symbol sufficient to cover the duration of the channel delay spread. These samples are known as the Cyclic Prefix (CP) and are discussed in detail in chapter 2. However, the use of the CP reduces the transmission efficiency. A method that is adopted widely in ADSL systems is to include a filter ahead of the demodulator (i.e. the Fast Fourier Transform (FFT)) known as the Time Domain Equaliser (TEQ). The purpose of the TEQ is to reduce the effect of the channel delay spread. Hence the Effective Impulse Response (EIR) after the TEQ is arranged to be shorter than that of the original channel, consequently the overall OFDM system is capable of working with a shorter CP. However, the current TEQ algorithms optimise the EIR only in the time domain, often resulting in deep nulls in the frequency response. Any subchannels that fall in to these frequency nulls will be severely degraded. Chapter 6 proposes a new algorithm, namely the Frequency Scaled Time Domain Equaliser (FSTEQ) that optimises both in the time and frequency domains so that the overall response avoids spectral nulls as well as reducing residuals in the time domain. Thus the overall performance is improved compared with that achieved when optimising in the time domain alone.

Conventional OFDM systems use rectangular windows to shape the transmitted OFDM symbols in the time domain and this leads to the high sidelobe levels as mentioned previously. One way of reducing the sidelobe levels is to employ non-rectangular window functions. Note that if these window types do not conform to the Nyquist criterion, they will give rise to a loss of orthogonality. In chapter 7 the use of Nyquist time domain windowing is investigated. However the use of non-rectangular Nyquist windows requires more uncorrupted samples within the CP if the OFDM symbols are to be processed without introducing ICI than does the use of a rectangular window. In the approach presented in chapter 7 it is proposed that uncorrupted samples in the CP are used to maintain orthogonality when non-rectangular windows are employed. However, if no uncorrupted samples are

available in the CP, the length of the CP will have to be extended specifically to accommodate the windowing function, leading to an increase in the transmission bandwidth and thus decreasing the SNR. It has been found that in such a scenario, non-rectangular windowing does not give any performance gains. It is recommended that windowing be employed only if there are uncorrupted samples available in the CP and if the system specification does not allow the length of the CP to be reduced.

Chapter 8 summarises the findings and proposes areas in which the presented work can be extended in the future.

Another area that is receiving attention is that of filterbank based modulation. FMT is one such scheme that was originally proposed for VDSL systems [26]. The filter banks that are employed provide very high sidelobe attenuation but with the penalty of introducing Inter Symbol Interference (ISI). The low sidelobe levels reduce the ICI but now per-subchannel equalisation is required to mitigate the effects of ISI. Decision Feedback Equalisers (DFEs) are often used for this purpose, however the per-subchannel error performance remains low using such an approach. Appendix C investigates the use of a Maximum Likelihood Sequence Estimator (MLSE) rather than a DFE for performing the per-subchannel equalisation in an FMT system. Some preliminary results are presented concerning the proposed approach and a comparison with a DFE based scheme is given. Minimising the computational burden is not the intension of the presented work, rather the aim being to understand the performance limits of per-subchannel equalisation in an FMT system.

In summary, the novel algorithms proposed and results presented in this work are as follows;

- The Common Phase Error Correction (CPEC) algorithm that corrects the CPE component owing to the phase noise in a coherently modulated OFDM system. The performance the algorithm in various systems is analysed and its performance is compared against other algorithms.

- The two-part Iterative Symbol Offset Correction Algorithm (ISOCA) that complements the symbol (frame) synchronisation function of the SCA and is shown to yield virtually perfect symbol synchronisation.

- The Residual Frequency Offset Correction Algorithm (RFOCA) that complements the frequency offset correction function of the SCA. The RFOCA is shown to reduce the variance of the residual frequency offset by several orders of magnitude.

- The Frequency Scaled Time Domain Equaliser (FSTEQ) that performs optimisation in both the time and the frequency domains and is shown to provide significant gains over existing proposals.

- An analysis of the effect of adaptive Time Domain Windowing (TDW) when applied to an OFDM system in a BFWA application. Simulations are performed when the windowing is applied at either the receiver or the transmitter.

- A preliminary analysis concerning the performance gains that can be obtained by replacing the usual DFEs by MLSEs for per-subchannel equalisation of an FMT system.

Chapter 2

Theory of OFDM

2.1 Introduction to Digital Communication

Figure 2.1 illustrates a functional block diagram of a digital communication system [27]. The message produced by the source is converted into one out of a finite set of sequences of binary digits. Ideally the aim is to represent the source output by as few binary digits as possible in order to increase the efficiency of representation. This process is called source encoding or data compression.

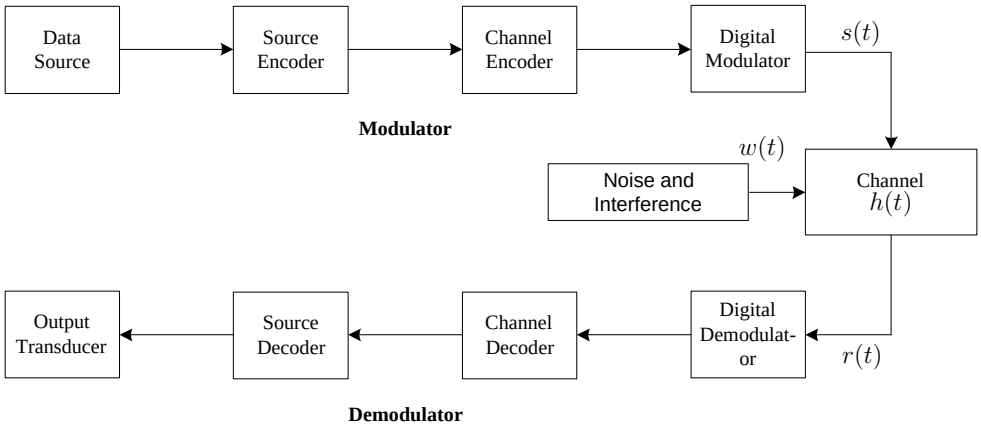

Figure 2.1: Basic elements of a digital communication system

The information sequence passes from the Source Encoder to the Channel Encoder, which introduces redundancy in a controlled manner, to overcome the

effects of noise and interference in the channel. The errors that are caused by the impairments are detected at the receiver and sometimes corrected. There are two encoding approaches, namely, block or convolutional encoding, such schemes are known as Error Control Coding (ECC). Although the use of an ECC greatly improves the overall error rate performance of the system the objective of the author of this thesis is to find the raw performance gains that could be obtained from using the proposed algorithms over the conventional OFDM system. Hence, the work presented in this thesis will not address Channel Encoding and hence this function is not included in the simulations. Besides, the use of an ECC would greatly increase the complexity of the system, thus the simulation time and resources will also be increased. The Digital Modulator maps the binary information sequence to a waveform capable of being transmitted over the channel and being retrieved at the receiver. The communication channel is the physical medium that is used to carry the signal from the transmitter to the receiver. Possibilities include wireless, local loop (telephone wires), optical fibre or coaxial cable etc. Whatever the channel, the transmitted data is corrupted in a random manner by a variety of possible mechanisms, the most common being additive thermal noise.

The Digital Demodulator takes the received analogue waveform and produces an estimate of the data stream originally applied to the Digital Modulator. The Channel Decoder removes the redundancy introduced by the Channel Encoder permitting errors at the Demodulator output to be identified and possibly corrected. Schemes that are capable of correcting errors at the receiver are known as Forward Error Correction (FEC) methods. Finally, the Source Decoder regenerates the original information. The challenge of the communication engineer is to design a system that ensures the retrieval of data at an acceptable level of fidelity for given channel conditions and available resources, e.g. transmitter power.

The received signal $r(t)$ after it has travelled through the channel is,

$$r(t) = (s(t) * h(t)) + w(t) \tag{2.1}$$

where $h(t)$ represents the channel response and $w(t)$ represents the additive noise and interference terms and $*$ represents the convolution operation. Note that all simulations and analysis in this thesis, unless stated otherwise, are performed

in the *complex baseband* domain. Please refer Appendix A for an introduction to the concepts of complex baseband. We may express the frequency response, $H(f)$, of the channel as

$$H(f) = |H(f)|\, e^{j\theta(f)} \tag{2.2}$$

where $|H(f)|$ and $\theta(f)$ are known as the amplitude response and the phase response, respectively. $H(f)$ is also known as the Channel Transfer Function (CTF). A channel is said to be non distorting or ideal if the amplitude response is constant for all significant frequencies and the phase response is a linear function of the frequency. Practical channels do not conform to these criteria perfectly. In a practical channel, as a result of the convolution operation, the successive transmitted signals will be smeared into one another. This phenomenon is called Inter Symbol Interference (ISI).

From this point onward the emphasis will be on wireless channels only. There are many modes of propagation for electromagnetic waves through a wireless medium. For frequencies above 2 GHz, the dominant mode of transmission is via Line-of-Sight (LOS) propagation. This means for terrestrial systems, the transmitter and the receiver antennas must be in direct LOS with relatively little obstruction in between. The dominant noise limiting the performance of such a system is thermal noise generated at the receiver and Co-channel Interference (CCI) from other users. Even if the antennas at both ends do have a LOS path, the transmitted signal may arrive at the receiver via multiple propagation paths. Delayed signals could be the result of reflections from terrain features such as trees, mountains or objects such as vehicles or buildings. This is very common and limits the performance of such a system in urban or mountainous areas. The multipath propagation gives rise to the reception of several copies of the same signal at the receiver antenna each with a random phase. This generally causes ISI and moreover, the received signals can add destructively, resulting in signal fading. See appendix B for details of the effects of multipath channels. Multitone Modulation (MTM) is a technique that is used to overcome the effects of multipath propagation.

2.2 Motivation to Use Multitone Modulation

The concept of MTM has been known since the middle of the 1960's [28, 29]. The approach is to transmit the data using a large number of subchannels, thereby reducing the symbol rate carried by each subchannel. The theoretically ideal MTM system has an infinite number of subchannels, and consequently a transmitted symbol with an infinite length. Hence, if the Channel Impulse response (CIR) is finite, the MTM system remains immune to distortion. However MTM was not practical to implement until the discovery that it could be achieved via the use of the Discrete Fourier Transform (DFT) [30]. Today it looks even more attractive owing to implementation of the DFT using the computationally efficient Fast Fourier Transforms (FFT). MTM has attracted much interest owing to the development of powerful Digital Signal Processing (DSP) circuits [31, 32]. There are various MTM techniques and they have been referred to by many names. Among them are Orthogonal Frequency Division Multiplexing (OFDM), Discrete Multitone (DMT) and Filtered Multitone (FMT).

In order to understand the reasoning behind the use of Multitone transmission, one must have a background of information theory. Claude Shannon in his revolutionary work [33] showed that given a transmission source with power P, and any linear time-invariant (LTI) channel with transfer function $H(f)$ and additive Gaussian noise with a two-sided Power Spectral Density (PSD) of $N_0/2$ W/Hz, it is possible to send a finite number of bits per second, R_b bps, over the channel with a probability of making an error approaching zero as long as R_b is lower than a value called the capacity, C. Readers are referred to Appendix A for an introduction to the PSD. For a perfectly bandlimited signal with bandwidth W Hz and noise PSD $N_0/2$ W/Hz, the capacity is given by,

$$C = W \log_2 \left[1 + \frac{P}{N_0 W}\right] \text{ bps} \tag{2.3}$$

here P/N_0W is the Signal to Noise Ratio (SNR). The signal power is related

to the signal PSD $P_s(f)$ by,

$$P = 2\int_0^\infty P_s(f)df \ . \tag{2.4}$$

For a general LTI channel $H(f)$, Shannon showed that the capacity is given by,

$$C = \int_0^\infty \log_2\left[1 + \frac{|H(f)|^2 P_s(f)}{N_0/2}\right] \text{bps} \ . \tag{2.5}$$

It is possible to maximise the capacity C, for a given value of P by optimising $P_s(f)$. It is given by,

$$P_s(f)_{opt} = \left[\lambda - \frac{N_0/2}{|H(f)|^2}\right] \tag{2.6}$$

where λ is the Lagrange multiplier. This is the popular 'water pouring' solution. The essence of the solution requires utilising the entire channel bandwidth, however the PSD of the transmitted signal is shaped such that $P_s(f)$ is higher where $H(f)$ is not attenuated and lower where $H(f)$ is attenuated.

Kalet has compared the use of multitone Quadrature Amplitude Modulation (QAM) to single carrier QAM in [34]. The performance improvement for the multitone system was not significant in Gaussian channels, however large improvements were shown for channels with spectral nulls and for dynamic channels. One particular form of MTM, namely OFDM will be discussed in detail in the next section.

2.3 Orthogonal Frequency Division Multiplexing

Multipath propagation is the main cause for signal fading in radio reception. The problem is exaggerated, if the receiver and/or the transmitter is/are mobile as the added dimension of mobility will introduce more sever temporal characteristics of the channel. In frequency selective fading, part of the frequency band will experience severe attenuation while in others the response may be enhanced. If the signal is narrowband and falls within a band where attenuation is high, it will result in a significant reduction of the received SNR.

If the bandwidth of the signal is less than the coherence bandwidth of the channel, the distortion is minimised and this is called a frequency flat or a 'flat' fading channel. However there is a significant chance that the signal will be subject to severe attenuation on some occasions, i.e. temporal fading. A wideband signal will experience more distortion, but will suffer reduced variations in terms of the total received power. OFDM overcomes multipath propagation by transmitting a large number of narrow band digitally modulated signals over a large bandwidth. Consequently, each channel experiences 'flat' fading.

Consider a typical channel with a deep null in the frequency response. A single carrier system, such as QAM, will need some form of time domain equalisation. Linear equalisation will increase noise, while a Decision Feedback equaliser (DFE) will be more complex and its ultimate performance is limited by error propagation. A Maximum Likelihood Sequence Estimator (MLSE) will be even more complex. Since multicarrier systems, such as OFDM, approximate a constant transfer function for each subchannel, equalisation becomes very simple. Recently there have been proposals to use frequency domain equalisation for SC systems (SC/FDE), for example [22, 35, 36]. The complexity of the SC/FDE system is similar to the OFDM system, but the method requires training symbols (also known as unique words) to be sent periodically to train the equalisers. Other advantages of MTM methods are the reduced effects of impulsive noise as a result of the extended symbol duration, the flexibility to not transmit in corrupted subchannels in the case of narrowband interference and the ability to transmit important data in subchannels with a high SNR. If the frequency separation between the subchannel carriers, Δf is chosen to be $1/T$, where T is the symbol duration of the subchannel carriers, then the complexity can be minimised by using FFT techniques for implementation.

The receiver may be viewed as a bank of demodulators translating each subchannel carrier to baseband and integrating over the bit period. The subchannel carrier frequencies are selected such that the subchannel spacing is an integral multiple of symbol periods (i.e. the carriers are orthogonal over the symbol period). Thus when integrated over the bit period, the other carriers yield a zero contribution.

The 'Frequency Division Multiplex' part in the terminology is due to the data

being divided among a large number of closely spaced subchannels. Often, practical OFDM systems, such as DAB and DVB-T, include a Forward Error Correction (FEC) stage for example using convolutional coding [14, 15]. Hence practical systems are known as Coded OFDM (COFDM). The sidebands of individual subchannels do overlap in the frequency domain but the signals are received without Inter Carrier Interference (ICI) owing to the orthogonal relationship between the subchannels.

Members of an orthogonal set are linearly independent. Mathematically, an element ψ_p in a set of signals ψ will have the following relationship in an orthogonal system;

$$\begin{aligned} \int_a^b \psi_p(t)\psi_q^*(t)dt &= K \quad \text{for } p = q \\ &= 0 \quad \text{for } p \neq q\,. \end{aligned} \tag{2.7}$$

2.3.1 Mathematical Description of OFDM

Mathematically, each subchannel carrier within the frequency multiplex may be represented by the complex signal given by,

$$s_c(t) = A_c(t)e^{j[2\pi f_c t + \phi_c(t)]} \tag{2.8}$$

where $A_c(t)$ and $\phi_c(t)$ are the amplitude and the phase of the carrier, which vary on a symbol-by-symbol basis. For QPSK, the amplitude is constant and the phase takes on one of four possible values per symbol. Note that the transmitted bandpass signal is the real part of $s_c(t)$. In OFDM we have many subchannels, thus for N subchannel carriers the *normalised* transmitted complex baseband signal is given by,

$$s(t) = \sqrt{\frac{1}{N}} \sum_{k=0}^{N-1} A_k(t)e^{j[2\pi f_k t + \phi_k(t)]}\,. \tag{2.9}$$

The subchannel carrier frequencies may be written in the following form;

$$f_k = f_0 + k\Delta f \text{ for } k = 0, 1, \ldots, N-1 \tag{2.10}$$

where $\Delta f = 1/T_s$. Here T_s is the duration of the QPSK symbols. Without loss of generality we can let $f_0 = 0$. If we assume that the phase and the amplitude of the transmitted signal do not change over a symbol period, we can neglect the amplitude and the phase dependence on time and express (2.9) as,

$$s(t) = \sqrt{\frac{1}{N}} \sum_{k=0}^{N-1} A_k e^{j[2\pi(\frac{k}{T_s})t + \phi_k]} \ . \tag{2.11}$$

This is a continuous time signal, which we wish to represent as a discrete time signal with sampling frequency of $1/T$, consequently $T_s = NT$, where T is the sample period and N is the number of samples per OFDM symbol. In discrete time format, (2.11) can be written as,

$$s(nT) = \sqrt{\frac{1}{N}} \sum_{k=0}^{N-1} A_k e^{j\phi_k} e^{j\frac{2\pi kn}{N}} \ . \tag{2.12}$$

Comparing this with the normalised form of Inverse Discrete Fourier Transform (IDFT),

$$g(nT) = \sqrt{\frac{1}{N}} \sum_{k=0}^{N-1} G\left(\frac{k}{NT}\right) e^{j\frac{2\pi kn}{N}} \tag{2.13}$$

we note the similarity between (2.12) and (2.13). It is evident that the required time domain signal $s(nT)$ can be obtained through an IDFT of the QPSK symbol $A_k e^{j\phi_k}$. Hence it is shown that the OFDM carriers could be generated by IDFT, or its efficient counterpart, the Inverse Fast Fourier Transform (IFFT). In general, $A_k e^{j\phi_k}$ can be taken from any QAM constellation.

2.3.2 Orthogonality of Subchannel Carriers

The subchannel carriers of the OFDM signal are given by,

$$\psi_k(t) = e^{j2\pi k\frac{t}{T_s}} \ . \tag{2.14}$$

Using (2.7) it follows that

$$\begin{aligned}\int_a^b \psi_p(t)\psi_q^*(t)dt &= \int_a^b e^{j[2\pi(p-q)t/T_s}dt \\ &= (b-a) \quad \text{for} \quad p=q \end{aligned} \tag{2.15}$$

$$\begin{aligned} &= \frac{e^{j[2\pi(p-q)b/T_s]} - e^{j[2\pi(p-q)a/T_s]}}{j2\pi(p-q)/T_s} \\ &= \frac{e^{j[2\pi(p-q)b/T_s]}\left[1 - e^{j[2\pi(p-q)(a-b)/T_s]}\right]}{j2\pi(p-q)/T_s} \\ &= \frac{e^{j[2\pi(p-q)\left(b+\frac{T_s}{2}\right)/T_s]}\left[e^{j[\pi(p-q)]} - e^{-j[\pi(p-q)]}\right]}{j2\pi(p-q)/T_s} \\ &= e^{j[2\pi(p-q)\left(b+\frac{T_s}{2}\right)/T_s]}\text{sinc}(p-q) \\ &= 0 \quad \text{for} \quad p \neq q\,. \end{aligned} \tag{2.16}$$

The integration period for a symbol is $(b-a) = T_s$, which is used in the 5th line of the derivation. Note that p and q are integers. Hence the carriers are orthogonal over time intervals equal to the symbol duration, or integer multiples of the symbol duration.

2.4 Simulated Conventional OFDM System

Figure 2.2 shows the block diagram of a conventional OFDM system. The performance of this baseline system will be used as a benchmark for comparison with similar OFDM systems employing the novel algorithms to be presented throughout this thesis. The input binary data stream is first distributed among the subchannels and mapped into a complex sequence using the chosen modulation constellation. In this thesis the mapping scheme employed is always QPSK and it is assumed that all the OFDM subchannels are used for data transmission.

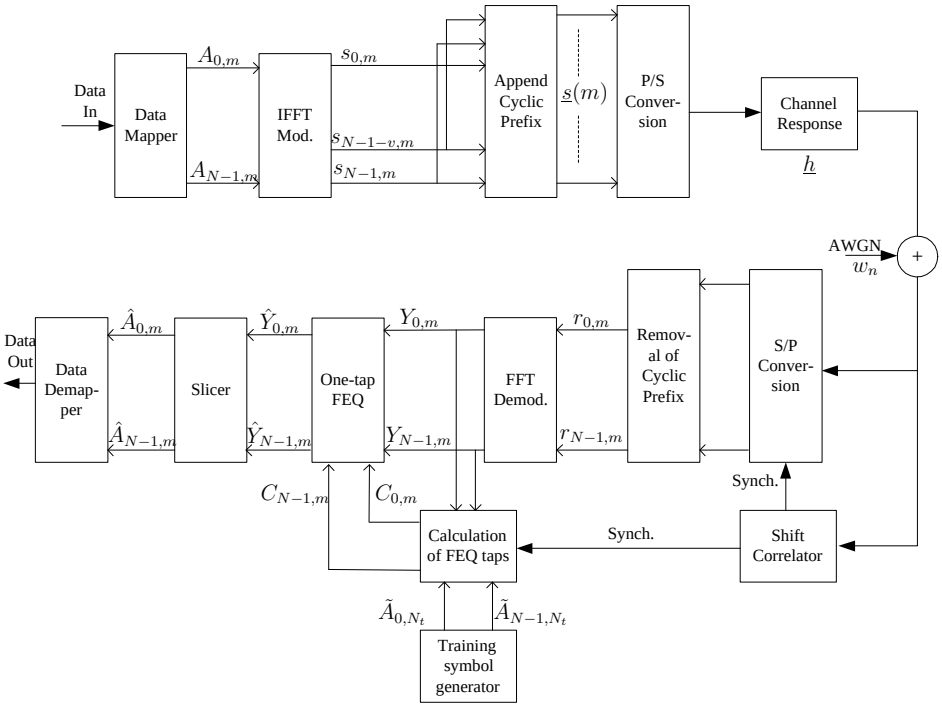

Figure 2.2: Block diagram of a conventional OFDM system

The nth sample of the mth OFDM symbol generated by the Inverse FFT (IFFT) at the transmitter is

$$s_{m,n} = \sqrt{\frac{1}{N}} \sum_{k=0}^{N-1} A_{m,k} e^{j2\pi \frac{kn}{N}}, \quad 0 \leq n \leq N-1 \tag{2.17}$$

where $A_{m,k}$ is the QPSK symbol modulated on to the kth subchannel of the mth OFDM symbol. Note that $s_{m,n}$ is the complex baseband equivalent of the transmitted OFDM signal. The data is converted into a serial sequence, then a Cyclic Prefix (CP) of length v is prepended. Thus the mth transmitted OFDM symbol is

$$\underline{s}(m) = [s_{m,N-v}, .., s_{m,N-1}, s_{m,0}, .., s_{m,N-1}]^T. \tag{2.18}$$

A finite length CIR is assumed having N_h samples, $\underline{h} = [h_0, .., h_{N_h-1}]^T$, where $v \geq N_h - 1$. The received sequence can be expressed as,

$$r_n = (s_n * h_n) + w_n \tag{2.19}$$

where s_n represents the serially concatenated transmitted symbols $\underline{s}(m)$ and w_n is the component due to Additive White Gaussian Noise (AWGN). The AWGN samples that are used in the simulations were drawn from a Gaussian process having a flat PSD over the entire signal bandwidth. The noise power for each transmitted burst was estimated by averaging over a sequence as long as the burst length. Finally, the noise power is averaged over all transmitted bursts before presentation of results. At the receiver, samples corresponding to the CP are discarded and the remaining samples of the active OFDM symbol are used for decoding. The symbol after FFT demodulation is

$$Y_{m,l} = \sqrt{\frac{1}{N}} \sum_{n=0}^{N-1} r_{m,n} e^{-j2\pi \frac{ln}{N}}, \quad 0 \leq l \leq N-1 \tag{2.20}$$

where $r_{m,n},\ 0 \leq n \leq N-1$ are the received samples of the FFT window for the mth OFDM block taken from r_n, as determined by the synchronisation algorithm. Chapter 4 will discuss the synchronisation method in more detail.

2.4.1 The effect of the Cyclic Prefix

Peled and Ruiz [37] first showed that digital parallel data transmission can be achieved through an FFT and that ISI and ICI can be combated by the use of a CP. If $\underline{A}(m) = [A_{m,0}, .., A_{m,N-1}]^T$ denotes the vector of N data symbols and $\mathbf{F}$ is the $N \times N$ DFT matrix, where the element $F_{k,n}$ is given by $e^{-j2\pi\frac{kn}{N}}$, the modulated OFDM symbol, as shown in (2.17) is given by $\frac{1}{\sqrt{N}}\mathbf{F}^*\underline{A}(m)$. Here $(.)^*$ represents the complex conjugation operation and $\frac{1}{\sqrt{N}}$ is used for the normalisation of power. The transmitted OFDM symbol including the CP is given by $\underline{s}(m) = \frac{1}{\sqrt{N}}\mathbf{T}\mathbf{F}^*\underline{A}(m)$, where $\mathbf{T}$ is a $(N+v) \times N$ matrix given by,

$$\mathbf{T} = \begin{bmatrix} O & I_1 \\ & I_2 \end{bmatrix} \tag{2.21}$$

where O is a matrix of size $v \times (N-v)$ containing zeros, I_1 is a identity matrix of size v and I_2 is an identity matrix of size N. The effect of the CP is that it converts the linear convolution of the CIR into a *circular* convolution. If $\underline{r}(m) = [r_{m,0}, .., r_{m,N-1}]^T$ is the vector of received OFDM symbols after discarding the CP and assuming *perfect synchronisation* and $v \geq N_h - 1$, it can be shown that,

$$\underline{r}(m) = \frac{1}{\sqrt{N}}\mathbf{H}\mathbf{F}^*\underline{A}(m) + \underline{w}(m) \tag{2.22}$$

where $\underline{w}(m)$ is the noise vector and $\mathbf{H}$ is the $N \times N$ circulant matrix given by,

$$\mathbf{H} = \begin{bmatrix} h_0 & 0 & \dots & h_{N_h-1} & \dots & \dots & h_1 \\ h_1 & h_0 & 0 & & h_{N_h-1} & \dots & h_2 \\ \vdots & \ddots & \ddots & & & \ddots & \vdots \\ & & \ddots & \ddots & & & h_{N_h-1} \\ h_{N_h-1} & & & \ddots & \ddots & & \\ \vdots & \ddots & & & \ddots & \ddots & \\ 0 & \dots & h_{N_h-1} & & \dots & h_1 & h_0 \end{bmatrix} \tag{2.23}$$

Demodulation by the normalised DFT at the receiver yields,

$$\frac{1}{\sqrt{N}}\mathbf{F}\underline{r}(m) = \frac{1}{N}\mathbf{F}\left(\mathbf{H}\mathbf{F}^{*}\underline{A}(m) + \underline{w}(m)\right) \tag{2.24}$$

which can be simplified into,

$$\frac{1}{\sqrt{N}}\mathbf{F}\underline{r}(m) = \mathbf{\Delta}\underline{A}(m) + \underline{W}(m) \tag{2.25}$$

where $\mathbf{\Delta}$ is the size N diagonal matrix containing the DFT of the CIR $\underline{h}$ and $\underline{W}(m)$ is the DFT of the noise vector. The DFT output consists of a summation of random complex exponentials. Hence, for a system with a sufficiently large value of N, from the Central Limit Theorem the output of the DFT will converge to a Gaussian distribution. Since the DFT is a linear operation, for an input signal $w(m)$ drawn from a Gaussian process, the output statistics of $\underline{W}(m)$ will also be Gaussian. It is assumed in the rest of this thesis that N is large enough so that $\underline{W}(m)$ has the same statistical characteristics as $\underline{w}(m)$. In other words, the demodulated output of the lth subchannel in the mth block is given by,

$$Y_{m,l} = A_{m,l}H_l + W_l \tag{2.26}$$

where H_l is the coefficient of the frequency domain CTF approximated at subchannel l. Under the same assumptions (2.26) can also be written as,

$$Y_{m,l} = \frac{1}{N}\sum_{n=0}^{N-1}\left\{\left\{\sum_{k=0}^{N-1} A_{m,k}H_k e^{j2\pi\frac{kn}{N}}\right\}\right\}e^{-j2\pi\frac{ln}{N}} + W_l \tag{2.27}$$

In practical OFDM systems, the filter elements will often not have a linear phase response and hence a constant group delay. Consequently, carriers of some subchannels will arrive at the receiver at different time delays to others. The CP of these systems are extended beyond the CIR length to absorb the variation in the group delay. In all systems presented in this thesis, it is assumed that the filters have linear phase response, yielding a constant absolute group delay hence, the CP is set to be equal to the CIR length.

2.4.2 Frequency Domain Equaliser

It is evident from (2.26) that the symbols on each subchannel can only be detected properly if the CTF is also estimated. The required correction amounts to only one complex division per subchannel, which is performed by the Frequency Domain Equaliser (FEQ) of the OFDM system. This is one major advantage of OFDM over Single Carrier (SC) systems that use time domain equalisation, which need complex and perhaps lengthy equalisers to nullify the effect of the channel. The method adopted for the conventional system employed in the simulations is to transmit a known training symbol occupying OFDM symbol number N_t of each burst. In the simulations it is set to $N_t = 0$, i.e. the training symbol is sent at the beginning of the burst. The training symbol is denoted as, $\underline{\tilde{A}} = [\tilde{A}_{N_t,0}, .., \tilde{A}_{N_t,N-1}]^T$. Using the corresponding demodulated symbols $Y_{N_t,l}$, $0 \leq l \leq N-1$, the FEQ coefficients are calculated as,

$$C_{N_t,l} = \frac{Y_{N_t,l}}{\tilde{A}_{N_t,l}}, \quad 0 \leq l \leq N-1 \tag{2.28}$$

where $C_{N_t,l}$ approximates CTF H_l on subchannel l. If the CIR is time varying, the FEQ coefficients will have to be updated accordingly using pilot symbols that are transmitted throughout the burst. Since it is assumed throughout this work that only short bursts are transmitted, it has been assumed that the CIR remains approximately constant throughout the burst (see appendix B for further details) and consequently the FEQ coefficients are not updated within the burst. This assumption is made throughout the thesis. The symbols after the FEQ for all other OFDM blocks m are given as,

$$\hat{Y}_{m,l} = \frac{Y_{m,l}}{C_{N_t,l}}, \quad 0 \leq l \leq N-1\,. \tag{2.29}$$

The decoded symbols, $\hat{A}_{m,l}$ are obtained by sending $\hat{Y}_{m,l}$ through a slicer. The CTF estimation by (2.28) is obviously affected by AWGN. The error can be reduced by sending more than one training symbol and taking an average of all the estimations. For the simulations presented in all chapters except for chapter 4 and chapter 5, an average of three such symbols is considered. Since the Schmidl

and Cox Algorithm (SCA) is used in the work presented in chapters 4 and 5, the second training symbol of the SCA is used for channel estimation. Since channel estimation is not the focus of the research presented in this work, it will not be dealt with in isolation in the following chapters, however any degradation that is introduced specifically by the channel estimation process is analysed via simulations where appropriate.

Having introduced the basic concepts underlying OFDM systems, in the next chapter the problem of Common Phase Error (CPE) arising as a result of oscillator phase noise will now be addressed by the use of a novel Common Phase Error Correction (CPEC) algorithm.

Chapter 3

Common Phase Error Correction

OFDM has proven to be more sensitive than SC systems to the Phase Noise (PN) of the oscillators used in the up and down conversion process employed at the transmitter and the receiver, respectively [38]. However in a BFWA scenario the Base Station (BS) will have an oscillator with a relatively high accuracy and stability. Consequently, the main contribution to the PN of the system will arise from the local oscillators in the Subscriber Units (SU). This is primarily due to the necessity for cheaper subscriber equipment which results in the use of inexpensive oscillators with lower accuracy and stability. In this chapter it will be assumed that PN will be introduced into the system only at the SU.

It is important to explain the DFT operation in order to understand the susceptibility of OFDM to PN. The DFT of a sampled signal $x(k)$ is defined as,

$$X(n) = \sqrt{\frac{1}{N}} \sum_{k=0}^{N-1} x(k) e^{-j2\pi \frac{kn}{N}} \tag{3.1}$$

where $X(n)$ is equal to the spectrum of $x(k)$ at the sampled frequency points n. The DFT of the complex exponential $x(k) = e^{j2\pi f_h kT}$ with frequency f_h and sample spacing T is given as,

$$X(n) = e^{j\pi f_h TN - n\frac{N-1}{N}} \frac{\sin[\pi(f_h TN - n)]}{\sin[\pi(f_h TN - n)/N]}. \tag{3.2}$$

Now let,

$$f_h TN = m + \epsilon \tag{3.3}$$

where m is the discrete frequency and ϵ is the relative frequency deviation. The magnitude response of (3.2) with the substitution of (3.3) is given as;

$$|X(n)| = \left| \frac{\sin[\pi(m - n + \epsilon)]}{\sin[\pi(m - n + \epsilon)/N]} \right|. \tag{3.4}$$

The response of $|X(n)|$ in (3.4) with frequency deviation, $\epsilon = 0$ is shown in figure 3.1 for $N = 16$ at two discrete frequencies, $m - n = 0$ and $m - n = -1$. It shows that an unwindowed (i.e. rectangular window) DFT response has high sidelobes with the first sidelobe just 13 dB below the mainlobe. However, as long as ϵ is zero (or an integer value) the responses remain orthogonal to each other.

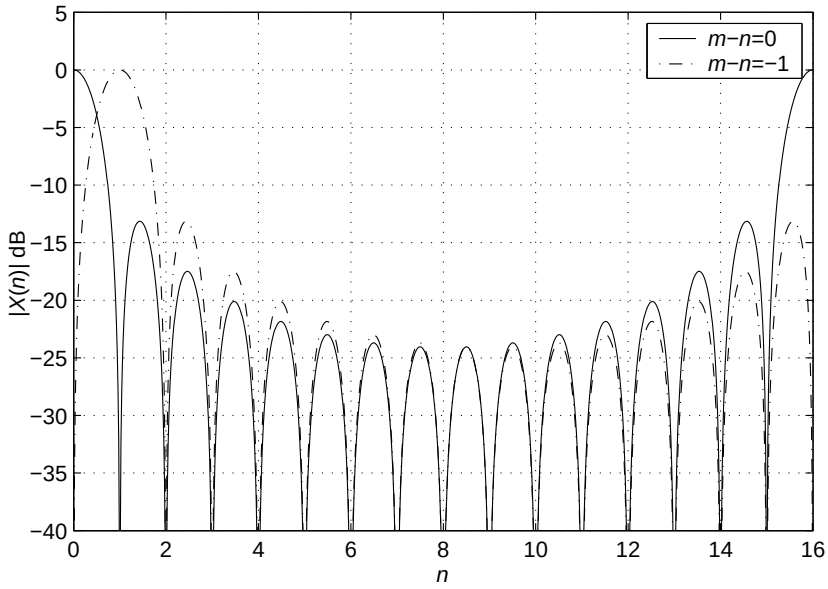

Figure 3.1: Magnitude response of the DFT due to a complex exponents of two different frequencies with $N = 16$

Figure 3.2 shows the effect of leakage caused by non zero values of frequency deviation, ϵ. It shows that even with a small value of deviation, e.g. $\epsilon = 0.4$, there is significant interference from the given subchannel to the others. Also the

relatively low data rate (and hence the bandwidth) of the OFDM carriers makes synchronisation more difficult which raises system susceptibility to PN [39].

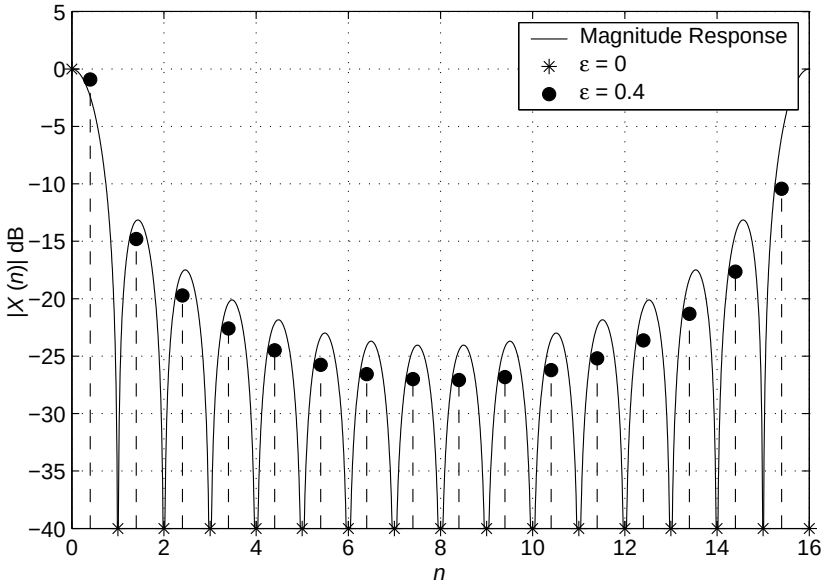

Figure 3.2: The effect of frequency deviation ϵ on the DFT due to a complex exponent of zero frequency with $N = 16$

3.1 Phase Noise Mask

The PN causes spurious signals to be added to the tuning voltage of the Voltage Controlled Oscillator (VCO). This in turn introduces undesired phase distortion depending on the magnitude of the PN. The quality of the oscillators is usually represented as the PN Power Spectral Density (PSD) as a function of the offset frequency. This characteristic is also known as the PN mask. The amplitude is given in dBc/Hz, which means the noise power density in a 1 Hz bandwidth relative to the total carrier power. However any phase information concerning the PN is lost when the oscillator quality is represented only as a PSD. If the PN has a phase component it will cause an amplitude distortion of the overall system besides the phase distortion it introduces [40]. The latter effect is more

significant [40] and hence in this work it will be assumed that the PN introduces only a phase distortion.

It is important to describe the components of a practical OFDM receiver to understand the effect of PN. The front end of the OFDM receiver contains a Tuner, an Intermediate Frequency (IF) amplifier, an I/Q demodulator and an A/D converter. The conversion to baseband may be either direct or more usually via single or double down conversions through one or two IF stages. The Radio Frequency (RF) modulated signal from the antenna is amplified by a Low Noise Amplifier (LNA) before frequency down conversion in a Mixer driven by a Local Oscillator (LO). The IF amplifier filters out the adjacent channels and amplifies the wanted signal. The I/Q demodulator delivers the complex baseband signal in the form of an in-phase component, I and a quadrature component Q. After lowpass filtering, A/D conversion yields sampled values of the received complex baseband signals.

To permit receiver tuning, the LO is usually implemented as a tunable VCO. The stability of the VCO is maintained by the use of a Phase Lock Loop (PLL). Figure 3.3 shows the main components of a PLL based frequency synthesiser [40].

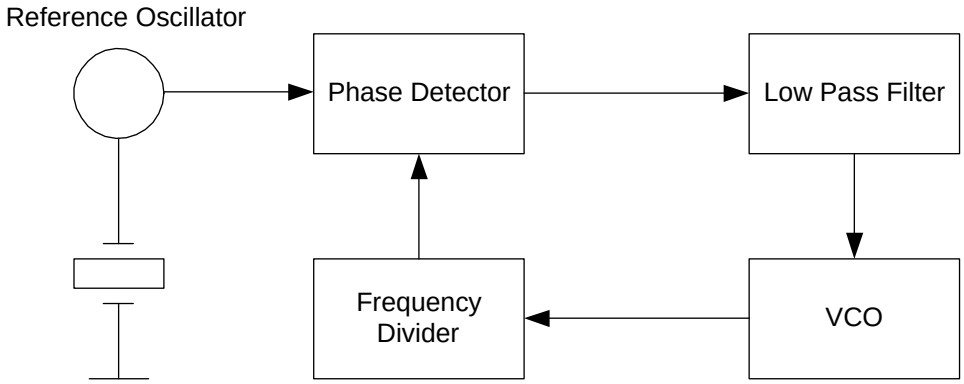

Figure 3.3: Block diagram of a PLL frequency synthesiser

The reference oscillator provides a stable frequency that is usually maintained by the use of a crystal tuning element. The phase detector compares the phase of the VCO signal (following frequency division) and generates an output proportional to the difference of the phase between this and the reference source. In

general the higher the carrier frequency, the greater is the oscillator PN. The VCO is the main cause of PN since it operates at the carrier frequencies. All disturbances of the VCO are imposed upon the signal. If the VCO has a wide frequency range the tuning sensitivity is very high. Consequently even the smallest spurious signals added to the tuning voltage will give rise to an undesired angle modulation when the VCO runs free [41]. The signal from the phase detector is passed through a low pass loop filter, to generate the VCO tuning voltage. The overall transfer function of the PLL determines the damping ratio and the loop bandwidth. The action of the PLL is to reduce the PN within the loop bandwidth, as given by its transfer function [40]. The total PN density of a PLL synthesiser system is given by,

$$S_{\psi}(f) = S_{VCO}(f)H_{PLL}(f) + S_{REF}n^2 + S_{\delta} \tag{3.5}$$

where S_{VCO} is the PN density of the VCO, H_{PLL} is the is the overall transfer function of the PLL, S_{REF} is the PN density of the reference oscillator, n is the divide ratio of the frequency divider and S_{δ} is the additional PN density of all other sources [40]. S_{REF} usually decreases with frequency and S_{VCO} is controlled by H_{PLL}. A typical one-sided spectrum for $S_{\psi}(f)$ is shown in figure 3.4.

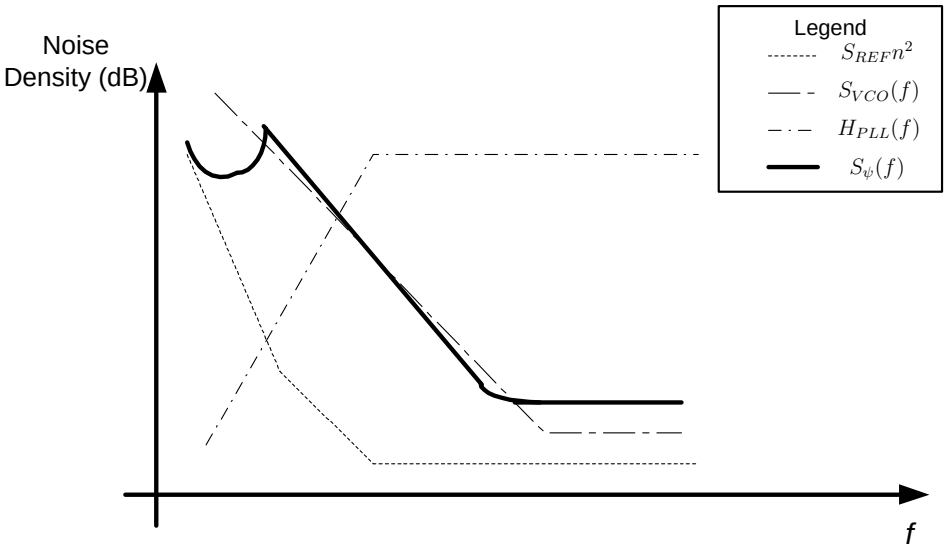

Figure 3.4: Components of the PN density

It can be concluded that a typical PN density will have a flat region close to the the carrier frequency and will then roll off to a PN floor. The published literature shows that there are two main approaches used to model the PN. The authors in [38, 42] model PN as a non stationary, infinite power Weiner process. More often as in [43] and [44], PN is considered as a stationary, band limited, finite power process. In such models, the PN is approximated by a piece-wise linear function in the log-linear domain. The latter model is adopted in this contribution.

The PN is modelled as a phasor $e^{j\psi(n)}$, where the sampled PN process $\psi(n)$ is zero-mean and wide-sense stationary with a narrow band Power Spectral Density (PSD) mask, $S_\psi(f)$ given by (3.6) having a finite power σ_ψ^2 [43]. So,

$$S_\psi(f) = 10^{-c} + \begin{cases} 10^{-a} & |f| < f_l, \\ 10^{-(f-f_l)(b/f_h-f_l)-a} & f > f_l, \\ 10^{(f+f_l)(b/f_h-f_l)-a} & f < -f_l \end{cases} \tag{3.6}$$

where parameter c determines the noise floor of the oscillator and a determines the noise PSD from the center frequency out to a frequency of $\pm f_l$. Parameter b gives the noise fall off rate and at f_h the noise PSD is 10b dB lower than the value at f_l (See figure 3.5). Typical parameter values for a 5.2 GHz synthesised source are $a = 8$, $b = 2$, $c = 12$, $f_l = 10$ kHz and $f_h = 100$ kHz [44]. Figure 3.6 shows the one-sided PN mask of the simulated PN mask for the same parameters. The frequency axis is normalised to half-sampling frequency. We have assumed that the sampling frequency is 20 MHz.

The oscillators practically used by operators for BFWA systems, for example [45, 46] have PSD of PN of a similar order as given in [44]. Typically, the values for f_h are of the order of 100 kHz and for a it is of the order of 7-12. Hence the models used in the following section are quite close representations of PN of oscillators used practically in the industry.

The two most important parameters in determining the quality of an oscillator are the PN bandwidth, which is mainly determined by f_l and the PN power, which is determined primarily by a and c. Signal to Phase Noise Ratio (SPNR) will be widely used as the performance criteria for the comparison of results in latter sections. It is defined as the ratio between the signal power and PN power. In

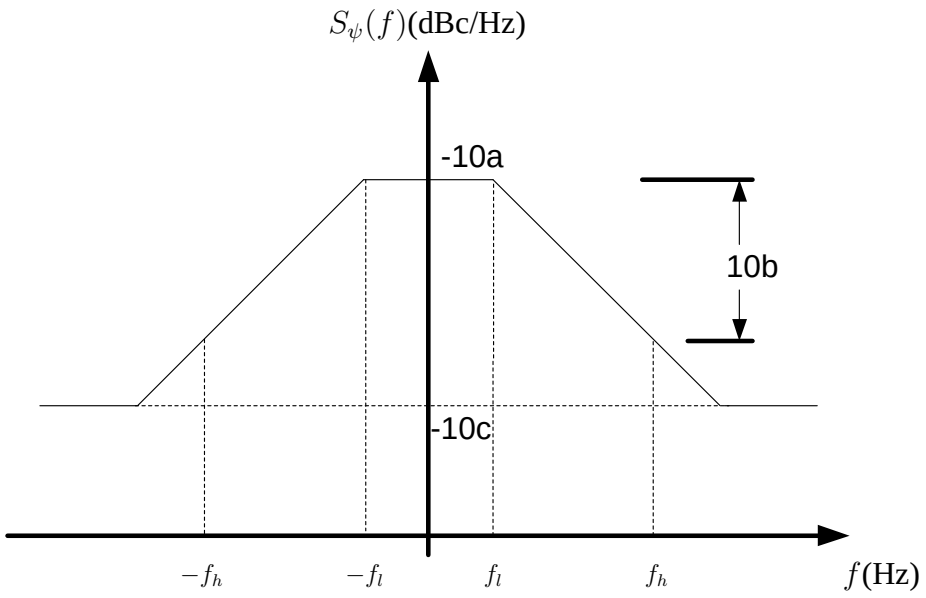

Figure 3.5: Phase Noise PSD of a typical oscillator

most cases, as is done in this work, the signal power and the carrier power are normalised to unity. In which case, the SPNR is equal to the inverse of the PN power. For a given PN bandwidth, SPNR will show how robust the system is against PN. It has been proven in [47, 48] that the degradation experienced in an OFDM system without any correction depends on PN variance but not the shape of the PN spectrum. Hence SPNR is a representative criteria to compare performance.

3.2 Analysis of the Effect of Phase Noise on OFDM

A good analysis on the subject is given in [48], but a different approach is adopted here. The results, however are similar. The PN is modelled as a multiplicative error term $e^{j\psi(n)}$ and the ideal received sequence given in (2.19) is changed to,

$$r_n = [(s_n * h_n) + w_n]\, e^{j\psi(n)}\ . \tag{3.7}$$

Assuming perfect synchronisation and the length of the Cyclic Prefix (CP) is

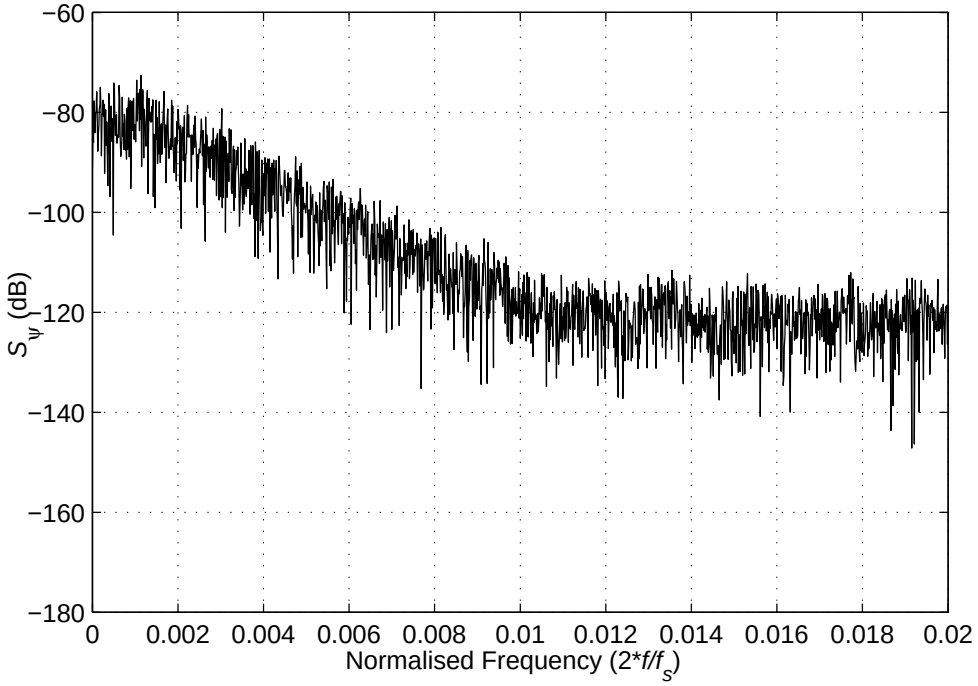

Figure 3.6: Simulated one-sided PN mask for $a = 8$, $b = 4$, $c = 12$, $f_l = 10$kHz, $f_h = 100$kHz at $f_s = 20$MHz

greater than the length of the Channel Impulse response (CIR), $v \geq N_h - 1$, the demodulated signal at the lth subchannel in the mth block is now given by [44],

$$Y_{m,l} = \frac{1}{N} \sum_{n=0}^{N-1} \left\{ \left\{ \sum_{k=0}^{N-1} A_{m,k} H_k e^{j2\pi \frac{kn}{N}} \right\} e^{j\psi(n)} \right\} e^{-j2\pi \frac{ln}{N}} + W_l \tag{3.8}$$

compared with that presented previously in (2.27). Here W_l is the contribution due to AWGN. Note that the rotation caused by PN does not change the statistical characteristics of AWGN [48]. If $\psi(n)$ takes small values, then for analytical purposes a simplifying assumption using the first two terms of the Taylor series expansion is,

$$e^{j\psi(n)} \approx 1 + j\psi(n), \quad \psi \ll 1 \,. \tag{3.9}$$

Using this assumption in (3.8) gives,

$$Y_{m,l} = \frac{1}{N}\sum_{n=0}^{N-1}\left\{\left\{\sum_{k=0}^{N-1} A_{m,k}H_k e^{j2\pi\frac{kn}{N}}\right\}(1+j\psi(n))\right\}e^{-j2\pi\frac{ln}{N}} + W_l \qquad (3.10)$$

which can be further simplified to,

$$\begin{aligned} Y_{m,l} \;\approx\; & A_{m,l}H_l + A_{m,l}H_l\frac{1}{N}\sum_{n=0}^{N-1} j\psi(n) + \\ & \frac{1}{N}\sum_{\substack{k=0\\k\neq l}}^{N-1} A_{m,k}H_k\sum_{n=o}^{N-1}(1+j\psi(n))e^{-j2\pi\frac{(l-k)n}{N}} + W_l \end{aligned} \qquad (3.11)$$

The first term on the r.h.s. of (3.11) is the useful component. The channel coefficient for subchannel l can easily be equalised by the FEQ coefficient $C_{N_t,l}$, as calculated in (2.28). The second component introduces an equal phase rotation on to each subchannel and is *independent* of the particular subchannel concerned, l. This is commonly known as the Common Phase Error (CPE). The third term is the Inter-Carrier Interference (ICI) caused by contributions from all subchannels $k \neq l$ on l owing to the loss of orthogonality. Let us denote these components as ψ_{CPE} and ψ_{ICI} respectively. Unlike the CPE, the ICI is not easy to estimate.

3.2.1 Common Phase Error

The CPE is given as,

$$\psi_{CPE} = \frac{1}{N}\sum_{n=0}^{N-1} j\psi(n) \qquad (3.12)$$

which results in a rotation of the entire signal constellation within an OFDM symbol. The CPE is linearly related to the sampled PN process $\psi(n)$ and as a result is Gaussian with mean and variance given by [39],

$$E[\psi_{CPE}] = \frac{1}{N}\sum_{n=0}^{N-1} jE[\psi(n)] = 0 \qquad (3.13)$$

$$\sigma^2_{CPE} = E[|\psi_{CPE}|^2] = \int_{-f_s/2}^{f_s/2} \frac{S_\psi(f)}{N^2}\left|\frac{\sin((\pi Nf)/f_s)}{\sin((\pi f)/f_s}\right|^2 df \qquad (3.14)$$

where f_s is the sampling frequency. It can be noted that the variance σ^2_{CPE} is monotonically decreasing with N. It implies that OFDM systems using fewer subchannels within a given bandwidth will experience a larger rotation of the constellation owing to CPE [39].

3.2.2 Inter Carrier Interference

The ICI component depends upon the data symbols in the current OFDM symbol. Assuming that the number of subchannels, N is large and since the data symbols are statistically independent, we can then assume that the ICI component is also a zero mean Gaussian process. Consequently, the effect of ICI is similar to that of AWGN. Since both CPE and ICI are Gaussian, the variance of both the CPE and the ICI should be equal to the variance of the sum of both components. Hence the variance of the ICI component can be calculated as [39],

$$\sigma^2_{ICI} = E[|\psi_{ICI}|^2] = \int_{-f_s/2}^{f_s/2} S_\psi(f)\, df - \int_{-f_s/2}^{f_s/2} \frac{S_\psi(f)}{N^2} \left| \frac{\sin((\pi N f)/f_s)}{\sin((\pi f)/f_s} \right|^2 df \tag{3.15}$$

It can be noted that σ^2_{ICI} is monotonically increasing as a function of N [39]. A similar conclusion is drawn in [43]. Intuitively, the effect of N on the CPE and the ICI components can be explained as follows. For a given transmission bandwidth the inter carrier spacing of the OFDM subchannels is reduced if a higher value of N is used. For a given non-ideal oscillator with a certain PN bandwidth, each subchannel will be corrupted by signals that fall within the PN bandwidth. Hence, the ICI will be higher for a higher N since there is a higher probability of more subchannels falling within the same PN bandwidth. Since the sum of the variances of CPE and ICI should remain the same, the CPE component will reduce with an increase in N. The figures in 3.7 show the demodulated constellation (i.e. after the FFT) at the receiver of all OFDM symbols of the *whole* burst for two systems, one with $N = 64$ and the other with $N = 256$. Both are subjected to a SUI-II [23] CIR and AWGN yielding an SNR of 20 dB and a SPNR of 15 dB. The plots are the result of demodulating 2500 OFDM symbols for the $N = 64$ system and 625 OFDM symbols for the $N = 256$ system. Both systems used QPSK for mapping and hence the total QPSK symbols demodulated for both systems was 160,000.

The plot for $N = 64$ shows a greater phase rotation owing to CPE, whereas for the system with $N = 256$ more dispersion is evident owing to the increased level of ICI. Alternatively, for a given OFDM system with a certain inter-carrier spacing (that is determined by N), the ICI will come to dominate CPE with an increasing PN bandwidth [49, 50].

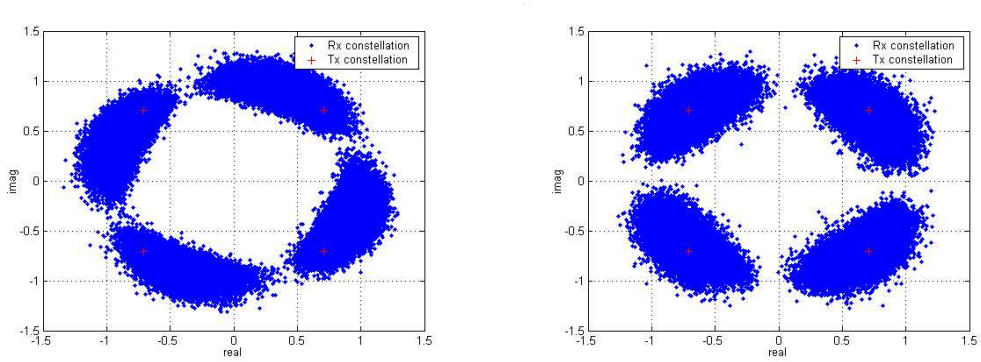

(a) $N = 64$ (b) $N = 256$

Figure 3.7: Constellation of post-FFT data symbols with an AWGN SNR of 20 dB and a SPNR at 15 dB with a SUI-II CIR

3.2.3 Probability of Error Analysis

The effect of CPE on OFDM will be modelled as a rotational component given by a multiplicative error $e^{j\psi_{CPE}}$. Hence if the received sample vector is denoted as r, then the result after CPE is,

$$\tilde{r} = re^{j\psi_{CPE}} \tag{3.16}$$

The ICI component is modelled as an additive Gaussian noise component with variance σ^2_{ICI}. Hence the total additive noise component is a zero mean Gaussian process with total variance being $\sigma^2_T = \sigma^2_{ICI} + \sigma^2_w$, where σ^2_w is the variance due to thermal noise. Hence the input to the slicer is [39],

$$y = \tilde{r} + w_T = (\tilde{x} + n_{Tr}) + j(\tilde{y} + n_{Ti}) \tag{3.17}$$

where $\tilde{x}$ and $\tilde{y}$ are the real and imaginary parts of $\tilde{r}$ respectively and n_{Tr} and n_{Ti} are the real and imaginary components of the total additive Gaussian noise component, respectively. The effect of both components of PN can be represented as shown in figure 3.8. This is a snapshot of *one* demodulated OFDM symbol. The concentric circles represent the contours of the Gaussian dispersion of the data points of each constellation point of the QPSK mapping. Here E_s is the transmitted symbol power.

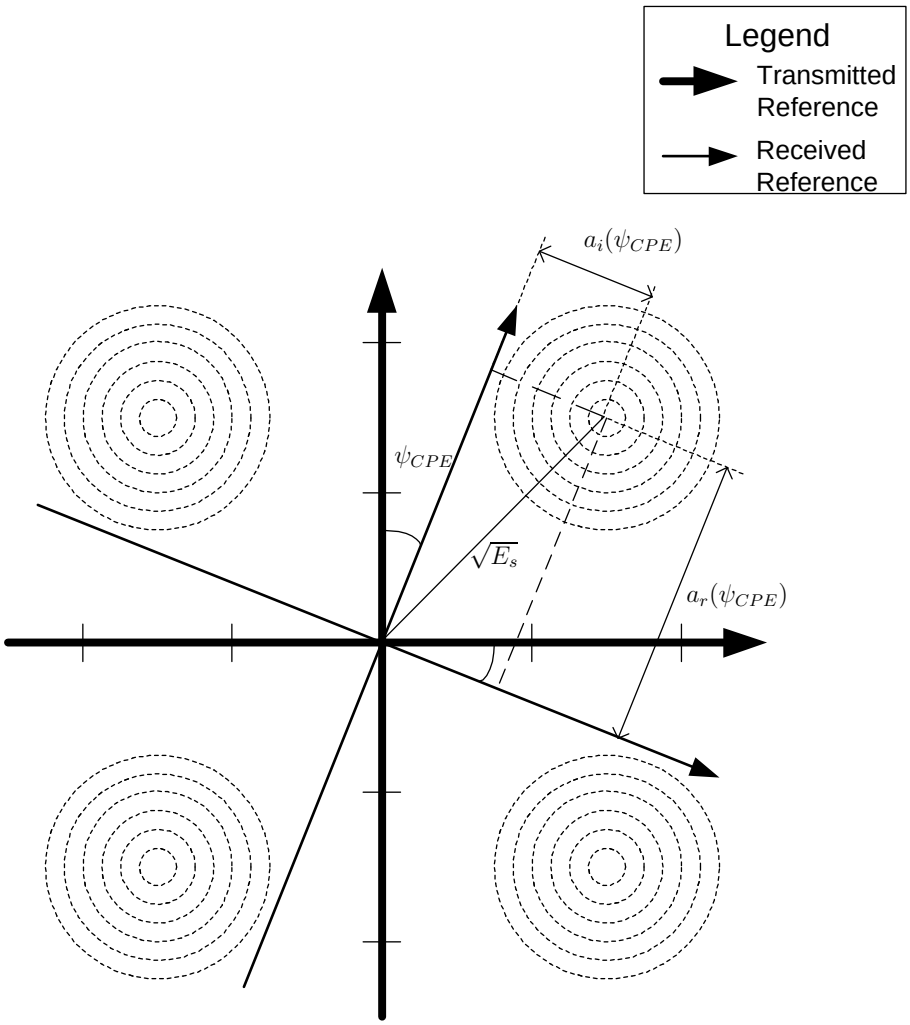

Figure 3.8: QPSK constellation subject to a phase rotation owing to ψ_{CPE}

The real and imaginary components of y are statistically independent Gaussian processes with equal variances. Hence their joint probability distribution is given by [39],

$$P\{x,y\} = \frac{1}{2\pi\sigma_T^2} exp\Big(-\frac{(x-\tilde{x})}{2\sigma_T^2}\Big) exp\Big(-\frac{(y-\tilde{y})}{2\sigma_T^2}\Big)\,. \tag{3.18}$$

The probability for a correct decision for a symbol in the presence of AWGN and PN can be expressed as [51],

$$P_c|_{\psi_{CPE}} = Q\Big(-\frac{1}{\sigma_T}a_r(\psi_{CPE})\Big).Q\Big(-\frac{1}{\sigma_T}a_i(\psi_{CPE})\Big) \tag{3.19}$$

where,

$$a_r(\psi_{CPE}) = \sqrt{E_s}\sin\Big(\frac{\pi}{4} - \psi_{CPE}\Big) \tag{3.20}$$

$$a_i(\psi_{CPE}) = \sqrt{E_s}\cos\Big(\frac{\pi}{4} - \psi_{CPE}\Big)\,. \tag{3.21}$$

The function $Q(.)$ is the area under the tail of the Gaussian PDF and is defined as [27, pg 40],

$$Q(x) = \frac{1}{\sqrt{2\pi}}\int_x^\infty e^{t^2/2}\,dt, \quad x \geq 0\,. \tag{3.22}$$

Hence the Symbol Error Rate (SER) of an OFDM system with no CPE correction for a given rotational angle of ψ_{CPE} can be calculated as [51],

$$\begin{aligned} P_e|_{\psi_{CPE}} \;=\; & Q\Big(\frac{1}{\sigma_T}a_r(\psi_{CPE})\Big) + Q\Big(\frac{1}{\sigma_T}a_i(\psi_{CPE})\Big) - \\ & Q\Big(\frac{1}{\sigma_T}a_r(\psi_{CPE})\Big).Q\Big(\frac{1}{\sigma_T}a_i(\psi_{CPE})\Big) \end{aligned} \tag{3.23}$$

Since Grey coding is used for the QPSK mapping, the overall BER can be assumed to be half of this value. Figure 3.9 shows the theoretical predictions based on (3.23) for OFDM systems with N equal to 64 and 256 subject to AWGN yielding a SNR of 20 dB and PN with $b = 4$, $f_l = 10$ kHz and $f_h = 100$ kHz. Equation (3.14) gives the SER for a particular value of the CPE phase, ψ_{CPE}. The SPNR and the variance of ψ_{CPE} (using equation (3.14)) is determined by the area under the PN mask. The variance of the ICI is determined using (3.15). It is assumed that the ICI has a similar effect to AWGN and that the total additive noise variance σ_T^2 in (3.23) is calculated as the sum of the variance of AWGN and ICI.

The theoretical curves for OFDM systems without CPE correction in figure 3.9 are evaluated by drawing values for ψ_{CPE} from a source having a Gaussian PDF with the variance given in (3.14) and, using expectation theory, integrating over all values of ψ_{CPE}. The simulated values are also shown as points for comparison. The figure shows that the theoretical predictions show very close agreement with the simulated points. It also proves that the performance of the OFDM system under consideration when subject to only AWGN and PN with $f_h = 100$ kHz does not depend upon the number of subchannels, N. It also shows an error floor at a BER of approximately 10^{-12}. This can be attributed to the fact that AWGN and ICI become more dominant over CPE at high values of SPNR.

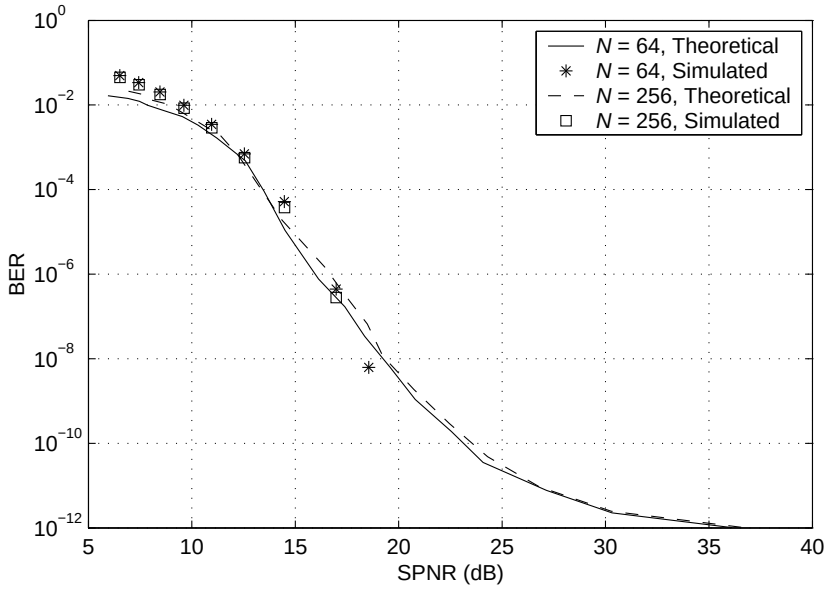

Figure 3.9: The theoretical and simulated results for OFDM systems without CPE correction with N = 64 and 256 subject to AWGN yielding an SNR of 20 dB and PN with f_h = 100 kHz

3.3 Related Work

In this section related work not cited previously in the chapter will be summarised. Pollet in [38] was the first to show that OFDM is orders of magnitude more sen-

sitive to PN and frequency offsets than Single Carrier (SC) systems. Many other authors have also analysed the effect of PN in terms of CPE and ICI, for example [43, 52, 44]. The author in [43] further proposes a feedback CPE correction method for an OFDM system with a total of 2048 subchannels by transmitting pilot symbols in some of the subchannels in every OFDM symbol. The pilot symbol positions are dynamically rotated after every OFDM symbol to avoid them falling into a frequency null. The known pilot symbols are used to estimate the CPE by determining the phase change of each received pilot. A reliability estimate is given to each pilot before the CPE is estimated, but the author does not specify how these reliability estimates are generated. The author in [53] assumes a PN mask model similar to that in [38]. Analytical solutions of the error rate performance are given for BPSK, QPSK, differential BPSK and differential QPSK. It is proposed to implement the differential modulation scheme within the OFDM symbol (in the frequency domain) rather than between adjacent OFDM symbols in order to minimise the effect of phase noise. The conclusions show that for QPSK, the performance strongly degrades if the 3dB bandwidth of the PN mask is greater than 0.04 of the intercarrier spacing. Armada in [52] concludes that the effects of PN can be corrected when the PN bandwidth is smaller than the intercarrier spacing. Hanzo in [41] compares the effect of PN on an OFDM modem and a serial modem. The comparisons use coloured (using a PN mask) and white PN models and it is found that the performance is similar for all PN models based on PN power. This confirms that irrespective of the mask, PN power determines the performance. The author in [47] analyses the effect of PN on Orthogonal Frequency Division Multiple Access (OFDMA) and Frequency Division Multiple Access (FDMA) systems in a multi user scenario and compares it with conventional OFDM. The authors concluded that when all subchannels have the same power and are subjected to the same PN mask, the degradation is equal to that in OFDM and also that FDMA is slightly more robust than OFDMA.

3.4 Common Phase Error Correction Algorithm

An algorithm is proposed in this section to estimate and correct for the CPE component in each OFDM symbol. Since the effect of ICI is similar to AWGN, and as-

suming that the number of subchannels in the OFDM system, N is large then with reference to (3.11) an estimate of the CPE for the mth OFDM symbol, $\hat{\psi}_{CPE,m}$, can be made by finding the mean of the phase rotations caused to all the subchannels in a particular symbol. In maintaining the argument that assigning subchannels to transmit pilot symbols leads to inefficiency in a BFWA scenario, the algorithm that is proposed in this section does *not* rely on pilot symbols. Instead it is data driven, utilising subchannels that are used to transmit data. However, the CPE estimate could be seriously affected by errors in those subchannels experiencing a low SNR owing to spectral nulls in the channel response H_l. Hence we only select those subchannels with $|H_l|$ above a certain threshold. The subset of subchannels is referred to as $\underline{d}$, where $\underline{d} \subset [0, ..N-1]$. The criteria applied is to select subchannels with $|H_l|$ in excess of a standard deviation above the mean of the Channel Transfer Function (CTF). Note that for any algorithm that has a fixed assignment of pilot symbols to subchannels, then they run the risk of falling in to these spectral nulls. Since the CPEC algorithm proposed here selects the subchannels at the receiver, it has the capability to adapt to varying channel conditions.

For post-FEQ symbol m, the outputs of these subchannels $\hat{Y}_{m,d}$ are sent through a slicer to obtain $\tilde{Y}_{m,d}$. If the number of subchannels selected for the CPE estimation is N_d, then the CPE estimate for symbol m is,

$$\hat{\psi}_{CPE,m} = \frac{1}{N_d} \sum_{\substack{l=0 \\ l \in \underline{d}}}^{N-1} (\angle \hat{Y}_{m,l} - \angle \tilde{Y}_{m,l}) \,. \tag{3.24}$$

This parameter will be referred to as the CPE Symbol Estimate (CPESE). The effect of CPE is cancelled by multiplying the post-FEQ symbol $\hat{Y}_{m,l}, 0 \leq l \leq N-1$ by $e^{-j\hat{\psi}_{CPE,m}}$. The CPE has to be estimated for each OFDM symbol at the output of the FEQ. Although the CPE changes slowly, it can have a considerable variance. Figure 3.10 shows the CPESE for a system with $N = 64$ at a SNR of 20 dB and a SPNR of 15.5 dB.

The channel estimation procedure required for the FEQ is conventionally performed at the beginning of the data burst and this estimate remains the same unless a new training symbol is sent. If the block containing the training symbol has a significant value of CPE, $\hat{\psi}_{CPE,N_t}$, then the channel phase estimation,

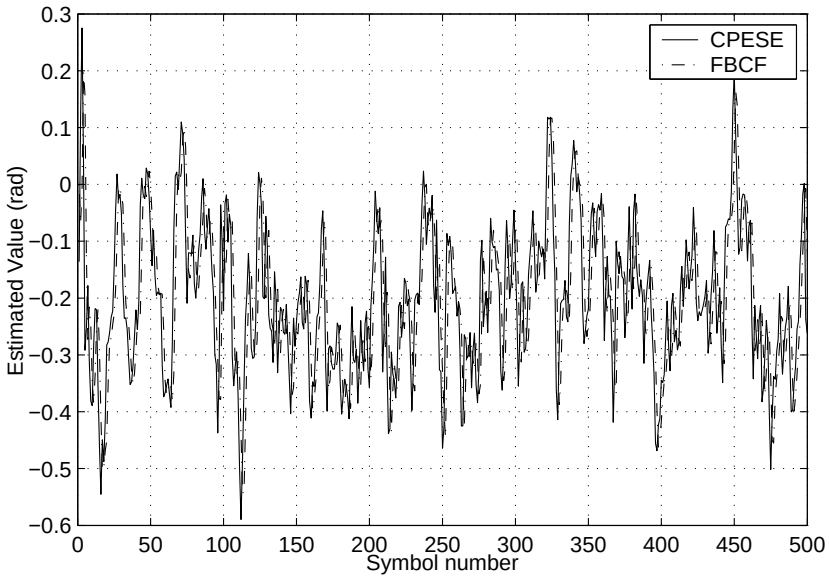

Figure 3.10: The variation of CPESE for $N = 64$ at an SNR of 20 dB and SPNR of 12.5 dB

$\angle C_{N_t,l}$ of (2.28) will be offset by a value approximately equal to $\hat{\psi}_{CPE,N_t}$. All estimates of the CPE for the subsequent symbol will be affected by the offset caused by the FEQ. (i.e. the total CPE estimate for any subsequent symbol m is $\hat{\psi}_{CPE,m} + \hat{\psi}_{CPE,N_t}$). Since the CPEC algorithm relies on data driven estimation, this may cause the selected subchannels in $\underline{d}$ to be phase rotated sufficiently so as to give rise to errors in those subchannels. Hence the CPESE will be prone to errors, which in turn renders the entire decoding process more susceptible to errors.

To remove the effect of $\hat{\psi}_{CPE,N_t}$ from subsequent symbols, it is proposed to include a simple Moving Average Filter (MAF) of length N_w containing CPESEs from previous symbols. The contents of the filter are,

$$\underline{\psi}_{CPE,m} = [\hat{\psi}_{CPE,m-1}, .., \hat{\psi}_{CPE,m-N_w}] \, . \tag{3.25}$$

The output of the filter is the mean of its contents and is noted as, $\underline{\bar{\psi}}_{CPE,m}$. This mean value is used to update the phase angles of the FEQ for all symbols

$m > N_t$,

$$\angle C_{m,l} = \angle C_{m-1,l} + \underline{\bar{\psi}}_{CPE,m}, \quad 0 \leq l \leq N-1 \,. \tag{3.26}$$

The parameter $\underline{\bar{\psi}}_{CPE,m}$ is referred to as the Feedback Correction Factor (FBCF). Figure 3.10 shows that the FBCF closely tracks the CPESE. The argument can be further explained in the following diagrams. Figure 3.11 shows the actual phase of the CTF and the estimated phase of the CTF ($\angle C_{N_t,l}$) when a low value of $\hat{\psi}_{CPE,N_t}$ is present. The OFDM system for this example has $N = 64$ with a SNR of 20 dB and a SPNR of 15 dB subjected to a SUI-II CIR. Figure 3.12(a) shows a polar plot of the demodulated data following the FEQ ($Y_{m,l}$) corresponding to the OFDM symbol that yields the greatest number of errors within the burst. It shows that the data points are rotated clockwise owing to a combination of the CPE of symbol m and N_t. The data points that are selected to calculate the CPESE are based on these points. It shows that most of the data points lie within the decision boundaries, i.e. the vertical and horizontal axes. A CPEC algorithm that relies only on a CPESE would perform adequately in this case. Figure 3.12(b) shows data points that result if the FEQ is used in conjunction with a FBCF. It shows that the FBCF maintains the data points further within the decision boundaries. Figure 3.12(c) shows the result after the proposed CPEC which employs both the FBCF and the CPESE. Following correction by both factors it can be seen that the data points lie very close to the original constellation points.

A second case is presented in figure 3.13 which shows the estimated phase of the CTF ($\angle C_{N_t,l}$) for a different transmission burst with the same CIR but this time for a larger value of $\hat{\psi}_{CPE,N_t}$. Since the state of the oscillator is random, this value is unpredictable. Figure 3.14(a) shows the demodulated data symbols of the OFDM symbol which generates the greatest number of errors. This time the constellation is rotated counter-clockwise. However it clearly shows that many of the data points after the FEQ ($Y_{m,l}$) have crossed the decision boundaries. Hence, a conventional OFDM system would be subjected to a large number of errors. In addition a CPEC algorithm that relies only on a CPESE will generate an erroneous estimate that will further rotate the data points counter-clockwise. Ultimately the data points will lie in a different quadrant compared to the transmitted ones. The constellation of data points following the FBCF for the same scenario is shown

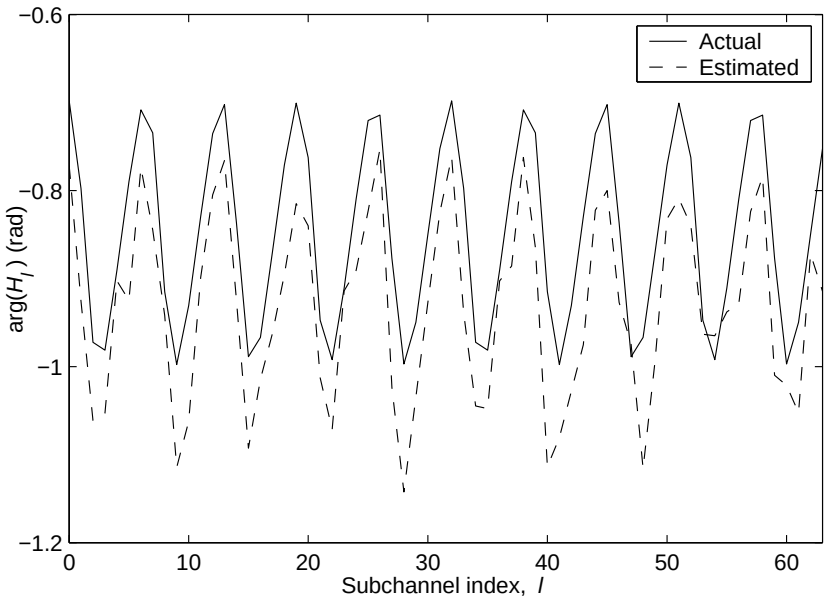

Figure 3.11: Estimation of the phase of the CTF which is offset owing to a low value of $\hat{\psi}_{CPE,N_t}$

in figure 3.14(b). It clearly shows that when the FBCF is used, it is able to track the rotation caused by the FEQ and the CPE and contain the data points to be within the correct quadrant. As shown in figure 3.14(c), a further correction by the CPESE that is based on the data points shown in figure 3.14(b) results in the corrected data points being very close to the original constellation points. Hence it is clear that the *data driven* CPEC algorithm proposed for a coherent OFDM system requires *both* the FBCF and the CPESE to be used.

Figure 3.15(a) shows a subchannel-wise error analysis of the whole burst conducted for the same OFDM system at a SPNR of 15.5 dB. It shows the subchannels selected for CPEC, and the number of errors in the I channel (in black) and the Q channel (in white) as a stacked bar graph. The magnitude plot of the estimated CTF, $|H_l|$ is also superimposed for clarity. At the chosen SPNR, the majority of the subchannels selected for the CPEC algorithm have a very low number of errors in the whole burst, justifying the selection criteria adopted for the algorithm. Figure 3.15(b) shows that all the subchannels are free from errors after the proposed CPEC is used. However, as shown in figure 3.16(a), when the PN power increases

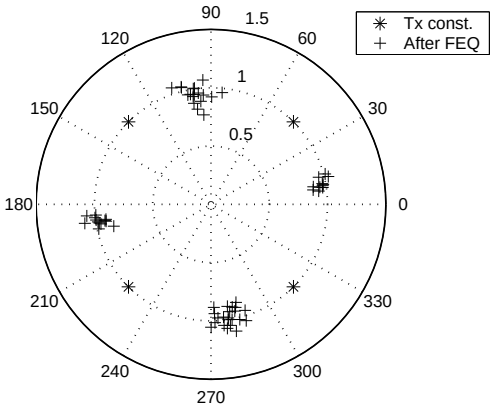

(a) after FEQ

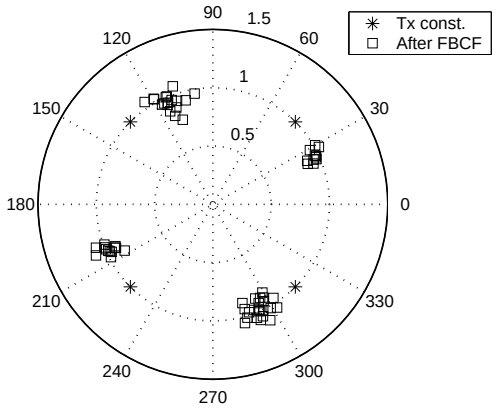

(b) after FBCF

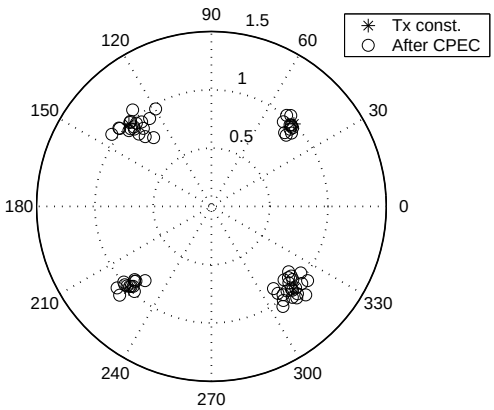

(c) after CPEC

Figure 3.12: Performance of the symbol with most errors and a low value of $\hat{\psi}_{CPE,N_t}$

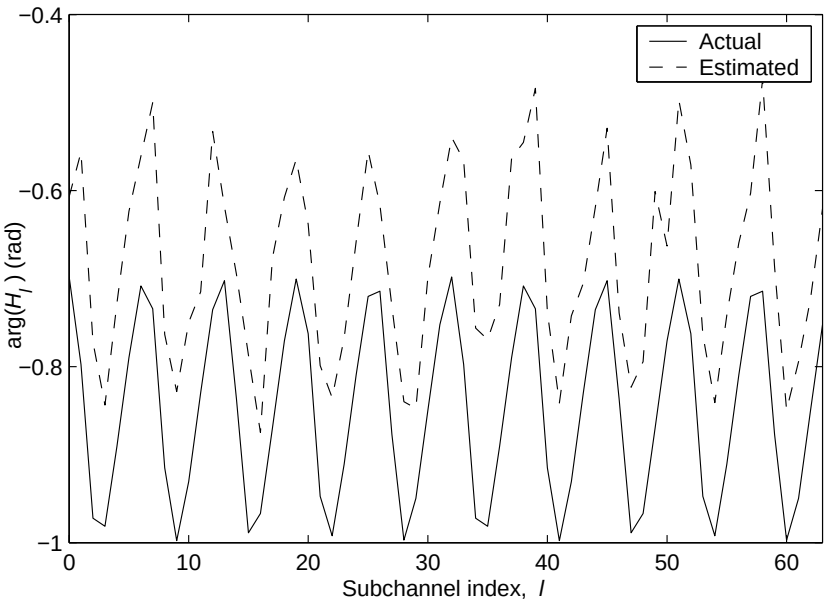

Figure 3.13: Estimation of the phase of the CTF which is offset owing to a high values of $\hat{\psi}_{CPE,N_t}$

beyond an acceptable level (e.g.a SPNR of 9.6 dB), the subchannels selected are no longer subjected to a low number of errors. This leads to errors being generated even when both components of the CPEC algorithm are employed, as shown in figure 3.16(b). Note however that even with errors in the estimation subchannels the total number of errors in the whole burst is significantly smaller after applying CPEC than without. Note also that the total number of errors are equal across the subchannels when the CPEC algorithm is used. This can be attributed to demodulated data symbols falling into the incorrect quadrants even after correction with the FBCF. Hence after subsequent correction with the CPESE, all data points will be rotated to an incorrect quadrant. This will result in the decoded data for these OFDM symbols being erroneous in each subchannel for all the subchannels. The low error rates suggest that the frequency of such an occurrence is very low. For instance in this example out of 2500 OFDM symbols used in the burst, 11 generated errors. Consequently, if a Forward Error Correction (FEC) scheme is used that is based on the data transmitted on each subchannel (rather than across subchannels), it will dramatically improve the BER performance.

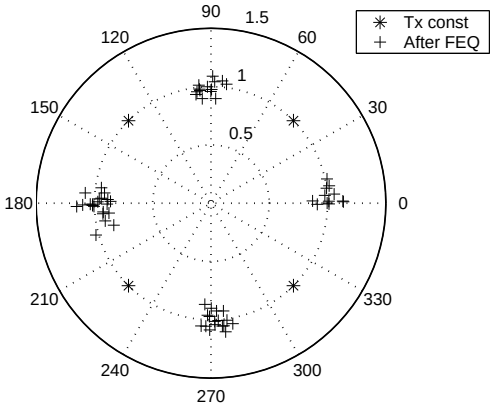

(a) after FEQ

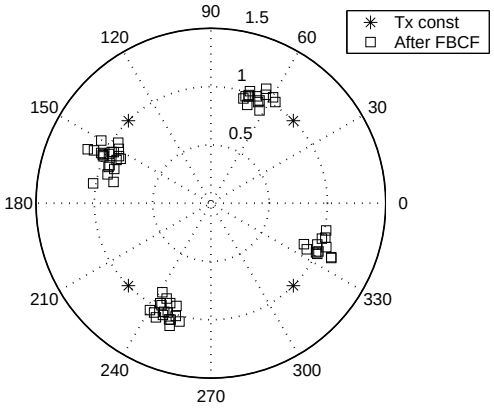

(b) after FBCF

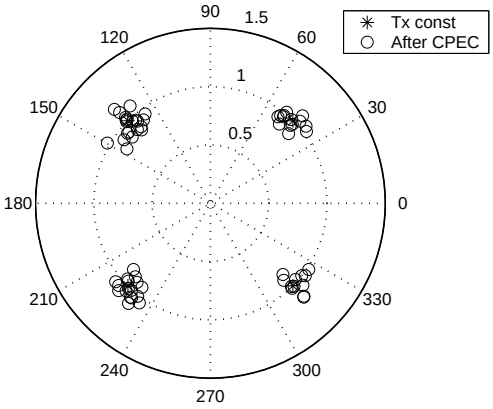

(c) after CPEC

Figure 3.14: Performance of the symbol with most errors and a high $\hat{\psi}_{CPE,N_t}$

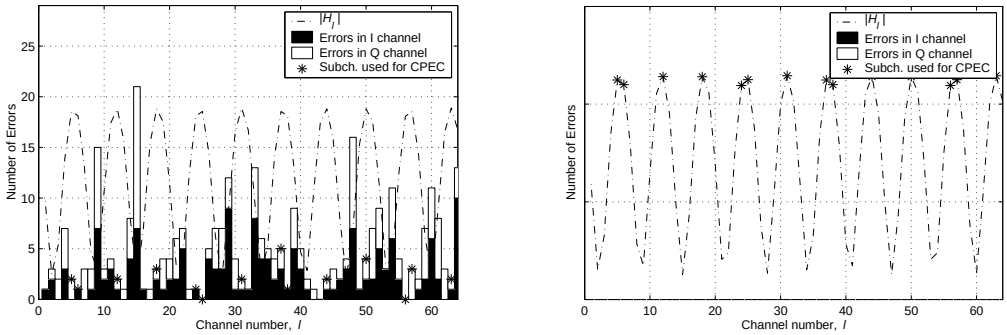

(a) Without CPEC (b) With CPEC

Figure 3.15: Individual subchannel error analysis of OFDM system with 20 dB SNR and 15.5 dB SPNR

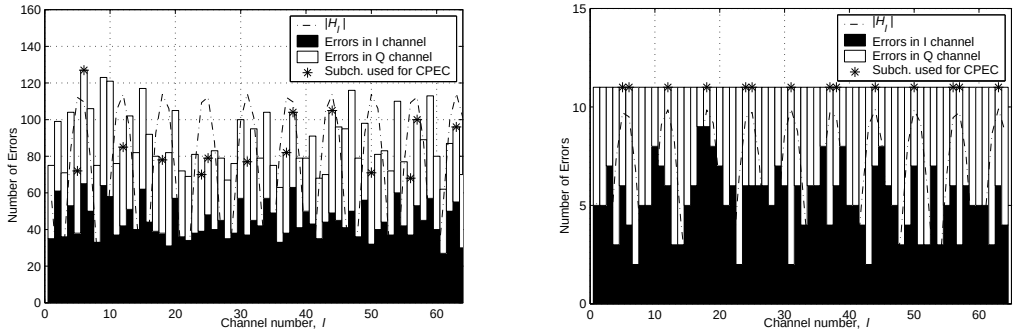

(a) Without CPEC (b) With CPEC

Figure 3.16: Individual subchannel error analysis of OFDM system with 20 dB SNR and 9.6 dB SPNR

The CPEC algorithm can be summarised as follows.

1. Select the subset of subchannels with peaks in the channel transfer function, $\underline{d}$, at the start of the burst based on the calculated FEQ values.

2. Evaluate $\underline{\bar{\psi}}_{CPE,m}$ by finding the mean of the previous N_w CPE estimates in the MAF.

3. Use $\underline{\bar{\psi}}_{CPE,m}$ for each symbol m to update the phase of the FEQ coefficients, $\angle C_{m,l}$. This effectively makes the FEQ track the CPE as closely as possible.

4. Obtain $\hat{Y}_{m,d}$ from the FEQ output and then $\tilde{Y}_{m,d}$ by the use of a slicer. Use the difference in angles of them to get an estimate of the CPE, $\hat{\psi}_{CPE,m}$. Use it to correct the CPE.

5. Update the MAF with $\hat{\psi}_{CPE,m}$ to estimate $\underline{\bar{\psi}}_{CPE,m+1}$.

Figure 3.17 illustrates the CPEC algorithm. The main advantage of the CPEC algorithm is its simplicity and low computational demand. Assuming that the determination of the phase of a complex number is performed via a look up table, the processing of each OFDM symbol requires an additional N_d subtractions, $N_d - 1$ additions and one division for the calculation of the CPESE as required in (3.24) and $N_w - 1$ additions and one division in the calculation of FBCF and finally N additions to update the FEQ angles, as shown in (3.26). Unlike the scheme proposed in [39], which only performs compensation using the CPESE $\hat{\psi}_{CPE,m}$, the FBCF in this scheme is able to continuously track and correct for the error caused by the PN in the FEQ.

Figure 3.18 shows the improvement the CPEC makes to the demodulated constellation for a system with $N = 64$ while figure 3.19 shows the results for a system with $N = 256$.

3.5 Simulation Parameters and Results

To maintain consistency, the SUI-II channel model has been assumed for the simulations [23]. OFDM systems with $N = 64, 128, 256$ have been simulated at a

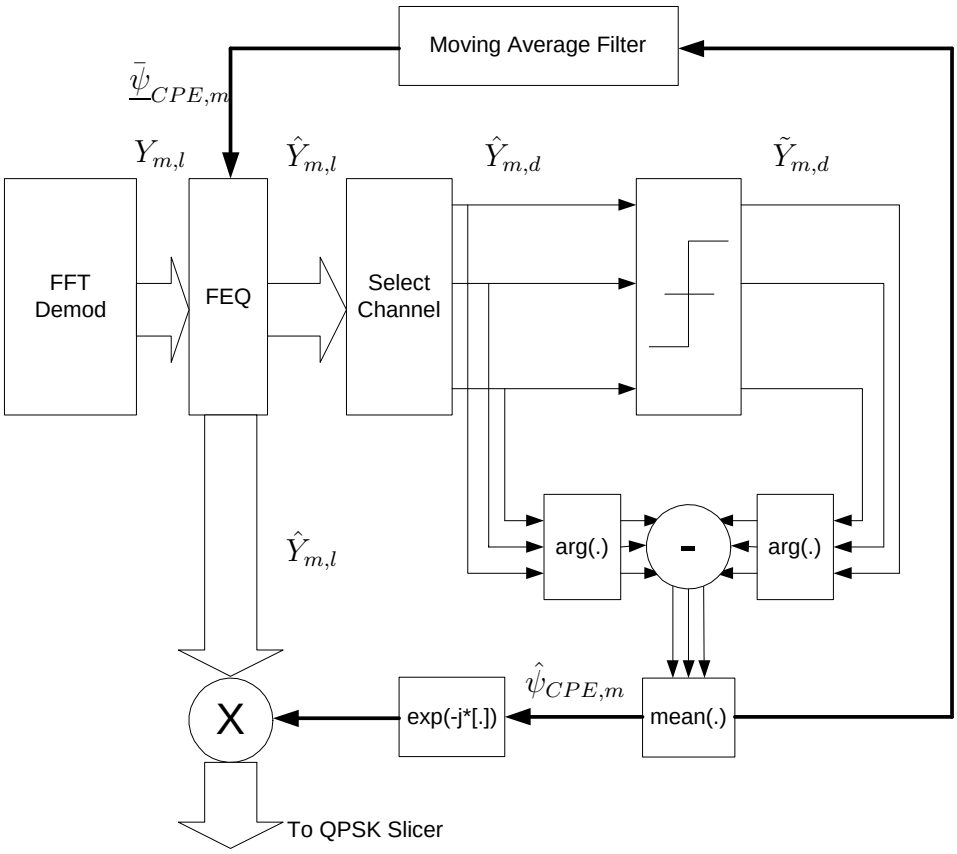

Figure 3.17: CPE Correction (CPEC) algorithm

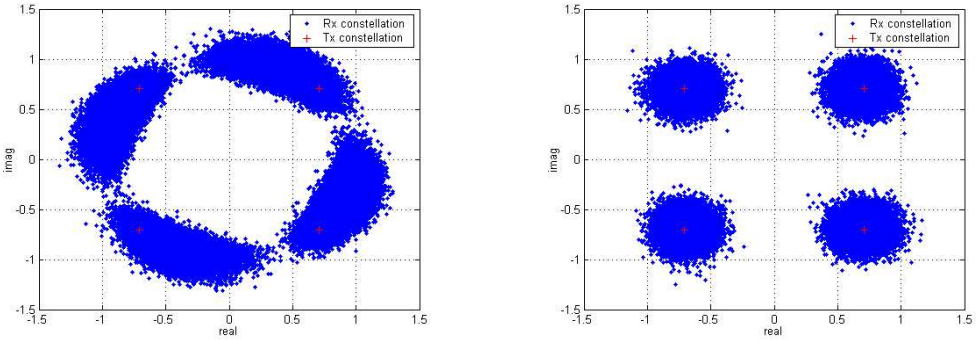

(a) Without CPEC (b) With CPEC

Figure 3.18: Demodulated constellations with (a) and without (b) CPEC for $N = 64$ and at 20 dB SNR and 15 dB SPNR with a SUI-II CIR

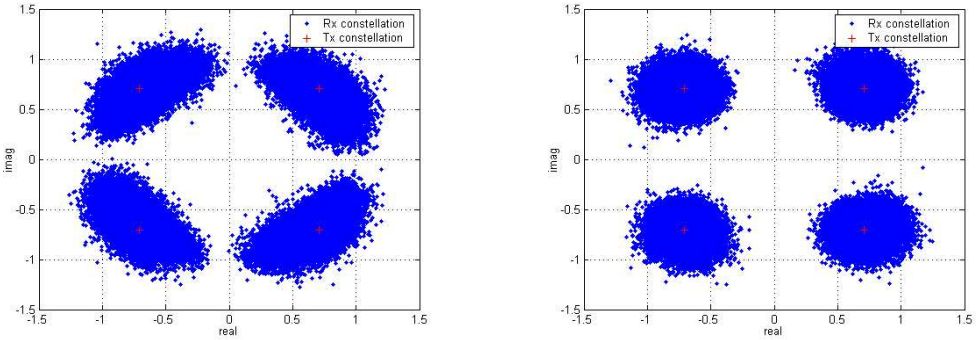

(a) Without CPEC (b) With CPEC

Figure 3.19: Demodulated constellations with (a) and without (b) CPEC for $N = 256$ and at 20 dB SNR and 15 dB SPNR with a SUI-II CIR

sampling rate of 20 MHz with a CP equal to 20 samples, thus the subchannel spacings are approximately 312 kHz, 156 kHz and 78 kHz respectively. QPSK mapping for all subchannels has been employed and all the subchannels are used to transmit data. A burst equivalent to 2500 OFDM symbols is transmitted and the channel is assumed to remain static within the burst. Each data point in the simulation results is obtained by averaging over 750 such bursts, each experiencing a random channel realisation in accordance with the SUI-II profile. The received Signal to Noise Ratio (SNR) due to AWGN is set at 20 dB for all of the simulations. The value selected for the FB buffer length, N_w is 2.

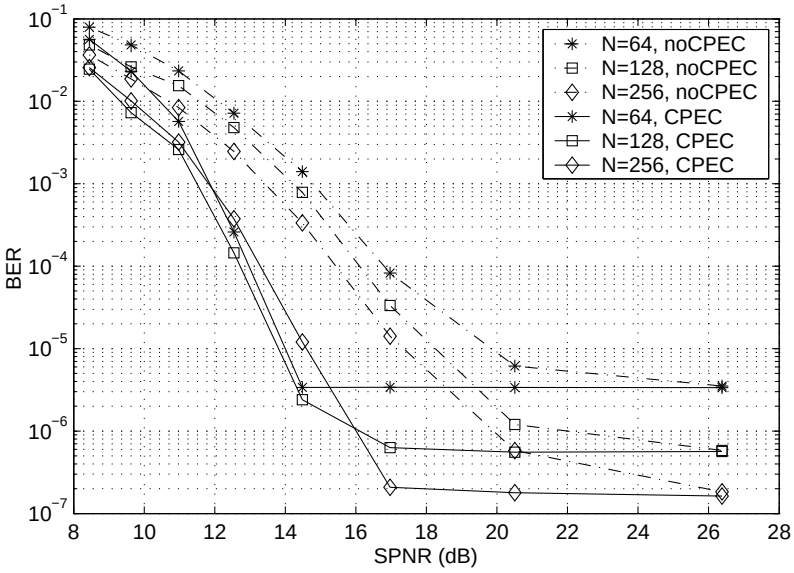

Figure 3.20: Performance of the CPEC algorithm for $b = 4$ and $f_h = 100$ kHz

Figure 3.20 shows the simulation results for the CPEC algorithm with $N = 64, 128, 256$ for PN mask parameters $f_h = 100$ kHz and $b = 4$. The received signal power and the LO power are normalised to unity. The curves are plotted against SPNR ($1/\sigma_\psi^2$). The PN variance is set using the parameters a and c. It can be seen that without the CPEC algorithm an OFDM system with $N = 64$ performs worse than the system with $N = 256$. This is because for the PN mask selected the conventional OFDM system with $N = 64$ suffers from greater CPE than does the $N = 256$ system. This can be confirmed by observing the greater rotation of

the constellations evident in figure 3.18 (a) compared with that in figure 3.19 (a). The rotation caused by the higher CPE power for $N = 64$ causes more bit errors than the lower CPE power present when $N = 256$.

It can also be seen in figure 3.20 that for $N = 64$, the CPEC algorithm achieves a performance gain of 6 dB at BER of 10^{-5} over a system without CPEC. The performance gain can be seen to decrease with increasing N, for example with $N = 256$ the gain is reduced to 3 dB. This can be attributed to the fact that the CPE variance decreases with increasing N, which is confirmed by the theoretical analysis presented previously in the section 3.2. The improvements are very small once SPNR is above 20 dB owing to AWGN becoming dominant over PN. It should be noted that for the SUI-II channel model at the selected SNR of 20 dB (AWGN only), a BER floor of the order of 10^{-7} is achieved. Obviously, if the SNR had been set higher, the improvements due to CPEC would be correspondingly greater.

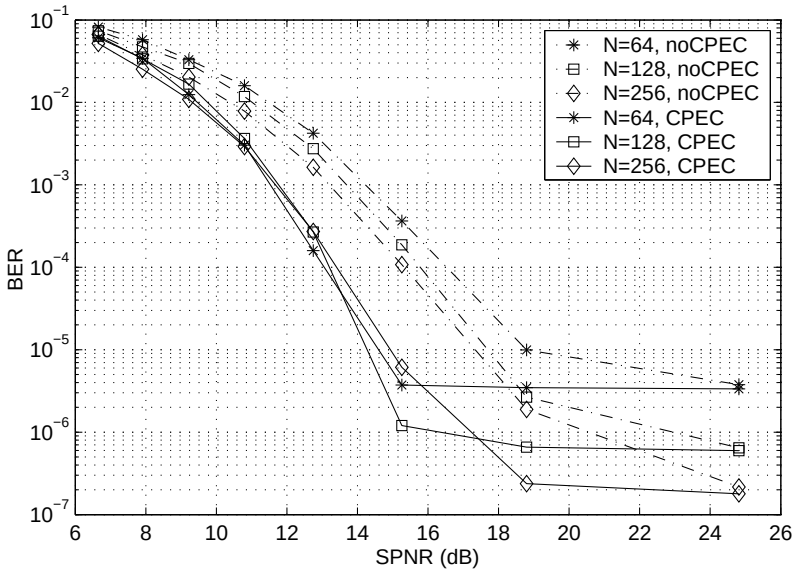

Figure 3.21: Performance of the CPEC algorithm for $b = 4$ and $f_h = 200$ kHz

Figure 3.21 shows the results of the simulations carried out using the PN mask with $f_h = 200$ kHz. All other parameters are similar to the previous case. Hence the PN will induce more spectral spillage and will have a higher variance for

the same values of the parameters a and c. The performance gain is 4 dB for $N = 64$ but is reduced to 2.3 dB for $N = 256$ at a BER of 10^{-5}. The number of subchannels selected in the CPE estimation, N_d averaged 12 for $N = 64$ over all bursts. Hence the total number of additional computations on average was 12 additions, 12 subtractions and 2 divisions per OFDM symbol. The gain due to CPEC algorithm is significant considering the low additional computation effort.

Other CPEC algorithms have been proposed by other authors. They are almost exclusively feedforward methods (i.e. the correction for CPE is made after the FEQ). The algorithms fall into two categories. In [43] a symbol-by-symbol estimation is performed in a manner similar to that if *only the CPESE* part of the algorithm proposed in this work is used. In [54], rather than relying on a single estimate, Onizawa proposed to correct for CPE after processing the CPESE values in a moving average filter in order to control their variance. Both of these schemes are different from the CPEC algorithm proposed in this work since the FBCF is implemented at the level of the FEQ, which modifies the data points prior to the calculation of CPESE. Another important point is that all these schemes rely on pilot symbols being transmitted, which reduces the throughput of the system. In addition, the algorithm proposed here can select the subchannels with the highest SNR for the estimation process. In [55] a similar scheme to the one proposed is presented. Here the FBCF is taken as the average of all the CPESEs up to that time. However since $E[\psi_{CPE}] = 0$ having a shorter window to calculate the FBCF appears to be more sensible. Also it does not propose a method to compensate for spectral nulls. Note that the CPEC presented in this work and the scheme presented in [55] have been developed simultaneously but independently.

Figure 3.22 shows the performance of the individual components of the proposed CPEC algorithm for an OFDM system with $N = 64$ subject to PN with mask parameters $b = 4$ and $f_h = 100$kHz. It shows that the performance gain obtained using the CPESE alone is only 2 dB at a BER of 10^{-5}. The use of both the CPESE and the FBCF is seen to give a 6 dB advantage. However, the use of FBCF alone also shows a performance improvement of 5.8 dB. Figure 3.23 shows the performance of a system with $N = 256$ in the same conditions. At a BER of 10^{-5} the use of the CPESE alone shows a gain of 1.8 dB while the use of the FBCF alone shows a gain of 0.5 dB. The combination of both CPESE and FBCF

gives a gain of 3 dB. This can be explained as follows. Compare the variation of CPESE for $N = 64$, as seen in figure 3.10 to that when $N = 256$, as seen in figure 3.24. Both plots were generated under similar conditions. They show that the CPESE varies at a slower rate when N is smaller. Hence for $N = 64$ the FBCF can track the CPESE and would expect a significant portion of the CPE to be corrected by the FBCF alone. However, for $N = 256$ the CPESE varies more rapidly and it is much more difficult for the FBCF to track the CPESE. Hence, the portion of CPE corrected by the FBCF alone will be correspondingly less.

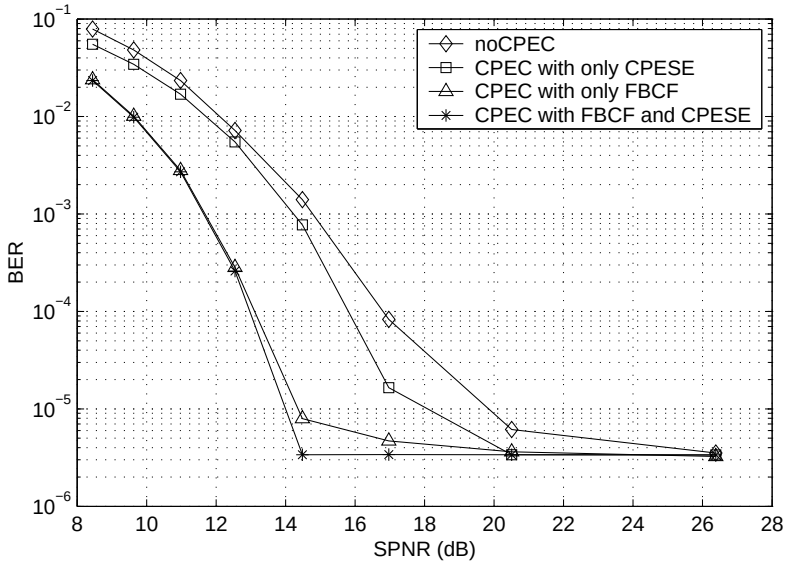

Figure 3.22: Performance of different components of the CPEC algorithm for $N = 64$, $b = 4$ and $f_h = 100$ kHz

Figure 3.25 shows a comparison with the algorithm proposed by Onizawa [54]. In this approach a MA filter processes the CPESEs and the result is used to correct for CPE at the feedforward stage *after* the FEQ. The results show that the Onizawa method shows very little gain compared to that achieved using only the CPESE. This is in marked contrast to the proposed CPEC algorithm where including the FBCF gives a significant improvement in performance compared with that using the CPESE alone.

Figure 3.26 shows the effect of AWGN on the CPEC proposed. It is clear that

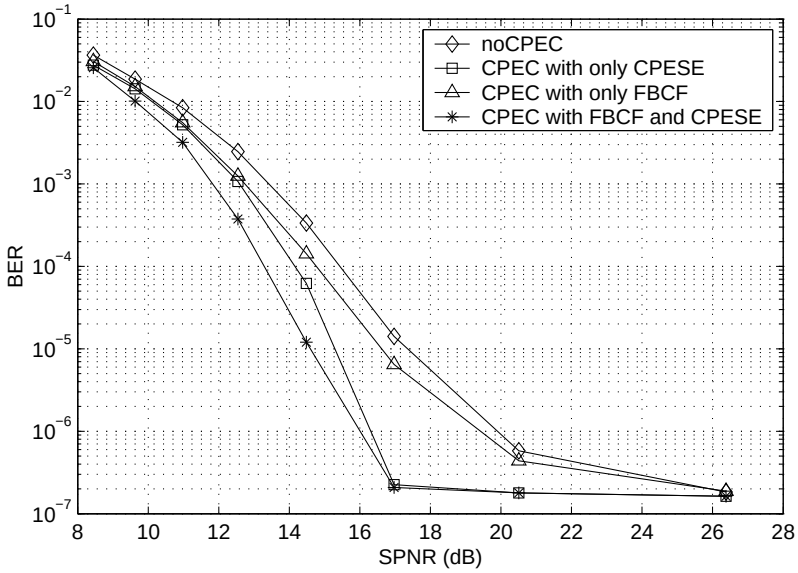

Figure 3.23: Performance of different components of the CPEC algorithm for $N = 256$, $b = 4$ and $f_h = 100$ kHz

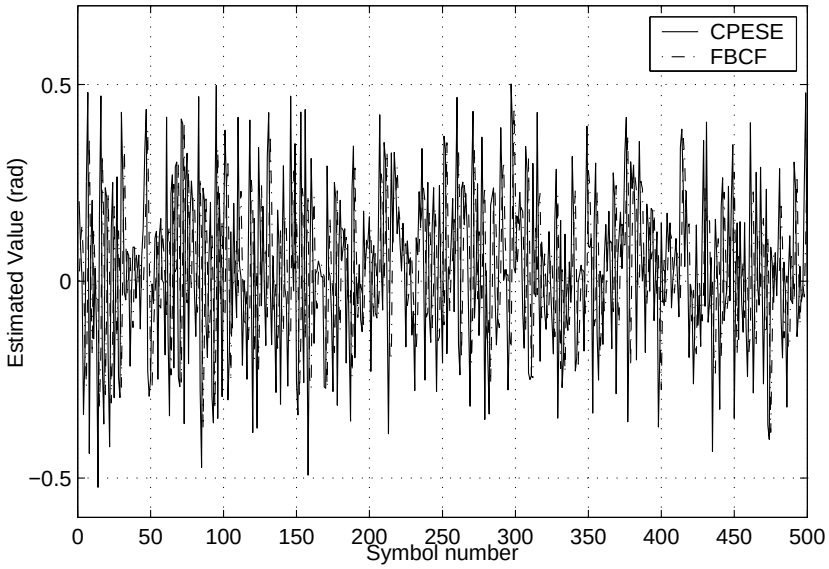

Figure 3.24: The variation of CPESE for $N = 256$ at an SNR of 20 dB and SPNR of 12.5 dB

	Performance gain in SPNR at an BER of 10^{-5} (dB)		
	Using only CPESE	**Using only FBCF**	**Using both**
$N = 64$	2	5.8	6
$N = 256$	1.8	0.5	3

Table 3.1: Performance gains obtained by different components of the CPEC with $b = 4$ and $f_h = 100$ kHz

the error floor observed at an BER of about 10^{-6} is mainly due to the presence of AWGN.

Figure 3.27 shows the effect that non-ideal channel estimation has on the performance of the proposed CPEC algorithm for the previous system. It is important to analyse the channel estimation since the selection of subchannels for the CPEC is based on the estimated CTF. If a perfect channel estimation can be made, a 3 dB gain in performance can be achieved even without the use of CPEC at a BER of 10^{-5}. With the assumption of perfect channel estimation the use of the proposed CPEC gives a performance gain of 5 dB compared to the case when CPEC is not used with the same assumptions. This is comparable with the 6 dB improvement shown previously in figure 3.20. Hence it is evident that channel estimation in itself does not significantly degrade the performance of the proposed CPEC algorithm.

3.6 Conclusion

The effect of PN in OFDM has been shown to have a dual effect. Specifically one component is found that affects all subchannels equally, which is termed CPE and another which affects the orthogonality of the subchannel carriers, is known as ICI. The theoretical and simulated BER performance as a function of SPNR of OFDM systems subject to AWGN and PN are shown to be in very close agreement. A simple, yet effective algorithm that has two correction factors has been

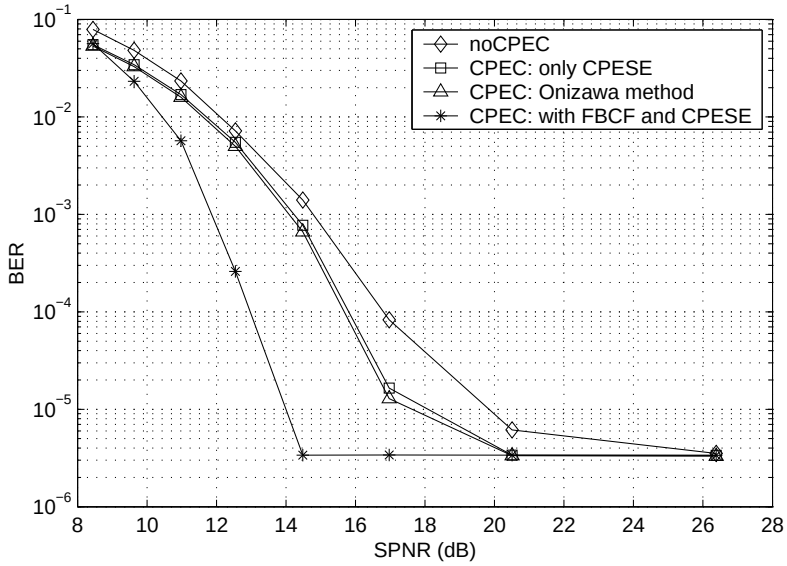

Figure 3.25: Comparison of the Onizawa CPEC algorithm for $N = 64$, $b = 4$ and $f_h = 100$ kHz

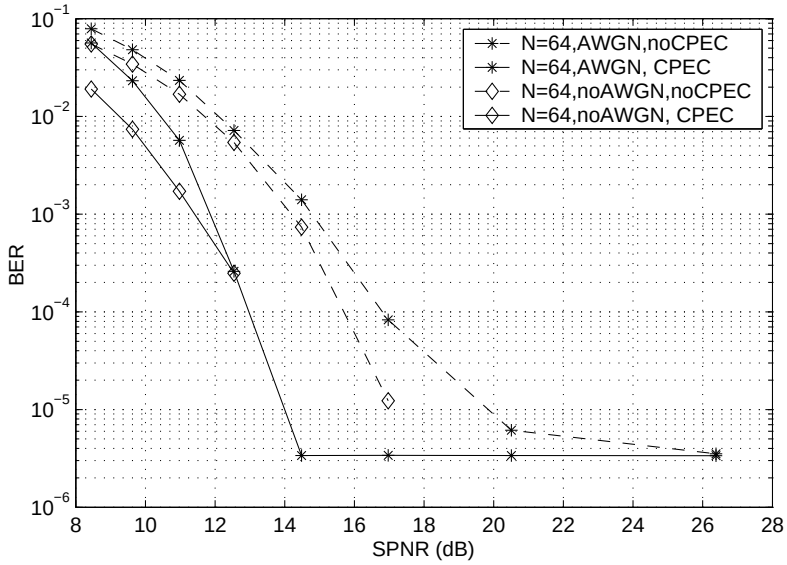

Figure 3.26: The effect of AWGN on the CPEC algorithm for $N = 64$, $b = 4$ and $f_h = 100$ kHz

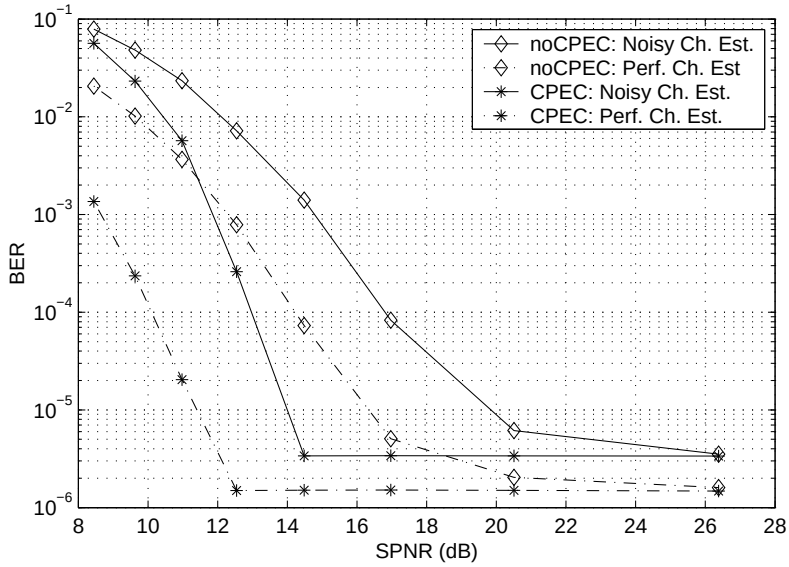

Figure 3.27: The effect of channel estimation on the CPEC algorithm for $N = 64$, $b = 4$ and $f_h = 100$ kHz

presented to remove the CPE. The performance gains obtained by each correction factor, acting alone and in combination, are investigated via simulations and are also compared with algorithms proposed by others. It has been shown that when the algorithm is applied to a BFWA system operating in the MMDS SUI-II channel at an SNR of 20 dB, performance gains of up to 6 dB are achieved. The use of the proposed CPEC algorithm might allow MMDS equipment manufacturers to use lower quality RF oscillators without performance degradation, thus allowing significant cost savings.

Chapter 4

Symbol Offset Correction

It has been shown in chapter 2 that OFDM is more robust in the presence of multipath propagation owing to the use of the Cyclic Prefix (CP) than SC systems. However, as was demonstrated in chapter 3, OFDM is very sensitive to oscillator Phase Noise (PN). Unfortunately OFDM is also sensitive to frequency offsets caused by oscillator tuning inaccuracies. In spite of these limitations, OFDM is quite robust in the presence of timing offsets [24]. Timing offsets can be further divided into symbol (frame) offsets and sampling clock offsets. The former refers to errors in determining the correct position of the FFT window required for demodulation at the receiver and the latter refers to timing errors in the receiver A/D converter sample clock. Throughout the work, ideal sampling clock synchronisation is assumed and in this chapter only symbol (frame) synchronisation will be addressed. Interested readers can find out more about the effects of sampling clock offsets in for example [56, 57]. Previous work has often addressed the issues of frequency offset synchronisation and symbol offset synchronisation in tandem since they can be mitigated using similar algorithms. One such algorithm is presented by T. M. Schmidl and D. Cox in [25, 58]. Henceforth it will be referred to as the Schmidl and Cox Algorithm (SCA). The SCA performs well for OFDM systems with large symbol lengths (N). However, the importance of using OFDM systems with smaller values of N for BFWA applications has already been mentioned in chapter 1. This chapter will concentrate on the symbol offset synchronisation function of the SCA and will then introduce a novel algorithm

that complements the SCA so that virtually perfect symbol synchronisation can be achieved even with lower values of N. The next chapter will deal with the issue of frequency offset synchronisation.

An OFDM system will be more robust if the length of the CP, v is selected to be slightly longer than the length of the CIR, N_h. Hereafter this difference will be denoted as the Excess Length, p (i.e. $p = v - N_h$). As long as the symbol synchronisation offset, ξ causes the start of each FFT window to be within the Excess Length (i.e. $-p \leq \xi \leq 0$), the decoded OFDM symbols will not be subject to Inter Block Interference (IBI) which is introduced when adjacent OFDM symbols cause interference to the OFDM symbol currently being detected [59]. Note for AWGN channels the start of the FFT window can be placed anywhere within the CP (i.e. $-v \leq \xi \leq 0$) without suffering any degradation in performance, provided that no other degradations are present, e.g. frequency offset. Although increasing p in general will make the system more robust against symbol synchronisation errors it also decreases throughput due to the use of an extended CP. This becomes even more significant when operating at higher sample rates since the length of the same CIR will now span a greater number of received samples.

This chapter is organised as follows. In section 4.1 a synopsis of the research carried out by other authors is presented. There have been numerous approaches to achieving symbol synchronisation in OFDM and they will be critically analysed in this section. Section 4.2 will introduce the theoretical derivations of the degradation caused by symbol offsets in OFDM and will highlight the motivation underlying the work. Section 4.3 introduces the SCA and identifies the limitations of the algorithm. The proposed Iterative Symbol Offset Correction Algorithm (ISOCA) is introduced in section 4.4. This is a two part iterative algorithm that complements SCA enabling it to be successfully used in BFWA applications. Section 4.5 presents results for OFDM systems when used in AWGN alone and for OFDM systems including a CIR appropriate for the BFWA scenario. The results will clearly show a significant increase in performance is brought about by the use of ISOCA. Finally, section 4.6 draws some conclusions.

4.1 Related Work

A good tutorial on the subject of symbol offset in OFDM is given in [60]. The algorithms that are already available for symbol synchronisation can be broadly categorised into Pilot Symbol Aided (PSA) and Non Pilot Symbol Aided (NPSA) schemes. PSA schemes are based on correlating the received signal with a known signal. These can be further divided into schemes that use a preamble or a known OFDM training symbol [25] or schemes that periodically insert pilot symbols on particular subchannels [61]. NPSA schemes are generally based on correlating received samples taken one OFDM symbol length apart, in order to make use of the periodicity created by the insertion of the CP [62]. Some schemes however employ a hybrid of PSA and NPSA methods [63, 64]. Another approach is the use of null symbols [65, 66]. The drop in receiver power is used to detect the start of a burst. This method would not perform well in BFWA systems which employ burst mode transmission since there would be no difference between the null symbol and the idle period between bursts. In [67], the authors propose a blind synchronisation method based on the second order statistics of the received signal, but it has a very high computational demand.

The authors in [64, 68, 69] extend the work of [62] that make use of the repetition introduced by the addition of the CP. In [64], a second estimation using pilot symbols is performed and in [69] the authors add a second correlator to the original output determined in [62] to be used in situations where the CIR is likely to have two equal paths. The original estimation in [62] can be biased heavily by the position of the main tap of the CIR [68]. Consequently the authors further propose a fine symbol synchronisation method that estimates the CIR using pilot symbols that are sent at intermediate positions of the OFDM symbol. However, in general it should be noted that the performance of schemes using Maximum Likelihood (ML) estimators that rely upon the repetition introduced by the CP decreases in the presence of frequency offsets.

The authors in [70] propose a ML based timing estimation algorithm for the WLAN specifications developed by the IEEE 802.11 standardisation group. This standard uses a preamble with short and long OFDM symbols. However the performance of the algorithm depends heavily on the fact that the initial timing esti-

mate falls within the Excess Length, p.

In some of the related work, the Inter-Block Interference (IBI) caused by a CIR that is longer than the CP is analysed [71, 72, 73]. In [71] the PSD of the IBI is characterised in terms of the length of the CP and it concludes that the samples corresponding with the tails of the CIR do not uniformly contribute to the PSD of the IBI, but rather the contribution grows linearly as the samples get closer to the edges of the CIR. The authors in [74, 75] address the issue of synchronisation in Digital Multitone (DMT) systems used in Asymmetric Digital Subscriber Line (ADSL) systems. The work of other authors will be presented in the next sections where they are directly relevant to the subject being addressed.

4.2 Effect of Symbol Offset in OFDM

Section 2.4 introduced the analysis of a conventional OFDM system assuming perfect synchronisation. The demodulated OFDM symbol under those assumptions is given in (2.20). The effect of a carrier frequency offset (relative to the intercarrier spacing), ϵ can be introduced to the system by redefining the demodulated symbol as,

$$Y_{m,l} = \sqrt{\frac{1}{N}} \sum_{n=0}^{N-1} r_{m,n} e^{-j2\pi \frac{ln+(\epsilon-\hat{\epsilon})}{N}}, \quad 0 \leq l \leq N-1 \tag{4.1}$$

where $r_{m,n}, 0 \leq n \leq N-1$ are the received samples of the FFT window for the mth OFDM block taken from the received sequence, that includes the component due to AWGN, w_n (see (2.19) and (2.20)). Here $\hat{\epsilon}$ represents the estimated carrier frequency offset at the receiver. For the purpose of analysing the effect of symbol offset it will be assumed that the Residual Frequency Offset (RFO) is zero (i.e. $\hat{\epsilon} - \epsilon = 0$) for the remainder of this section. If perfect symbol synchronisation is achieved the samples selected for decoding symbol m are,

$$\underline{r}_m = [r_{m,0}, r_{m,1}.., r_{m,N-1}] \tag{4.2}$$

and hence,

$$Y_{m,l} = A_{m,l} H_l + W_l \tag{4.3}$$

where W_l is the component due to AWGN and H_l is the coefficient of the Channel Transfer Function (CTF) approximated at subchannel l. It will be assumed that W_l has the same statistics as w_n. In order to understand the effect of symbol offset on performance, initially the demodulation of OFDM is investigated for the situations where AWGN is the only channel impairment. Two different values of symbol offset, ξ are considered.

4.2.1 Symbol Offset $-v \leq \xi < 0$

In this case, the FFT window selected for decoding is,

$$\underline{r}_m = \left[r_{m,N-\xi}, .., r_{m,N-1}, r_{m,0}, .., r_{m,N-1-\xi}\right] . \tag{4.4}$$

Then,

$$\begin{aligned} Y_{m,l} &= \frac{1}{N}\sum_{k=0}^{N-1} A_{m,k} \sum_{n=0}^{\xi-1} e^{j2\pi\frac{k(n+N-\xi)-nl}{N}} + \\ &\quad \frac{1}{N}\sum_{k=0}^{N-1} A_{m,k} \sum_{n=\xi}^{N-1} e^{j2\pi\frac{k(n-\xi)-nl}{N}} + W_l \end{aligned} \tag{4.5}$$

and hence,

$$Y_{m,l} = A_{m,l} e^{j2\pi\frac{\xi l}{N}} + W_l . \tag{4.6}$$

Equation (4.6) shows that so long as the symbol offset results in the beginning of each FFT window to lie within the CP, the orthogonality of the carriers is maintained. The desired term experiences a phase shift, which can be estimated and corrected.

4.2.2 Symbol Offset $\xi > 0$

In this situation, the FFT window selected for decoding is,

$$\underline{r}_m = \left[r_{m,\xi}, .., r_{m,N-1}, r_{m+1,N-v}, .., r_{m+1,N-v-1+\xi}\right] \tag{4.7}$$

here, it is assumed $\xi \leq v$. Then,

$$\begin{aligned} Y_{m,l} &= \frac{1}{N}\sum_{k=0}^{N-1} A_{m,k} \sum_{n=0}^{N-\xi-1} e^{j2\pi\frac{k(n+\xi)-nl}{N}} + \\ &\quad \frac{1}{N}\sum_{k=0}^{N-1} A_{m+1,k} \sum_{n=N-\xi}^{N-1} e^{j2\pi\frac{k(n+\xi-v)-nl}{N}} + W_l \end{aligned} \tag{4.8}$$

$$\begin{aligned} Y_{m,l} &= \frac{N-\xi}{N} A_{m,l} e^{j2\pi\frac{\xi l}{N}} + \\ &\quad \frac{1}{N}\sum_{\substack{k=0 \\ k\neq l}}^{N-1} A_{m,k} \sum_{n=0}^{N-\xi-1} e^{j2\pi\frac{k(n+\xi)-nl}{N}} + \\ &\quad \frac{1}{N}\sum_{k=0}^{N-1} A_{m+1,k} \sum_{n=N-\xi}^{N-1} e^{j2\pi\frac{k(n+\xi-v)-nl}{N}} + W_l \,. \end{aligned} \tag{4.9}$$

The first term on the r.h.s. of the equation (4.9) shows that the desired term experiences an attenuation and a phase shift. The second and the third terms are the ICI and ISI respectively. A similar result can be obtained if $\xi > v$. The analysis can be extended to the case when a CIR is included. In this case unless the symbol offset lies within $-p \leq \xi \leq 0$, the demodulated symbols are given by [76],

$$Y_{m,l} = \frac{N-\xi}{N} A_{m,l} H_l e^{j2\pi\frac{\xi l}{N}} + W_{\xi,l} + W_l \tag{4.10}$$

where $W_{\xi,l}$ is the interference term caused by ISI and ICI. It also proves to be the dominant interference term, the power of which can be approximated by zero-mean Gaussian noise with power [76],

$$\sigma_\xi^2 = \sum_i |hi|^2 (2\frac{\Delta_i}{N} - (\frac{\Delta_i}{N})^2) \tag{4.11}$$

where

$$\Delta_i = \begin{cases} \xi - i & \xi > i, \\ i - v - \xi & 0 < \xi < -(v-i), \\ 0 & \text{else.} \end{cases} \tag{4.12}$$

Symbol offset in a coherent OFDM system has an even more severe effect

on performance. Symbol synchronisation not only determines the position of the FFT window for the subsequent OFDM symbols, it also implicitly determines the channel estimation by the FEQ coefficients. If $\xi > 0$ or $\xi < -p$ the interference term $W_{\xi,l}$ will affect the channel estimation and consequently the decoding of all the symbols in the data burst. OFDM systems that are used in rapidly changing channels require the FEQ coefficients to be updated frequently. To do so, pilot symbols are embedded in to each OFDM symbol at periodic intervals, which are then used to estimate the FEQ coefficients by using interpolation to generate coefficients for every subchannel over which data is sent. Consequently a symbol offset in such a system would cause even more severe degradation owing to the poor estimation of the FEQ coefficients. In the absence of noise, the Mean Squared Error (MSE) of the channel estimate is given as [61],

$$\text{MSE} = \sum_{l=0}^{N-1} \left| H_l - \hat{H}_l(\xi) \right|^2 \tag{4.13}$$

where $\hat{H}_l(\xi)$ is the estimated CTF as a function of ξ. The important point that should be noted from equations (4.5)-(4.10) is that the demodulated OFDM symbols will *always* contain a phase rotation proportional to the symbol offset, ξ and the subchannel index, l as evidenced by the term $e^{j2\pi\frac{\xi l}{N}}$ in equation (4.10). In the next two sections, an algorithm that uses this phase rotation to determine and correct the symbol offset is presented.

4.3 Schmidl and Cox Algorithm

A robust scheme to estimate both symbol synchronisation and frequency offset estimation is the SCA [25, 58]. It uses two training symbols with the first one having identical first and second halves (neglecting the CP). This is achieved by utilising only the even subchannels and setting the odd subchannels to zero at the input to the IFFT modulator. Figure 4.1 shows the organisation of the two training symbols in the SCA.

Symbol (frame) synchronisation is achieved by searching for a training symbol with two identical halves. If $L = N/2$, the sum of L consecutive correlations

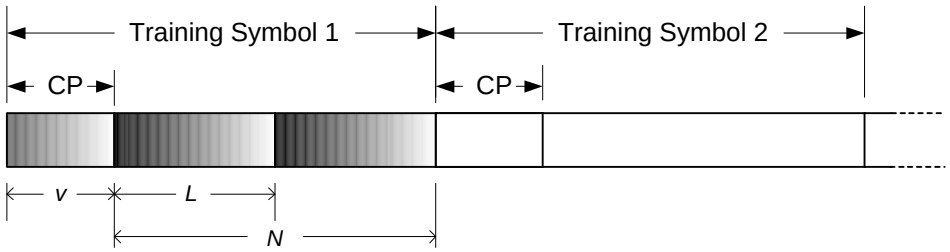

Figure 4.1: Training symbols in SCA

between pairs of samples spaced L samples apart is found as,

$$P(d) = \sum_{n=0}^{L-1} (r^*_{d+n} r_{d+n+L}) \tag{4.14}$$

which can be recursively implemented as,

$$P(d+1) = P(d) + (r^*_{d+L} r_{d+2L}) - (r^*_d r_{d+L}) \,. \tag{4.15}$$

The received energy for the second half-symbol which is given by

$$R(d) = \sum_{n=0}^{L-1} |r_{d+n+L}|^2 \tag{4.16}$$

can also be recursively implemented as,

$$R(d+1) = R(d) + |r_{d+N}|^2 - |r_{d+L}|^2 \tag{4.17}$$

and is used to normalise the correlator output. This yields a timing metric given by,

$$M(d) = \frac{|P(d)|^2}{(R(d))^2} \,. \tag{4.18}$$

The timing metric, given by (4.18) will reach a peak at the end of the CP of the first training symbol. The peak is actually maintained for a length equal to the Excess Length, $(p+1)$ just prior to the end of the CP of the first training symbol (i.e. the beginning of the useful part of the first training symbol). Thus the correlator output will take the form of a plateau. This is because the last p

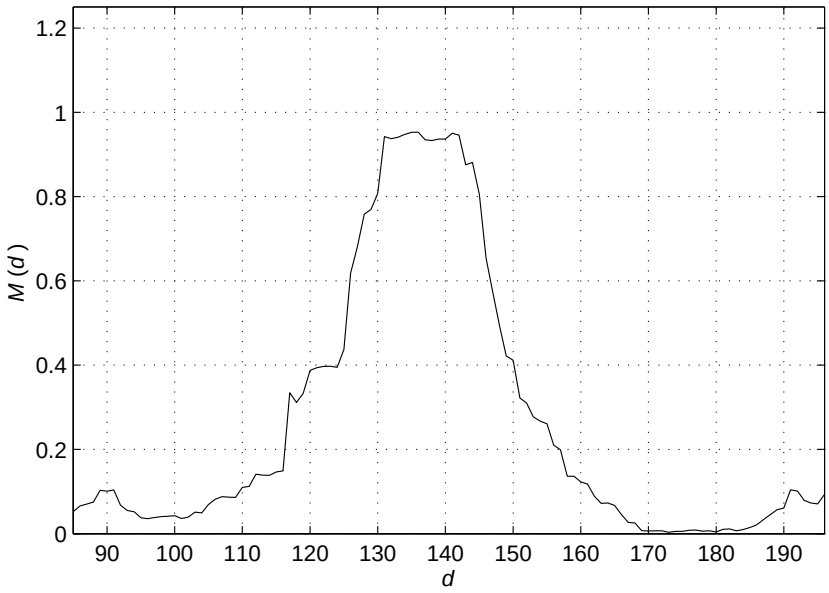

Figure 4.2: Output of the timing metric for $N = 64$ and $p = 10$ at an SNR of 20dB

samples of the CP are not corrupted by the CIR. Figure 4.2 shows a typical output for $M(d)$ for $N = 64$ and $p = 10$ at an SNR of 20 dB. If it is not possible to find such a plateau region it is assumed that the SCA has resulted in a condition of non acquisition. The method adopted to locate this region is explained in detail in the following paragraphs.

Symbol synchronisation is achieved by locating the end of this plateau, denoted as d_{opt}. The authors in [25] propose a different method to identify the optimal synchronisation point. Firstly, the sample corresponding to the maximum of the timing metric, given by (4.18) is found. Then the sample positions to the left and the right of the identified point which have an amplitude equal to 90% of the maximum are found. The optimum point, d'_{opt} is selected as the mean position between these two points. The objective of this procedure was to find the mid point of the CP. Preliminary simulation results showed that although d'_{opt} fell within the CP for higher values of SNR, the method failed badly at lower SNR values. To overcome this problem, the following approach has been developed. First of all, the variance for p consecutive samples of the timing metric is calculated. The

position of d_{opt} is taken to be the point when the minimum variance occurs. The rationale for doing this is that the p samples corresponding to the plateau will be very similar and hence will generate the minimum variance. Note that for AWGN channels, the number of consecutive samples selected will be v. The superiority of this method will be demonstrated in the simulation results to be presented later in this chapter. Hence,

$$d_{opt} \stackrel{\triangle}{=} \stackrel{\min}{d} \frac{1}{p-1} \sum_{i=0}^{p-1} [M(d-i) - \overline{M(d)_p}]^2 \tag{4.19}$$

where $\overline{M(d)_p}$ is the mean of the samples from d to $d-p+1$. The Start of Frame (SOF) is determined as the start of first training symbol, given by $d_{opt} - v$. The estimated SOF given by the SCA is denoted as $\hat{\text{SOF}}_{SCA}$. Since the CP ensures that there is no Inter Block Interference (IBI) between OFDM symbols, the effect of the CIR on the first training symbol is cancelled if the conjugate of a sample from the first half is multiplied by the corresponding sample from the second half. Hence the phase difference between the two halves of the first training symbol is caused by the frequency offset, i.e. $\phi = \pi\epsilon$. The phase difference can be estimated as,

$$\hat{\phi} = 1/(p+1) \sum_{n=0}^{p} \angle P(d_{opt} - n) \, . \tag{4.20}$$

If $\epsilon < 1$ there is no phase ambiguity in $\hat{\phi}$ and the fractional part of the frequency offset can be estimated as,

$$\hat{\epsilon}_{SCA} = \hat{\phi}/\pi \tag{4.21}$$

The second training symbol is used in order to avoid potential ambiguity and determine the integer part of the frequency offset. This technique will be considered fully in the next chapter when relative frequency offsets in excess of unity are addressed. Note that the algorithms about to be presented perform equally well for relative frequency offsets in excess of unity, i.e. having an integer part. For purposes of brevity it will be assumed that $\epsilon < 1$ for the remainder of this section.

If $\hat{\text{SOF}}_{SCA}$ is different from the actual Start of Frame namely, SOF_{ideal} it gives

rise to a symbol offset, ξ_{SCA}. i.e.

$$\xi_{SCA} = \hat{\text{SOF}}_{SCA} - \text{SOF}_{ideal} \, . \tag{4.22}$$

The effect of AWGN on the correct estimation of d_{opt} and hence $\hat{\text{SOF}}_{SCA}$ is reduced with higher values of L, and hence the number of FFT points N, particularly when operating at low values of SNR. It has been shown that the SCA performs well for OFDM systems with N in excess of 1000 [25]. However, for BFWA systems, data is transmitted in short bursts, particularly in the uplink. In this situation, it would be wasteful to use an OFDM system with a large value of N. When the SCA is used for systems with lower values of N, the estimate $\hat{\epsilon}_{SCA}$ is no longer sufficiently accurate. This error results in a residual frequency offset that rotates the received constellation at a reduced rate, but one that is still significant enough to cause bit errors in coherently demodulated OFDM systems. Hence OFDM systems with low values of N will require a residual frequency offset correction algorithm to continuously track the carrier frequency offset. Some of the proposed algorithms [77] (which will be presented in the next chapter) rely on the phase gradient of the decoded OFDM symbols to estimate the residual carrier frequency offset. Even though $-p \leq \xi_{SCA} \leq 0$ will not result in any Inter Block Interference (IBI), the additional phase gradient caused by a non zero value of ξ_{SCA} will seriously affect residual carrier frequency offset correction algorithms based on the measurement of the phase gradient. This will be demonstrated in section 5.5 in the next chapter. Hence it is imperative that perfect symbol synchronisation is achieved (i.e. the final symbol offset, $\xi_F = 0$). In the next section an Iterative Symbol Offset Correction Algorithm (ISOCA) is proposed that employs a two step process that virtually guarantees perfect symbol synchronisation even under conditions of very low SNR.

An approach to increase the performance of the timing synchronisation of the SCA is presented in [78, 79]. The authors propose two methods, one using a sliding window method to smooth out the plateau at the correlator output and another based on dividing the training symbol into four parts, with the last two parts being the sign negative of the first two. Even though the correlator output gives a sharper peak, the FFT size, N needs to be quite large for the algorithm

to perform well. Indeed the authors only consider FFT sizes in excess of 1024. In [80, 81] the author proposes to follow the symbol estimate determined using the sliding window correlator of the SCA with a matched filter based correlator. This method generates a more significant peak at the matched filter output, hence detection of the SOF is more accurate than using the plateau of the timing metric as utilised by the SCA.

Another algorithm that makes use of the phase gradient that is a result of symbol offset is presented in [82]. In their scheme, the estimated time offset per pair of adjacent tones is,

$$\hat{\xi} = \frac{N}{2\pi}\Big[\angle\Big(\frac{Y_{m,l}}{\hat{A}_{m,l}}\Big) - \angle\Big(\frac{Y_{m,l+1}}{\hat{A}_{m,l+1}}\Big)\Big] \tag{4.23}$$

where $Y_{m,l}$ and $\hat{A}_{m,l}$ are the demodulated symbol and the decoded symbol at lth subchannel in OFDM symbol m. Each tone pair provides a separate noisy estimate of ξ. The data is modulated with differential QPSK across the subchannels. Hence the above estimate will create a QPSK constellation that is slightly rotated depending on ξ. For a QPSK constellation each pair of tones will differ in phase from each other by a multiple of $\pi/4$. This effect on the rotated constellation can be eliminated and all the points brought in to the same quadrant by raising the complex points to the 4th power. Finally, ξ is estimated by locating the centroid of the noisy constellation points. This estimate is quite robust in frequency selective fading since even if a pair of tones fall in to a frequency null in the CTF, the pair will only have a low amplitude when used in (4.23). Consequently, it will contribute less when locating the centroid. This scheme appears to be quite robust, but it assumes that initial symbol offset is less than half of the FFT size (i.e. $\xi \leq N/2$). Although this is a safe assumption for higher values of N, it might not be the case for lower ones. In [83] the authors also make use of the phase gradient caused by symbol offset. It relies on sending pilot tones continuously within OFDM symbols. An estimate of the symbol offset is generated after every OFDM symbol and the final estimate is updated by finding the average of the symbol-by-symbol estimates found up to that point. The authors in [84] also look at the same principle, but to avoid the symbol offset from causing the SOF to fall into adjacent OFDM symbols, it proposed to use long cyclic prefix and a cyclic

postfix. The novel iterative algorithm proposed in the next chapter performs well even when only a prefix is used.

4.4 Iterative Symbol Offset Correction Algorithm

A novel algorithm that is developed by the author, which is based on the phase gradient caused by the symbol offset is presented in this section. It is divided into two parts. The first is the Iterative Symbol Offset Estimation, in which the symbol offset is iteratively estimated until the value is zero. The second part is the Error Comparison, where a second estimate is used that is based on the errors generated within the second training symbol of the SCA. If the ISOCA fails in the Error Comparison stage, the Iterative Symbol Offset Estimation is repeated after a reinitialisation. Both parts of the algorithm must should yield a positive result for the ISOCA to return a final estimated SOF. There are numerous check points in the algorithm to prevent it from iterating in an infinite loop. The two parts of the ISOCA algorithm are discussed in detail in the next two subsections.

4.4.1 1st Part - Iterative Symbol Offset Estimation

Using the SCA an initial estimate of both the SOF and the frequency offset namely $\hat{\text{SOF}}_{SCA}$ and $\hat{\epsilon}_{SCA}$, are made. It is proposed to estimate the symbol offset at the end of the SCA, ξ_{SCA} based on the phase gradient it gives rise to, as indicated in (4.10). To do this, the demodulated output of the second SCA training symbol $Y_{N_{t2}}$ is utilised. Here, it is assumed that the two training symbols of the SCA occupy the symbol positions at the start of the frame, specifically N_{t1} and N_{t2}. The phase difference between the received and the transmitted second training symbol of the SCA is calculated as follows,

$$\theta_i = \angle(Y_{N_{t2},i}/A_{N_{t2},i}), \quad 0 \leq i \leq N-1 \tag{4.24}$$

where $A_{N_{t2},i}$ and $Y_{N_{t2},i}$ represent the N_{t2}th transmitted and demodulated symbols of the ith subchannel, respectively based on the use of $\hat{\text{SOF}}_{SCA}$.

Figure 4.3 shows a typical plot of θ_i against the subchannel index for $N = 64$

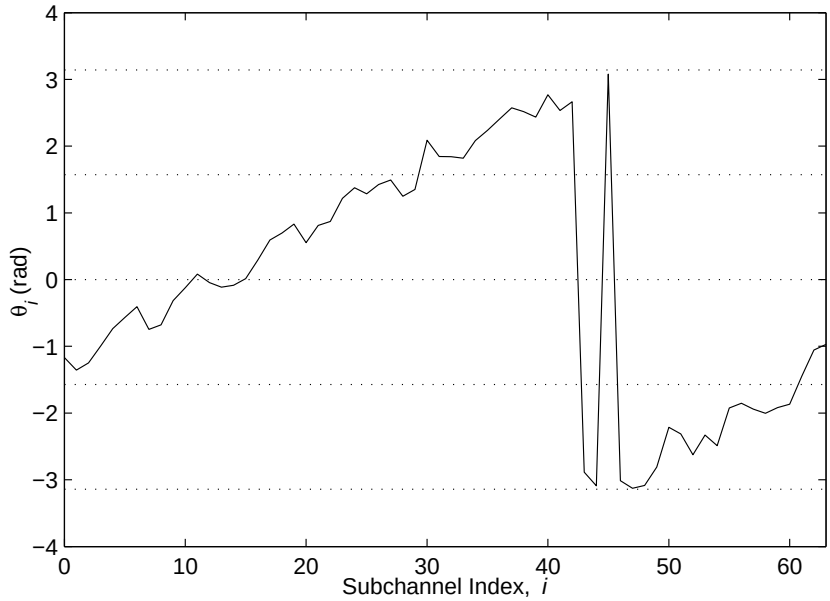

Figure 4.3: Variation of θ_i for $N = 64$, $\epsilon = 0.5$, with AWGN only at 15 dB SNR

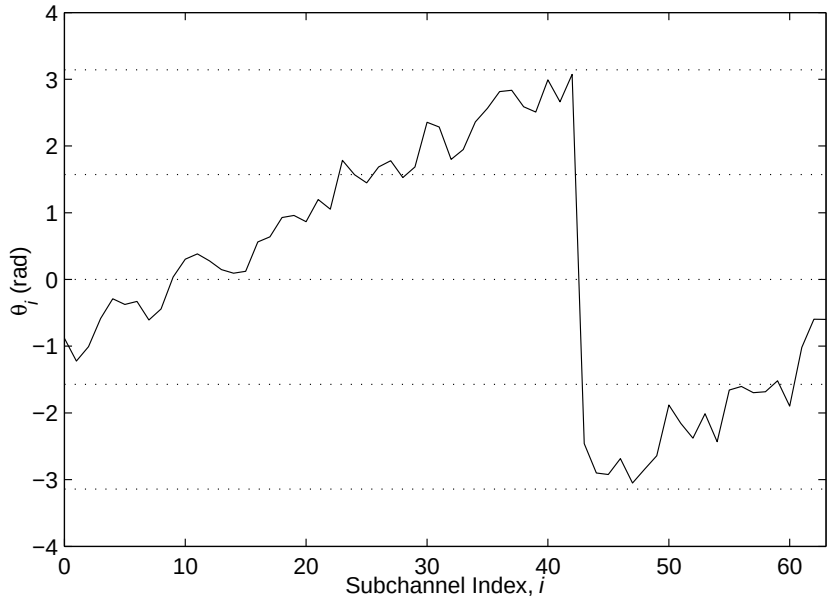

Figure 4.4: Variation of θ_i for $N = 64$, $\epsilon = 0.5$ with AWGN at 15 dB SNR and CIR

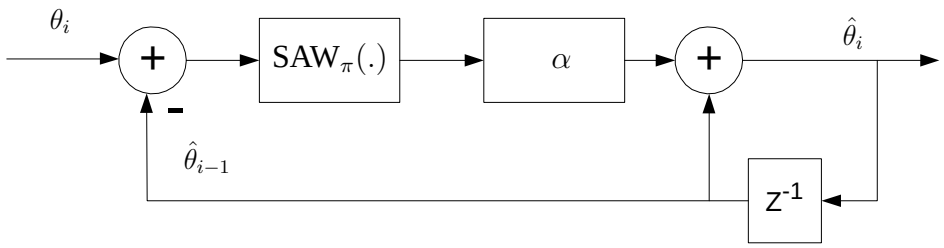

Figure 4.5: Phase unwrapping algorithm

$\epsilon = 0.5$ and $\xi_{SCA} = 1$ including AWGN at an SNR of 15 dB. The frequency offset is corrected using the estimate $\hat{\epsilon}_{SCA}$ made using the SCA. The phase gradient caused by the residual frequency offset is very small compared to that caused by the symbol offset. This will be demonstrated in section 5.5 of the next chapter. Thus it can be assumed that $\epsilon - \hat{\epsilon}_{SCA} \approx 0$ during the estimation of the symbol offset. Figure 4.4 shows a similar plot, this time with the inclusion of a 3-tap SUI-II CIR appropriate for the BFWA scenario with $v = 20$ and $p = 10$. As seen from the figures 4.3 and 4.4, θ_i maintains a distinct gradient even when a representative CIR is included. However due to the phase wrapping effect, θ_i must be first unwrapped by a suitable unwrapping algorithm. Although accurate phase unwrapping algorithms are available, they are very complex. Since the algorithm only makes use of the phase gradient and not the absolute phase values, a relatively simple scheme was selected for the unwrapping of the phase [85]. For purposes of clarity, the ith sample of the wrapped phase and the unwrapped phase are denoted as θ_i and $\hat{\theta}_i$, respectively. The phase unwrapping algorithm can be expressed as,

$$\hat{\theta}_i = \hat{\theta}_{i-1} + \alpha \text{SAW}_\pi(\theta_i - \hat{\theta}_{i-1}) \tag{4.25}$$

where SAW$_\pi(.)$ is a sawtooth function that limits the output to $\pm\pi$ and α is a parameter that controls the variance of the unwrapped phase. The algorithm is illustrated in figure 4.5. Figure 4.6 shows the action of the unwrapping algorithm for the same scenario that produced the results presented in figure 4.4 with $\alpha = 1$.

The estimate of the symbol offset is calculated as the gradient of the un-

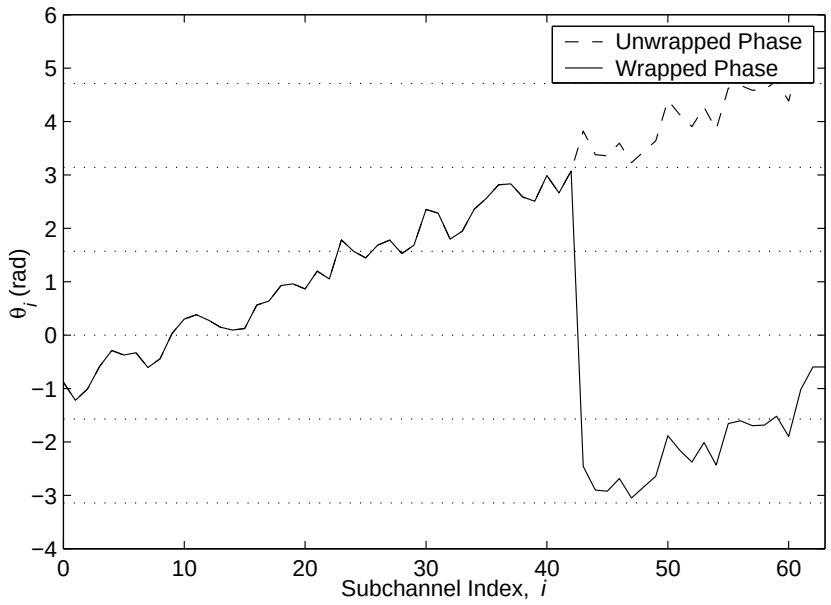

Figure 4.6: Performance of the unwrapping algorithm for $N = 64$, $\epsilon = 0.5$, with AWGN at 15 dB SNR and CIR at $\alpha = 1$

wrapped phase sample vector $\underline{\hat{\theta}} = [\hat{\theta}_0, .., \hat{\theta}_{N-1}]$,

$$\hat{\xi} = \text{ROUND}(\text{GRAD}(\underline{\hat{\theta}}).N/2\pi) \tag{4.26}$$

where the GRAD$(.)$ function finds the Maximum Likelihood (ML) gradient of the parameter in a least-squares sense and the ROUND$(.)$ function rounds the parameter to the nearest integer. Now $\hat{\xi}$ is used to update the initial SOF, namely the $\hat{\text{SOF}}_{SCA}$. However, a single estimate may not be accurate in the presence of channel impairments. Hence it is proposed to repeat the above process until $\hat{\xi} = 0$, updating the estimated SOF at the end of each iteration. (i.e. at the end of mth iteration $\hat{\text{SOF}}(m) = \hat{\text{SOF}}(m-1) + \hat{\xi}(m)$). Note that $\hat{\epsilon}$ is estimated at each step to increase the accuracy. The number of iterations taken to achieve the condition $\hat{\xi} = 0$ is denoted as u. The iterative process is initialised by letting $\hat{\text{SOF}}(0) = \hat{\text{SOF}}_{SCA}$. It is found that in most cases the algorithm achieves the correct SOF within a few iterations even when a CIR is included. However at very low SNR values, there is a small probability of non-convergence. To prevent continual iteration,

the algorithm is allowed to iterate only a predetermined number of times, N_{it} (i.e. $u \leq N_{it}$). In practice, this does not pose a significant problem, since the receiver can always request a retransmission if convergence is not achieved. This is a far better option than estimating the SOF incorrectly and as a consequence obtaining samples comprising two OFDM received symbols in the FFT window. In this case the error rate will be very high.

4.4.2 2nd Part - Error Comparison

Figure 4.7 shows how the ISOCA works for two possible scenarios. The first is when $\xi_{SCA} < N/2$ as shown in figure 4.7(a). The symbol offset is estimated and corrected at the end of the iterative part of the ISOCA after u iterations. In the unlikely event that $\xi_{SCA} > N/2$, the gradient of θ_i actually changes sign. This will result in the unwrapping algorithm calculating a gradient with the opposite sign to that required, which will subsequently cause the estimated symbol offset, $\hat{\xi}$ during the iterative process to move away from SOF$_{ideal}$. In this case when the iterative process terminates, the estimated SOF will be more than $N/2$ samples away from the desired position as shown in figure 4.7(b).

To address this situation, a second correction is made at the end of the iterative process. Here the decoded output due to the second training symbol, $\hat{A}_{N_{t2}}$ determined using the estimated SOF at end of iterative process, $\hat{\text{SOF}}(u)$ is compared with the transmitted symbol, $A_{N_{t2}}$. However, the resulting comparison will be seriously affected by subchannels experiencing a low SNR resulting from spectral nulls in the channel response H_l. To overcome this problem, an estimate of the channel response $\hat{H}_l$ is made by comparing the transmitted and demodulated output of the second training symbol, specifically,

$$\hat{H}_l = Y_{N_{t2}}/A_{N_{t2}} \tag{4.27}$$

Only those subchannels with $|\hat{H}_l|$ above a certain threshold are selected. This subset of subchannels is denoted as $\underline{d} \subset [0, ..N-1]$. The chosen criteria selects only those subchannels with $|\hat{H}_l|$ in excess of a standard deviation above the mean. The outputs of these subchannels $\hat{Y}_{N_{t2},d}$ are sent through a slicer to

obtain $\hat{A}_{N_{t2},d}$, where $d \in \underline{d}$. If the number of symbol errors between $\hat{A}_{N_{t2},d}$ and $A_{N_{t2},d}$ exceeds a predefined threshold, N_{er} it is assumed that the iterative estimation has diverged from SOF_{ideal}. Otherwise it is assumed that ideal symbol synchronisation has been achieved. An estimate of the direction of divergence is made by analysing the SOFs estimated during the iterative process, specifically $[\hat{\text{SOF}}_{SCA}, \hat{\text{SOF}}(1), .., \hat{\text{SOF}}(u)]$. For example, in figure 4.7(b) the successive estimated SOFs will increase in value. In this case, the iterative process is reinitialised by letting $\hat{\text{SOF}}(0) = \hat{\text{SOF}}_{SCA} - N/4$ as shown in figure 4.7(c) and then the iterative process is repeated. As shown in figure 4.7(d), the iterative process now converges to the correct SOF. Obviously, the direction of divergence cannot be estimated if the iterative procedure completes with just one iteration (i.e. $u = 1$), in which case it will result in a non-convergence error being generated. A similar situation to that already described exists if $\xi_{SCA} < 0$ to begin with. However in this case comments concerning $\hat{\theta}$ and $\hat{\xi}$ and the direction of adjustment are the reverse of the previous scenario. Figure 4.8 shows the flow graphs for the ISOCA.

4.5 Simulation Parameters and Results

Firstly, OFDM systems with $N = 64$ have been simulated in the presence of AWGN alone. QPSK mapping for all subchannels has been employed and all the subchannels are used. The sampling rate is assumed to be 20 MHz. A burst of 2500 OFDM symbols are transmitted, which takes less than 10 ms, consequently the channel is assumed constant for the duration of each burst. Each data point in the simulation results is obtained by averaging over 500 such bursts. A relative frequency offset of $\epsilon = 0.5$ is assumed. Figure 4.9 shows the probability of having a particular symbol offset at the end of the acquisition stage of the SCA using the original proposal to find d'_{opt} given in [25]. Figure 4.10 shows the probability of symbol offset at the end of the acquisition stage of the SCA, i.e. ξ_{SCA} based on d_{opt} using the proposal of equation (4.19). Note that all similar 3D figures presented in this section that show the performance in terms of SNR vs Symbol Offset and the probability of achieving that particular symbol offset are based on those data bursts that were able to converge only. Plots showing the probability of

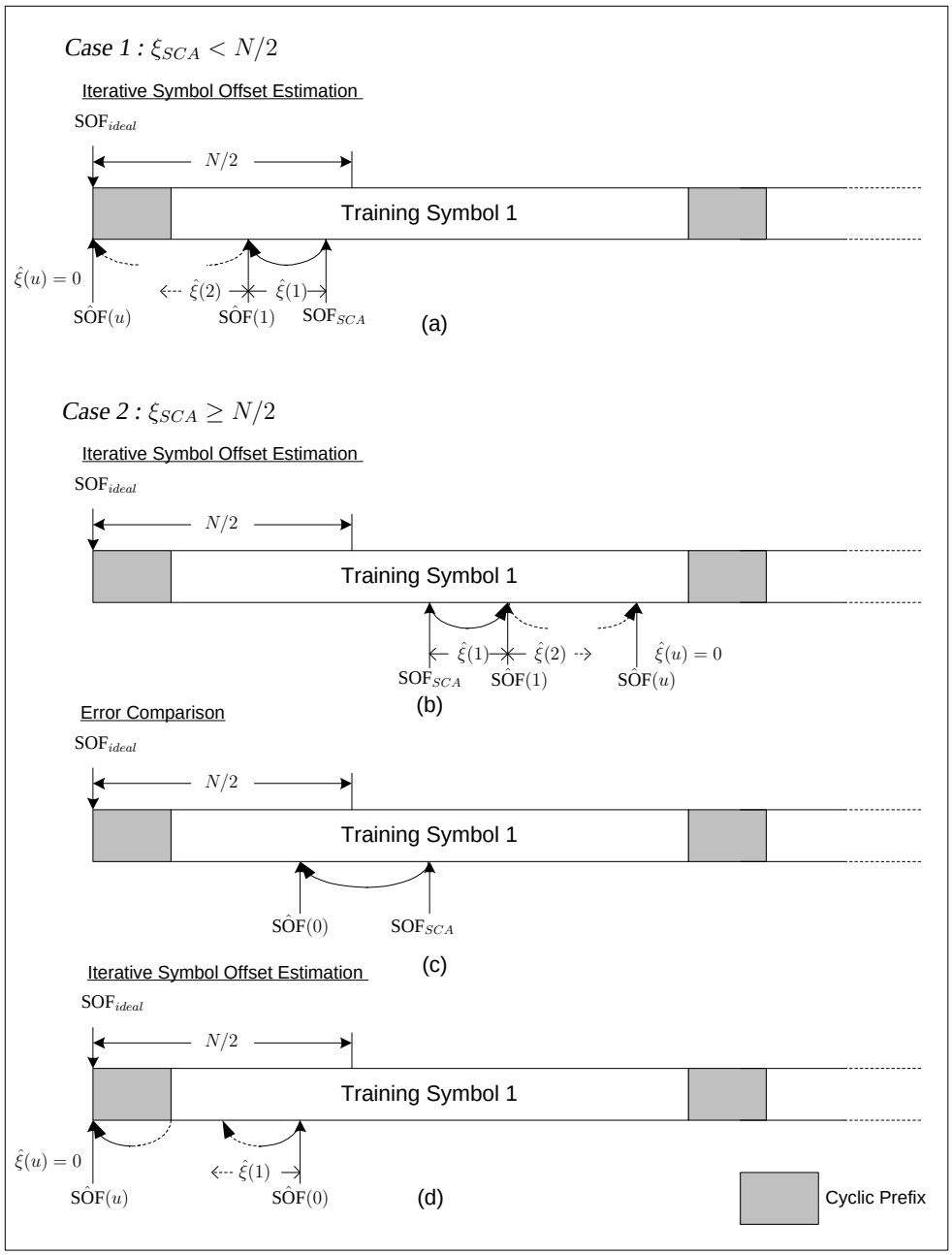

Figure 4.7: Two cases of ISOCA correction

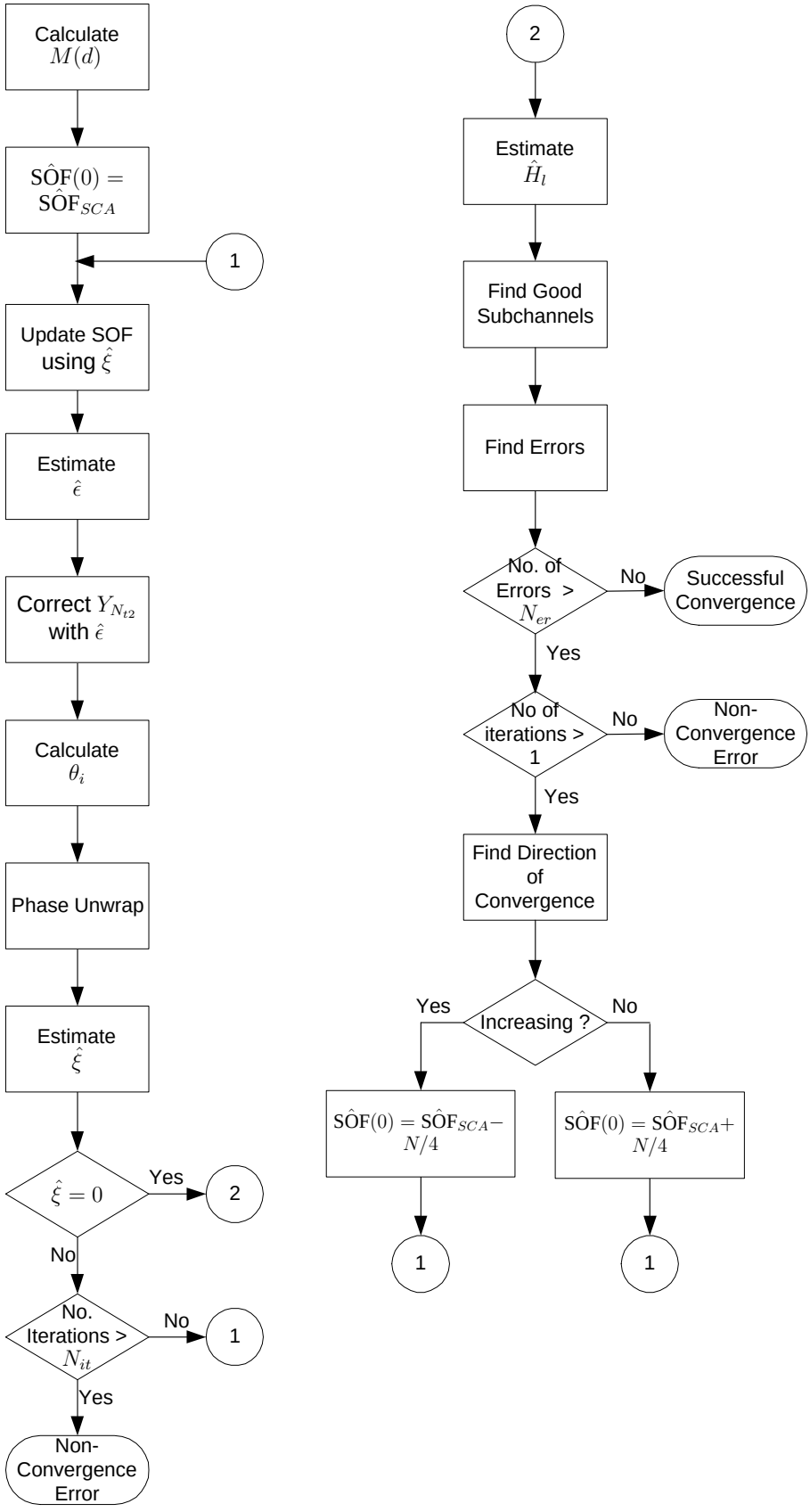

Figure 4.8: ISOCA flow graphs: First correction (left), second correction (right)

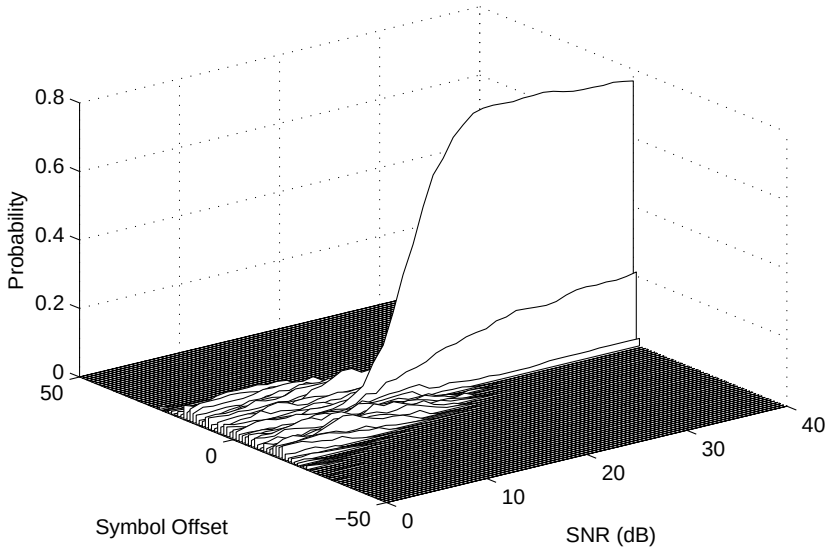

Figure 4.9: Performance after SCA using the original algorithm with AWGN alone for $N = 64$, $\epsilon = 0.5$

non-convergence are shown separately later on. The original proposal is devised to locate d'_{opt} at the mid point of the timing metric plateau. In the case of AWGN channels the length of the timing metric plateau is equal to the length of the CP, i.e. v. Hence the SOF is estimated as $\hat{\text{SOF}}_{SCA} = d'_{opt} - v/2$. From figure 4.9 it can be seen that the estimation process performs badly at SNRs less than 15 dB. At these SNR levels there is a high probability of even getting a positive symbol offset. The maximum probability of getting perfect symbol synchronisation is 0.75 even at high SNR levels. The new proposal as expressed in (4.19) is in contrast devised to find the edge of the plateau. From figure 4.10 it can be seen that in most instances ξ_{SCA} lies within the CP following application of the modified SCA. (i.e. the condition $-v \leq \xi_{SCA} \leq 0$ is satisfied). The probability of achieving perfect symbol synchronisation has now increased to 0.9 at high SNR levels. However the range of symbol offsets present are quite significant still. Hereafter unless stated otherwise, it will be assumed that the new proposal using equation (4.19) will be used for the estimation of the SOF for the SCA, namely $\hat{\text{SOF}}_{SCA}$.

The results after performing the first correction process of the ISOCA are shown in figure 4.11 (i.e. $\hat{\xi}(u)$ reached at the end of the first correction process).

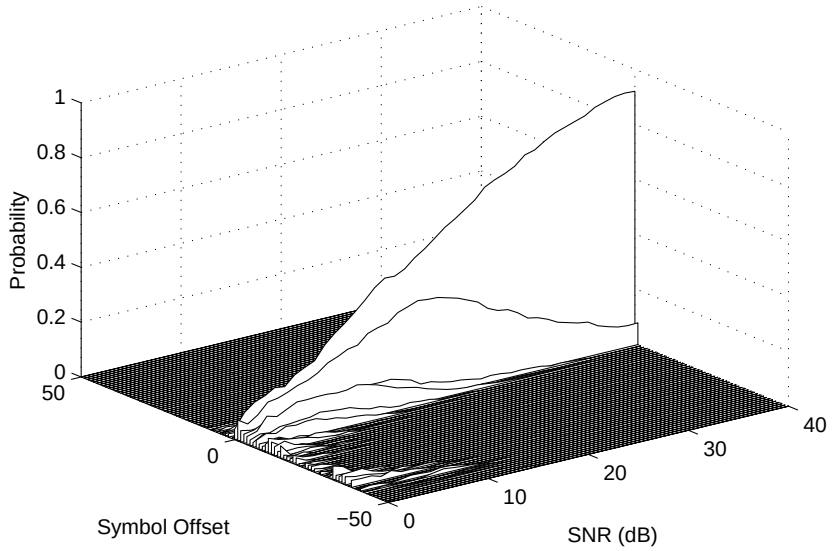

Figure 4.10: Performance after SCA using the modified algorithm with AWGN alone for $N = 64$, $\epsilon = 0.5$

This shows that the first correction is adequate at most values of SNR to achieve perfect symbol synchronisation. However at very low SNR levels, there is a small probability of $\hat{\xi}(u)$ lying beyond $N/2$ owing to the divergence of successive $\hat{\xi}$ values in the first iterative process, as explained in section 4.4. Note that after the the application of 2nd correction process of the ISOCA, ideal symbol synchronisation is achieved even at very low SNR values as shown in figure 4.12. Figure 4.13 shows a comparison of the probability of convergence failure between ISOCA and SCA in AWGN. The failure rate due to non convergence of the ISOCA becomes significant (i.e. defined as a probability in excess of 20%) at an SNR of less than 4 dB. Note that probability of failure of SCA acquisition is not significantly better.

Figure 4.14 summarises the results in terms of the variance of the estimated SOF with respect to SOF_{ideal}. It shows that the SCA using the original proposal for estimating d_{opt} has a similar performance to the modified acquisition method. Note that this plot weights the positive and the negative symbol offsets equally when calculating the variance. Application of the first ISOCA process alone is able to guarantee perfect symbol synchronisation at practical values of SNR as

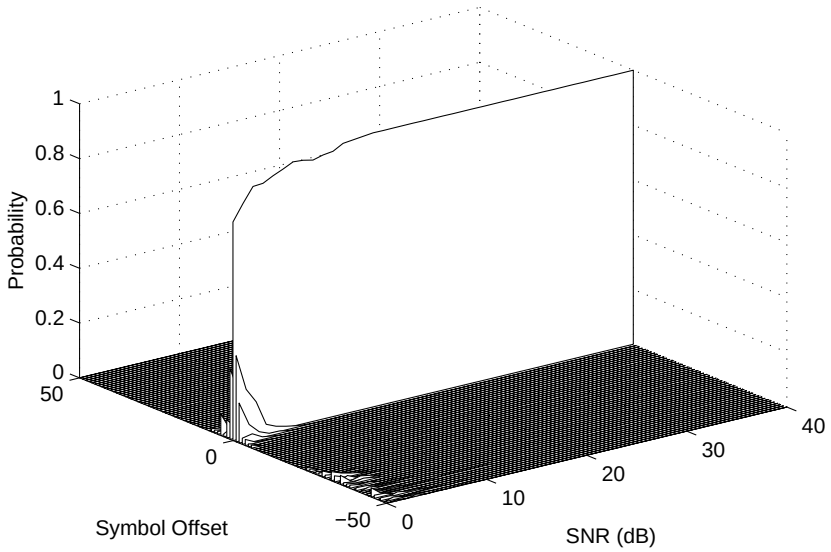

Figure 4.11: Performance after the 1st correction process of the ISOCA with AWGN alone for $N = 64$, $\epsilon = 0.5$

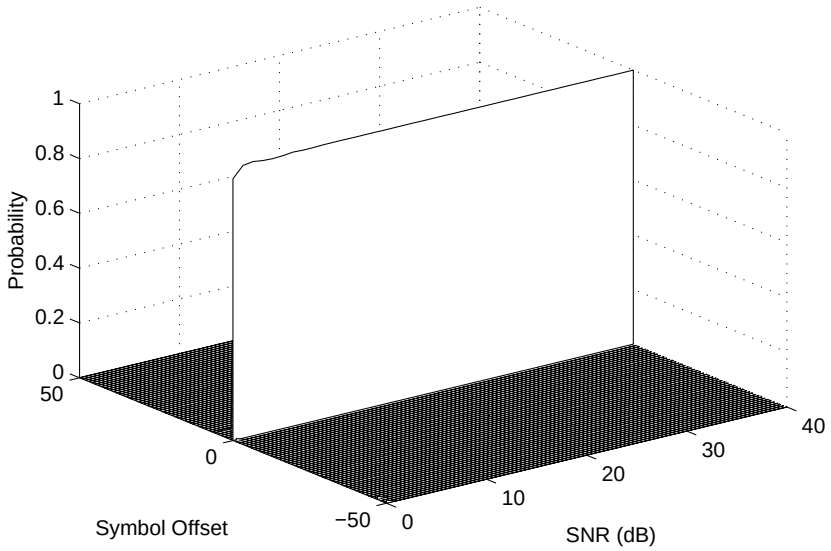

Figure 4.12: Performance after the 2nd correction process of the ISOCA with AWGN alone for $N = 64$, $\epsilon = 0.5$

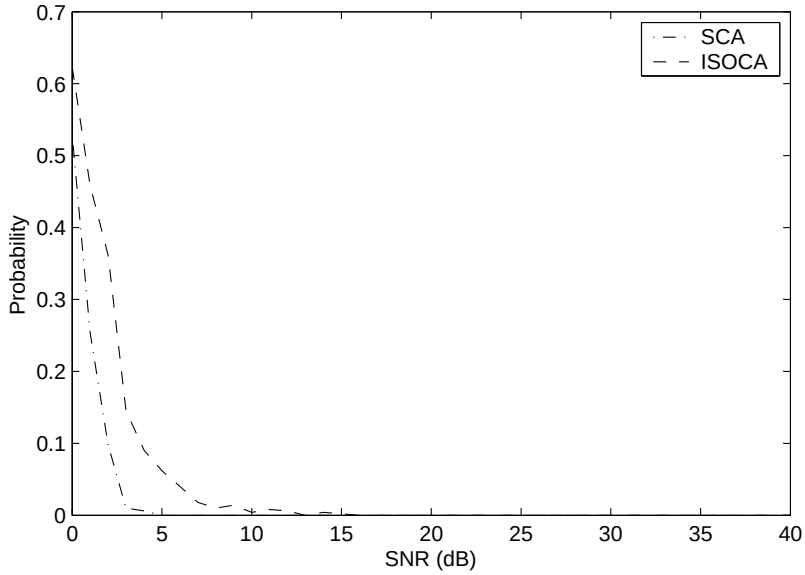

Figure 4.13: Probability of convergence failure with AWGN alone for $N = 64$, $\epsilon = 0.5$

shown in figure 4.11, although the variance increases significantly at low SNR values. However, even at very low SNR values (< 10 dB), the application of both parts of the ISOCA significantly reduces the variance. Figure 4.15 shows similar results, this time for $N = 128$ and $N = 256$. It shows that there is a finite probability of symbol offset at very low SNR values after employing only the first part of ISOCA . The results given by the second ISOCA process cannot be presented in the same figure since the simulated offset results are zero. Consequently, perfect synchronisation is achieved when both parts of the ISOCA are employed.

Next the performance of ISOCA is analysed in the presence of SUI-II channels [23]. OFDM systems with $N = 64$ have been simulated at a sampling rate of 20 MHz with a guard interval, v equal to 20 samples for all symbols except the first training symbol. To improve the acquisition performance of the SCA, the length of the CP of the first training symbol is increased to give an Excess Length, $p = 10$.

Figure 4.16 shows that the performance of the modified SCA deteriorates significantly from that achieved in AWGN alone when the SUI-II CIR is incorpo-

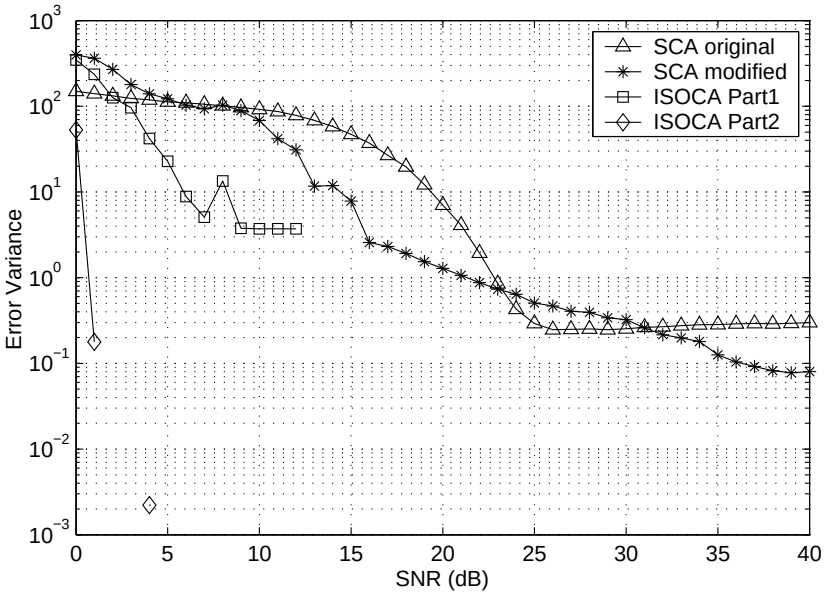

Figure 4.14: Variance of the estimated SOF with respect to SOF_{ideal} for AWGN channels with $N = 64$ and $\epsilon = 0.5$

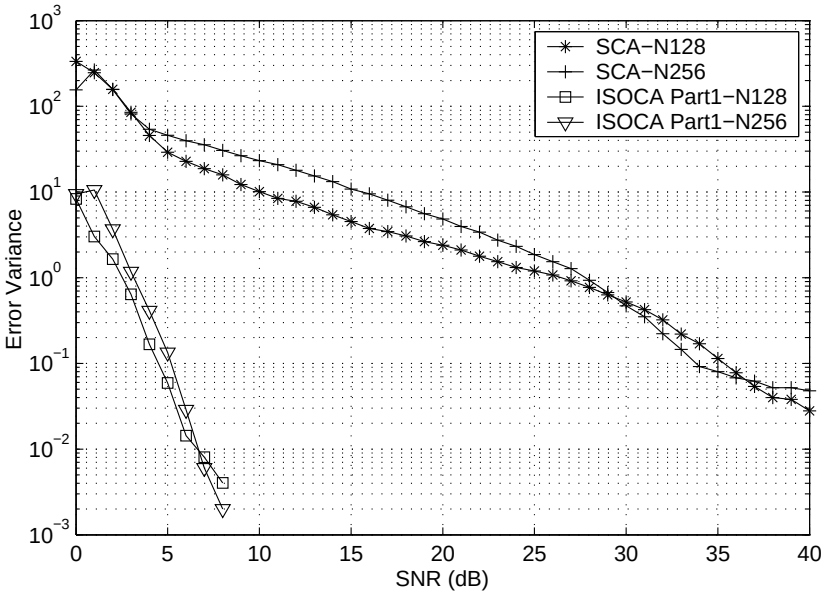

Figure 4.15: Variance of the estimated SOF with respect to SOF_{ideal} for AWGN channels with $N = 128, 256$ and $\epsilon = 0.5$

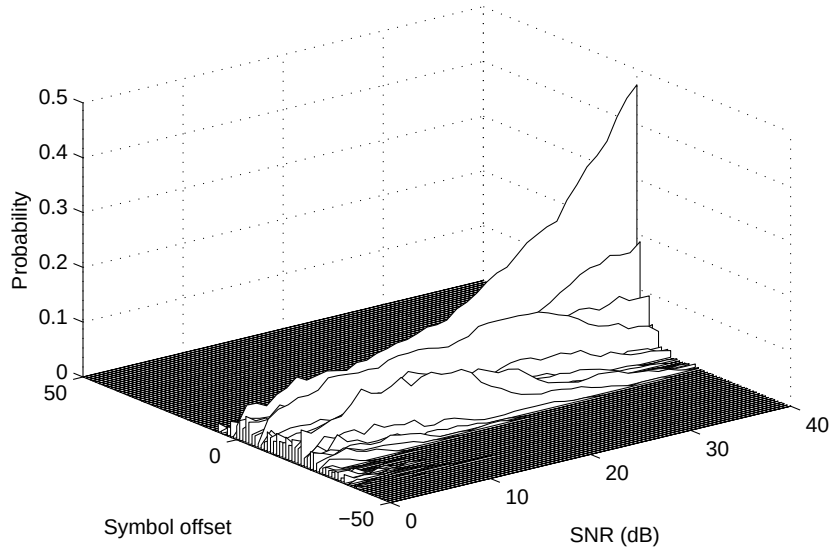

Figure 4.16: Performance after the modified SCA with AWGN and SUI-II CIR for $N = 64$, $\epsilon = 0.5$

rated. The probability of achieving perfect symbol synchronisation is now reduced to 0.48. The estimated SOF now has a much larger spread away from SOF$_{ideal}$. Note that there is a considerable probability of SOF$_{SCA}$ having an offset greater than p. There is also a significant probability of achieving a positive symbol offset. In this case the FFT window will take samples of two consecutive OFDM symbols for demodulation. Since the CIRs that are common in BFWA applications are asymmetric, this would seriously degrade the BER performance. Figures 4.17 and 4.18 show the performance of the ISOCA in the same conditions without and with the 2nd correction, respectively. The 1st correction process provides perfect symbol synchronisation even with a SUI-II channel for practical SNR levels. Note that after the correction by the second process of the ISOCA virtually perfect symbol synchronisation is maintained even at very low SNR values as shown in figure 4.18. Figure 4.19 shows that the probability of convergence failure has not deteriorated significantly for the ISOCA as compared with the previous AWGN only case.

Figure 4.20 shows the SOF error variance after each stage of the symbol synchronisation process. The results for SCA using the original proposal are also

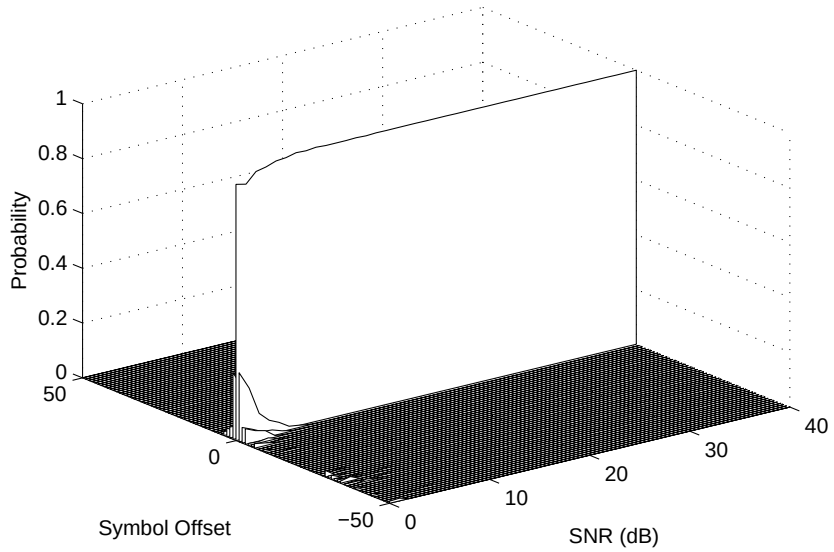

Figure 4.17: Performance after the 1st correction of ISOCA with AWGN and the SUI-II CIR for $N = 64$, $\epsilon = 0.5$

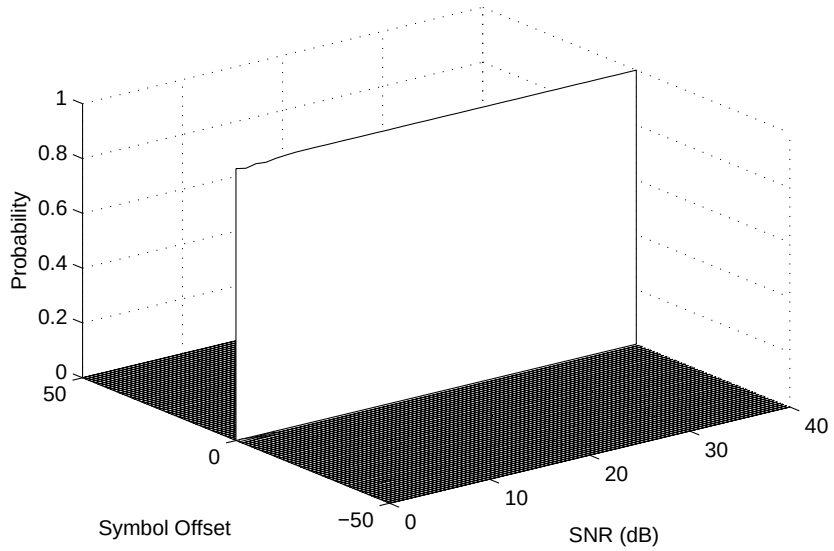

Figure 4.18: Performance after the 2nd correction of ISOCA with AWGN and the SUI-II CIR for $N = 64$, $\epsilon = 0.5$

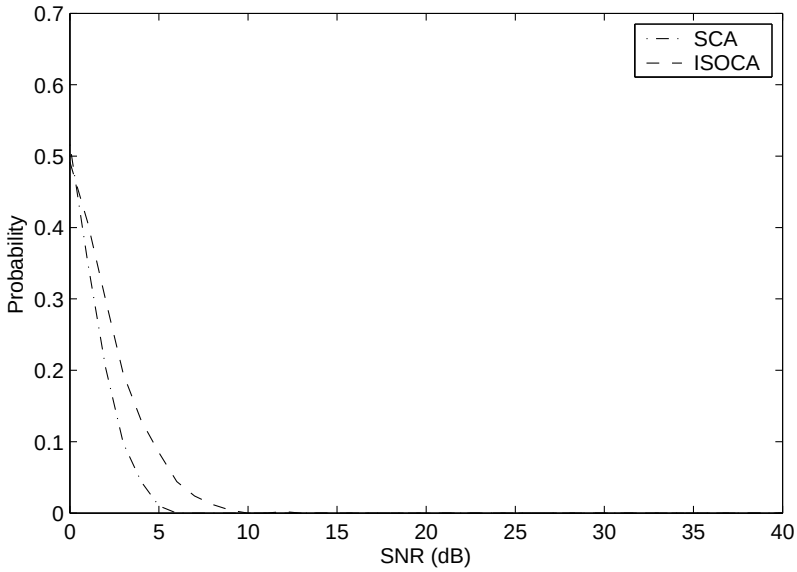

Figure 4.19: Probability of convergence failure with AWGN and the SUI-II CIR for $N = 64$, $\epsilon = 0.5$

included. The length of the timing metric plateau is now assumed to be p, hence the SOF is estimated as $\hat{\text{SOF}}_{SCA} = d'_{opt} - p/2$ for the original proposal. Compared to the AWGN only results presented in figure 4.14, it shows that even when the modified method for acquisition of d_{opt} is employed, SCA suffers considerable symbol offset. As in figure 4.14 the positive and negative offsets are weighted the same in this figure. As previous results have shown, whereas the SCA alone has a significant probability of giving positive symbol offsets at lower SNR values, the ISOCA has a higher probability of yielding only the less damaging negative symbol offsets. Employing only the first part of the ISOCA is shown to improve the performance giving perfect symbol synchronisation at practical values of SNR. Figure 4.21 shows results for similar conditions for $N = 128$ and 256. It shows similar results on completion of the first ISOCA process. The simulation results also showed that employing both parts of the ISOCA achieved perfect synchronisation even at very low values of SNR for $N = 128, 256$. Again, these results cannot be presented since the variance was zero at all values of SNR tested.

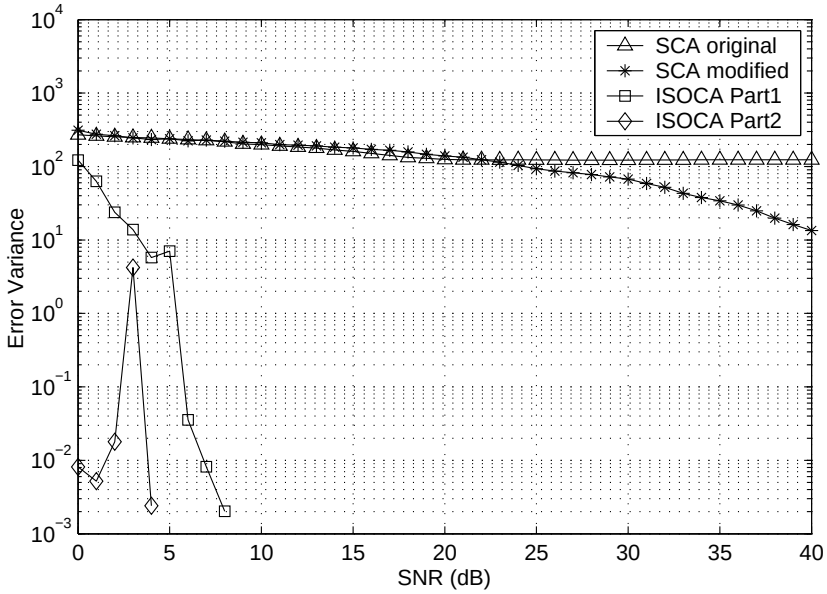

Figure 4.20: Variance of the estimated SOF with respect to SOF$_{ideal}$ for the SUI-II channels with $N = 64$ and $\epsilon = 0.5$

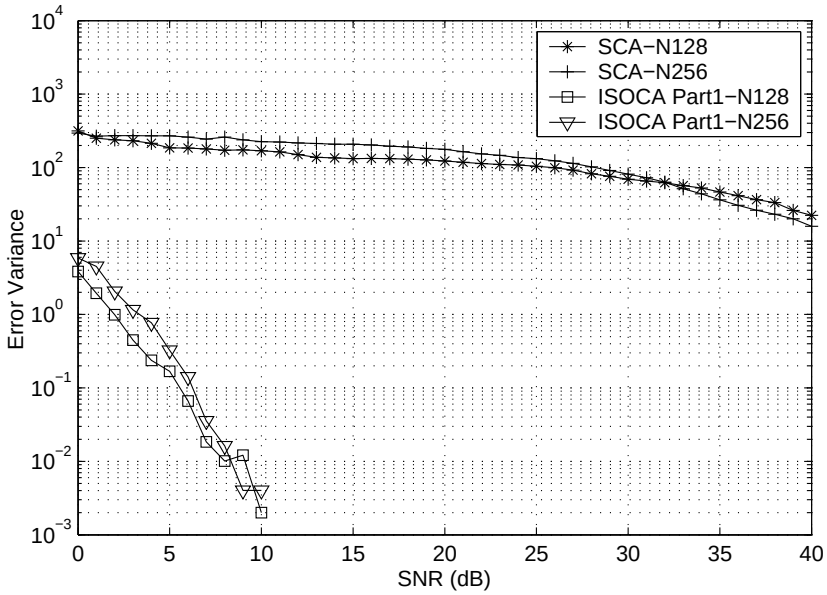

Figure 4.21: Variance of the estimated SOF with respect to SOF$_{ideal}$ for the SUI-II channels with $N = 128, 256$ and $\epsilon = 0.5$

4.6 Conclusions

In this chapter an Iterative Symbol Offset Correction Algorithm (ISOCA), that complements the symbol synchronisation performed by the Schmidl and Cox Algorithm (SCA) is presented. It achieves this by iteratively tracking the phase gradient caused by the ratio between the demodulated and the transmitted second training symbol of the SCA. It has been shown analytically that this is possible for different ranges of the symbol offset, ξ. It is also shown through computer simulations that the ISOCA performs remarkably well and achieves virtually perfect symbol synchronisation even at very low values of SNR for OFDM systems with $N = 64, 128, 256$ in the presence of the SUI-II BFWA channel. The SCA by contrast has only a 0.48 probability of achieving perfect symbol synchronisation even at high SNR levels. The algorithm however has a very low but finite probability of failing to converge to the actual SOF, but this is apparent only at SNR values below 4 dB. At SNR levels that are appropriate in practical transmissions, the system is shown to perform very well.

Chapter 5

Residual Frequency Offset Correction

Chapter 4 showed the effect that symbol offset has on the performance of OFDM systems and presented the Schmidl and Cox Algorithm (SCA) [25, 58] which may be used to achieve both symbol synchronisation and frequency offset synchronisation. The same chapter identified performance limitations of the symbol synchronisation function of the SCA when applied to OFDM systems in BFWA channels. To overcome these limitations the Iterative Symbol Offset Correction Algorithm (ISOCA) is proposed which complements the SCA. It has been shown via extensive simulations that the ISOCA greatly improves the acquisition of symbol timing in this application. In this chapter attention is directed toward the frequency offset synchronisation function of the SCA. Throughout this chapter it will be assumed that the system achieves perfect symbol synchronisation. This assumption is valid since we have shown in chapter 4 that the ISOCA achieves virtually perfect symbol synchronisation for the BFWA channels under consideration. The frequency offset in this chapter is defined relative to the intercarrier spacing and is denoted as ϵ.

This chapter is organised as follows. Section 5.1 presents the work carried out by others in the same area. Section 5.2 will show the effects of frequency offset and highlight its severe impact on performance. The SCA will be presented in section 5.3 with particular emphasis directed towards its ability to correct frequency

offset. As noted earlier, the SCA does not perform well with OFDM systems having a low number of subchannels, N. The Residual Frequency Offset Correction Algorithm (RFOCA) to be presented in section 5.4 complements the frequency offset correction functions of the SCA to reduce any Residual Frequency Offset (RFO) remaining after application of the SCA. Section 5.5 presents results obtained through computer simulations which investigate the performance of the RFOCA in both AWGN and BFWA channels. Section 5.6 will draw conclusions.

5.1 Related Work

Moose was one of the first authors to present a frequency offset correction method for OFDM that utilises repetitive sections of the transmit data [86]. He proposed to have two repetitive OFDM symbols. Hence the relative frequency offset, ϵ that can be estimated without phase ambiguity is equal to half the intercarrier spacing (i.e. $|\epsilon| < 0.5$). The SCA uses a training symbol that is repetitive with a period equal to half the symbol period. Hence using only the first training symbol, the estimation limit was increased to the intercarrier spacing (i.e. $|\epsilon| < 1$). The authors in [87] propose to use only the first training symbol of the SCA but to form it from more than two identical parts. The fractional part of the frequency offset estimate is modified compared with that of the SCA and is computationally much more intensive. Usually, the frequency offset and symbol synchronisation is done using the same training symbols. Adding more repetitions to the first training symbol of the SCA also compromises the symbol synchronisation part of the SCA. In general, having a training symbol with M identical parts increases the frequency offset estimation range to $\pm M/2$ intercarrier spacings. Even though increasing the training symbol repetition further increases the resolution, it will compromise the accuracy of the frequency offset estimate owing to the smaller number of samples used by the correlation filter [88]. The WLAN standards such as HIPERLAN/2 and IEEE 802.11a use two OFDM symbols as a preamble, one symbol being divided into short subsequences and the other into two identical subsequences. One of the uses of the preambles is to estimate the frequency offset. Two estimates are performed, the first is a coarse frequency offset estimation made using a delay and correlate method between the shorter sequences. A fine frequency offset

estimation is then made by calculating the angular rotation between the post-FFT samples of the two training symbols [24].

Other suggestions utilise the correlation between the cyclic prefix and the last few samples of the OFDM symbol [62]. In [89] the authors extend the work of [62] by proposing a new likelihood function for joint estimation of symbol and frequency offset based on direct matrix inversion. Once again though, its performance for dispersive channels is not acceptable for small values of N.

The authors in [90, 91] propose to periodically scatter the pilot symbols in some subchannels in the time-frequency grid. This avoids the use of OFDM symbols for training. The estimate has to be averaged over a number of OFDM symbols to get a reasonable estimate even with the assumption of perfect channel knowledge. As noted in chapter 1, in general for short burst data transmission, the use of some subchannels for pilot symbols is not practical.

Other approaches are the self-cancellation schemes presented in [92] and [93, 94], where the data to be transmitted is mapped repeatedly on to adjacent pairs of subchannels rather than on to a single subchannel. If the data is negated in one of the adjoining subchannels the overall effects of ICI due to frequency offset can be eliminated. Again, when N is low this approach is not practical and the number of available subchannels is also reduced by at least one half.

In [95, 96, 97, 98] blind frequency offset estimation techniques are proposed. These techniques avoid the use of training symbols and rely on the second order statistics of the received signal and generally have a high computational burden. The authors in [99, 100] propose algorithms to estimate only the integer part of the frequency offset. It is assumed that the fractional part can be estimated and corrected perfectly by some other technique such as the SCA. This assumption is not correct as will be shown in later sections. The authors in [101] show analytically that the use of non-rectangular windowing reduces the effect of ICI caused as a result of frequency offset. The use of such windows will be investigated in more detail in chapter 7.

In section 5.4 a novel algorithm will be presented that does not utilise any continuous pilots nor null symbols yet tracks the residual offset quite effectively. It also performs very well for BFWA applications.

5.2 Effect of Frequency Offset in OFDM

Assuming that the length of the Cyclic Prefix (CP) is longer than the length of the CIR (i.e. $v \geq N_h - 1$), and that N is large enough such that the frequency selective channel is divided into contiguous flat fading subchannels the expression of (2.27) for the demodulated symbol of lth subchannel in mth OFDM block is modified to,

$$Y_{m,l} = \frac{1}{N} \sum_{n=0}^{N-1} \left\{ \left\{ \sum_{k=0}^{N-1} A_{m,k} H_k e^{j2\pi \frac{n(k+\epsilon)}{N}} \right\} \right\} e^{-j2\pi \frac{ln}{N}} + W_l \tag{5.1}$$

for $0 \leq n \leq N-1$. Here H_k is the Channel Transfer Function (CTF) at the subchannel index k, W_l is the component due to AWGN and ϵ is the frequency offset relative to the intercarrier spacing. The expression in (5.1) allows the output of the lth subchannel to be expressed as the sum of three components,

$$Y_{m,l} = R_l + I_l + W_l \tag{5.2}$$

where R_l and I_l are the desired and the Inter Carrier Interference (ICI) terms, respectively. By substituting the condition $k = l$ in the inner sum of (5.1), we can obtain R_l. Thus,

$$\begin{aligned} R_l &= \frac{1}{N} \sum_{n=0}^{N-1} (A_{m,l} H_l) e^{j2\pi \frac{n(l+\epsilon)}{N}} e^{-j2\pi \frac{nl}{N}} \\ &= \frac{A_{m,l} H_l}{N} \frac{1 - e^{j2\pi\epsilon}}{1 - e^{j2\pi\epsilon/N}} \\ &= (A_{m,l} H_l) \frac{\sin(\pi\epsilon)}{N \sin(\pi\epsilon/N)} e^{j\pi\epsilon \frac{N-1}{N}} \ . \end{aligned} \tag{5.3}$$

Equation (5.3) shows that the desired term $A_{m,l}H_l$ experiences amplitude reduction and phase rotation. Since $N \gg \pi\epsilon$, $\sin(\pi\epsilon/N)$ can be approximated by $(\pi\epsilon)/N$. Hence,

$$R_l \approx A_{m,l} H_l \frac{\sin(\pi\epsilon)}{N(\pi\epsilon/N)} e^{j\pi\epsilon \frac{N-1}{N}} = A_{m,l} H_l \text{sinc}(\epsilon) e^{j\pi\epsilon \frac{N-1}{N}} \ . \tag{5.4}$$

As $\epsilon \to 0$, $R_l \to A_{m,l}H_l$, hence the degradation of the required term vanishes

when the received data does not experience any frequency offset. In practice, the effect of the channel transfer function H_l is removed by the FEQ following the FFT, as shown in section 2.4.

The effect due to ICI in (5.2) can be calculated as,

$$\begin{aligned} I_l &= \frac{1}{N}\sum_{\substack{k=0\\k\neq l}}^{N-1}\sum_{n=0}^{N-1}(A_{m,k}H_k)e^{j2\pi\frac{n(k+\epsilon)}{N}}e^{-j2\pi\frac{nl}{N}} \\ &= \sum_{\substack{k=0\\k\neq l}}^{N-1}\frac{A_{m,k}H_k}{N}\frac{1-e^{j2\pi(k+\epsilon-l)}}{1-e^{j2\pi(k+\epsilon-l)/N}} \\ &= \sum_{\substack{k=0\\k\neq l}}^{N-1}(A_{m,k}H_k)\frac{\sin\pi(k+\epsilon-l)}{N\sin\pi(k+\epsilon-l)/N}e^{j\pi(k+\epsilon-l)\frac{N-1}{N}} . \end{aligned} \tag{5.5}$$

If we assume that the transmitted data is zero mean and uncorrelated (i.e. $E[A_{m,k}] = 0$ and $E[A_{m,l}A^*_{m,k}] = \sigma_A\delta_{l,k}$, then $E[I_l] = 0$. Hence the ICI power is,

$$E[|I_l|^2] = \sigma_A[\sin\pi\epsilon]^2\sum_{\substack{k=0\\k\neq l}}^{N-1}\frac{E[|H_k|^2]}{[N\sin\pi(k+\epsilon-l)/N]^2} . \tag{5.6}$$

A measure of the impact of frequency offset is given by defining the Carrier to Interference Ratio (CTIR) in an OFDM system as, CTIR $= E[|R_l|^2]/E[|I_l|^2]$. Assuming the average channel gain, $E[|H_k|^2$ is unity and with zero AWGN, (i.e. $W_l = 0$) then,

$$\text{CTIR} = \frac{\sum_{\substack{k=0\\k\neq l}}^{N-1}1/[N\sin\pi(k+\epsilon-l)/N]^2}{[N\sin(\pi\epsilon/N)]^2} . \tag{5.7}$$

A similar analysis on the effect of frequency offset on OFDM can be found in [86] and [94]. Also see [102] for an analysis of the ICI power when the OFDM system is subject to channels giving rise to Doppler spreading. Figure 5.1 shows the CTIR in decibels as a function of ϵ. Simulated CTIR values for $N = 64$ and 256 using QPSK data mapping are also shown. It shows that the CTIR drops significantly when the relative frequency offset, ϵ increases beyond 0.1. An important observation is that the CTIR is insensitive to the values of N between 64

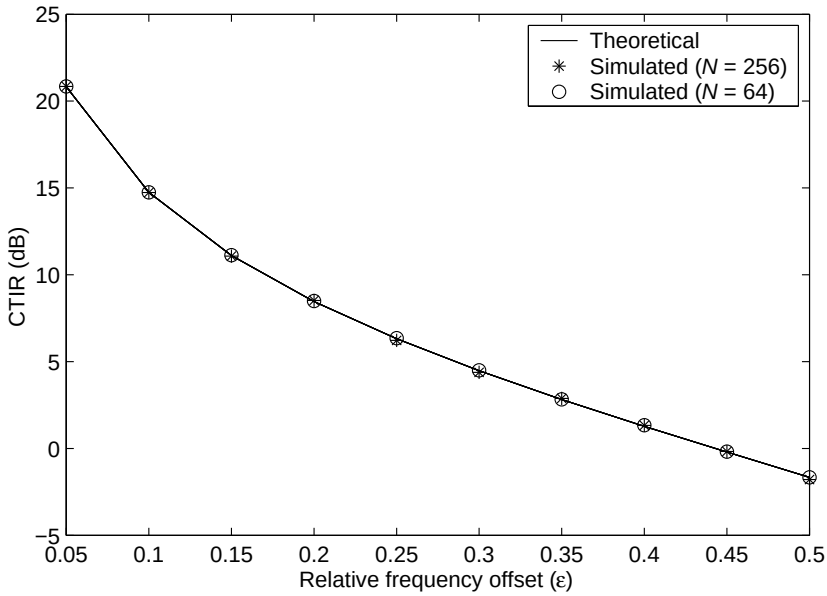

Figure 5.1: Analysis of CTIR vs relative frequency offset, ϵ

and 256. The authors in [57] derive a similar parameter and are able to show that the interference due to frequency offsets across the subchannels also remains virtually the same except for the ones at the edges of the OFDM multiplex.The authors in [103] derive the probability of bit error for a QPSK mapped OFDM system as a function of the frequency offset.

5.3 Schmidl and Cox Algorithm

As stated previously, the SCA is utilised to estimate both symbol timing and frequency offset. In section 4.3 the symbol synchronisation function of SCA was introduced. In this section the frequency offset correction function will be investigated. Perfect symbol synchronisation is assumed to be achieved using the ISOCA presented previously.

For perfect symbol synchronisation the Start of Frame (SOF) will be determined as the start of first training symbol, given by $d_{opt} - v$ as explained previously in section 4.3. The phase difference between received samples $L = N/2$

samples apart is estimated as,

$$\hat{\phi} = 1/(p+1) \sum_{n=0}^{p} \angle P(d_{opt} - n) \tag{5.8}$$

where $P(d)$ is the correlator output given in (4.14). The fractional part of ϵ is estimated as,

$$\hat{\epsilon}_{SCA} = \hat{\phi}/\pi \; . \tag{5.9}$$

In order to resolve potential ambiguity due to the integer part of ϵ, use is made of the second SCA training symbol. By estimating the phase shift between the two training symbols, the integer part of the ϵ can be estimated. First, the training symbols are corrected using $\hat{\phi}/\pi$ and then any additional phase shift due to the integer part of the frequency offset is found as the value of g, namely $\hat{g}$ that maximises the function

$$B(g) = \frac{|\sum_{k \in X} \; x^*_{1,k+2g} \, v^*_k \, x_{2,k+2g}|^2}{2(\sum_{k \in X} \; |x_{2,k}|^2)^2} \tag{5.10}$$

where $x_{1,k}$ and $x_{2,k}$ are the FFT demodulated outputs corresponding with the two training symbols, that have already undergone partial frequency offset compensation using $\hat{\phi}/\pi$ and v_k is the ratio of the two symbols being transmitted in the even subchannels of the two SCA training symbols [25]. Note g is the index spanning the even subchannels i.e. $X = \{0, 2, \ldots, N-4, N-2\}$, hence the total frequency offset is estimated as [25],

$$\hat{\epsilon}_{SCA} = \hat{\phi}/\pi + 2\hat{g} \; . \tag{5.11}$$

Note that if ϵ has only a fractional part, $\hat{g}$ would yield zero when calculated using (5.10). In theory, this method can estimate frequency offsets in the range $-(L+1) < \epsilon < (L-1)$. In [88] and [104] the authors propose to use only the first training symbol of the SCA to estimate the frequency offset. They estimate the fractional part of the frequency offset in a similar manner to that proposed in the SCA. The integer part of the SCA will introduce a shift in the positions of the demodulated data across the subchannels. They propose to estimate the integer part by modulating the first training symbol differentially across the subchannels [88]

or to simply find the position shift using the even frequencies of the first training symbol of the SCA [104]. The residual frequency offset following application of the fractional correction part must be very small to achieve acceptable system performance.

As stated previously, it should be noted that the effect of AWGN on the correct estimation of ϵ depends on the number of FFT points, N. The SCA performs well for OFDM systems with frequency offsets when N is in excess of 1000 [25]. When the SCA is used for systems with lower values of N, the estimate $\hat{\epsilon}_{SCA}$ results in a Residual Frequency Offset (RFO), $\tilde{\epsilon}$ that rotates the received constellation at a reduced rate, but one that is still significant enough to cause bit errors in coherently demodulated OFDM systems. Hence OFDM systems with low values of N will require a RFO correction algorithm to continuously track the carrier frequency offset. In the next section the proposed Residual Frequency Offset Correction Algorithm (RFOCA) is presented. This algorithm complements the SCA by cascading it with a tracking function that continuously compensates for the RFO.

5.4 Residual Frequency Offset Correction Algorithm

In the approach proposed here, an initial frequency offset estimation is made using the SCA. The resulting RFO, $\tilde{\epsilon}$ is estimated by tracking the rate of change of phase of the demodulated data at the FEQ outputs, $\hat{Y}_{m,l}$ as shown in figure 5.2. However, the estimate of $\tilde{\epsilon}$ could be seriously affected by subchannels with a low SNR owing to spectral nulls in the channel response H_l. An estimate of H_l is made by taking the ratio between the transmitted and decoded output of the second training symbol of the SCA. Hence only those subchannels with $|H_l|$ above a certain threshold are selected. This subset of subchannels is denoted as $\underline{d} \subset [0, ..N-1]$. The criteria applied is to select subchannels with $|H_l|$ in excess of a standard deviation above the mean. For symbol m, the outputs of these subchannels $\hat{Y}_{m,d}$ are sent through a slicer to obtain $\tilde{Y}_{m,d}$, where $d \in \underline{d}$.

For symbol m the phase errors between the demodulated data, $\hat{Y}_{m,d}$ and the

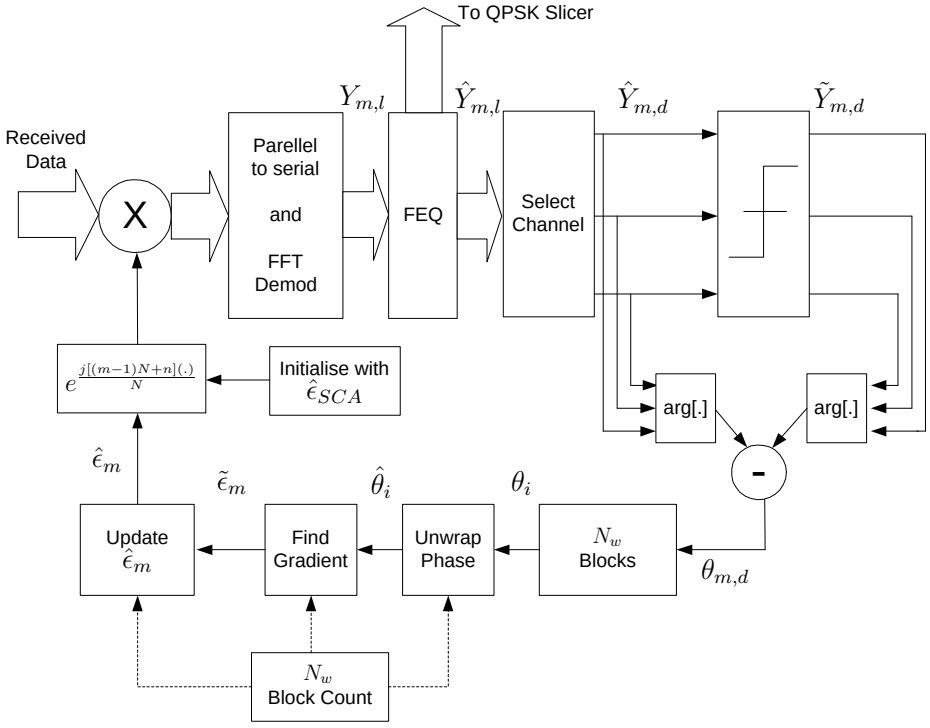

Figure 5.2: Block diagram of the Residual Frequency Offset Correction Algorithm (RFOCA)

detected data, $\tilde{Y}_{m,d}$ of the selected subchannels, namely $\theta_{m,d}$ are found as,

$$\theta_{m,d} = \angle\hat{Y}_{m,d} - \angle\tilde{Y}_{m,d} \, . \tag{5.12}$$

The phase errors are stored in a buffer, $\underline{b}$ for a block of N_w OFDM symbols. Note that only the selected subchannels will be stored. Hence if the number of subchannels selected in $\underline{d}$ is N_d then the length required for the buffer is only $N_d N_w$. Note, in this thesis QPSK data mapping is assumed although the technique could be extended to other constellations. Initially, $\tilde{\epsilon}$ can be quite high and if the values of the phase errors, $\theta_{m,d} > \pi/4$, then it results in decoding errors being produced by the slicer which subsequently results in phase wrapping of $\theta_{m,d}$ at $\pm\pi/4$. Hence it is imperative that $\theta_{m,d}$ is first unwrapped before the calculation of $\tilde{\epsilon}$ begins. As before the simple phase unwrapping algorithm that is presented in [85] is employed. Note that phase unwrapping is also required in frequency offset estimation algorithms proposed for the Single Carrier (SC) systems in [105, 106]. For reasons of clarity, the ith sample of the wrapped phase and the unwrapped phase are denoted as θ_i and $\hat{\theta}_i$, respectively. The phase unwrapping algorithm in this instance can be expressed as

$$\hat{\theta}_i = \hat{\theta}_{i-1} + \alpha \text{SAW}_{\pi/4}(\theta_i - \hat{\theta}_{i-1}) \tag{5.13}$$

where $\text{SAW}_{\pi/4}(.)$ is a sawtooth function that limits the output to $\pm\pi/4$ and α is a parameter that controls the variance of the unwrapped phase. Note that the unwrapping algorithm will be used only once every N_w OFDM symbols are demodulated (i.e. when the buffer is full). The Maximum Likelihood (ML) estimate of the RFO is calculated as the gradient of the unwrapped values stored in the buffer. If q denotes a positive integer and $\underline{\hat{\theta}}$ denotes the vector of unwrapped phase values at a particular iteration, then the estimated RFO after qN_w blocks is given as,

$$\tilde{\epsilon}_{qN_w} = \text{GRAD}(\underline{\hat{\theta}}) \tag{5.14}$$

where $\text{GRAD}(.)$ function finds the ML gradient. The error due to frequency offset is compensated for by multiplying the pre-FFT received symbols, $r_{m,n}$ with $e^{j\hat{\epsilon}_m[(m-1)N+n]/N}$, where $\hat{\epsilon}_m$ is the frequency offset correction factor for symbol

m. Note that $\hat{\epsilon}_m$ is initialised to $\hat{\epsilon}_{SCA}$ following the initial estimation made using the SCA. The correction factor is updated after every N_w OFDM symbols using $\tilde{\epsilon}_{qN_w}$. Hence at symbol number qN_w, $\hat{\epsilon}_{qN_w}$ is updated according to

$$\hat{\epsilon}_{qN_w} = \hat{\epsilon}_{qN_w-1} + \tilde{\epsilon}_{qN_w} \tag{5.15}$$

For OFDM symbols $(q-1)N_w$ to $qN_w - 1$, $\hat{\epsilon}_{(q-1)N_w}$ is used as the frequency offset correction factor.

The choice of N_w is critical since a large value will cause the updating of $\hat{\epsilon}_m$ with too high a latency and will require more memory. However after a few updates the values of $\tilde{\epsilon}_{qN_w}$ become quite small. Hence to get a better estimate in the presence of AWGN, a larger value of N_w is more appropriate since this will reduce the variance. The RFOCA can be summarised as follows.

1. Perform an initial frequency offset estimation $\hat{\epsilon}_{SCA}$ using the SCA.

2. Select the subset of subchannels with magnitudes exceeding the defined threshold in the channel transfer function, $\underline{d}$, at the start of the burst.

3. Obtain $\hat{Y}_{m,d}$ from the FEQ output and then $\tilde{Y}_{m,d}$ by use of a slicer for each symbol m, where $d \in \underline{d}$. Calculate and store $\theta_{m,d}$ for a block of N_w OFDM symbols.

4. Find the unwrapped phase $\hat{\theta}$ from the wrapped phase θ. Find the gradient of $\hat{\theta}$, namely $\tilde{\epsilon}_{qN_w}$. This process is done once every N_w symbols.

5. Once every N_w OFDM symbol blocks, calculate the new frequency offset correction factor $\hat{\epsilon}_{qN_w}$ using $\tilde{\epsilon}_{qNw}$.

Another RFO correction algorithm has been presented by Kobayashi in [107]. He proposes having two training symbols and estimates the frequency offset in two steps. The first estimation is made by multiplying the received training symbols with the conjugate of the transmitted training symbols. By taking an FFT over both symbols a coarse estimate of frequency offset is given by detecting the peak of the FFT output. A fine estimate is then taken based on the phase shift between the two training symbols. In this proposal both estimates are based on

the initial two training symbols and it is not updated within the data burst. In another proposal [108] the RFO is estimated using the difference of phase before and after the slicer. Hence the estimate is data driven and does not use any pilot symbols, in a similar manner to the RFOCA presented in this section. However in [108] an estimate is made for each subchannel output and the final correction factor is estimated using an integrator, i.e. it is taken as the average of the subchannel estimates up to that point. This method does not provide a protection method for subchannels being affected by spectral nulls. Also, as will be proved later via simulations, when N is small a RFO estimate done using a low number of OFDM symbols is prone to error. Another per-block estimation of RFO is presented in [109]. Although it provides significant gains, the algorithms was intended for applications where the value of N is at least 1024.

5.5 Simulation Parameters and Results

OFDM systems with $N = 64, 128, 256$ have been simulated at a sampling rate of 20 MHz with a guard interval length equal to 20 samples, thus the subchannel spacings are approximately 312 kHz, 156 kHz and 78 kHz respectively. QPSK mapping for all subchannels has been employed and all the subchannels are used. A burst of 2500 OFDM symbols is assumed to be transmitted. Each data point in the simulation results is obtained by averaging over 500 such bursts. The CIR for each burst is generated randomly based on the SUI-II profile [23]. In order to test the performance of the RFOCA with frequency offset alone, perfect symbol synchronisation is assumed for the simulated coherent OFDM systems. After much testing, the values selected for N_w are $250, 250, 125$ for systems with $N = 64, 128, 256$, respectively. Figure 5.3 shows a comparison of the frequency offset error variance at the end of the acquisition stage made using the SCA and that following application of the RFOCA for $N = 64, 128, 256$ as a function of the Signal to Noise Ratio (SNR), with $\epsilon = 0.5$. It shows that the RFOCA error variance is many orders of magnitude lower than at the end of the acquisition stage. Note the appearance of a threshold effect in the RFOCA at an SNR of about 16 dB, below which the error variance increases rapidly. It has been found that this is mainly due to the failure of the phase unwrapping algorithm. This will be

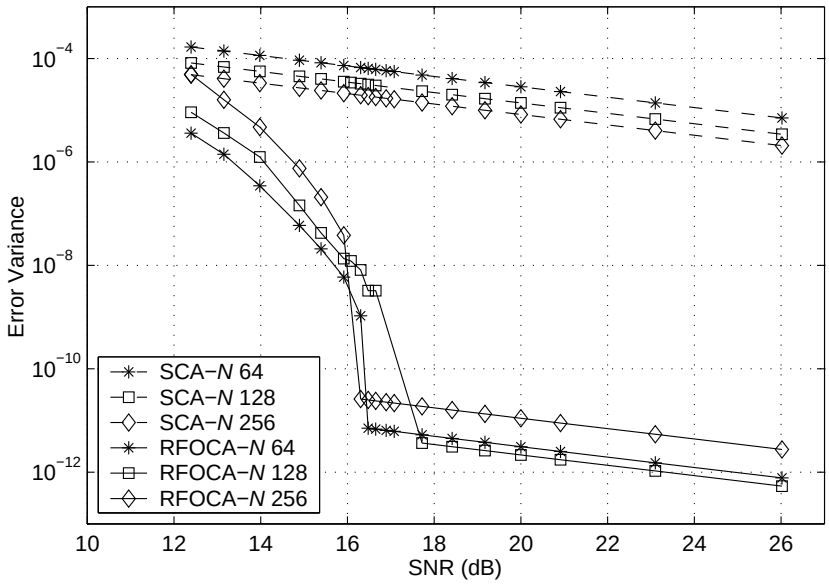

Figure 5.3: Comparison of the frequency offset error variance for SCA and RFOCA in AWGN for $N = 64, 128, 256$ and $\epsilon = 0.5$

discussed in more detail later in the section. Figure 5.4 shows the performance of the RFOCA in terms of Bit Error Rate (BER) vs SNR again in AWGN. The BER is virtually zero at values of SNR above 16 dB but increases markedly below this value. This result is a direct consequence of the threshold effect observed with the previous error variance results presented in figure 5.3. It is observed in the simulations that at an SNR of 16 dB only a few out of the total of 500 received bursts give rise to errors. However, these errors are significant giving rise to a high overall BER. Such occurrences became more common when the SNR is reduced below 15 dB, thus increasing the BER very rapidly.

Figures 5.5 and 5.6 show the simulation results for identical systems to those simulated previously, but this time with a larger relative frequency offset, i.e. $\epsilon = 1.5$. Since ϵ now has both a fractional and an integer part, the latter will be determined as shown in (5.10) and (5.11). Comparison with the previous results presented in figure 5.3 and 5.4 show that the performance of RFOCA does not degrade with increasing values of ϵ.

Figure 5.7(a) shows the effect that symbol timing offsets have on the perfor-

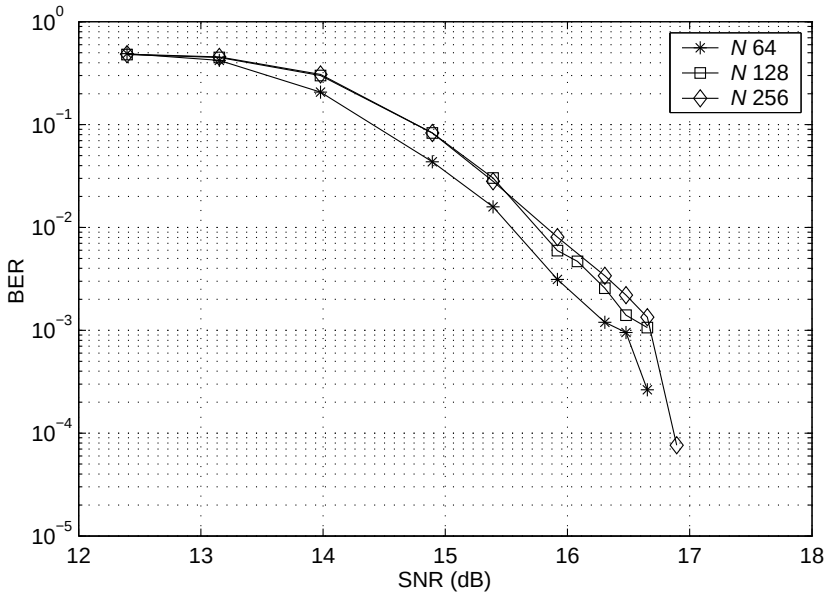

Figure 5.4: Performance of RFOCA in AWGN for $N = 64, 128, 256$ and $\epsilon = 0.5$

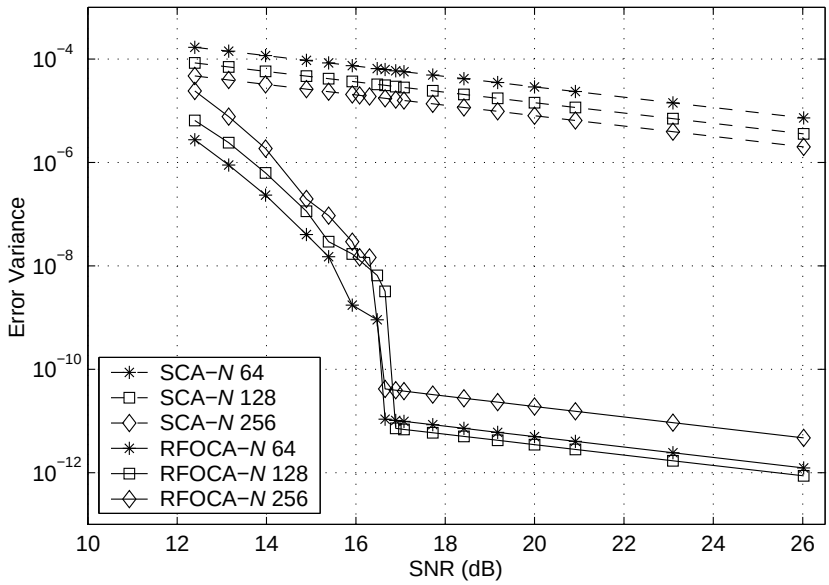

Figure 5.5: Comparison of the frequency offset error variance for SCA and RFOCA in AWGN for $N = 64, 128, 256$ and $\epsilon = 1.5$

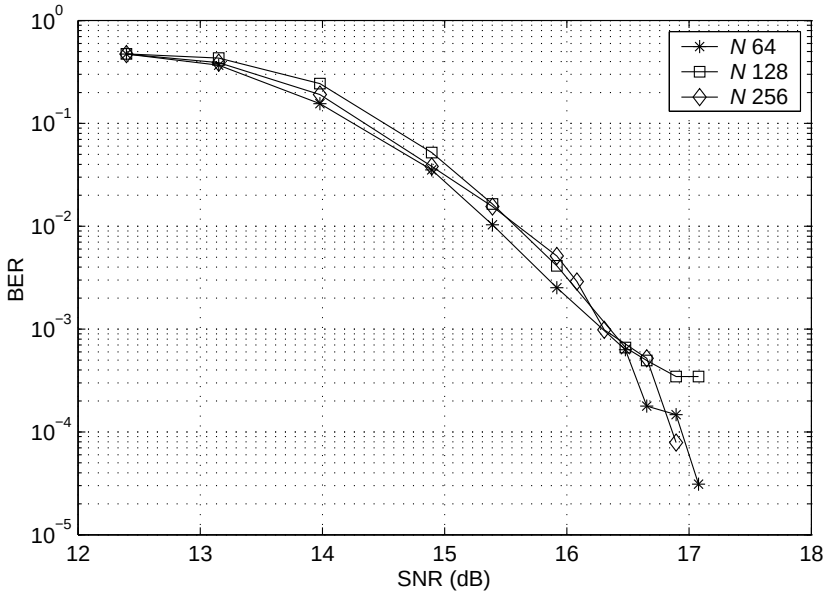

Figure 5.6: Performance of RFOCA in AWGN for $N = 64, 128, 256$ and $\epsilon = 1.5$

mance of the RFOCA. It plots the error variance for a system with $N = 256$ and $\epsilon = 0.5$ using two approaches to determine the SOF. The first approach assumes ideal symbol synchronisation (shown as SOF$_{ideal}$) and the other uses the SOF as determined using the SCA alone (shown as $\hat{\text{SOF}}_{SCA}$). It shows that the performance of the RFOCA degrades severely when subjected to the symbol offset introduced by the SCA. This is primarily due to the fact that the presence of symbol offset introduces an additional phase gradient when calculating θ in (5.12) in addition to that owing to the RFO alone. The gradient introduced by the symbol offset is much higher than that owing to the RFO. Even though the phase gradient induced by symbol offset is absorbed by the FEQ, the estimation of the $\hat{\epsilon}_{SCA}$ using (5.9) and (5.8) is degraded by the symbol offset. Figure 5.7(b) shows the results for the same scenario in terms of BER vs SNR.

In order to maintain consistency with other results presented in this thesis the second model of the Stanford University Interim channels (SUI-II) [23] has been selected as the BFWA channel model. The transmitted burst takes less than 10 ms to send at the selected sampling frequency and consequently the channel is assumed constant for the duration of each burst.

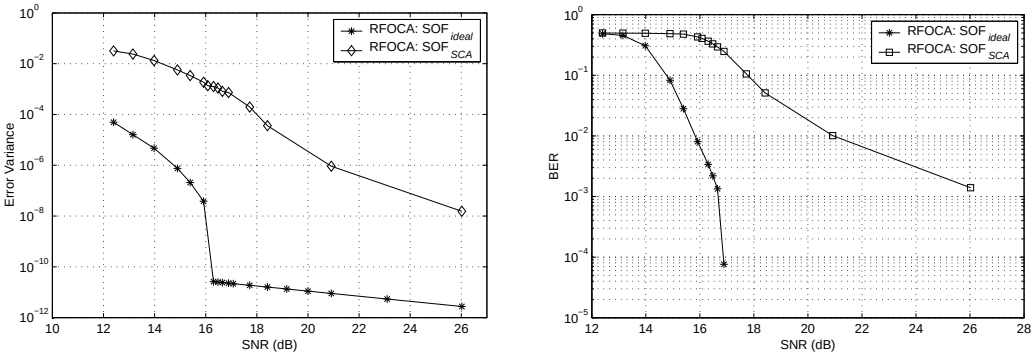

(a) Frequency offset error variance

(b) BER

Figure 5.7: Comparison of the effect of symbol offset on RFOCA in AWGN for $N = 256$ and $\epsilon = 0.5$

Figure 5.8 allows a comparison of the frequency offset error variance due to the SCA and that following the RFOCA for an OFDM system with $\epsilon = 0.5$ in the SUI-II channel. A new channel in accordance with the SUI-II profile is randomly generated for the transmission of each burst. The RFOCA error variance is seen to be many orders of magnitude lower than that due to the SCA alone despite the presence of the SUI-II channel.

Figure 5.9 shows the performance of the RFOCA in terms of BER vs SNR for the SUI-II channel and again $\epsilon = 0.5$. The threshold effect now occurs at an SNR in the region of 20 dB owing to the effect of the SUI-II channel. It shows that the performance of the RFOCA degrades with the increase of N. Clearly, the subchannels are placed more closely together with a larger value of N. Consequently, a given residual offset not corrected by the algorithm yields more ICI that will degrade the estimation process according to (5.12) to (5.14). Since RFOCA is a feedback correction method, this in turn affects the correction factor in (5.15). Also, the RFOCA selects the subchannels used for the estimation process based on the estimated CIR. A higher ICI will also affect the estimation of the CIR.

Figures 5.10 and 5.11 show the results for identical systems to those simulated previously, this time with a relative frequency offset of $\epsilon = 1.5$ (i.e. it has an integer part). The results are similar to that shown previously in figures 5.8 and 5.9.

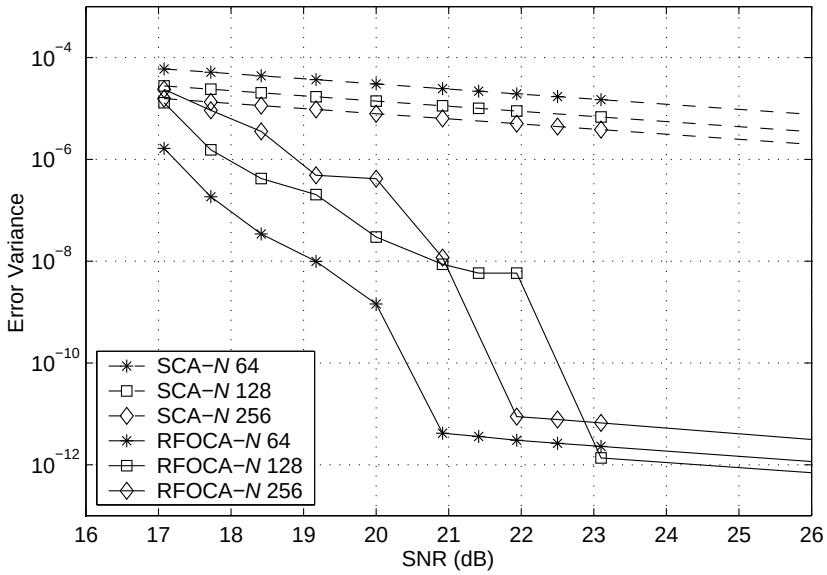

Figure 5.8: Comparison of the frequency offset error variance for SCA and RFOCA with AWGN and SUI-II CIR for $N = 64, 128, 256$ and $\epsilon = 0.5$

Hence it shows that the performance of the RFOCA does not depend on the initial relative frequency offset ϵ.

An investigation into the threshold effect that is apparent in the RFOCA will now be presented. Figure 5.12(a) shows the typical performance of the phase unwrapping algorithm in RFOCA during the first iteration for an OFDM system with $N = 64$, $\epsilon = 0.5$ and at an SNR of 20 dB. Note that the superimposed estimated gradient follows the unwrapped phase closely. Figure 5.12(b) shows the how the residual frequency offset is tracked by the RFOCA at an SNR of 20 dB. This type of illustration is referred to as the Dynamic Residual Offset Tracking (DROT). It shows the absolute error at end of each iteration. The iteration process is initialised to the estimate of frequency offset given by the SCA, namely $\hat{\epsilon}_{SCA}$. The error between $\hat{\epsilon}_{SCA}$ and the actual value is shown as the DROT value at iteration 0. In this case, following the SCA the error is of the order 10^{-5}. Immediately after the first iteration, the error has been reduced to the order of 10^{-7} and remains at this order of magnitude for subsequent iterations. The result of this is that the RFO is so small that a large number of samples are required to estimate it accurately. That is the reason why N_w has to be selected in the order of hundreds. The other

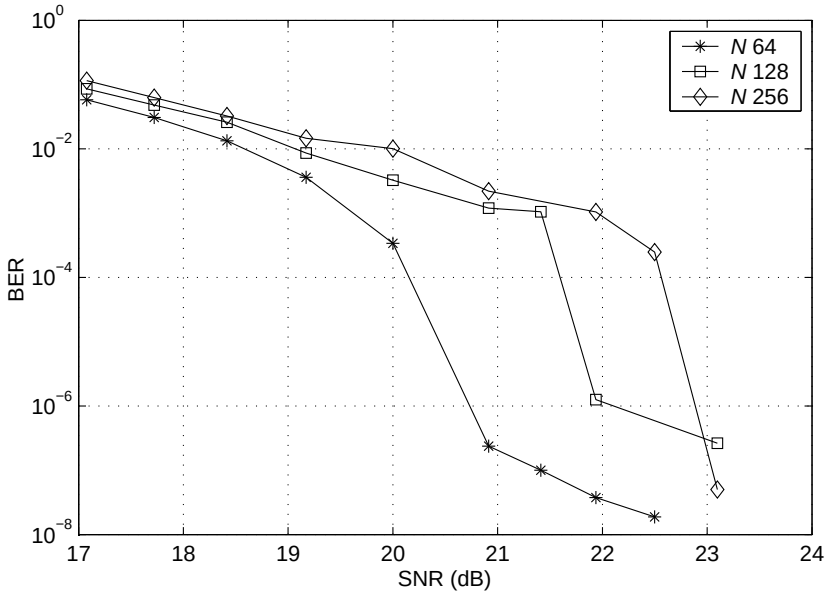

Figure 5.9: Performance of RFOCA with AWGN and SUI-II CIR for $N = 64, 128, 256$ and $\epsilon = 0.5$

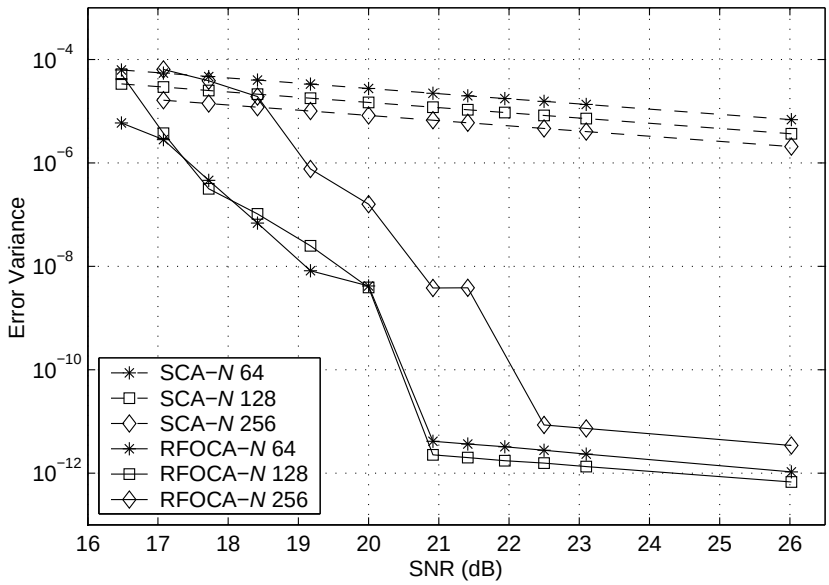

Figure 5.10: Comparison of the frequency offset error variance for SCA and RFOCA with AWGN and SUI-II CIR for $N = 64, 128, 256$ and $\epsilon = 1.5$

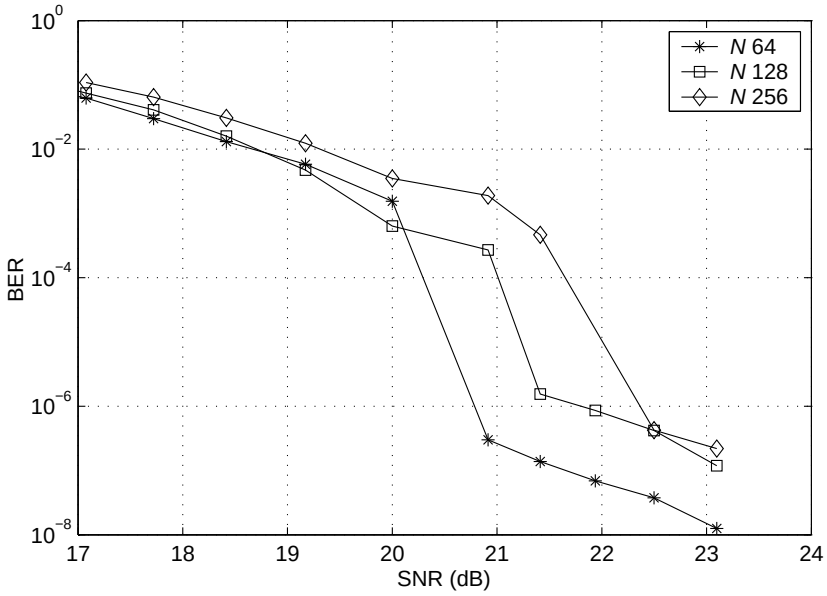

Figure 5.11: Performance of RFOCA with AWGN and SUI-II CIR for $N = 64, 128, 256$ and $\epsilon = 1.5$

effect to note is that since the phase gradient is small, most of the time the phase does not need to be unwrapped after the first few iterations at high SNR values.

When the SNR is low, the probability of triggering the phase unwrapping algorithm owing to noise is high. Figure 5.13(a) shows how the phase unwrapping algorithm fails at an SNR of 14 dB for the same system at the end of the 5th iteration. Figure 5.13(b) shows the corresponding analysis of the DROT for this case. Even though the error at the end of SCA is now increased to the order of 10^{-3}, it is immediately reduced to the order of 10^{-6} after the first iteration. However the incorrect triggering of the phase unwrapping algorithm affects the estimation of the phase gradient drastically. The incorrect estimation of the gradient is shown by a peak in the DROT plot at the 5th iteration. Even though the RFOCA is able to correct the error immediately at the sixth iteration, the number of errors caused during the 5th iteration is found to be quite significant. This effect on the phase unwrapping algorithm becomes more pronounced as the SNR is reduced. Assuming that phase unwrapping is generally not necessary after a few iterations, and hence to avoid the possibility of a failure of the unwrapping algorithm, some simula-

tions have been performed where the unwrapping algorithm is only active during the first three iterations and disabled thereafter. Figure 5.14 shows the results for the cases where the unwrapping algorithm is used for all iterations and for only three iterations for comparison. The results show that disabling the unwrapping algorithms gives only a modest gain in performance. Changing the variance control parameter of the unwrapping algorithm, α in (5.13) did not show a significant change in performance, however a more complex adaptive method to change α proportional to the variance of the final estimate in (5.15) could have shown some improvement.

Figure 5.15 shows the effect of varying the the number of OFDM symbols stored in the buffer, N_w. (in other words the frequency with which updates of the RFO correction factor, $\hat{\epsilon}_m$ occur). It shows the RFO error variance for an OFDM system with $N = 64$ for three different values of N_w. Updating the RFO correction factor after every symbol gives a worse performance than the SCA. This is because the number of noisy samples is not enough to make a reasonable estimate. It further shows that to obtain a good estimate, N_w should be of the order of 100.

Figure 5.16(a) and 5.16(b) shows the effect of channel estimation on the performance of RFOCA in terms of error variance and BER vs SNR, respectively. The curve 'RFOCA: ideal ch. est' refers to the case when the perfect knowledge of the channel is assumed at the receiver and the curve 'RFOCA: non-ideal ch. est' refers to the case when the channel is estimated using the second training symbol of the SCA. From figure 5.16(b), it can be seen that ideal channel estimation gives an improvement in the performance of RFOCA of about 3.5 dB for an OFDM system with $N = 64$ at a BER of 10^{-4}. Channel estimation in this scheme is performed using only one training symbol. Obviously, if a more elaborate scheme were adopted, the performance of the RFOCA would improve towards that achieved with ideal channel estimation. In any case, channel estimation is not the focus of the work in this thesis.

A further analysis has been carried out to show the effect of symbol timing offset on the performance of the RFOCA. Figure 5.17(a) shows the actual and the estimated phase of the CTF when perfect symbol synchronisation is achieved. Note that the FEQ is updated with the inverse of the estimated CTF. The difference

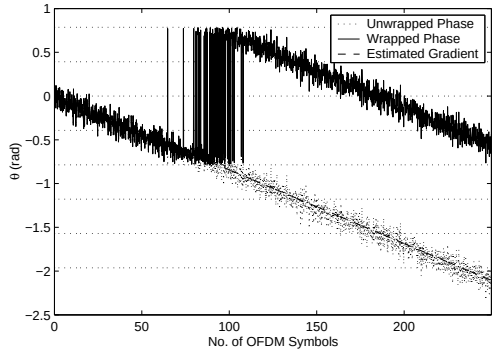

(a) Phase unwrap: 1st iteration

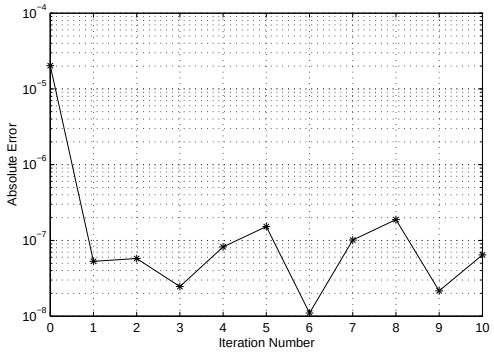

(b) DROT

Figure 5.12: Performance of the phase unwrapping algorithm and DROT for $N = 64$ and $\epsilon = 0.5$ and at 20 dB SNR

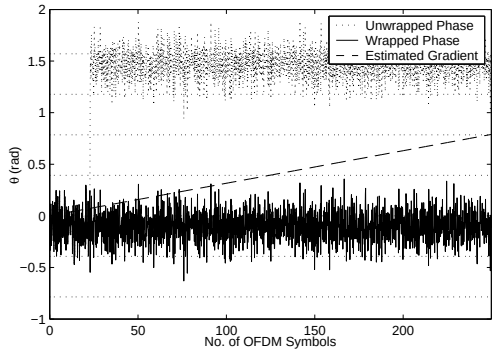

(a) Phase unwrap: 5th iteration

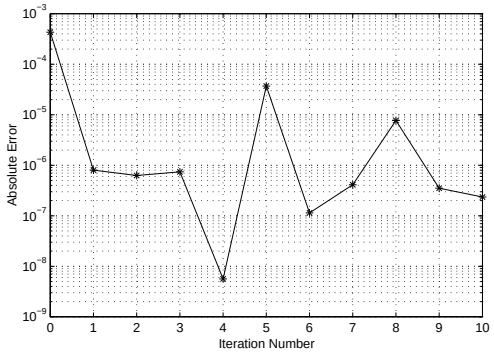

(b) DROT

Figure 5.13: Performance of the phase unwrapping algorithm and DROT for $N = 64$ and $\epsilon = 0.5$ and at 14 dB SNR

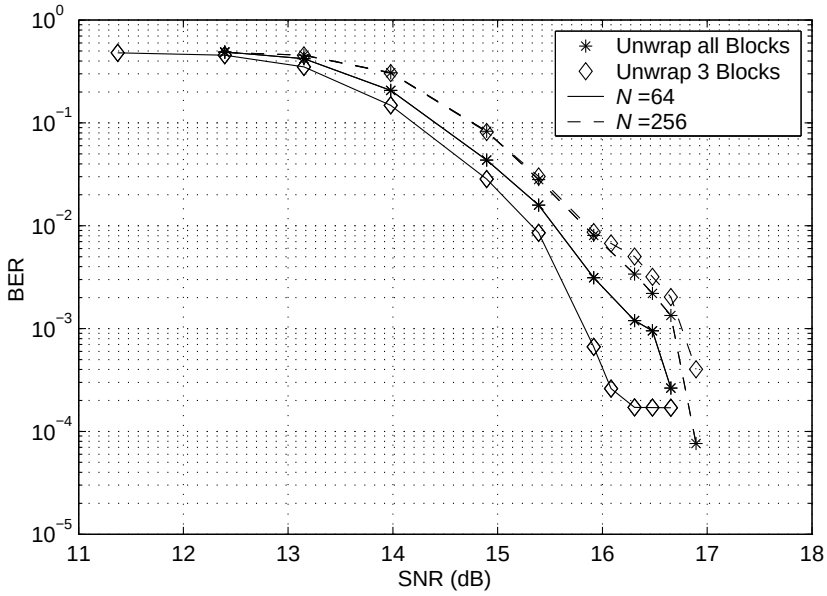

Figure 5.14: The effect of using the unwrapping algorithm for different numbers of iterations, for $N = 64, 256$, $\epsilon = 0.5$

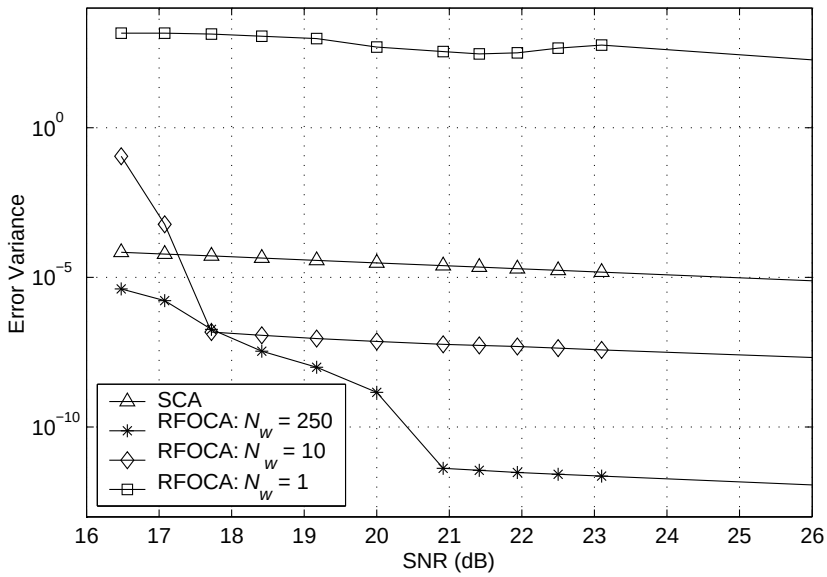

Figure 5.15: Comparison of the effect of N_w on the performance of the RFOCA for $N = 64$ and $\epsilon = 0.5$

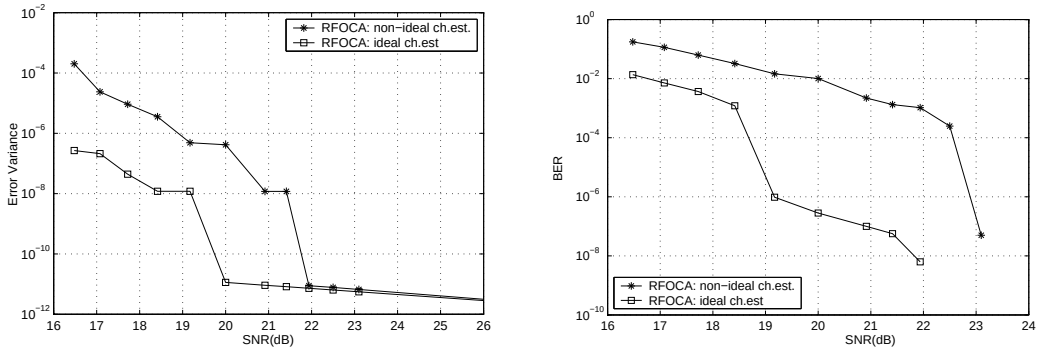

(a) Frequency offset error variance

(b) BER

Figure 5.16: Effect of imperfect estimation of CIR on the performance of the RFOCA for $N = 64$ and $\epsilon = 0.5$

in the plotted results is due to the arbitrary phase of the received samples. The SCA only estimates the ϵ and not the arbitrary phase. The actual and the estimated CTF outputs with a symbol offset of 2 are shown in 5.17(b) (i.e. $\xi = 2$). The distinct phase gradient is owing to the non-zero ξ. At first glance, the symbol offset does not seem to cause any degradation as the phase gradient caused by it seems to be corrected by the FEQ. However, figure 5.18 shows the DROT for three cases of symbol offset, specifically $\xi = 0, -12, 2$). Clearly the RFOCA is susceptible to the ICI caused by symbol offset. Hence it is essential that perfect symbol synchronisation be achieved before frequency offset is estimated using the phase gradient. It was seen that for this system the RFOCA is quite robust with negative symbol offsets $0 > \xi > -10$. This is because the SUI-II CIR has positions at 0, 10 and 20 at sampling rate of 20 MHz. The length of the CP in this case was set to 20. The third tap is quite small in magnitude and hence as long as $0 > \xi > -10$, the ICI contribution will only be due to the third tap. But once $\xi < -10$, both the second and third taps will contribute to the ICI, which explains the cause of the sudden degradation in performance. However, the RFOCA is very susceptible to even small positive symbol offsets. This is caused by the IBI, as a result of taking samples from two adjacent OFDM symbols into one FFT processing window.

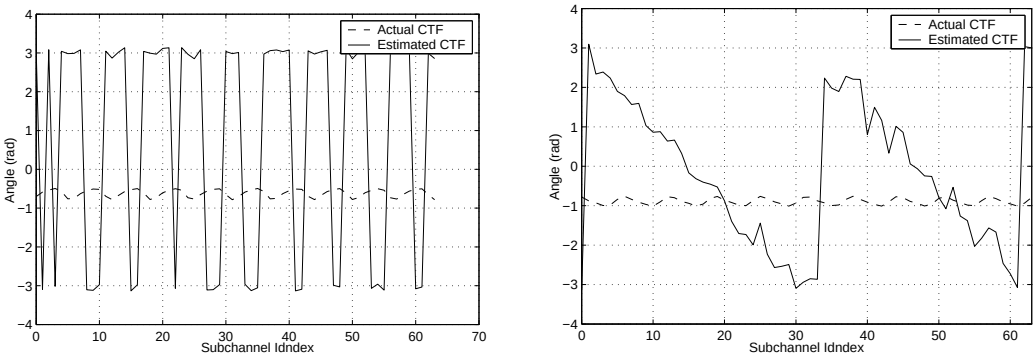

(a) $\xi = 0$ (b) $\xi = 2$

Figure 5.17: Estimation of the phase of the CTF for different symbol timing offsets, ξ for $N = 64$ and $\epsilon = 0.5$

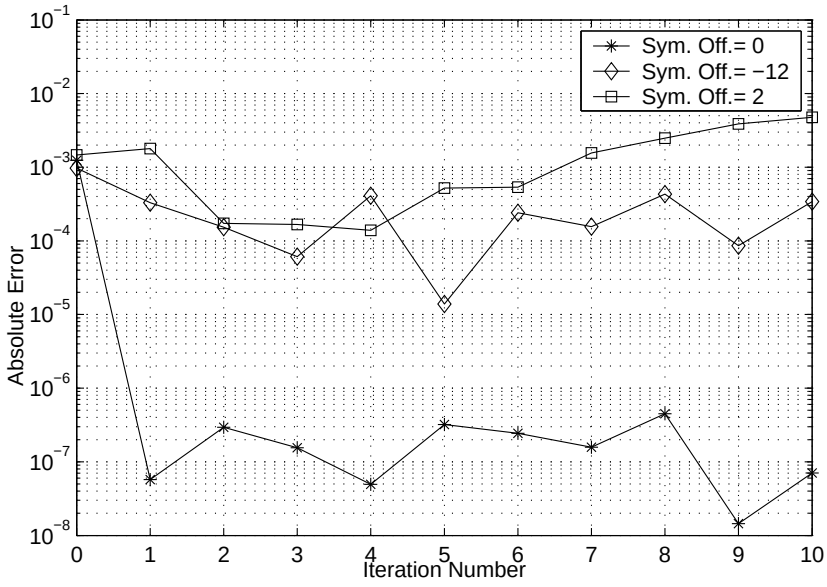

Figure 5.18: The DROT with symbol offset = 0,2,-12 for $N = 64$ and $\epsilon = 0.5$

5.6 Conclusion

In this chapter the Residual frequency Offset Correction Algorithm (RFOCA), which complements the initial frequency acquisition process performed by the Schmidl and Cox Algorithm (SCA) has been presented. The RFOCA continuously tracks and compensates for the RFO that is present after the acquisition stage. The RFOCA is applied for OFDM systems operating over both AWGN and BFWA channels (SUI-II channel profile), and is shown to give a significant reduction in the frequency error variance. Although the algorithm may appear to suffer from a threshold effect it still gives a significant performance advantage at realistic signal to noise ratios. The performance of RFOCA is analysed through extensive simulations. It is concluded that the threshold effect of the RFOCA is primarily due to the failure of the phase unwrapping algorithm. The RFOCA is also susceptible to non-ideal symbol synchronisation, however this does not pose a serious problem as perfect symbol synchronisation can be achieved using the ISOCA presented in chapter 4.

Chapter 6

Time Domain Equalisation

As shown previously in section 2.4, the orthogonality of consecutive OFDM symbols is maintained by prepending a length v Cyclic Prefix (CP) at the start of each symbol [37]. One major disadvantage with the OFDM system is the reduction in the transmission efficiency by a factor $N/(N+v)$ caused by the CP. This is of even greater concern when the transmitted symbol rate is higher, because this makes a Channel Impulse Response (CIR) with the same rms delay spread span a greater number of samples, hence necessitating the use of a longer CP. Future broadband wireless applications are likely to require data rates in excess of 50 Mb/s. Although a typical wireless fixed access channel delay spread is short in comparison to the symbol duration for transmission rates that are in use today, it will not be the case for higher symbol rates. One way of increasing the efficiency is to increase the FFT size, N. The consequences of increasing N were highlighted in chapter 1.

An alternative to increasing the number of subchannels is to precede the FFT demodulator at the receiver with a Time Domain Equaliser (TEQ) in order to constrain the length of the overall response to be shorter than the original CIR. The cascade of the channel and the TEQ response is hereafter referred to as the Effective Channel Impulse Response (EIR). This permits the use of a much shorter CP than could otherwise be employed and so raises the transmission efficiency. A TEQ is almost essential in DMT systems when used in Digital Subscriber Line (DSL) applications owing to their relatively long CIRs. As far as the author of this

thesis is aware, the application of a TEQ to compensate for the CIRs experienced in broadband wireless applications has not been throughly investigated to date. In this chapter a novel TEQ algorithm is presented, namely, the Frequency Scaled Time Domain Equaliser (FSTEQ). The FSTEQ is designed specifically to be used in BFWA channels.

This chapter is organised as follows. Section 6.1 briefly introduces relevant previous work concerning TEQs while section 6.2 presents the theory of TEQ design. The next two sections introduce two TEQ algorithms. The first described in section 6.3 is the Dual Optimising Time Domain Equaliser (DOTEQ), which is a modified version of a design previously presented by another author [110]. The limitations of using the DOTEQ in wireless channels are highlighted and in section 6.4 the novel FSTEQ is introduced which overcomes most of the limitations of the DOTEQ. A Z-plane analysis of the performance of the DOTEQ and the FSTEQ is performed in section 6.5 and a comparison of the computational complexity of the TEQ schemes presented is undertaken in section 6.6. Section 6.7 presents the results obtained via computer simulations and finally the conclusions are drawn in section 6.8.

6.1 Related Work

Time Domain Equalisation is a very rich and deep area of research. There have been contributions by many authors and the objective here is to highlight the most important and relevant ones. CIR shortening has been proposed as long ago as 1973 to permit the design of practical Maximum Likelihood Sequence Estimation (MLSE) receivers based on the Viterbi Algorithm [110]. Later there was a flurry of research aimed at reducing the length of the CP in DMT systems [111, 112, 113, 114]. The first two references are based on the Minimum Mean Squared Error (MMSE) criterion to arrive at the solution for the TEQ. The latter two references seek to minimise the so called Shortened SNR (SSNR), where the ratio between the power in a set of consecutive v samples of the EIR to the power in the rest of the residuals is considered. To avoid trivial all-zero solutions, additional constraints such as the Unit Energy Constraint (UEC) [110] or the Unit Tap Constraint (UTC) [111, 115] are set on the Target Impulse Re-

sponse (TIR) when the MMSE criterion is used. The TIR, as will be shown later, is used to generate the error term in the adaptation process. However the emphasis is to reduce the power of the residuals of the EIR in the time domain. The transfer function of the resulting EIR in the frequency domain often has spectral nulls causing some subchannels to have a low SNR and consequently rendering them unusable. A different equalisation criterion is introduced in [112, 116], namely the 'geometric SNR'. The objective here is to maximise the overall bit rate of a DMT system. The structure is the same as for the MMSE case, but the objective function is based on optimising the SNR of individual subchannels, and hence the bit rate. It was later extended by optimising the bandwidth in [117]. The authors in [118, 119] include ISI in the objective function of the original geometric mean criterion to improve the performance. The geometric SNR criterion is ideal for DMT systems since the modulation of DMT presumes data is mapped into the subchannels at various rates using different modulation constellations. In another modification of the original geometric SNR criterion, the authors in [120] include the effect of Inter-Block Interference in the optimisation process. However, the algorithm is very complex and needs several FFT operations at each iteration.

To overcome the slow convergence of adaptive algorithms, some authors have proposed channel estimate based methods [121, 111]. The former paper also proposes how the delay between the TEQ and the TIR may be optimised. It involves optimising the algorithm for each value of the delay and selecting the delay that provides the minimum error. This method is much more efficient than that proposed in [111]. The delay is indeed critical when the channel responses have pre-cursors and post-cursors since it is used to locate the main tap of the CIR. However the broadband wireless channels under consideration in this work generally do not have precursors and so optimising the delay is not such an important issue in this case.

Attempts have also been made to optimise the TEQ in the frequency domain [122, 123]. An issue with [122] in particular is that the solution rarely results in a global minimum error. The authors in [124] introduce the concept of weighting the frequency domain coefficients, which appears to improve upon the original frequency domain criterion. The authors in [123, 125] propose the 'per-tone equaliser' which operates in the frequency domain. The TEQ in the

time domain is converted into an equivalent FEQ with multiple taps at each subchannel output of the IFFT demodulator. Even though this method appears to be more robust to delay differences between the equaliser and the TIR, the implementation is more complex and needs a significant amount of memory. The authors in [126, 127] propose a version of a TEQ that uses a feedback path from the point after the FEQ rather than from the TIR. Due to the parallel processing of the OFDM symbols, the feedback path is effectively only used once per OFDM symbol. This necessitates a high SNR for the algorithm to perform effectively.

The MMSE TEQ does its best to emphasise the low noise part of the received signal, while suppressing the channel noise over the rest of the frequency band. This process however generates nulls in the effective transfer function [128]. For a DMT system, the consequence is that quite a few subchannels are not assigned any data. The same paper proposes guidelines for designing a better TEQ, specifically it suggests optimising the TIR such that it does not contain nulls in the frequency response and also keeps the Mean Squared Error (MSE) relatively low. It proves that the geometric SNR criterion is a generalised form of avoiding spectral nulls. Since the original proposal utilising the geometric SNR criterion is computationally expensive, the authors propose a more simple eigen filter approach. A similar approach is adopted in [129]. It can be noted that the FSTEQ that is proposed in section 6.4 does conform to the guidelines proposed in [128].

6.2 Basics of Time Domain Equalisation

Channel shortening with the use of a TEQ in the MMSE sense can be explained with reference to the block diagram shown in figure 6.1. For clarity the transmission variables are given in vector form in this chapter. Unless otherwise stated, an underlined variable will denote a vector and a variable that is not underlined with a numeric subscript will denote the individual elements in the vector. In general, variables in the time domain will be denoted in the lower case and those in the frequency domain in the upper case.

The objective is to shorten the sampled CIR of length N_h, $\underline{h} = [h_0, .., h_{N_h-1}]^T$ to an EIR having significant samples for a length N_b, where $N_b < N_h$, with the use of a TEQ of length N_f, $\underline{f} = [f_0, .., f_{N_f-1}]^T$. The error sequence, $e(n)$ is generated

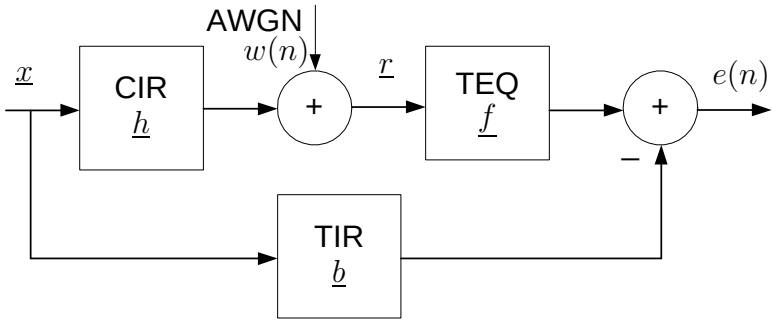

Figure 6.1: Block diagram of the TEQ

by comparing the output sequence of the TEQ to the result of convolving the transmitted data stream, $\underline{x} = [x(n), .., x(n - N_b + 1)]^T$, with a desired TIR, $\underline{b} = [b_0, .., b_{N_b-1}]^T$ of length N_b. Here, n represents the time index and $x(n) = 0$ for $n < 0$. If the TEQ performs perfectly, the OFDM system can now operate with a shorter CP of length $N_b - 1$ (i.e. $v = N_b - 1$).

If the received data is given by $r(n)$, then,

$$r(n) = \underline{h}^T \underline{x}' + w(n) \tag{6.1}$$

where $w(n)$ is the zero mean Additive White Gaussian Noise (AWGN) term and $\underline{x}' = [x(n), .., x(n - N_h + 1)]^T$. Hence the error signal after the TEQ is given as,

$$e(n) = \underline{f}^T \underline{r} - \underline{b}^T \underline{x} \tag{6.2}$$

where $\underline{r} = [r(n), .., r(n - N_f + 1)]^T$. The time index n is defined as before with $r(n) = 0$ for $n < 0$. The squared error is given by,

$$E\{|e(n)|^2\} = \underline{f}^T R_{rr} \underline{f}^* + \underline{b}^T R_{xx} \underline{b}^* - \underline{f}^T R_{rx} \underline{b}^* - \underline{b}^T R_{rx} \underline{f}^* \tag{6.3}$$

where $(.)^*$ denotes complex conjugation and R_{rr} ,R_{xx} and R_{rx} are the corresponding correlation matrices of $\underline{r}$ and $\underline{x}$. The optimal equaliser tap coefficients can be obtained by solving for the MMSE given by,

$$d(E\{|e(n)|^2\})/d\underline{f} = 0 \tag{6.4}$$

which leads to,

$$\begin{aligned} \Re[\underline{f}_{opt}] &= R_{rr}^{-1} R_{rx} \Re[\underline{b}] \\ \Im[\underline{f}_{opt}] &= R_{rr}^{-1} R_{rx} \Im[\underline{b}] \end{aligned} \tag{6.5}$$

where $\Re$ and $\Im$ are the Real and the Imaginary part of a complex variable, respectively. Note that the solution of (6.5) depends on $\underline{b}$. Substituting the above relation in equation 6.3 results in

$$E\{|e(n)|^2\} = \underline{b}^T (R_{xx} - R_{rx}^T R_{rr}^{-1} R_{rx}) \underline{b}^* = \underline{b}^T \mathbf{O}\, \underline{b}^* \; . \tag{6.6}$$

By minimising equation 6.6 the optimal coefficients for the TIR, namely b_{opt} can be found as the eigenvector corresponding to the smallest eigenvalue of the matrix $\mathbf{O}$. Solutions for the case of real data can be found in [130].

6.3 Dual Optimising Time Domain Equaliser

An alternative iterative solution is presented in [110] for real data, a modified form of which is presented here for the case of complex data. Assuming the transmitted sequence is known during training, both the TIR coefficients $\underline{b}$, and the TEQ coefficients $\underline{f}$, can be obtained iteratively via steepest descent gradient methods such as Least Mean Square (LMS). Hence,

$$\underline{f}^{n+1} = \underline{f}^n - \Delta_f \, e(n) \underline{r}^* \tag{6.7}$$

and

$$\underline{b}^{n+1} = \underline{b}^n + \Delta_b \, e(n) \underline{x}^* \tag{6.8}$$

where $\underline{f}^n$ and $\underline{b}^n$ are the tap coefficients at the n^{th} iteration and Δ_f and Δ_b are the LMS convergence control parameters. To avoid the trivial all-zero solution, the UEC constraint on the TIR is used. This is achieved using,

$$\underline{b}^{n+1} = \frac{\underline{b}^{n+1}}{|\underline{b}^{n+1}|} \; . \tag{6.9}$$

This algorithm is referred to as the Dual Optimising TEQ (DOTEQ). Figure 6.2 shows the performance of the DOTEQ algorithm in the time domain using the UEC for a TIR length of 14 at an SNR of 20 dB. The original CIR is assumed to be 40 samples long, with only 3 significant taps. It can be observed that the EIR is similar to the TIR within the length of the TIR. The length of the TEQ is 60 samples and hence the EIR has 100 samples. More importantly, the residuals beyond the TIR length (and hence the CP) are low in magnitude compared with the samples lying within the TIR length.

Hereafter, the transfer functions in the frequency domain of the CIR, TIR and EIR are defined as the Channel Transfer Function (CTF), the Target Transfer Function (TTF) and the Effective Transfer Function (ETF), respectively. However, as shown in figure 6.3, the ETF obtained using the DOTEQ algorithm for the time domain EIR shown in figure 6.2 has deep spectral nulls. Consequently subchannels that fall in to the nulls will be severely degraded giving rise to a low subchannel SNR. This situation will not be improved by the FEQ since its coefficients are given by the inverse of the ETF. To address this problem, an algorithm will now be presented that achieves both a flatter ETF (frequency domain) and also a reduction of the residuals of the EIR (time domain).

6.4 Frequency Scaled Time Domain Equaliser

The objective of the FSTEQ in the time domain is to iteratively obtain an optimal solution to the TEQ. Thus the CIR will be processed to yield an EIR with a length (defined as that spanning the significant coefficients of the EIR) that is much shorter than that of the CIR. The purpose of also optimising in the frequency domain is to avoid the spectral nulls that are usually created by the DOTEQ algorithm. Hence, the overall system can effectively operate with a much shorter CP of length v.

As noted in appendix B, the antennas used for Point-to-Point (PTP) and Point-to-Multipoint (PMP) communication in the BFWA scenario are of high gain and directivity. Hence the CIRs that are encountered are not severe, usually having a dominant direct path and a small number of weak delayed paths. The CIRs experienced in good terrain conditions, which are those pertaining to the proposed

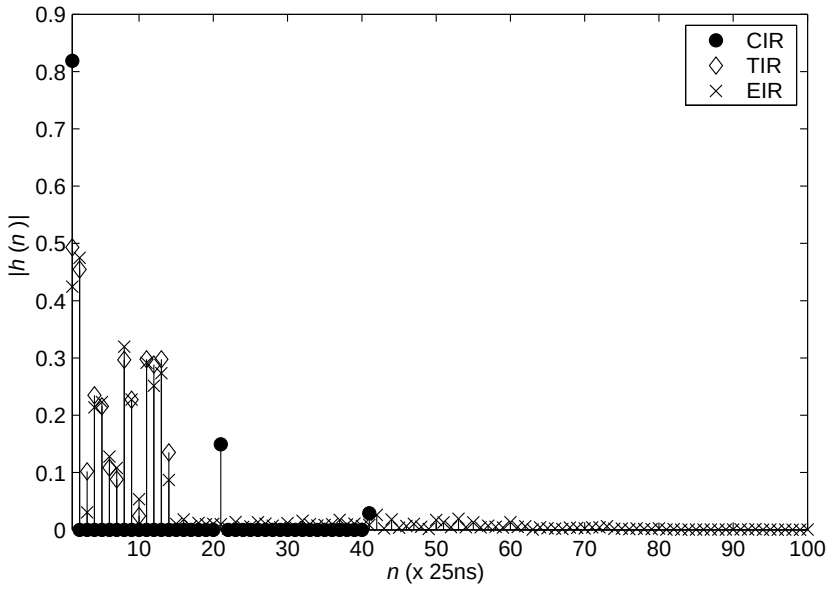

Figure 6.2: DOTEQ performance: Impulse responses

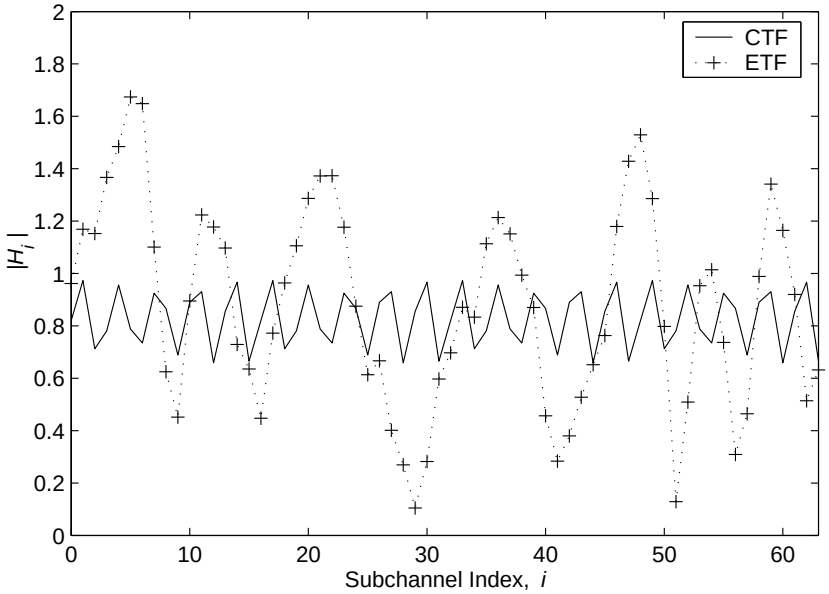

Figure 6.3: DOTEQ performance: Transfer functions

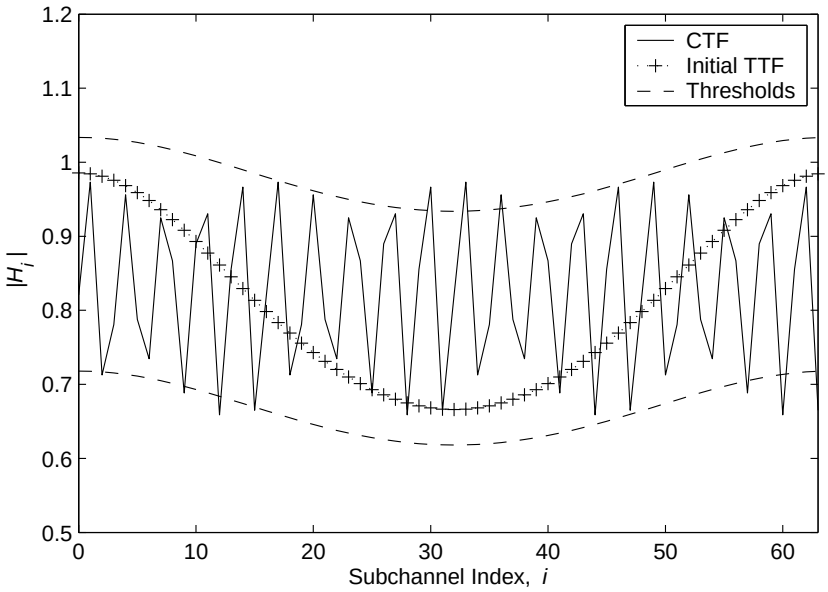

Figure 6.4: FSTEQ algorithm: Initial TTF

SUI-II delay profile [23], also have a high Ricean factor in the direct path. The consequence of this is that the delay profile is likely to have an exponentially decaying envelope. The FSTEQ is designed with this kind of delay profile in mind. The design criteria of the FSTEQ is to convert the exponentially decaying CIR into an EIR which is also exponentially decaying but at a much faster rate. Thus the ETF will have a smoother response than the CTF.

In order to initialise the FSTEQ an estimate of the CTF is required. A known training symbol is sent by the transmitter so that the coefficients of the FEQ can be calculated at the receiver. The ratio of the known transmitted training symbol to the corresponding demodulated OFDM data symbols *before* applying the TEQ is employed to estimate the CTF. This is so because the TEQ will modify the CTF.

All FFT and IFFT operations performed hereafter in the FSTEQ are of length N unless otherwise stated. Using the *average* delay profile of the SUI-II channel profile, namely $\underline{g}$ two thresholds are calculated in the frequency domain. The average delay profile can be calculated by averaging over a large number of channel estimates made on different bursts or simply by using channel models such as the

SUI model. Note that this does not require knowledge of the CIR experienced by a particular transmitted data burst. The transfer function of $\underline{g}$, denoted by $\underline{G}$, is calculated by taking an FFT of $\underline{g}$. The actual coefficients of $\underline{G}$ are a system parameter and can be selected at implementation. Subsequent simulations have shown that the performance is not sensitive to the values selected for $\underline{G}$, provided that they approximately follow the envelope of the CTF. The mean and the standard deviation of the gain of CTF are calculated from the estimate made previously. These values are denoted as μ_H and σ_H, respectively. An upper threshold, $\underline{G}_u$ and a lower threshold, $\underline{G}_l$ are set as follows,

$$\begin{aligned} \underline{G}_u &= \underline{G} + \mu_H + \sigma_H \\ \underline{G}_l &= \underline{G} + \mu_H - \sigma_H \, . \end{aligned} \tag{6.10}$$

The values for μ_H and σ_H are estimated at the start of each received burst but since $\underline{G}$ is a predefined system parameter it could be implemented as a look-up table. The purpose of the two thresholds is to follow the envelope of the CTF magnitude response, and as will be described later, to limit the magnitude variation of the TTF (frequency domain). If (6.10) is used to determine the thresholds, they span a range which is twice the standard deviation of the estimated CTF. Figure 6.4 shows the calculated thresholds for a typical SUI-II channels profile.

To ensure that the solution converges correctly, the length of the TIR is set equal to the desired CP length, v. The next step of the algorithm is to decide on an initial TIR, $\hat{\underline{b}}^0$ where the superscript refers to the iteration number. Initial tests showed that using an arbitrary or a null TIR to start with does not guarantee that the algorithm will converge quickly. Hence, it is proposed to use an initial TIR function which is exponentially decaying but at a much faster rate than that of the CIR power profile. To determine the decay rate (i.e. the time constant), a desired attenuation at the end of the TIR length, v is selected. Denoting this desired value as κ, then the decay rate is found as $\lambda = \ln|\kappa|/(v-1)$. The *unscaled* initial TIR, $\underline{b}^0$ is defined as,

$$\underline{b}^0 = [1, e^{\lambda}, .., e^{\lambda(v-1)}] \, . \tag{6.11}$$

The convergence rate of the ETF depends upon the initial TIR. Since the goal

of the algorithm is to obtain a TEQ that yields an ETF that lies within the thresholds, the gain of the unscaled initial TTF, $|\underline{B}^0|$ must be scaled so that it lies within the calculated frequency domain thresholds before iteration begins. To do this, the minimum and the maximum gains of the TTF have to be found. They are denoted as $|\underline{B}^0|_{min}$ and $|\underline{B}^0|_{max}$ respectively. The scaled gain of the initial TTF is given as,

$$|\hat{\underline{B}}^0| = \frac{(|\underline{B}^0| - |\underline{B}^0|_{min}).2\sigma_H}{(|\underline{B}^0|_{max} - |\underline{B}^0|_{min})} + \underline{G}_l \tag{6.12}$$

which is now guaranteed to lie within the two thresholds as shown in figure 6.4. Unless otherwise stated, the scaled variables are denoted by the symbol '^'. The complete initial TTF is determined by setting the phase of the scaled initial TTF to be equal to the phase of the unscaled initial TTF, $\angle\underline{B}^0$. i.e.,

$$\hat{\underline{B}}^0 = |\hat{\underline{B}}^0|\, e^{j\angle\underline{B}^0} \,. \tag{6.13}$$

In other words, only the gain and not the phase of the TTF is scaled. This holds true at each iteration. The scaled initial TIR, $\hat{\underline{b}}^0$ is found by taking an IFFT of length N of the initial scaled TTF, $\hat{\underline{B}}^0$. Since N is longer than the TIR length v, only the first v samples of the IFFT output are used to initialise the TIR. Once the TIR is initialised, the final solution of the FSTEQ is achieved in the MMSE sense using a steepest gradient optimisation method. If the LMS algorithm is used, the TIR and the TEQ are updated in a similar manner to that employed in the DOTEQ as given by equations (6.7) and (6.8). However LMS is known to converge slowly and the rate of convergence can be improved dramatically by using the Recursive Least Squares (RLS) algorithm at the expense of an increase in the number of computations [27, pg. 654]. The RLS algorithm when used for the FSTEQ requires 6 parameters to be evaluated for each iteration of the algorithm to calculate the TEQ and TIR coefficients. For the TEQ a weighting factor Ω_f (where $0 > \Omega_f > 1$), a Kalman gain vector $\underline{K}_f^n$ (of length N_fx1) and a square inverse correlation matrix $\mathbf{P}_f^n$ (of size N_fxN_f) need to be evaluated. Again the superscript refers to the iteration number and the subscript f is used to identify them as TEQ parameters. Similarly, for the TIR, Ω_b ($0 > \Omega_b > 1$), $\underline{K}_b^n$ (of length N_bx1) and the square matrix $\mathbf{P}_b^n$ (of size N_bxN_b) need to be evaluated.

The interested reader is referred to [27] for more details about the RLS algorithm. The correlation matrices are initialised to identity matrices. Once the TEQ output, the TIR output and the error is calculated as given in (6.2), the TEQ parameters are updated using the RLS algorithm as follows,

$$\begin{aligned} \underline{K}_f^{n+1} &= \frac{\mathbf{P}_f^n \, \underline{r}^*}{\Omega_f + \underline{r}^T \, \mathbf{P}_f^n \, \underline{r}^*} \\ \mathbf{P}_f^{n+1} &= \frac{1}{\Omega_f}[\mathbf{P}_f^n - \underline{K}_f^n \, \underline{r}^T \, \mathbf{P}_f^n] \\ \underline{f}^{n+1} &= \underline{f}^n - \underline{K}_f^{n+1} \, e(n) \, . \end{aligned} \tag{6.14}$$

The first equation of (6.14) computes the Kalman gain vector, the second updates the inverse of the correlation matrix and the third updates the TEQ coefficients. Note that all 3 steps have to be performed at each iteration. Similarly, the corresponding equations for the TIR are,

$$\begin{aligned} \underline{K}_b^{n+1} &= \frac{\mathbf{P}_b^n \, \underline{x}^*}{\Omega_b + \underline{x}^T \, \mathbf{P}_b^n \, \underline{x}^*} \\ \mathbf{P}_b^{n+1} &= \frac{1}{\Omega_b}[\mathbf{P}_b^n - \underline{K}_b^n \, \underline{x}^T \, \mathbf{P}_b^n] \\ \underline{b}^{n+1} &= \underline{b}^n + \underline{K}_b^{n+1} \, e(n) \, . \end{aligned} \tag{6.15}$$

However the TIR coefficients obtained at a particular iteration may exceed the previously calculated frequency domain thresholds. Hence, after the unscaled TIR coefficients are obtained at the $(n+1)$th iteration using either the LMS algorithm, as given in (6.8) or by using the RLS algorithm, as shown in (6.15), the unscaled TTF, $\underline{B}^{n+1}$ is obtained using an FFT of size N. If $|\underline{B}^{n+1}|$ exceeds the thresholds, it is scaled to obtain $|\hat{\underline{B}}^{n+1}|$ in a similar manner to that employed at initialisation as given by (6.12). The complete TTF is obtained by multiplying with the phase response in a similar way to that shown in (6.13). Figure 6.5 shows the block diagram of the FSTEQ algorithm.

To prevent the FSTEQ converging to a null solution it has been discovered that rather than using the UEC as employed in DOTEQ, the convergence is faster if the UTC is adopted. Besides, the UEC criterion requires a significant number of computations to implement. Consequently, the first tap of the TIR is not changed

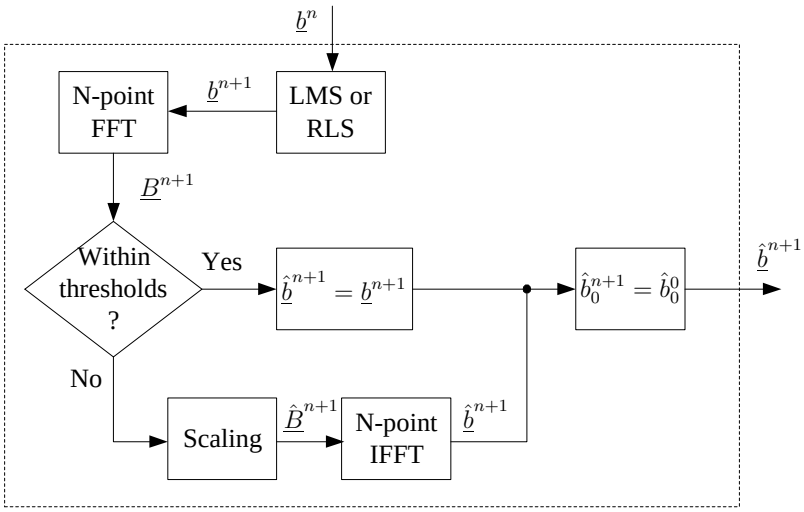

Figure 6.5: FSTEQ algorithm: Block diagram

during the iterations, i.e. $\hat{b}_0^{n+1} = \hat{b}_0^0, \forall\, n \geq 0$.

Finally, after the iterations are complete the FEQ needs to be updated with the inverse of the ETF (and not the CTF). The ETF is estimated by sending the received training symbol through the converged TEQ and then taking the ratio between the transmitted and the decoded symbols. The algorithm can be summarised as follows,

1. Using the CTF, set both Upper and Lower frequency domain thresholds ($\underline{G}_u$ and $\underline{G}_l$, respectively). The thresholds are selected such that they follow the envelope of the power delay profile of the channel as shown in figure 6.4. These thresholds are used to constrain the TTF (frequency domain), thus reducing the null depths in the ETF.

2. The TTF is initialised to be an exponentially decaying function so that the initial TTF is within the two threshold values. The initial TIR is set to be the IFFT of the initial TTF.

3. At each iteration, the TIR and TEQ are optimised concurrently in the time domain using the LMS algorithm as in (6.7) and (6.8) or by use of the RLS

algorithm as in (6.14) and (6.15). In other words, the unscaled TIR $\underline{b}^{n+1}$ is calculated from $\underline{b}^{n}$.

4. Next the TTF, namely $\underline{B}^{n+1}$ of size N is calculated by taking the FFT of $\underline{b}^{n+1}$. If $|\underline{B}^{n+1}|$ exceeds the two threshold values, it is scaled so that the resulting $|\hat{\underline{B}}^{n+1}|$ lies within the thresholds. The updated TIR coefficients, $\hat{\underline{b}}^{n+1}$, are calculated by performing an IFFT on $\hat{\underline{B}}^{n+1}$.

5. The TIR coefficients are updated by the scaled values $\hat{\underline{b}}^{n+1}$, except for $\hat{b}_0^{n+1}$ which is forced to be equal to $\hat{b}_0^0$ of the initial TIR. Thus the TTF is constrained to lie within the upper and lower thresholds.

6. The FEQ coefficients are calculated based on the converged ETF.

It has been observed that training the TEQ needs at least 1500 iterations when the LMS algorithm is used. The overhead of transmitting such a long training sequence cannot be justified. This is avoided by sending a shorter training sequence and passing the same training sequence through the equaliser several times until an acceptable level of convergence is achieved. This method is known as accelerated (or multiple) training [131, 132].

Figure 6.6 shows the performance of FSTEQ algorithm in the time domain for the same CIR used to give the DOTEQ results presented in figure 6.2. Note that the peak magnitude of the EIR occurs at the beginning and is well within the length of the CP. The FSTEQ has effectively converted the CIR into an exponentially decaying EIR, which has a much higher rate of roll-off in the time domain. The residuals beyond the TIR length of 14 are also reduced to values with insignificant power. Figure 6.7 shows the corresponding ETF (frequency domain). The final ETF shows very close convergence to the Initial TTF (see figure 6.4) and more significantly, an absence of deep nulls in the ETF as compared with that achieved by the DOTEQ results presented in figure 6.3.

6.5 Z-Plane Analysis of FSTEQ

An FIR filter is inherently stable. However the zeros, or the roots of the filter polynomial, determine its frequency response. If all the zeros fall within the unit

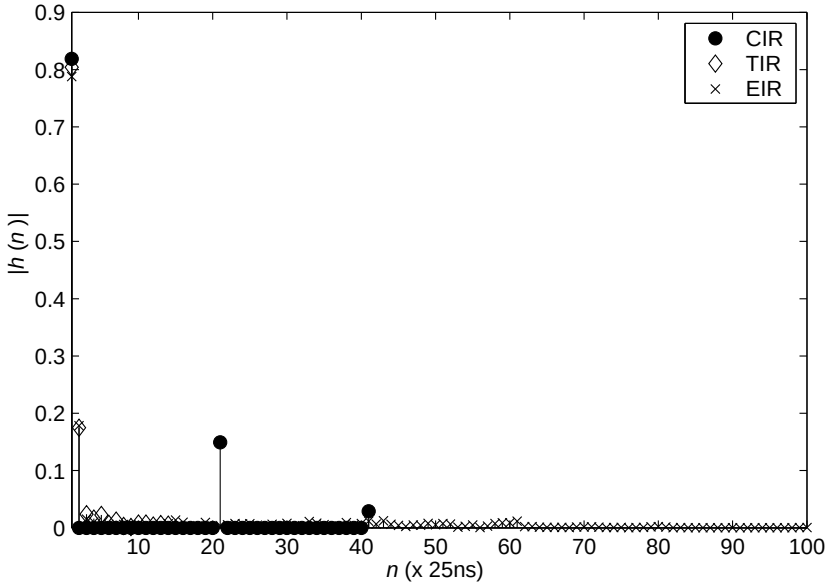

Figure 6.6: FSTEQ performance: Impulse responses

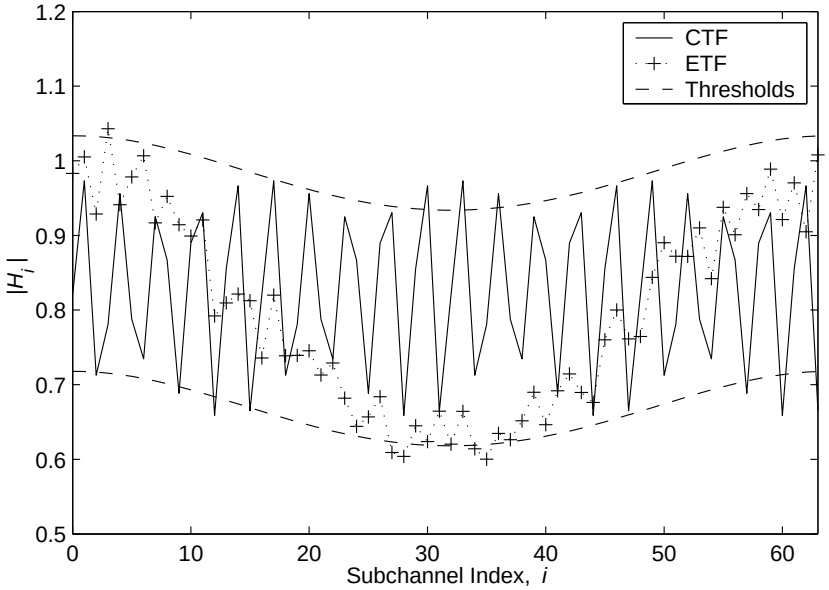

Figure 6.7: FSTEQ performance: Transfer functions

circle in the Z-plane, the filter response is deemed minimum phase. There are several characteristics of a minimum phase response. One is that the group delay is minimum and also the partial energy (defined as the sum of magnitude squared impulse response from $-\infty$ to n) is maximum among all filters of the same magnitude response [133, pg. 250]. This is equivalent to the impulse response of the minimum phase system being more concentrated near to the origin than any other system. Hence, the peak of the impulse response would lie closer to the origin. An exponentially decaying response is an example of a minimum phase response. It is also shown in [134] that for an exponentially decaying response with a time constant λ, most zeros are close to the circle $r = e^{\lambda/2}$ in the Z-plane. Hence an exponentially decaying response will have most of its zeros within the unit circle with a very high probability.

Figure 6.8 shows an example, but nevertheless representative, Z-plane analysis of the roots of the final converged EIR when a DOTEQ is used. The initial CIR is also included for comparison. Since the CIR has the profile of an exponentially decaying function, all of its zeros lie within the unit circle and thus it is minimum phase. However once the DOTEQ is used, some of these zeros are pushed outside the unit circle and some are even placed very close to the unit circle. The zeros that are close to the unit circle are called critical zeros. The critical zeros pull the transfer functions to a null at the corresponding frequency. Since some of the zeros lie outside the unit circle it makes the overall EIR non-minimum phase (mixed phase). A filter that provides the reciprocal of a particular response is known as the inverse filter. Thus $\hat{H}(z)$ is an inverse filter to the response of $H(z)$ in the following system

$$\hat{H}(z) = 1/H(z)\ . \tag{6.16}$$

If $H(z)$ is minimum phase, the inverse filter is causal and stable [135] as the poles of the inverse filter lie in the unit circle. In an OFDM system, the FEQ is used to generate the inverse response of the ETF. If the ETF contains nulls, it will cause the FEQ to have coefficients with high gain. This can lead to non-ideal characteristics such as AWGN and Phase Noise (PN) being boosted along with the signal.

Figure 6.9 shows the zeros of the converged EIR when the FSTEQ is used for

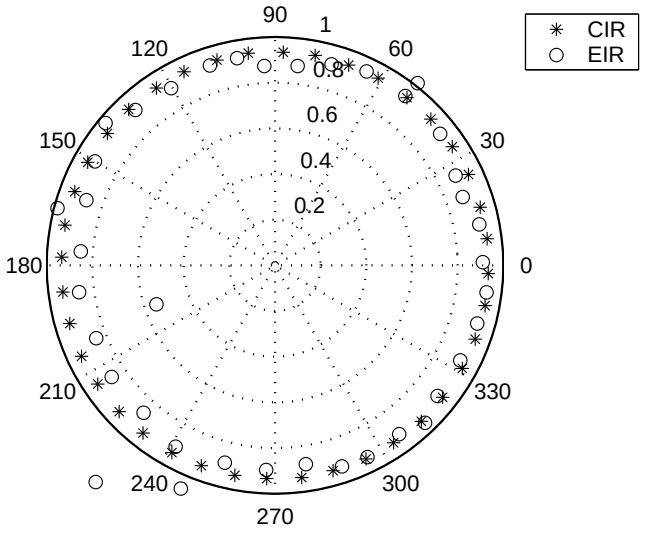

Figure 6.8: Z-plane analysis: DOTEQ response

the same CIR as used for the previous DOTEQ example. It clearly shows that the minimum phase characteristic is still retained by the FSTEQ even at the end of the convergence. Furthermore, there are no critical zeros. This is achieved because the algorithm is designed to specifically avoid spectral nulls.

6.6 Comparison of Computational Complexity

The following analysis is performed per iteration and all the multiplications and additions considered are complex. The calculation of the error term given in (6.2) requires $N_f + N_b$ multiplications, $N_f + N_b - 2$ additions and one subtraction. This is common to all the algorithms discussed in this chapter. Updating the TEQ coefficients using the DOTEQ algorithm, given in (6.7) requires $N_f + 1$ multiplications and N_f subtractions. Similarly updating the TIR coefficients using (6.8) requires $N_b + 1$ multiplications and N_b additions. Enforcing the UEC criterion, given in (6.9), requires N_b multiplications to calculate the energy, a square root operation and a further N_b divisions.

FSTEQ algorithms only require two FFT operations per iteration unlike the

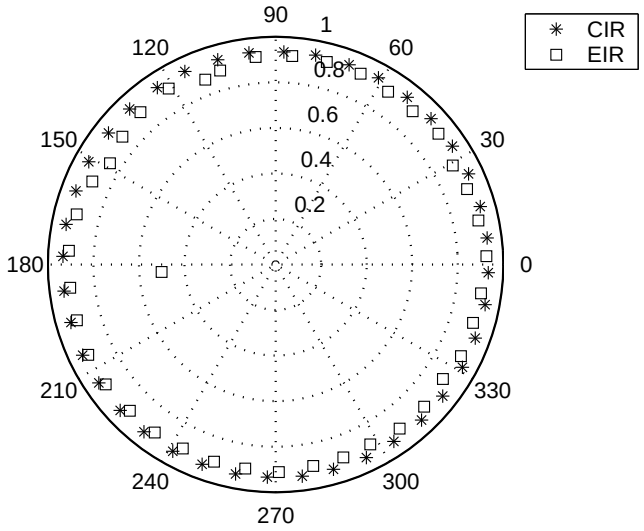

Figure 6.9: Z-plane analysis: FSTEQ response

algorithm proposed in [120]. Ignoring the computations required for the initialisation of the TIR, the LMS version of the FSTEQ requires (6.7) and (6.8) to be evaluated. It will be assumed that the FFT operation required to obtain the unscaled TTF coefficients require $N \log_2 N$ additions and $N/2 \log_2 N$ multiplications [136, Ch.6]. The comparison with the two thresholds requires $2N$ subtractions. If the TTF has crossed the thresholds, calculating the minimum and the maximum values require a further $2N$ subtractions. The scaling operation, given in (6.12) needs $N + 1$ subtractions, N multiplications and N additions. To find the complete TTF, given in (6.13) requires N multiplications. Converting the TTF to the scaled TIR coefficients requires the IFFT operation.

The RLS version of the FSTEQ requires the same number of operations for the scaling function, but the RLS operation requires a much higher number of computations. Updating the Kalman gain factor of the TEQ in (6.14) requires $3N_f^2$ multiplications, $3N_f(N_f - 1) + 1$ additions and N_f divisions. Updating the correlation matrix requires $2N_f^2 - 1$ additions, $2N_f^2$ multiplications, N_f^2 subtractions and a similar number of divisions. Finally updating the TEQ coefficients requires N_f multiplications and N_f subtractions. Hence in total, updating the TEQ using

the RLS algorithm requires $5N_f^2 - 3N_f + 1$ additions, $5N_f^2 + N_f$ multiplications and $N_f(N_f - 1)$ subtractions and divisions. Similarly updating the TIR requires $5N_b^2 - 3N_b + 1$ additions, $5N_b^2 + N_b$ multiplications and $N_b(N_b - 1)$ subtractions and divisions. Even though the number of computations appears to be high at first glance, there are number of algorithms that perform the RLS more efficiently [137]. Also note that the above calculation is per iteration, so since the RLS requires fewer iterations, the overall number of computations is not exceedingly high.

Algorithm	**Additions**	**Subtractions**	**Multiplications**	**Divisions**
DOTEQ	$N_f + N_b$ -2	$N_f + N_b$ $+1$	$2N_f + 3N_b$ $+2$	N_b
FSTEQ (LMS)	$N_f + N_b$ $+2N\log_2 N$ $+N - 2$	$N_f + N_b$ $+5N$	$2(N_f + N_b)$ $+N\log_2 N$ $+2(N + 1)$	1
FSTEQ (RLS)	$5(N_f^2 + N_b^2)$ $-2(N_f + N_b)$ $+2N\log_2 N$ $+N$	$N_f(N_f + 1)$ $+N_b(N_b + 1)$ $+5N$	$5(N_f^2 + N_b^2)$ $+2(N_f + N_b)$ $+2N\log_2 N$ $+2N$	$N_f(N_f + 1)$ $+N_b(N_b + 1)$ $+1$

Table 6.1: Comparison of computational complexity per iteration

Table 6.1 shows the total computational load required by each algorithm per iteration. It can be stated that the computational complexities per iteration are of the order of $\mathcal{O}(N_f + N_b)$, $\mathcal{O}(N_f + N_b + N\log_2 N)$ and $\mathcal{O}(N_f^2 + N_b^2)$ for DOTEQ, FSTEQ (LMS) and FSTEQ (RLS) respectively. For an OFDM system with $N = 64$, $N_f = 60$ and $N_b = 14$, the complexity per iteration for DOTEQ, FSTEQ (LMS) and FSTEQ (RLS) are of the order 74, 458 and 3796, respectively.

6.7 Simulation Parameters and Results

For the simulations, OFDM systems with $N = 64$ have been selected. Without loss of generality, QPSK mapping for all subchannels has been employed and all subchannels are used. The maximum burst length is set to 2500 symbols. As in

the other simulations performed in this thesis, the SUI-II channel profile is selected and it is assumed to be constant over duration of the transmitted burst. The FSTEQ has proved to perform well even in more hostile channels [138], however for brevity, only the results corresponding to SUI-II channels are presented here. It should be noted that the advantage of the FSTEQ becomes more apparent for channels with more delay spread. The maximum length of the SUI-II CIR is 1μs, hence it is only 20 samples long at a sample rate of 20 MHz. But if the required data rate to be transmitted is assumed to be greater than 60 Mb/s a higher sampling rate is required. Hence the sampling rate has been initially set at 40 MHz. This dictates a data rate of $40 * 2 * N/(N + v) * 10^6$ bits/s. For instance, for $v = 15$ the corresponding data rate is 64.8 Mb/s. At this sampling rate the CIR will be 40 samples long. An OFDM system with $N = 64$ will have to use a CP of length 40 to completely eliminate the effects of the CIR. Since this is quite inefficient, the use of the FSTEQ is justified in such a scenario.

Each data point in the simulation results is obtained by averaging over 1000 such bursts and the channel filter tap coefficients are updated randomly in accordance with the power delay profile specified by the SUI-II channel model. The received SNR is set to 20 dB for the simulations unless the SNR is used as the variable parameter. The TEQ training header has a length of 5 symbols and unless otherwise stated, it is run through the TEQ 7 times during training. Hence the total number of iterations is $64 * 5 * 7 = 2240$. The parameters for the LMS version of the FSTEQ are $\Delta_f = 0.005$ and $\Delta_b = 0.085$ while for the RLS version of the FSTEQ are $\Omega_f = 0.9999$ and $\Omega_b = 0.999$.

Figure 6.10 shows the BER as a function of TIR length for both DOTEQ and FSTEQ, with the TEQ length being set to 60. Alternatively, this may be viewed as varying the length of the CP for a given TEQ length. Two cases of FSTEQ are shown, one using LMS and the other using RLS for adaptation. The performance without a TEQ is also included for comparison. It can be seen that using DOTEQ gives an inferior performance to that when TEQ is not used at all. This is due to the nulls created by DOTEQ in the ETF. There is little difference in performance between FSTEQ using either LMS or RLS adaptation. This is because the training time used is sufficient for the TEQ to converge and achieve a stable MSE even for the LMS algorithm. As shown the FSTEQ gives a BER improvement of the order

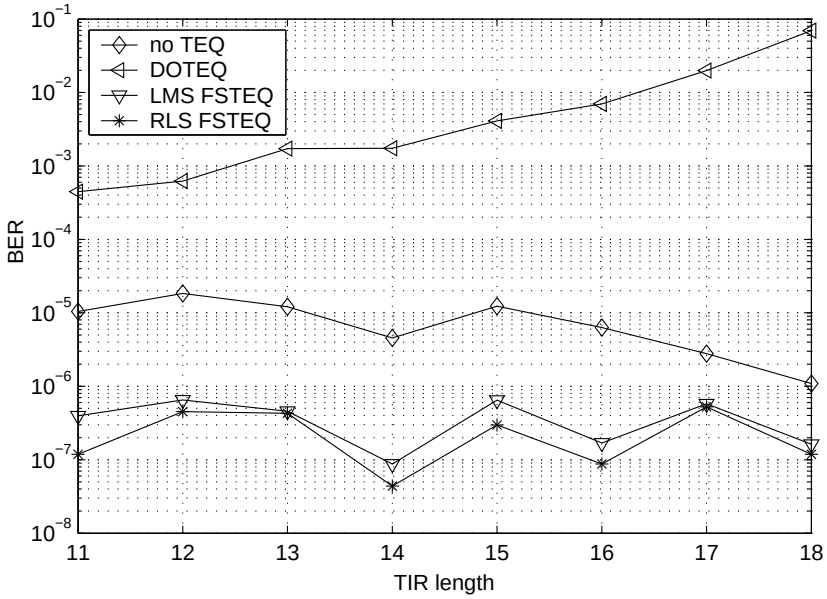

Figure 6.10: Comparison of the schemes for a TEQ length of 60, at a sample rate of 40 MHz and 2240 training iterations

of 10-100 over the case where no TEQ is used. Figure 6.11 shows the MSE as a function of the number of iterations for various TEQ schemes. The plots were obtained after averaging over 200 realisations. Note that the MSE of DOTEQ is high even after 1200 iterations. The FSTEQ achieves a much lower MSE but note that the LMS based training seems to be slightly more erratic at the beginning of the training period.

Figure 6.12 shows the effect of using only 1280 iterations for training. It shows a slight performance degradation of the LMS based FSTEQ owing to its slow convergence, but the RLS based FSTEQ loses little in performance. Figure 6.13 shows the effect of SNR on the performance of various schemes with a TEQ length of 60 and a TIR length (i.e. system CP length) of 14 when using the original training length of 2240. It shows that significant gains cannot be achieved at an SNR below 16 dB even with the use of FSTEQ. At an SNR in excess of 20 dB the RLS based FSTEQ has a slight advantage over that of the LMS based one.

Figures 6.14 and 6.15 show the performance for TEQ lengths of 50 and 40

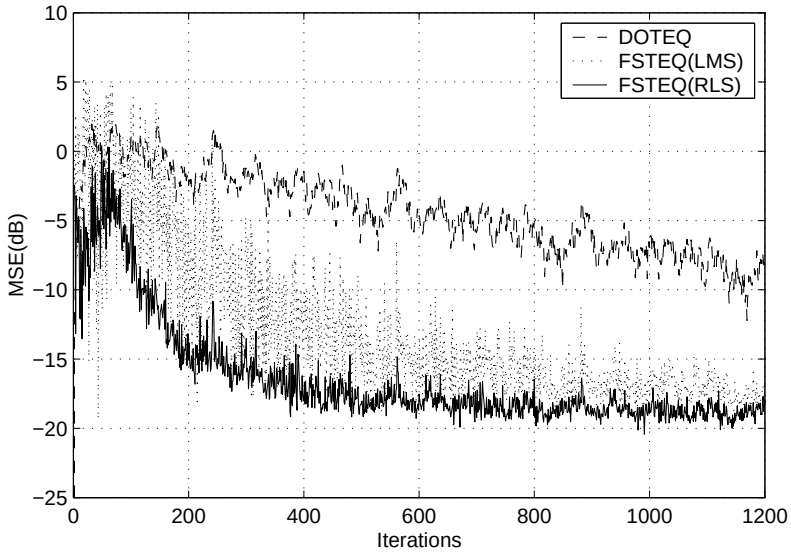

Figure 6.11: Comparison of the MSE for various TEQ schemes with a length of 60, at a sample rate of 40 MHz

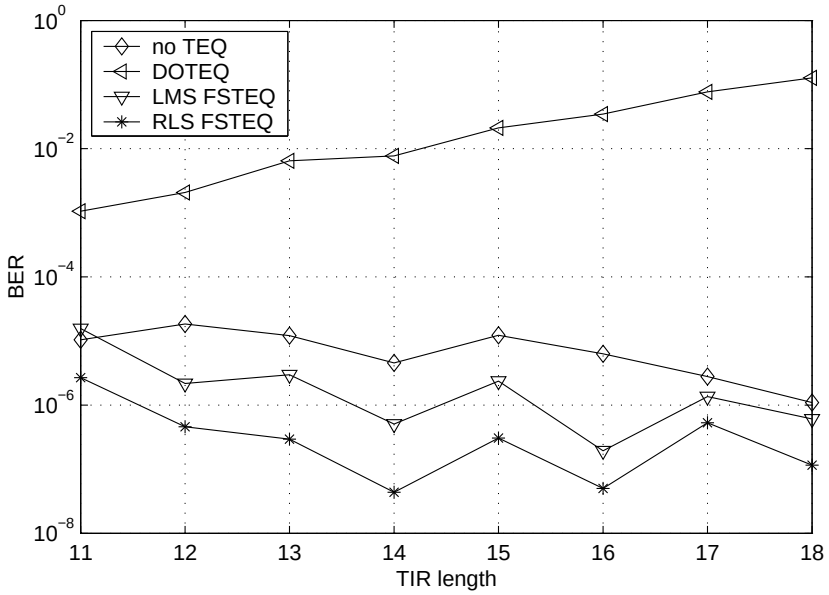

Figure 6.12: Comparison of the schemes for a TEQ length of 60, at a sample rate of 40 MHz but 1280 training iterations

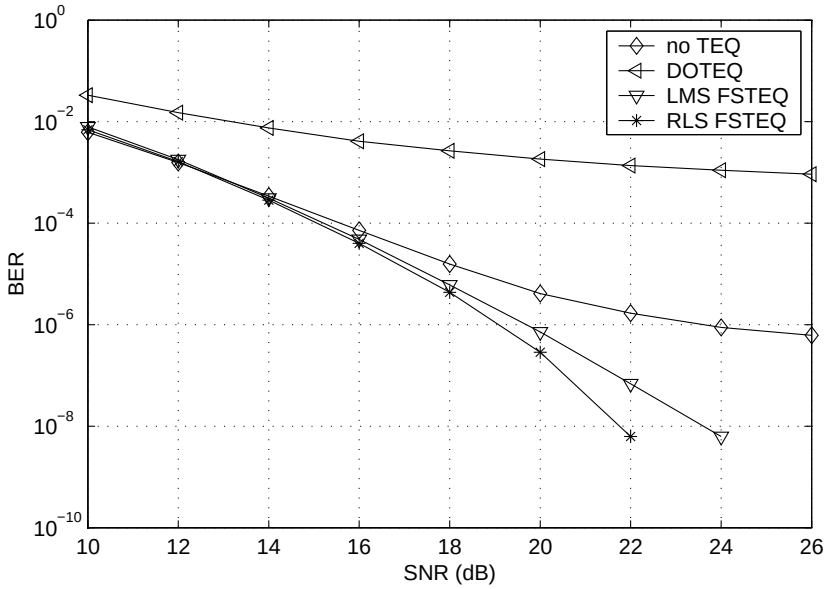

Figure 6.13: The effect of SNR on different TEQ schemes with a length of 60, a CP of length of 14 and a sample rate of 40 MHz

respectively with the other parameter values identical to those used in figure 6.10. It appears that the ability of the TEQ to force the EIR towards the initial TIR increases with the length of TEQ. If the TEQ length is too short, the time domain residuals beyond the TIR length (and hence the CP) become significant and give rise to both ISI and ICI. Since a CIR length of 40 samples is assumed it has been observed that, the TEQ should be at least as long as the CIR for the TEQ to give a significant performance gain. This is demonstrated in figures 6.10 and 6.15, where for example with a TIR length of 11 samples a FSTEQ length of 60 performs much better than one of length 40.

To investigate the performance of FSTEQ with shorter channels, a series of simulations have been performed at sample rate of 20 MHz using the same system as before. Hence the SUI-II channel is now only 20 samples long. Figure 6.16 shows the BER performance with TEQ of length 30 and TIR lengths (i.e CP lengths) in the range from 4 to 11. It shows that the performance gains are reduced compared with the previous scenario.

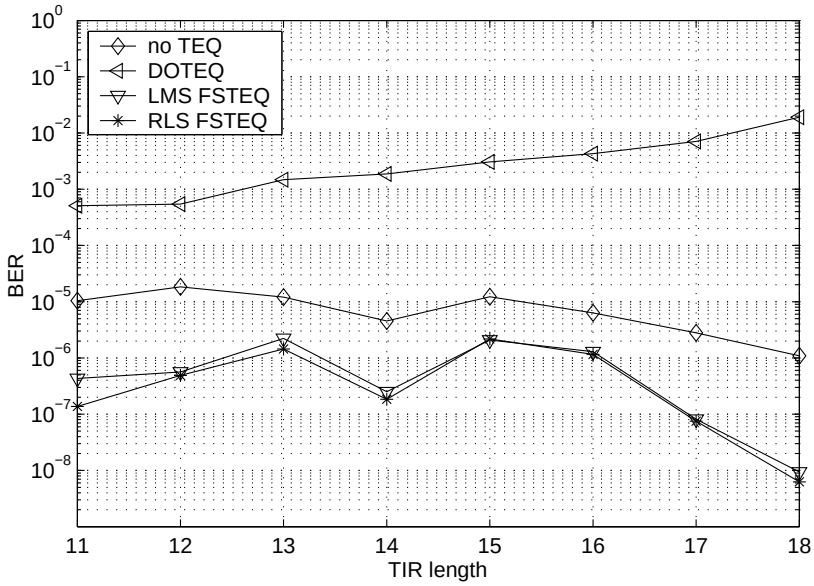

Figure 6.14: Comparison of the schemes for a TEQ length of 50 at a sample rate of 40 MHz and 2240 training iterations

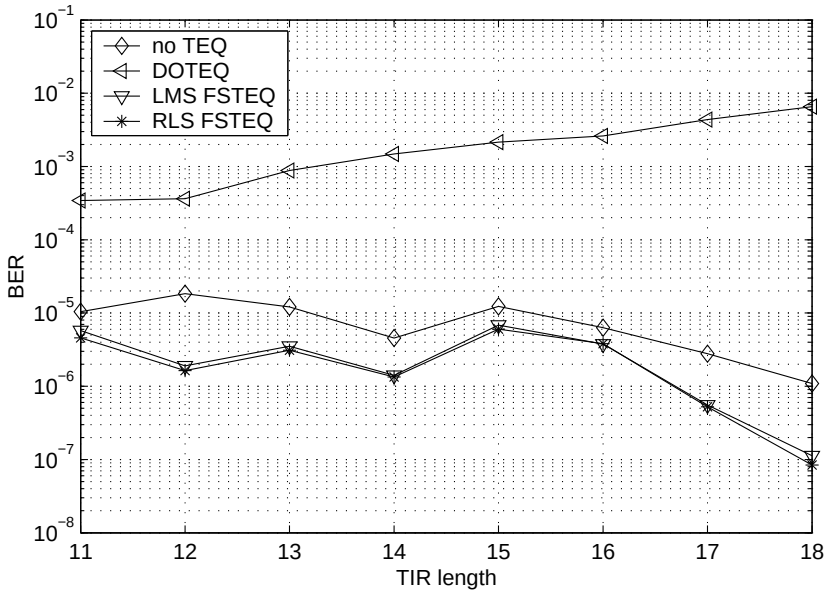

Figure 6.15: Comparison of the schemes for a TEQ length of 40 at a sample rate of 40 MHz and 2240 training iterations

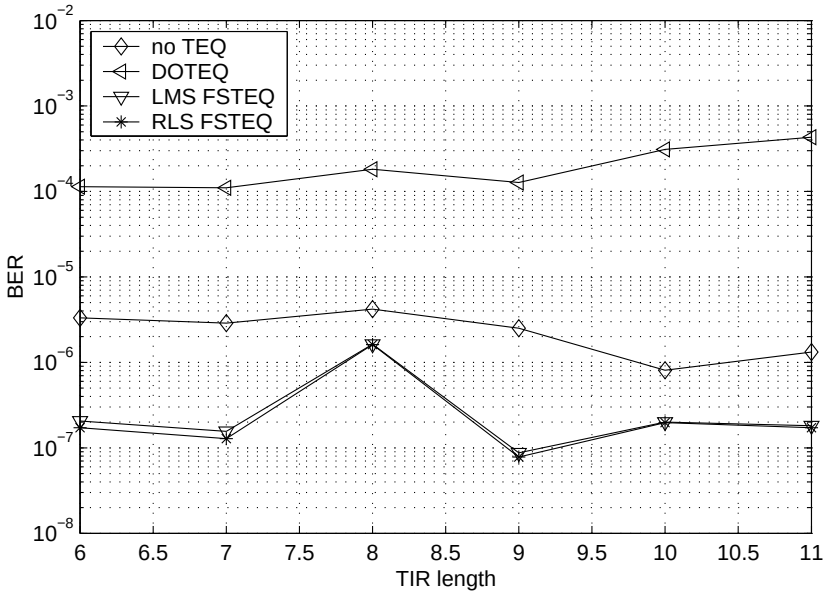

Figure 6.16: Comparison of the schemes for a TEQ length of 30 at a sample rate of 20 MHz and 2240 training iterations

6.8 Conclusions

An algorithm that optimises the TEQ design both in the time and frequency domains has been presented in this chapter. It has been shown through simulations that the BER performance can be improved by a factor of 10-100 compared with that achieved by OFDM without FSTEQ in SUI-II channels. Admittedly the algorithm needs a reasonable amount of processing time and memory to store the incoming data during the training of the TEQ. However the objective here is not to optimise the resources used, but rather to see what performance gains are made possible by the use of TEQ for OFDM in the broadband fixed wireless scenario. Hence considering the computational demand of FSTEQ, it is recommended that the algorithm be used only if the wireless channel spans a length more than half the OFDM symbol length. It should be noted that since the FFT is already implemented in the OFDM demodulator, the additional hardware required for the implementation of the FSTEQ is somewhat relieved.

Chapter 7

Adaptive Time Domain Windowing

As noted previously in chapter 2 the use of rectangular pulse shapes in conventional OFDM systems result in 'sinc' sidelobes being generated in the frequency domain. The presence of these high sidelobe levels is found to render OFDM systems sensitive to Phase Noise (PN) and frequency offsets. An intuitive approach to reduce these problems is to use Time Domain Windowing (TDW) to lower the sidelobe levels. For example time domain windowing is introduced in the IEEE 802.11a standard to smooth out the transitions between consecutive OFDM symbols and to reduce the out-of-band spectral spillage [139]. However unless a window is used which satisfies the Nyquist pulse shaping criterion, the windowing process will cause the OFDM carriers to lose their orthogonality. Thus a non-Nyquist window will introduce severe Inter Carrier Interference (ICI) even though the sidelobe levels in the frequency domain may be low. In this chapter an investigation is performed to quantify the performance gains that are available with the use of Nyquist windowing in OFDM systems when applied to BFWA networks.

A Nyquist window has a roll off region at either end. For an active OFDM symbol with length N, the Nyquist window length, D will be $N < D < 2N - 1$. Hence in order to incorporate windowing, uncorrupted contiguous samples of a length greater than N are required for each OFDM symbol at the receiver. This will in general require the transmission of extra samples, however if the CIR length is less than the CP length, it is possible to use the last few samples of the

CP to lie within the roll-off region of the window function. In the former case, the extra samples would increase the bandwidth, which in turn would increase the received noise power. In the second case, the SNR will remain the same as that of a conventional OFDM system, since we are not using any additional samples. The latter case will be assumed by default in this chapter, although performance comparisons with the former case will be presented later in the chapter. In order to use windowing the proposal is to make use of the all the samples in the CP in the case of AWGN only channels or to use only those samples lying within the Excess Length of the CP (i.e. the last $p = v - N_h$ samples in the CP) for channels with delay spread. If the OFDM system uses a cyclic prefix as well as a cyclic postfix, these samples can lie within the roll off regions at either side of the window function. However this approach is not possible in conventional OFDM systems since only a cyclic prefix is used. In this situation the proposal is to use the samples available in the Excess Length of the CP and the ones in the active part of the transmitted symbol. The process is explained in detail in section 7.2.

Only a limited amount of research has previously been carried out in this area, the most important of which will be described in section 7.1. In this chapter the analysis of the effect of time domain windowing on OFDM systems is divided into two parts. Section 7.2 introduces the effect of windowing at the receiver and section 7.3 introduces the effect of windowing at the transmitter. Finally section 7.4 draws some conclusions.

7.1 Related Work

Different types of windows have been proposed by various authors. The author in [140] uses Raised-Cosine (RC) windowing at the receiver, while in [141] Root Raised Cosine (RRC) windowing is used at both the transmitter and the receiver. The authors in [142] use modified window shapes that introduce significant changes to the structure of the transmitter, which go beyond the scope of this chapter. The authors in [143, 144] introduce an algorithm to optimise the window coefficients in the MMSE sense when the OFDM system is subjected to frequency offsets and they conclude that the RC window shapes are far from optimal. Indeed their investigations show that the Trapezoidal Window (TPW) is very

close to the optimal window function. Several authors, for example [141, 101] have investigated the effect that time domain windowing has on the tolerance of OFDM systems to time and frequency synchronisation errors. They conclude that the windowed OFDM system is more tolerant to such errors than is a conventional system. The author in [92] provides a brief discussion of related work concerning time domain windowing.

The authors in [141, 145, 146] investigate the use of time domain windowing but do not apply the Nyquist criterion to the window function. Although such window functions reduce OFDM subchannel sidelobe levels they introduce interference by sacrificing the orthogonality between the subchannels. To counter the loss of orthogonality, per-subchannel Decision feedback Equalisers (DFEs) are used after the FFT demodulator.

A considerable amount of work has also been performed concerning the effect of frequency domain windowing during channel estimation. In systems subjected to fast fading channels, in order to maintain the accuracy of the channel estimate pilot symbols are sent continuously in some subchannels. After obtaining the channel coefficients corresponding to the subchannels corresponding to the pilot symbols, the coefficients of the other subchannels are obtained through interpolation or a weighted IDFT/DFT operation. In the later case windowing may be used to reduce errors due to aliasing [147]. However this is not the focus of the work presented in this chapter.

7.2 Time Domain Windowing at the Receiver

The window function, g_k has a maximum non-zero length of $2N-1$ samples. Subchannel orthogonality is maintained if the time domain window complies with the Nyquist criterion, which is given by [144],

$$\sum_{i=-\infty}^{\infty} g_{k+iN} = \mathbf{const}, \quad 0 \leq k \leq N-1 \tag{7.1}$$

with $g_k = 0$ for at least $k < -N/2$ and $k > 3N/2$. An example of a Nyquist

window is the rectangular window, which can be written as,

$$c_k = \begin{cases} 1 & 0 \leq k \leq N-1, \\ 0 & k < 0 \text{ or } k \geq N. \end{cases} \tag{7.2}$$

Any sample within the region $k < 0$ and $k \geq N$ are called the roll-off samples. Hence, the rectangular window does not have any non-zero roll-off samples. Figure 7.1 shows the decomposition of a typical Nyquist Window. The rectangular window is also included for comparison. Any non-rectangular Nyquist window will have up to $v_\beta + 1$ non-zero samples in the roll-off region. The window is extended by v_β samples on its left hand side and $v_\beta + 1$ samples on its right hand side. The roll-off factor, $\alpha = (2v_\beta + 1)/N$ determines v_β [144]. The longest window length is reached if the roll off factor is equal to unity. As shown in figure 7.1, a Nyquist window can be generated from the rectangular window function by using time limited roll-off modification samples β_k, provided that the following condition holds [144]

$$g_k = c_k + \beta_k - \beta_{k-N} \, . \tag{7.3}$$

Figure 7.2 shows the time domain characteristics of the RC window and the TPW with $\alpha = 0.5$. The rectangular window is also shown for comparison. The effect of the window functions is more obvious in the frequency domain plots given in figure 7.3. The TPW and the RC window functions show very high sidelobe decay rates whereas the first sidelobe of the rectangular window function shows the familiar 13 dB reduction in comparison to the main lobe. However the fast sidelobe decay rates of the non-rectangular windows are achieved at the cost of longer time domain pulses. Muschallik in [140] showed that the conventional OFDM system is equivalent to a filter bank system with rectangular windows. The noise power in each subchannel is equivalent to the integrated power of the common area between the window transfer function placed at the subchannel frequency and the noise PSD. He further showed that non-rectangular Nyquist windows by having lower sidelobes will ensure lower subchannel noise powers. Hence non-rectangular windowing improves the performance even in AWGN channels [140].

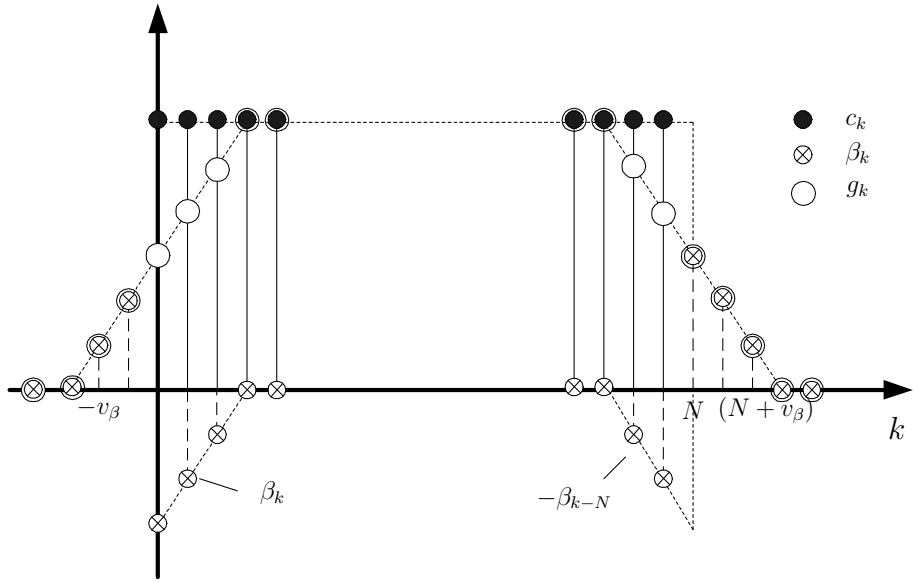

Figure 7.1: Decomposition of a Nyquist window

The demodulated OFDM symbol $Y_{m,l}$ of the lth subchannel of the mth block in a conventional OFDM system is shown in (2.20). To incorporate windowing, it is modified to become

$$Y_{m,l} = \sqrt{\frac{1}{N}} \sum_{n=0}^{N-1} \left(\sum_{\nu=-1}^{\nu=+1} g_{\nu N+n} r_{m,(\nu N+n)\mathbf{MOD}N} \right) e^{-j2\pi \frac{ln}{N}}, \quad 0 \leq l \leq N-1 \quad (7.4)$$

where $r_{m,n}$ are the samples of the active part of the OFDM symbol. The inner summation in (7.4) describes the preprocessing required to fold the roll-off samples of the window function. Hence, the outer sum, which describes the N point FFT remains the same as in a conventional OFDM system. Figure 7.4 illustrates the processing required at the receiver. Figure 7.4(a) shows how the first $v-p$ samples in the CP are corrupted by the CIR because they are affected by Inter Block Interference (IBI) from the previous OFDM symbol. Here p represents the Excess Length and we set $v_\beta = (p-1)/2$. The receiver selects the last $N+2v_\beta+1$ samples of the transmitted OFDM symbol to be multiplied by the window function as shown in figure 7.4(b). The result is zero padded using $N - v_\beta$ samples on the

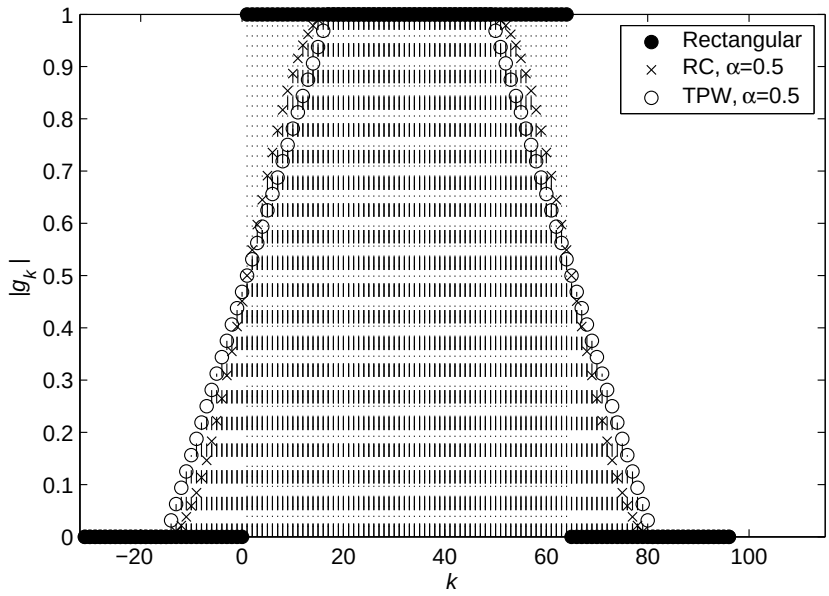

Figure 7.2: Comparison of different Nyquist windows in the time domain with $\alpha = 0.5$

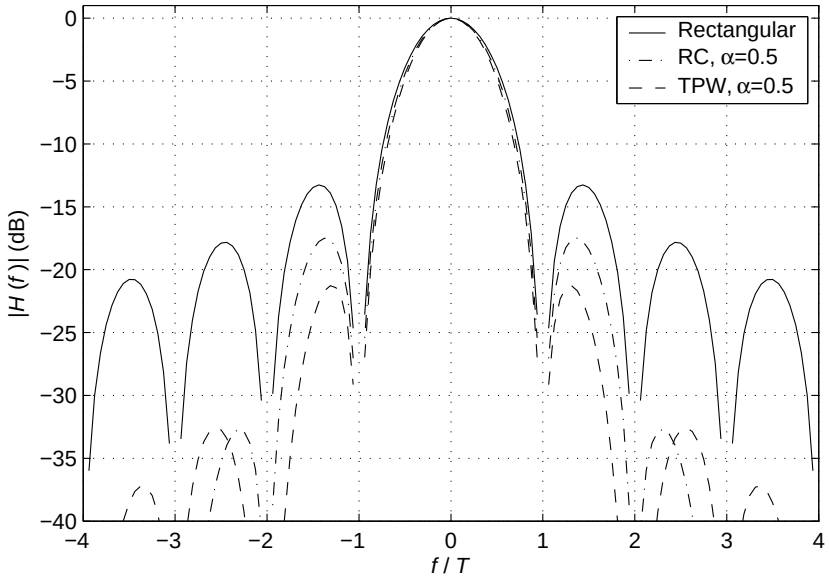

Figure 7.3: Comparison of different Nyquist windows in the frequency domain with $\alpha = 0.5$

left hand side and $N - v_\beta - 1$ samples on the right hand side. Then every Nth sample is summed to form a vector of length N as shown in figure 7.4(c). Then it is sent to an N point FFT for demodulation. In [140] the authors use a $2N$ point FFT instead. The demodulated symbols are then taken only from the even subchannels of the $2N$ point FFT. The results of this system are the same under AWGN as the one presented in this section.

If the condition in (7.1) is satisfied, the orthogonality between the subchannels is preserved. The MOD function in the inner summation of (7.4) ensures that the roll off samples of the window function are multiplied with the cyclic prefix and the cyclic postfix of the OFDM symbol. If a cyclic postfix is not used, the uncorrupted samples in the cyclic prefix of the OFDM symbol are multiplied with the roll-off samples instead. The start of the receive FFT window of the OFDM symbol is shifted $v_\beta + 1$ samples to the left. Hence (7.4) is modified to

$$Y_{m,l} = \sqrt{\frac{1}{N}} \sum_{n=0}^{N-1} \left(\sum_{\nu=-1}^{\nu=+1} g_{\nu N+n} r_{m,(\nu N+n+v_\beta+1)\mathbf{MOD}N} \right) e^{-j2\pi \frac{ln}{N}},\ 0 \leq l \leq N-1. \tag{7.5}$$

This however causes the demodulated signals to experience a phase shift, which can be eliminated by multiplying the lth subchannel with $\exp(j2\pi(v_\beta + 1)l/N)$. The required phase rotation does not require additional computations since it can be easily incorporated with the FEQ.

7.2.1 Simulation Parameters and Results

OFDM systems with QPSK mapping and $N = 64$ subchannels are selected for simulation. As in previous simulations, a burst length of 2500 OFDM symbols is transmitted. The effect of time domain windowing in the receiver is investigated for both AWGN and SUI-II channels.

Figure 7.5 shows the performance gains that can be obtained for AWGN channels using RC windowing for different values of the roll-off factor, α. The results are based on the assumption that a CP of a similar length is also transmitted in the conventional OFDM system. It shows that the overall gains that can be obtained are not that great. For example $\alpha = 0.25$ gives a gain of 0.3 dB over rectangular windowing at a BER of 10^{-4}. The gain increases to 0.6 dB for $\alpha = 0.5$.

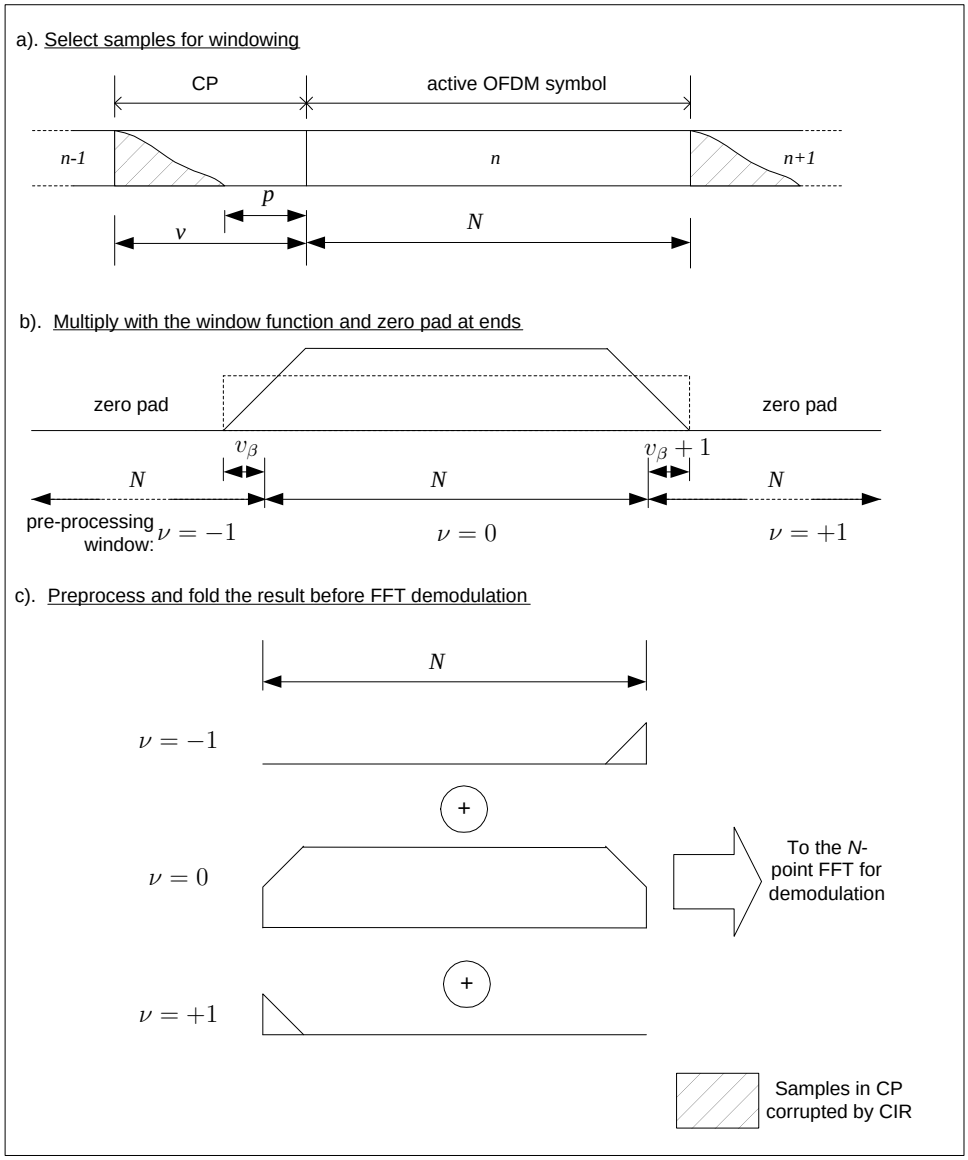

Figure 7.4: Processing required at the receiver for the windowed OFDM system

These results confirm the results observed in [140]. If the conventional system is assumed to have transmitted no CP and only the windowed system to have transmitted a CP of length $v = p$ in AWGN, then the additional bandwidth introduces a SNR penalty equivalent to a factor of $(N + p)/N$ to the windowed system. For a windowed system with $N = 64$ and $\alpha = 0.25$ and the Excess Length required,

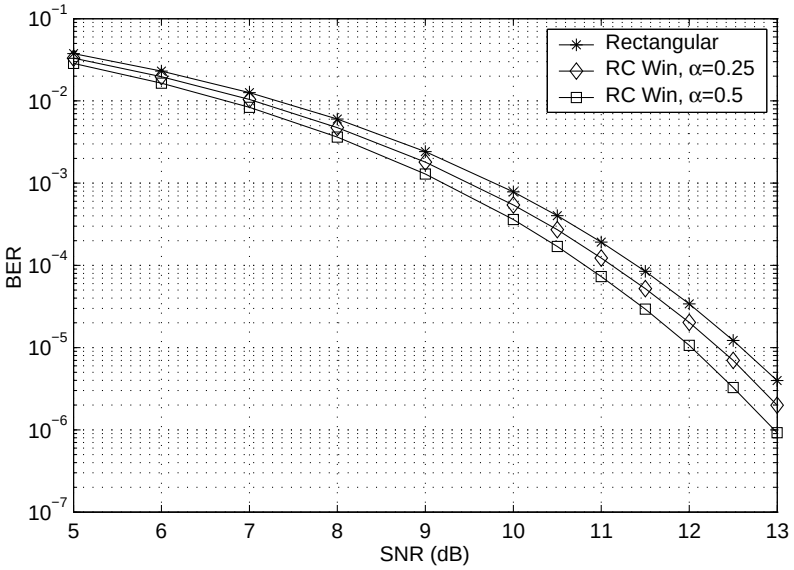

Figure 7.5: Comparison of the effect of RC Nyquist windowing at the the receiver with AWGN channels

p is equal to 16. Hence the SNR penalty is 0.9 dB. It increases to 1.7 dB for a system with $\alpha = 0.5$. If the SNR is normalised to reflect any additional bandwidth required by the windowing system, the results for the windowed schemes are actually worse.

Figure 7.6 shows the effect of using different types of windows, namely the RC and the TPW function. It shows that the use of a TPW gives a slight advantage over RC windowing. This coincides with the observation made by [144] that RC pulses are suboptimal and TPW is very close to the optimal window function. Hence from this point on, the simulations will be performed using only TPW. Even so, it will be evident that the performance gains recorded are not that high.

Figure 7.7 shows the BER performance of the OFDM system using a TPW at the receiver in the presence of SUI-II channels. The gains compared to rectangular windowing again are small. At a BER of 10^{-4} the gains are 0.3 dB and 0.5 dB for $\alpha = 0.25$ and 0.5, respectively. Here too, the assumption is made that the CP length is greater than the CIR length and that the samples in the Excess Length are adequate for windowing to be incorporated. If we change the assumption so

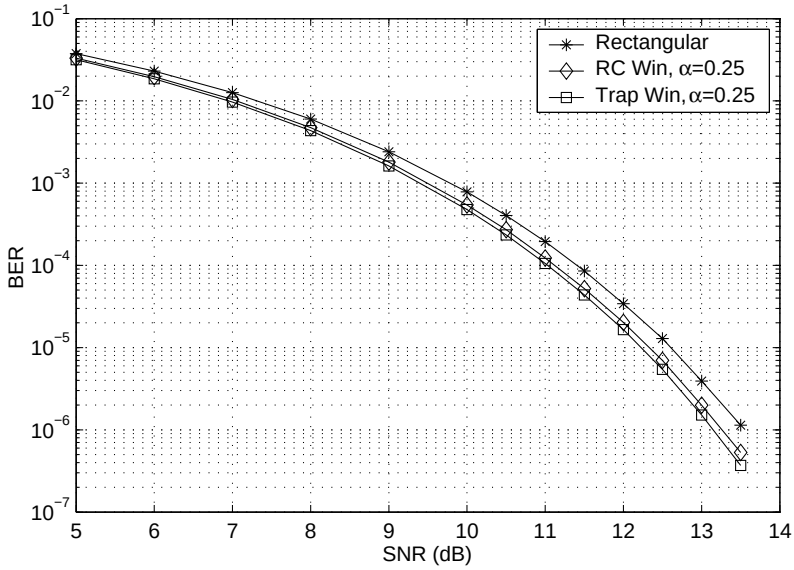

Figure 7.6: Comparison of the effect of various Nyquist windows with $\alpha = 0.25$

that the CP length is equal to the CIR length, then the windowed system will be penalised by a factor of $(N + v + p)/(N + v)$ for the additional bandwidth required. Assuming the conventional system requires only $v = 21$ samples in the CP to completely eliminate IBI due to the SUI-II channel profile, then the windowed system with $N = 64$ will require $p = 16$ additional samples if $\alpha = 0.25$. Hence the SNR penalty is now 0.74 dB. This increases to 1.38 dB for a system with $\alpha = 0.5$. This again shows that windowing at the receiver is not effective if additional samples need to be transmitted solely for the purpose of the windowing function. However, if there are uncorrupted samples in the CP, then it is worthwhile to apply windowing. Although the overall gains are not high the low computational demand makes it a viable option.

Simulations have also been carried out to see if any gains can be obtained by using TPW at the receiver when the system is subject to Phase Noise (PN) for an OFDM system with $N = 64$. Figure 7.8 shows the results when the system is sent through a SUI-II channel profile and is also subject to PN with masks having an upper cut off frequency $f_h = 200$ kHz and $f_h = 400$ kHz (See chapter 3 for the design of PN masks) and AWGN at an SNR of 20 dB. The results are

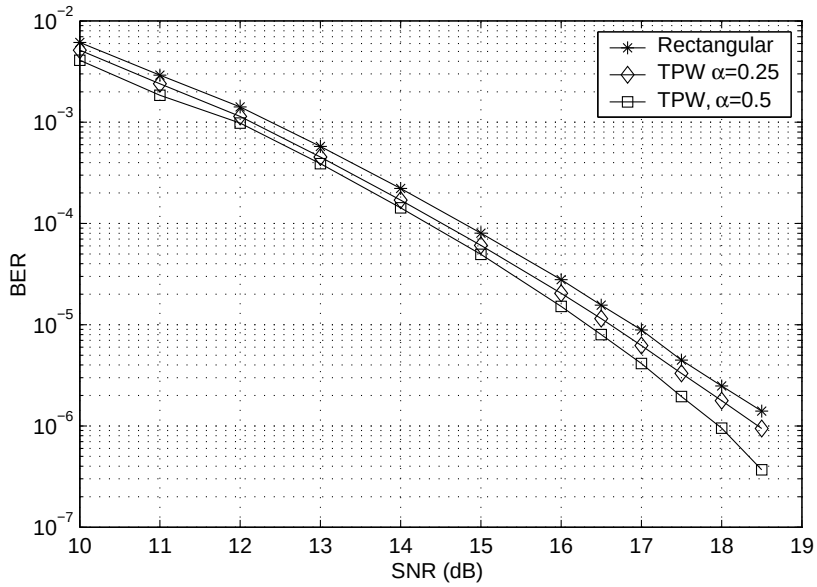

Figure 7.7: Comparison of the effect of TPW for SUI-II channels with $\alpha = 0.25$ and 0.5

presented in terms of Signal to Phase Noise Ratio (SPNR). The gain at a BER of 10^{-5} with the mask at $f_h = 200$ kHz is 0.2 dB in terms of SPNR, but is increased to 0.6 dB when the mask has $f_h = 400$ kHz. This can be explained as follows; as explained in chapter 3 the effect of PN on OFDM is two-fold. Specifically, the presence of Common Phase Error (CPE) rotates the received constellation and Inter-Carrier Interference (ICI) has a similar effect to AWGN. When f_h is increased the number of adjoining subchannels that fall into the PN mask of a particular subchannel increases. Hence the ratio between the ICI power to the CPE power increases. TPW is incapable of mitigating CPE but has a small effect on ICI. Since the mask with $f_h = 400$ kHz gives rise to more ICI then windowing produces greater gains than with $f_h = 200$ kHz and hence a better gains are seen with it. Even so, the overall gains are not significant. To mitigate the effects of CPE, the CPE Correction (CPEC) algorithm presented previously in section 3.4 will also have to be used.

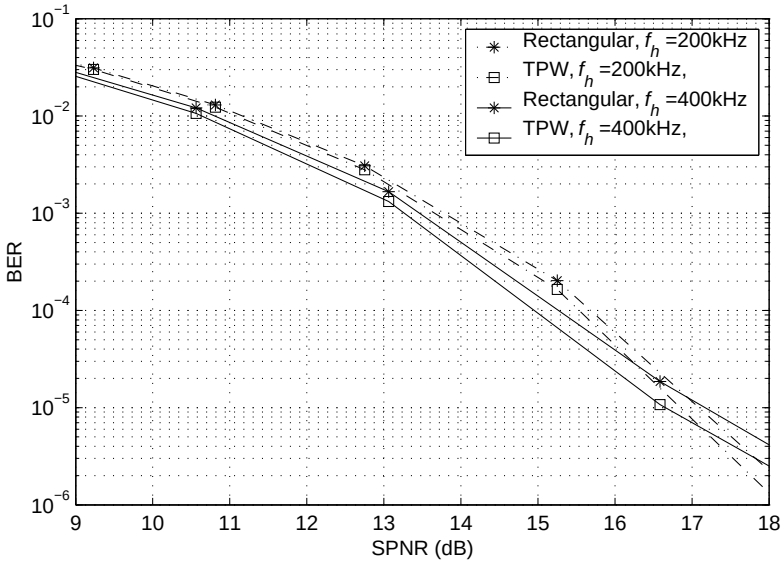

Figure 7.8: The effect of TPW with $\alpha = 0.5$ for SUI-II channels with PN and AWGN at a SNR of 20 dB

7.3 Time Domain Windowing at the Transmitter

Figure 7.9 illustrates the processing that is required if the windowing is performed at the transmitter rather than at the receiver. Firstly, the channel length has to be estimated. The samples that are not going to be corrupted by the CIR during transmission will be used for windowing as discussed in the previous section. However, it is imperative to *transmit zeros* during the first few samples of the CP, the duration of which is equal to the channel length, N_h as shown in figure 7.9(a). Otherwise orthogonality is lost at the receiver due to the lengthening of each symbol owing to the CIR which gives rise to IBI. As shown in figure 7.9(b), the receiver will have to consider these samples during the processing of each OFDM symbol. Hence the number of samples selected at the receiver for each OFDM symbol will be $2v_\beta + N + N_h + 1$. Compare this to the number of samples selected when the windowing is performed at the receiver, which is $2v_\beta + N + 1$. (see figure 7.4). Another difference is the number of zeros that are padded at either end before preprocessing; if the windowing is performed at the receiver the numbers are equal but this is not the case if the windowing is performed at the transmitter. As shown

in figure 7.9(c) every Nth sample is summed to form a vector of length N, which is sent to a N-point FFT for demodulation.

Even though selecting an additional N_h samples at the receiver will maintain orthogonality, it will also introduce more noise to the system. If the additional N_h samples at the tail of the symbol are not considered for processing at the receiver (in a similar fashion to that described in the previously in section 7.2), it will result in the introduction of ICI. However the interference power introduced will not be significant if the CIR is not too hostile. This is certainly the case for SUI-II channels and as will be as shown in the next subsection, the noise power that is introduced to the system by considering the additional N_h samples is greater than that of the interference power that it avoids. Multiplication performed by the TDW at the transmitter is equivalent to a convolution of the subchannel sinc spectrum with the spectrum of the window function in the frequency domain. In theory, this means the windowing process can be corrected in the frequency domain as part of the correction process at the FEQ. However, the method that is proposed here guarantees orthogonality. Besides, the additional computation effort required in the proposed method is not too high to warrant a frequency domain correction method.

7.3.1 Simulation Parameters and Results

Figure 7.10 shows the performance of a TPW system in the SUI-II channel, with $\alpha = 0.25$ at the transmitter and for comparison, that of a conventional OFDM system. Here too, it has been assumed that there are sufficient uncorrupted samples available in the CP to be included within the roll off samples of the window function. Since zeros are transmitted within the first part of the CP for the windowed system, the average power of the transmitted signal will be lower than that of the conventional OFDM system. To get a meaningful comparison, the power of the windowed system is normalised to a value similar to that of the simulated conventional OFDM system, which in this case is unity. For TPW, the results are presented for two cases. The curve labelled as 'TPW: Full' relates to the case where all $2v_\beta + N + N_h + 1$ samples are considered during the demodulation at the receiver. This system will not introduce ICI since orthogonality is maintained,

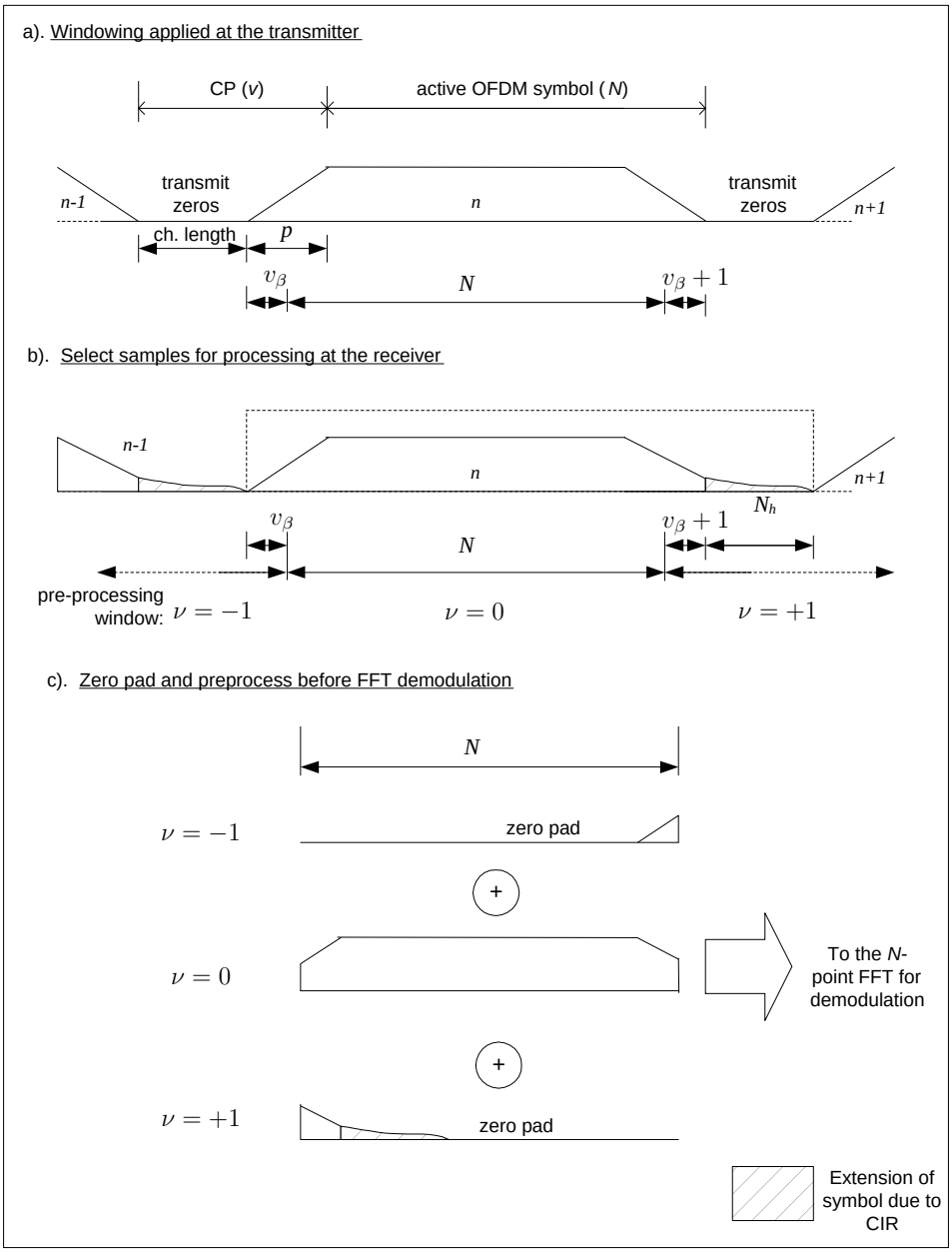

Figure 7.9: Windowing transmitted OFDM symbols and the processing required at the receiver to maintain orthogonality

but more noise will be introduced because more samples are considered during the FFT demodulation. The case where the number of samples considered is reduced to $2v_\beta + N + 1$ is shown as 'TPW: Reduced'. It clearly shows that including the additional N_h samples gives a worse BER performance. To get another comparison, the first N_h samples of the conventional OFDM system have also been zero padded, and again the average power is normalised to unity. This result is labelled as the 'Rect Win: with zeros' in figure 7.10. At a BER of 10^{-4} the windowed system that considers the decay samples shows a gain of 0.3 dB over the conventional OFDM system that does not transmit zeros in the CP. The performance gain increases to 0.9 dB if the decay samples are avoided. The Rectangular windowed OFDM system with zeros transmitted in the CP performs similarly to the TPW system with no delay samples. If the windowed system requires the transmission of additional samples, as calculated in the previous section the SNR penalty of 0.74 dB has to be applied. This largely negates any performance gains achieved owing to the use of windowing.

Figure 7.11 shows the performance of an OFDM system using a TPW at the transmitter with $\alpha = 0.5$, again in a SUI-II channel. The labelling of the plots follows the convention established in figure 7.10. The windowed system that uses the decay samples shows a performance gain of 0.8 dB over the conventional OFDM system. This increases to 1.4 dB if the decay samples are not included during processing at the receiver. If additional samples requires transmission solely for the purpose of windowing as shown in previous section, the penalty increases to 1.38 dB.

7.4 Conclusion

In this chapter the use of Time Domain Windowing (TDW) is investigated in the context of OFDM systems operating in BFWA channels. The windowing is applied separately in the receiver and the transmitter and their performance is compared with a conventional OFDM system. Irrespective of whether windowing is applied at the transmitter or the receiver, the performance gains that have been achieved are not substantial and indeed if the transmission of additional samples is required, the performance is actually worse. However the computational burden

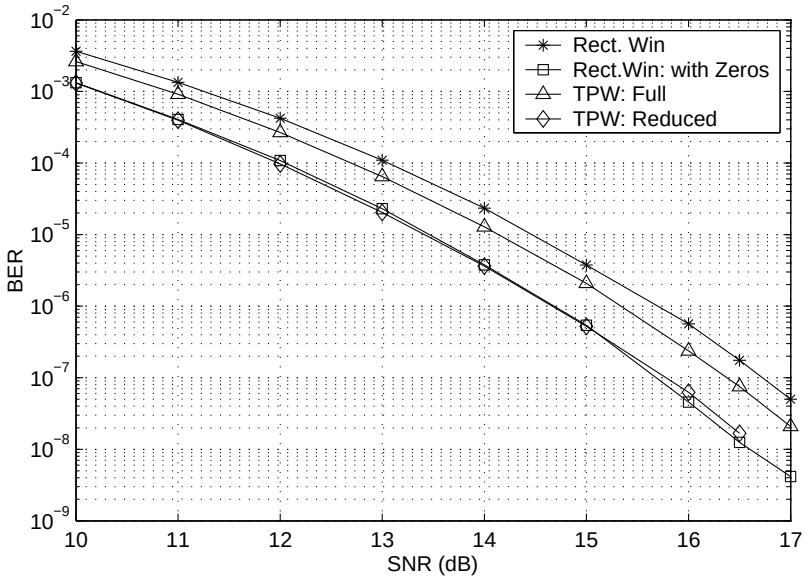

Figure 7.10: Effect of TPW at the transmitter for SUI-II channels for $\alpha = 0.25$

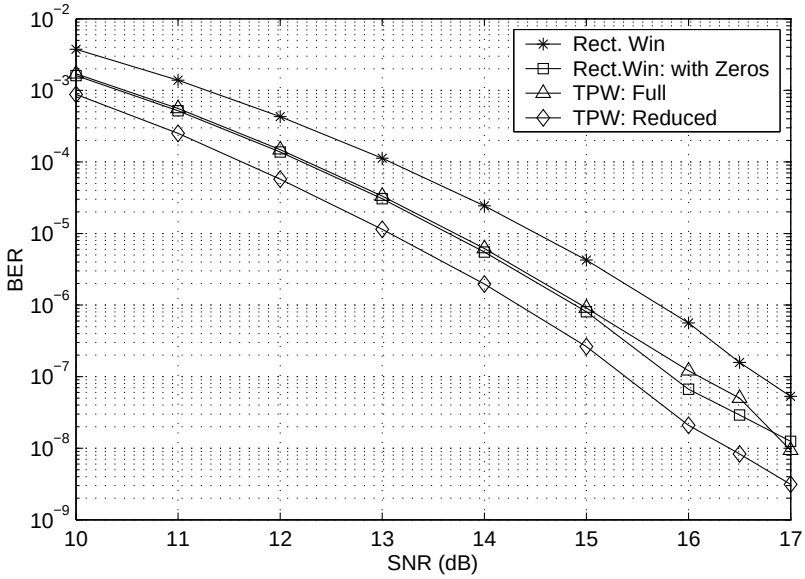

Figure 7.11: Effect of TPW at the transmitter for SUI-II channels for $\alpha = 0.5$

of the windowing process is relatively low and so it is proposed that windowing should only be used if there are uncorrupted samples within the Excess Length of the CP. If the terrain conditions are extremely good, which results in a very short CIR, there may be suitable uncorrupted samples available within the CP of the transmitted symbols. If the length of the CP is set according to a particular standard and cannot be reduced, windowing could be viable in these conditions.

Chapter 8

Conclusions and Future Work

In chapter 3 the effect of Phase Noise (PN) on the performance of coherent OFDM systems is analysed and is found to have a dual effect. Specifically, one component is found to rotate all the subchannels equally and gives rise to Common Phase Error (CPE) and the other which affects the orthogonality of the subchannel carriers giving rise to Inter-Carrier Interference (ICI). The chapter also derives an analytical result to estimate the Bit Error Rate (BER) when OFDM is subject to a particular level of AWGN and PN. Subsequent simulations show a close match with the analytical derivations. The PN mask, which describes the PSD of the PN process is also introduced and the shape of the PN mask that is selected for the simulation work is justified by comparison with the PSD of practical oscillators. The effect of PN on coherent OFDM systems subject to SUI-II channels is also analysed. An algorithm to correct the CPE component found to be present in coherent OFDM systems subject to PN is presented. The so called Common Phase Error Correction (CPEC) algorithm is entirely data driven and contains two correction factors, namely the CPE Symbol Estimate (CPESE) and the Feedback Correction Factor (FBCF). The CPESE is calculated for each demodulated OFDM symbol and previous CPESEs are used to generate the FBCF which tracks the CPE variation at the Frequency Domain Equaliser (FEQ). It has been shown via extensive simulation results that both components of the algorithm are necessary for optimum performance when applied to coherent OFDM systems in the BFWA scenario. The performance of the algorithm is tested via simulations and is also

compared against other CPEC algorithms. It is shown that the use of the algorithm will allow performance gains of up to 6 dB in terms of SPNR at a BER of 10^{-5} for a coherent OFDM systems with $N = 64$, a PN mask bandwidth of $f_h = 100$ kHz and a SNR of 20 dB in the SUI-II channel.

Chapter 4 analyses the effect of symbol (frame) offsets in OFDM. It is shown that symbol offset results in a distinct phase gradient that is seen across the demodulated subchannel outputs. It also introduces the symbol synchronisation function of the Schmidl and Cox Algorithm (SCA), which is shown to perform sub-optimally in a BFWA scenario. However the use of only two training symbols and the avoidance of pilot symbols in the SCA make it a strong contender for application to BFWA systems. The chapter also proposes an improved method for determining the Start of Frame (SOF) compared to the method originally proposed in [25]. The chapter also proposes a very robust symbol synchronisation algorithm, namely the Iterative Symbol Offset Correction Algorithm (ISOCA) that complements the symbol synchronisation function of the SCA. The ISOCA makes use of the phase gradient that occurs as a result of the symbol offset and has two functional parts. The ISOCA demonstrates an ability to obtain perfect symbol synchronisation in a system subject to a BFWA channel at reasonable values of SNR while maintaining a low probability of non-convergence at very low values of SNRs. This is a remarkable improvement considering that using the SCA alone yields a probability of only 0.48 of achieving perfect symbol synchronisation. The results are presented in a comprehensive manner to show the performance on completion of each part of the two-part algorithm. Simulation results are presented for both AWGN and SUI-II channels.

The effect of frequency offset on coherent OFDM systems is analysed in chapter 5. It is shown that the Carrier-to-Interference Ratio (CTIR) drops significantly even with a low relative frequency offset of 0.1. Again the SCA is selected because of its low level of computational complexity and its broad frequency offset acquisition range. The frequency offset function of the SCA is analysed in detail and it is found that the SCA, when used in a BFWA scenario, gives rise to a significant Residual Frequency Offset (RFO). To address this problem an algorithm to complement the frequency offset correction function of the SCA, namely the Residual Frequency Offset Correction Algorithm (RFOCA) is proposed. It is

important to note that the RFOCA is entirely data driven and is based on tracking the rotating phase of the demodulated OFDM symbols. The simulated results show that the RFO error variance can be reduced by several orders of magnitude compared to the values that are observed at the end of the acquisition stage of the SCA, for both AWGN and in the presence of SUI-II channels. Simulations have also been carried out which show that the performance of the RFOCA does not degrade even with a relative frequency offset that has an integer part. The presented simulation results show the performance of the RFOCA for various BFWA scenarios.

Chapter 6 introduced the concept of using a Time Domain Equaliser (TEQ) for OFDM systems in BFWA. The chapter first discusses different approaches to TEQ design with the emphasis on the Minimum Mean Squared Error (MMSE) criterion. An iterative method for training the TEQ which was first proposed for real data in [110], is modified for the case of complex data. This approach is known as the Dual Optimising Time Domain Equaliser (DOTEQ) since the adaptation is applied to both the Target Impulse Response (TIR) and the TEQ coefficients. However the algorithm only performs optimisation in the time domain, resulting in severe nulls being generated in the frequency domain of the Effective Impulse Response (EIR). A modified version of the DOTEQ is proposed, namely the Frequency Scaled Time Domain equaliser (FSTEQ), which in contrast optimises both in the time and the frequency domain. In this case the suitability of both the Least Mean Square (LMS) and the Recursive Least Square (RLS) algorithms for the adaptation of the FSTEQ is investigated. Comprehensive investigations are then performed concerning the FSTEQ in terms of a Z-plane analysis and also its computational complexity. Simulation results show that the FSTEQ improves the BER performance of OFDM by up to two orders of magnitude while still maintaining a superior rate of convergence compared to the original DOTEQ.

Chapter 7 investigated the use of window functions that adhere to the Nyquist criterion to shape the OFDM symbols. The length of the window function is made adaptive relative to the length of the CIR and it proposes to use the uncorrupted samples lying within the Excess Length of the Cyclic Prefix (CP) as the roll off samples. Consequently, the FFT window is shifted to include part of the CP. The phase change of the demodulated symbols that is a direct consequence of this op-

eration is corrected at the FEQ. It is seen that Trapezoidal Windowing (TPW) provides slightly better performance than Raised Cosine (RC) windowing in AWGN. In the first instance, the windowing operation is performed at the receiver. It is observed in this case that windowing provides very modest gains in the presence of AWGN and PN. The analysis and the simulation is then extended to the case where windowing is performed at the transmitter. To preserve orthogonality, zeros are transmitted at the beginning of the CP. However, if orthogonality is to be maintained at the receiver, the number of samples selected has to be greater than is the case when the windowing is performed at the receiver. It is found that for SUI-II channels, the noise enhancement caused by having to use a higher number of samples is greater than the interference it avoids in terms of ICI and ISI. It is recommended that windowing be applied to an OFDM system only if uncorrupted samples are available in the CP and if the specifications do not allow the CP of the OFDM system to be shortened.

8.1 Future Work

The investigations presented in this thesis are limited to coherent OFDM systems based on QPSK mapping. However, the novel algorithms proposed in this thesis could also be applied to other modulation schemes e.g. QAM. An investigation into the performance of such systems could be undertaken in the future. The channel model selected for use throughout this work is the SUI-II channel profile since this is representative of many typical environments where BFWA systems will be deployed. The performance of the proposed algorithms could be investigated for more hostile channels.

Chapter 3 proposes a CPEC algorithm that uses two functional elements, namely the CPESE and the FBCF to successfully correct the CPE component of PN in a coherent OFDM system. However, further investigation could be carried out to determine, both analytically and via simulations, the exact contributions made by each of these components. The channel selection criteria used prior to the calculation of the CPESE and the FBCF is currently to select those subchannels whose gain is a standard deviation above the mean. The same channel selection criterion is also adopted in chapters 4 and 5. However, since the SUI-II channel is not too

hostile, the selection criteria does not significantly affect the overall performance. However, for more difficult channels a different approach to subchannel selection may have to be adopted. Also the performance of the CPEC algorithm proposed in this work can be compared against a CPEC algorithm that is based on pilot tone.

The ISOCA that is proposed in chapter 4 shows a very small probability of non-convergence at very low SNR levels. Further investigations could be carried out to try to reduce this already low probability.

The RFOCA that is proposed in chapter 5 is shown to suffer from a threshold effect at low values of SNR owing to the triggering of the phase unwrapping algorithm by spurious noise. Future work could be carried out to modify the unwrapping algorithm to avoid this phenomenon. It has also been observed that the residual frequency offset values become very small particularly after a few iterations of the RFOCA. Consequently, the number of OFDM symbols that need to be buffered before each iteration is in the order of 100 to achieve good performance. This increases the memory requirements and hence the latency of the overall system. Further investigations could focus on reducing the number of symbols that need to be buffered. A possibility is that the algorithm could be made adaptive in terms of the buffer size and also determining when the phase unwrapping algorithm should be triggered.

The FSTEQ presented in chapter 6 requires an FFT and an IFFT operation at each iteration in order to scale the Target Transfer Function (TTF). This places a high computational burden on the receiver. This is a limitation to the practical application of the FSTEQ. The FFT/IFFT operations could be made adaptive so that they are only performed after a certain number of iterations depending upon the rate of convergence and the Channel Impulse Response (CIR). Even though the two thresholds that need to be calculated do not dramatically affect the performance of the FSTEQ, the proposed method requires knowledge of the power delay profile of the CIR. Also it is seen that the actual initial Target Impulse Response (TIR) selected determines the speed of convergence of the equaliser. In this proposal a profile having a faster decay rate than the CIR is used as the initial TIR. It is possible that the selection of the initial TIR could be obtained in a more optimum manner. Also the performance of FSTEQ can be compared against

Multiple-Output-Multiple-Input (MIMO) OFDM systems.

Chapter 7 discussed the use of Time Domain Windowing (TDW), both at the transmitter and at the receiver. If all samples of the CP are used for windowing, rather than being limited to those samples within the excess length, it will certainly introduce interference in terms of ICI and ISI. Investigations could be carried out to determine the performance trade-off available between reducing input thermal noise compared to the additional ISI and ICI introduced. Also the analysis in chapter 7 is limited to windowing in the presence of AWGN and PN. This could be extended to encompass frequency offsets.

Throughout the thesis, various impairments to OFDM systems are treated in isolation and algorithms are presented to counter these effects. Investigations could also be carried out to find the optimum parameters for the situation where combinations of these algorithms are applied to a complete system.

All results presented in the thesis were obtained based on computer simulations. In general, ideal conditions were assumed and possible implementation impairments such as I-Q imbalance, DC offsets, Automatic Gain Control (AGC) errors and quantisation effects were ignored. Prior to implementing the algorithms proposed in this thesis it would be prudent to determine how these practical considerations impact the performance.

Finally, the initial work undertaken concerning the use of MLSE for per-subchannel equalisation presented in appendix C could be extended to address areas such as complexity reduction and performance in BFWA channels.

Appendix A

Complex Baseband Representation

In this appendix the complex baseband representation of modulated signals is introduced very briefly. A latter section will introduce the Power Spectral Density (PSD) of stochastic processes. Any real modulated signal can be represented as,

$$s(t) = a(t)\cos(\omega_c t + \phi(t)) \tag{A.1}$$

where, t is the representation of time, ω_c is the carrier frequency and $a(t)$ and $\phi(t)$ are the time varying amplitude and phase of the signal. Now, the $\cos$ term in (A.1) can be represented as a real part of a complex signal. Hence,

$$\begin{aligned} s(t) &= \Re[a(t)\, e^{j(\omega_c t+\phi(t))}] \\ &= \Re[p(t)\, e^{j(\omega_c t)}] \end{aligned} \tag{A.2}$$

where,

$$p(t) = a(t)\, e^{j\phi(t)}\ . \tag{A.3}$$

This is known as the *complex baseband* equivalent of the modulated signal. It is also known as the 'lowpass equivalent' or the 'phasor representation'. Note that $p(t)$ is devoid of the effects of carrier frequency [27, pg155]. Analysis of the modulated signals in the complex baseband domain will require less computational power. Therefore all simulations presented in this thesis are performed in the complex baseband domain. The signal in (A.3) is in general complex and can

be written as

$$p(t) = s_i(t) + js_q(t) \tag{A.4}$$

where,

$$\begin{aligned} s_i(t) &= a(t)\cos(\phi(t)) \\ s_q(t) &= a(t)\sin(\phi(t)) \end{aligned} \tag{A.5}$$

also, substituting (A.4) in (A.2) yields,

$$s(t) = s_i(t)\cos(\omega_c t) - s_q(t)\sin(\omega_c t)\ . \tag{A.6}$$

A.1 Spectra of Signals

Let us consider the real, unmodulated carrier signal, $s_c(t) = \cos(\omega_c t)$. Note that it is preferred to have the frequency scale in Hz rather than rad/s when representing spectra, hence a *one-sided* spectrum of $s_c(t)$ would show a non-zero value of power at frequency $f = f_c$, where $f_c = \omega_c/2\pi$. In such a spectrum, frequencies are considered to be purely positive. However it is convenient to represent signals in terms of complex exponentials or phasors. To represent a real cosinusoidal signal using Fourier theory, two complex exponential (or phasor) terms are required, that is one phasor rotates anti-clockwise (known as the positive frequency) and the other clockwise (known as the negative frequency). Equivalently, we can show that the Fourier Transform (FT) of $s_c(t)$ is,

$$S_c(\omega) = \mathcal{F}\{s_c(t)\} = \frac{1}{2}[\delta(\omega - \omega_c) + \delta(\omega + \omega_c)] \tag{A.7}$$

Note the representation of (A.7) has two non zero components, at $f = f_c$ and $f = -f_c$. As mentioned previously, the latter component is known as the negative frequency component. Since the spectrum of (A.7) has both positive and negative frequencies, we call such a representation a *two-sided* spectrum of $s_c(t)$.

It is interesting to note the relationship between the spectra of the modulated signal, $s(t)$ and the complex baseband representation, $p(t)$. Equation (A.2) can be

represented as,

$$s(t) = \Re[p(t)\, e^{j\omega_c(t)}] = \frac{1}{2}[p(t)\, e^{j\omega_c(t)} + p^*(t)\, e^{-j\omega_c(t)}]\,. \tag{A.8}$$

If the FT of $p(t)$ is given by $P(\omega)$, then FT of $p^*(t)$ is given by $P^*(-\omega)$. Consequently,

$$S(\omega) = \mathcal{F}\{s(t)\} = \frac{1}{2}[P(\omega - \omega_c) + P^*(-(\omega - \omega_c))]\,. \tag{A.9}$$

Equation (A.9) reveals that if $P(\omega)$ is sufficiently narrowband relative to ω_c, then $S(\omega)$ comprises of $P(\omega)$ shifted to ω_c and the conjugated, reversed version of $P(\omega)$ shifted to $-\omega_c$ [148]. Figure A.1 shows the relationship between $P(\omega)$ and $S(\omega)$ with the two-sided bandwidth of $P(\omega)$ being B. Note that the amplitude A in the $P(\omega)$ is halved in $S(\omega)$.

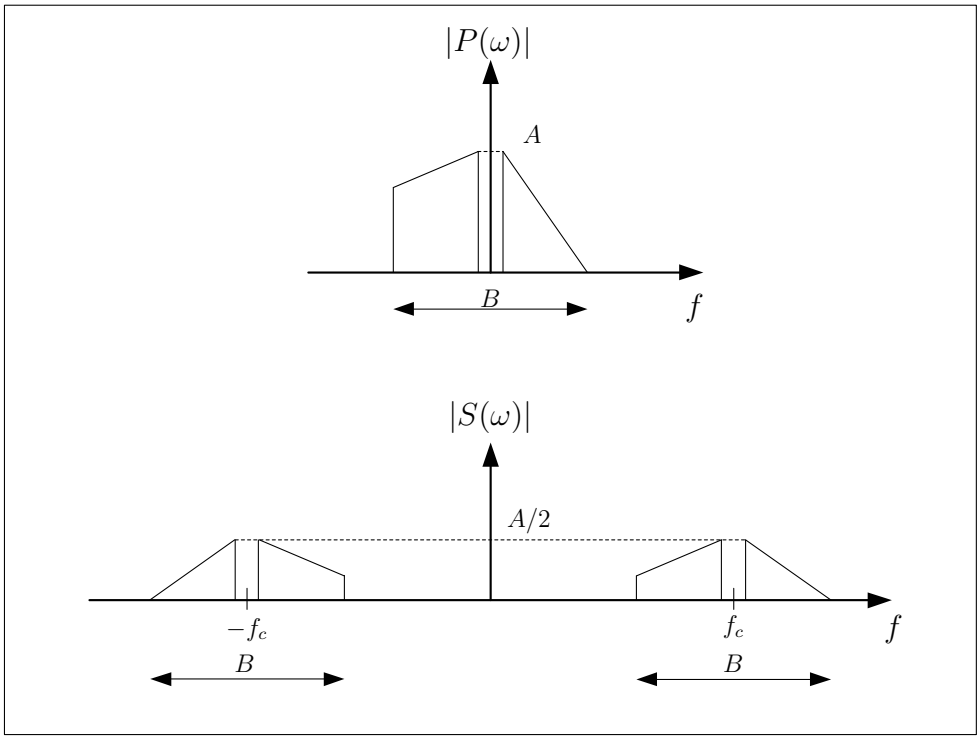

Figure A.1: Comparison of $P(\omega)$ and $S(\omega)$

A similar analysis can be performed on AWGN. Real, bandlimited AWGN $w_c(t)$ can be represented in terms of complex baseband equivalent, $w(t)$

$$w_c(t) = \Re[w(t)e^{j\omega_c t}] \tag{A.10}$$

where,

$$w(t) = [w_i(t) + w_q(t)]e^{j\phi_w} \ . \tag{A.11}$$

Here, $w_i(t)$ and $w_q(t)$ are real uncorrelated, independent noise waveforms. ϕ_w is an arbitrary constant.

A.2 Power Spectral Density

A stationary stochastic process is an infinite energy signal and, hence, its FT does not exist [27, pg67]. The spectral characteristics of a stochastic signal are obtained by computing the FT of the Autocorrelation Function (ACF). This is known as the Power Spectral Density (PSD). For a random process X_t, (here, t shows the relationship with time), the ACF is defined as,

$$E(X_{t1}X_{t2}) = \int_{\infty}^{\infty}\int_{\infty}^{\infty} x_{t1}x_{t2}p(x_{t1}, x_{t2}) \quad dx_{t1}d_{x2} \tag{A.12}$$

where, $E(.)$ is the expectation operator, x_{t1} and x_{t2} are samples drawn from X_t at time $t1$ and $t2$, and $p(.)$ is the joint probability between the two samples. For a *stationary* process,

$$E(X_{t1}X_{t2}) = \psi(t1, t2) = \psi(t1 - t2) = \psi(\tau) \ . \tag{A.13}$$

In other words, for a stationary signal the ACF depends on the time difference, τ and not the exact values of time. Hence, the PSD of a stationary stochastic signal is given by [27, pg67],

$$\Psi(f) = \int_{\infty}^{\infty} \psi(\tau)e^{-j2\pi f\tau} \quad d\tau \ . \tag{A.14}$$

The inverse Fourier relationship is given by,

$$\psi(f) = \int_{\infty}^{\infty} \Psi(\tau) e^{j2\pi f\tau} \quad df \; . \tag{A.15}$$

The PSD is the distribution of power of the stochastic process as a function of frequency. Hence the units of the PSD are W/Hz. Also note that the area under the PSD is equal to the average power of the signal [27, pg67]. The PSD is very important in understanding the characteristics of the stochastic process. For instance, AWGN will have equal power across all frequencies, hence the PSD of AWGN is flat. This is in contrast to Phase Noise (PN) where the power density closer to zero frequency is greater than at higher frequencies.

Appendix B

Channel Models

Accurate channel modelling is essential for the realistic and successful simulation of communication systems. A review of channel models will now be undertaken. The statistics of the received power level can be divided into large-scale and small-scale effects [149]. The local mean of the received signal power is affected by effects such as Line of Sight (LOS) path loss and shadowing. The signal envelope undergoes rapid fluctuations due to multipath propagation and movement of the receiver or transmitter antenna, which in turn cause small-scale effects. The proposed work is based on data transmission at high rates, so it is prudent to discuss issues such as the delay spread and Doppler spread, which severely limit the data rate.

B.1 Large-Scale Variations of the Signal Envelope

These issues will now be discussed below

B.1.1 Free Space Propagation

We begin with a description of radio propagation in a single-path free space channel. In free space, the relationship between the transmitted power P_t and the

received power P_r is given by,

$$P_r = P_t G_t G_r \left(\frac{\lambda}{4\pi d}\right)^2 = \frac{P_0}{d^2} \tag{B.1}$$

where G_t and G_r are the transmitter and receiver antenna gains respectively, and d is the distance between the transmit and the receive antennas, $\lambda = c/f$ is the wavelength of the transmitted signal and c is the velocity of radio wave propagation in free space. Defining $P_0 = P_t G_t G_r (\lambda/4\pi)^2$, it can be seen that over a single path, the received signal power reduces with the square of the distance.

B.1.2 Two Ray Model

The most simple multipath propagation models is one with a single direct path and a single strong reflected path, often from the ground. In general if we assume a single sinusoid is transmitted, the received signal power with L received paths is given by,

$$P_r = P_0 \left| \sum_{i=1}^{L} \frac{a_i}{d_i} e^{j\phi_i} \right|^2 \tag{B.2}$$

where, a_i, d_i and ϕ_i are the reflection coefficient, the distance travelled by and the received phase respectively of the ith path. Figure 5.1 depicts a possible two-path scenario with the height of the transmitter and the receiver antennas being h_1 and h_2, respectively. If we assume the distance between the two ends, d to be much greater than the antenna heights, and that the ground reflection coefficient is -1, then the received power can be approximated as

$$P_r \cong \frac{P_0}{d^2} \left| 1 - e^{j\Delta\phi} \right|^2 \tag{B.3}$$

where $\Delta\phi$ is the phase difference between the two paths. Using the same assumption the difference between the two paths can be approximated as,

$$\Delta d = \frac{2h_1 h_2}{d} \tag{B.4}$$

and hence

$$\Delta\phi = \frac{2\pi}{\lambda} \times \frac{2h_1 h_2}{d} \tag{B.5}$$

for small values of $\Delta\phi$, we have,

$$\left|1 - e^{j\phi}\right| \cong |1 - (1 - j\Delta\phi)| = |\Delta\phi| \ . \tag{B.6}$$

Hence

$$P_r = \frac{P_0}{d^2}\left(\frac{2\pi}{\lambda}\right)^2 \times \frac{4h_1^2 h_2^2}{d^2} \tag{B.7}$$

Note the exponent of the distance-power relationship is increased to four. In general the received power as a function of the distance d from the transmitter is proportional to d^{-n}, where n is the *path loss exponent*. The value for n is 2 for free space, 1.6 to 1.8 for indoor line of sight, 4 to 6 for obstructed indoor, 2.7 to 3.5 for urban cellular radio and 3 to 5 for shadowed urban cellular [149]. Many of these values are found empirically from propagation measurements.

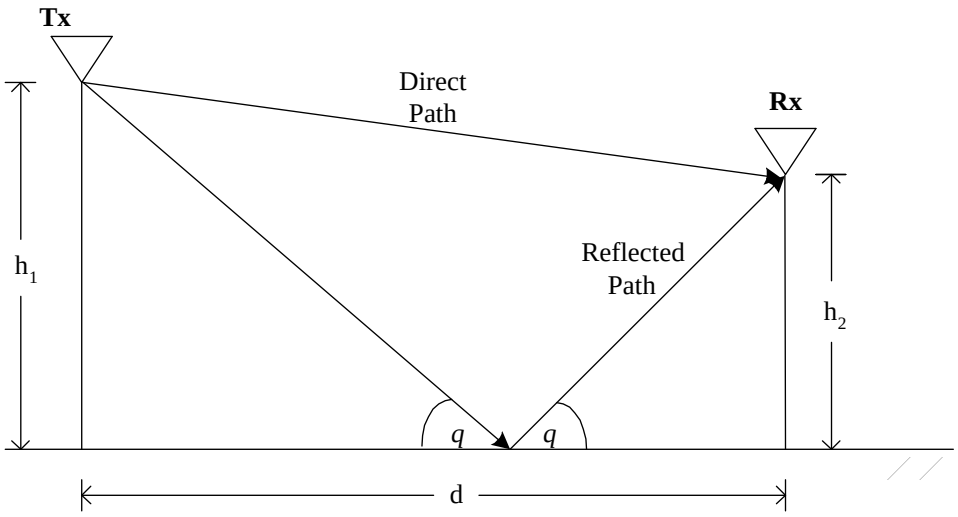

Figure B.1: Two-ray model

B.1.3 Log-Normal Shadowing

The local mean in a particular area also experiences some additional variation about its average caused by the presence of obstructions in the transmission path. At a particular location at distance d from the transmitter, the local mean received power, s can be modelled as a log-normal distribution around the mean of all locations $\bar{s}$, given by

$$p(s) = \frac{1}{\sigma\sqrt{2\pi}} \exp\left[\frac{-(s-\bar{s})^2}{2\sigma^2}\right] . \tag{B.8}$$

B.2 Small-scale Variations of the Signal Envelope

The signal envelope can have extreme variations over a short distance of about half a wavelength or over a short period of time owing to constructive or destructive interference between signals arriving via paths with different/varying lengths.

B.2.1 AWGN Channel

The Additive White Gaussian Noise (AWGN) channel is the simplest model which effectively only accounts for impairments owing to the thermal noise at the receiver. Usually performance in the AWGN channel is used as a benchmarker for comparison of performance achieved in other channels. The received constellation points are spread over the region with a pattern equivalent to a Gaussian distribution function. It is evident that as the variance is increased, the probability of a transmitted constellation point falling onto the 'wrong side' of the decision threshold increases dramatically, thus increasing the Bit Error Rate (BER).

B.2.2 Multipath Channel

Multiple copies of the transmitted signal can arrive at the receiver antenna delayed in time and with varying amplitudes due conditions such as reflections, refractions and scattering. The receiver will experience a superposition of all such copies. To model a specific case very accurate knowledge of the characteristics of each

reflector, its position and its mobility is required. Since this data is usually unavailable, an accepted approximation is the multipath delay line channel model. A time varying Channel Impulse Response (CIR) can be modelled as,

$$h(\tau, t) = A_0 \sum_{i=1}^{L} \frac{a_i(t)}{d_i} e^{j\phi_i(t)} \delta(t - \tau_i) \; . \tag{B.9}$$

Assuming a stationary CIR,

$$h(\tau) = A_0 \sum_{i=1}^{L} \frac{a_i}{d_i} e^{j\phi_i} \delta(t - \tau_i) \tag{B.10}$$

where the notations are as (B.2) with $A_0 = \sqrt{P_0}$. If we assume $\beta_i = A_0 a_i / d_i$, we have,

$$h(\tau) = \sum_{i=1}^{L} \beta_i e^{j\phi_i} \delta(t - \tau_i) \; . \tag{B.11}$$

The output of the channel neglecting noise is,

$$r(t) = \sum_{i=1}^{L} \beta_i e^{j\phi_i} s(t - \tau_i) \tag{B.12}$$

where, $s(t)$ is the transmitted data sequence. The equation (B.12) is used for statistical modelling of both indoor and outdoor radio propagation using the tapped delay model shown in figure B.2. The tap gains depend on the rate of fluctuation, the modelling of which will be discussed later. The phase is usually taken as having a uniform distribution between [0, 2π] radians. Often the assumption of *wide-sense stationary uncorrelated scattering* (WSSUS) is used. The first and second order statistics are invariant in time and frequency in a WSSUS channel [150]. The physical meaning of the channels is that signal variations on paths arriving at different delays are uncorrelated and the correlation properties of the channel are stationary. Thus the amplitudes of the tap gains can be generated independently as long as they conform to the assumed probability density function.

In order to assess the performance of various wireless systems it is necessary to have a convenient numerical measure of the *multipath delay spread*. The dif-

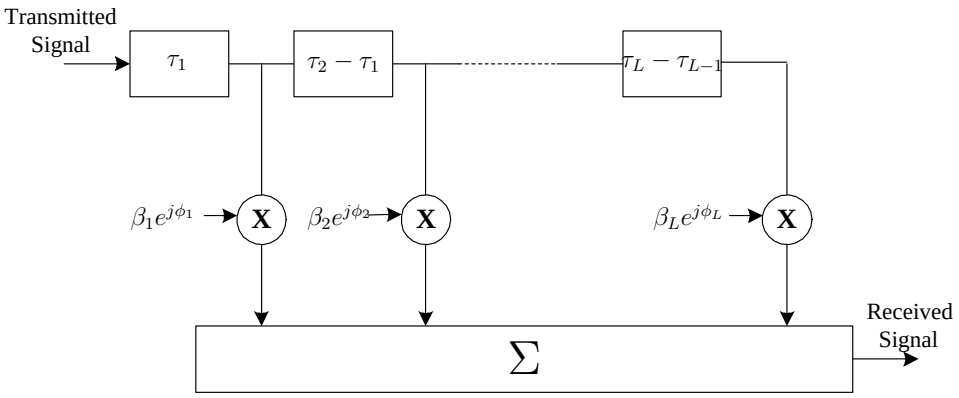

Figure B.2: Tapped delay line channel model

ference between the earliest and the latest arrival is termed as *excess delay spread*. Since the received signal is often a continuum, this measure is often defined as the time taken for the delay spread to fall below a particular level (typically 20 or 30 dB) below the strongest path. However this is not a good indicator as different channels with the same excess delay spreads can have different profiles. A better indicator is the *rms delay spread*, which is the second central moment of the channel impulse response. For a carrier frequency of about 900 MHz, the rms delay spread is of the order from 1.3 to 25 μs in an urban environment, 200 to 2110 ns in a suburban environment and 10 to 1470 ns in a indoor environments [149]. It is defined in [151] as,

$$\tau_{RMS} = \sqrt{\overline{\tau^2} - (\bar{\tau})^2} \tag{B.13}$$

where,

$$\overline{\tau^n} = \frac{\sum_i^L \tau_i^n (\beta_i)^2}{\sum_i^L (\beta_i)^2}, \quad \text{with } n = 1, 2\,. \tag{B.14}$$

For reliable digital transmission, the symbol duration should be much longer than the rms delay spread. Another parameter that is associated with the multipath delay spread is the *coherence bandwidth*, which is the inverse of a certain percentage of the rms delay spread. It is the measure of the range of frequencies over which the signal of a certain frequency shows a high degree (usually 90%) of correlation with a signal of another frequency. It is obvious that the transmitted signal bandwidth should be much less than the coherence bandwidth to avoid

distortion. If it is greater than the coherence bandwidth, the channel is termed as *frequency selective*. Such systems have to rely on equalisation to avoid the effects of significant variations in frequency response.

B.2.3 Distribution of Signal Envelope

When there are several paths of approximately equal power arriving at the receiver, the signal envelope can be modelled as a Rayleigh distribution with the Probability Density Function (PDF),

$$p(r) = \frac{r}{\sigma^2} \exp\left[\frac{-r^2}{2\sigma^2}\right], \quad 0 \leq r \leq \infty \tag{B.15}$$

where σ is the rms value of the received signal voltage. The mean of the distribution is $\sigma\sqrt{\pi/2}$ and the variance is $\sigma^2(2-\pi/2)$. If the signal has a strong LOS path, the signal envelope is modelled using the Rician PDF given by,

$$p(r) = \frac{r}{\sigma^2} \exp\left[\frac{-(r^2+A^2)}{2\sigma^2}\right] I_0\left(\frac{Ar}{\sigma^2}\right), \quad A \geq 0 \text{ and } r \geq 0 \tag{B.16}$$

here $I_0(.)$ is the modified Bessel function of the first kind and A is the amplitude of the dominant component. When modelling assuming the WSSUS frequency selective channel, the amplitudes of the tapped delay line are selected independently using a Rayleigh distribution with the required parameters. For a Rician distribution, an additional constant term is added to the delay line output. Other distributions that are used in practise are, the Suzuki, the Weibull and the Nakagami distributions. These are used mainly for the modelling of envelope fading in indoor and urban radio channels. These distributions have the disadvantage of having complicated mathematical forms, which limit the use of them practically.

B.2.4 Local Movements and Doppler Shifts

It is well known that whenever the transmitter and the receiver antennas are in relative motion, the received carrier frequency is shifted relative to the transmitted

one. This is known as the Doppler effect. If the transmitter and the receiver are stationary and the distance between two terminals is d_o, the received signal is represented by,

$$r(t) = \Re[A_r e^{j2\pi f_c(t-\tau_0)}] \tag{B.17}$$

where $\tau_0 = d_0/c$ is the time required for the radio wave to travel between the terminals at a velocity of c. Now, assuming one of the terminals travels toward the other at a speed of v_m, then the propagation time will change with time as,

$$\tau(t) = \frac{d(t)}{c} = \frac{d_0 - v_m t}{c} = \tau_0 - \frac{v_m}{c} t \, . \tag{B.18}$$

Then the received signal will be,

$$r(t) = \Re[A_r e^{j2\pi f_c(t-\tau(t))}] = \Re[A_r e^{j[2\pi(f_c+f_d)t-\phi]}] \tag{B.19}$$

where $\phi = 2\pi f_c \tau_0$ is a constant and

$$f_d = \frac{v_m}{c} f_c = \frac{v_m}{\lambda} \tag{B.20}$$

is known as the *Doppler frequency shift*. Note the maximum Doppler frequency shift can occur when either the transmitter or the receiver is moving directly toward or away from the other. If the receiver is moving directly towards the wave, then the apparent frequency would be $f_c + f_d$, and if it is moving away, the apparent frequency is $f_c - f_d$. A vehicle travelling at the speed of 126 km/h (35 m/s) will be subjected to a Doppler shift of 233 Hz at a carrier frequency of 2 GHz, whereas a pedestrian walking at a typical speed of 1.25m/s will be subjected to a Doppler shift of only 8.3 Hz at the same carrier frequency.

Assuming that the arrival angles of each path are uniformly distributed in [0, 2π], then the Doppler shift at a given azimuth angle θ is given by $f(\theta) = f_m \cos(\theta)$, where f_m is the maximum Doppler shift given in (B.20). Then the Doppler power spectrum is given by,

$$D(f) = \frac{1}{2\pi f_m} \left[1 - \left(\frac{f - f_c}{f_m} \right)^2 \right]^{-1/2} \qquad |f - f_c| \leq f_m \, . \tag{B.21}$$

Such a spectrum rises to two high peaks at the edge frequencies of $f_c \pm f_m$ [150] and has been confirmed by practical signal measurements. Figure B.3 shows the typical Doppler spread of Rayleigh and Rician distributed envelopes. Note the impulse in the Rician channel due to the dominant path. From equation (B.21), it is evident that if f_m is very small, the received spectrum will undergo little spreading and will have little effect on the received signal. The *Doppler bandwidth* is defined as twice the maximum Doppler shift. If the signal has a bandwidth much larger than the Doppler bandwidth, the signal will experience little effect from Doppler shifts. *Coherence time* is defined as the time over which the signal remains relatively constant. In other words, time duration over which the samples remain fairly correlated. Hence to maintain correlation between samples and avoid distortion, the symbol duration of the signal should be less than the coherence time. The coherence time is inversely proportional to the Doppler bandwidth.

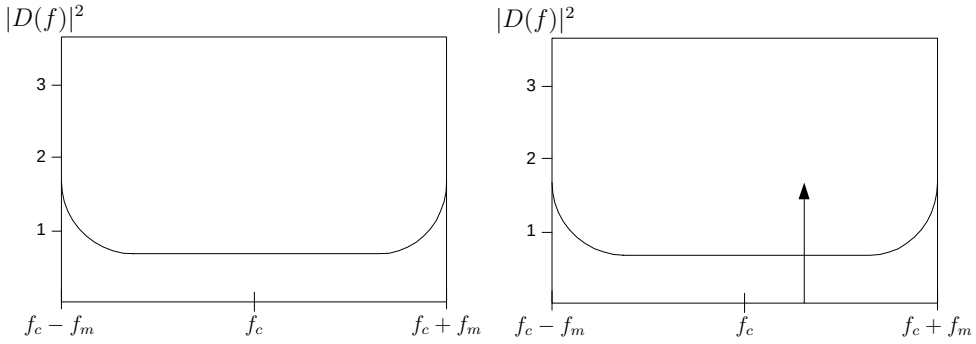

Figure B.3: Typical Doppler spectra for Rayleigh (left) and Rician (right) distributed mobile channels

B.3 Stanford University Interim Channel Models

Accurate channel models for the Broadband Fixed Wireless Applications were still being discussed while the research presented by this thesis was being undertaken. At the time the Stanford University Interim (SUI) channel models presented for the IEEE 802.16 Broadband Wireless Access Working Group [23] were achieving widespread acceptance. The Point to Point (PTP) and the Point to Mul-

tipoint (PMP) systems considered for the BFWA systems in this research are associated with highly directional antennas at the Base Station (BTS), and near Line of Sight (LOS) conditions. Trials have shown that microwave propagation in the MMDS band with directional and omni-directional antennas will provide a channel with maximum delay spread that is well under 1 μs [152]. Consequently the CIR is not hostile. Typical scenarios for the SUI channel models are very similar. Some of the conditions are,

- Cell size radius: 6.4 km (4 miles)
- BTS antenna height: 17 m (50 ft)
- Receive antenna height: 3 m (10 ft)
- BTS antenna beamwidth: 120°
- Receive antenna beamwidth: Omnidirectional (360°) and 30°
- Vertical Polarisation only

Six channel models are proposed in total with two for each of the three terrain conditions. Category A has the maximum path loss associated with hilly terrains with moderate to heavy tree densities. Category C has the minimum path loss and is associated with mostly flat terrain with light tree densities. Category B is defined for intermediate conditions. Out of the 6 models, the SUI -II channel model with an Omnidirectional receiver antenna was selected as the standard CIR model for all the simulations undertaken in this work. Owing to the time required to perform each simulation, the algorithms presented have not been tested using other channel models. The characteristics of the SUI-II channel model are given in the table B.1

The sampling frequencies considered for the simulated systems in this work are 20MHz or higher. The transmitted frames have a maximum of 2500 OFDM symbols. Hence the time taken to transmit each frame is approximately 10 ms. As noted in table B.1, the Doppler frequencies are significantly low and consequently it is assumed that the channel remains static throughout each transmitted data frame. Channel Estimation is performed at the beginning of each frame using

	Tap1	**Tap2**	**Tap3**	**Units**
Delay	0	0.5	1	μs
Power (Omni ant.)	0	-12	-15	dB
Power (30° **ant.)**	0	-18	-27	dB
K factor	10	0	0	
Doppler$*$	0.4	0.4	0.4	Hz
Terrain Type: C, overall K = 5 (linear) RMS delay spread for Omnidirectional antennas: 0.2 μs. $*$ Rounded Doppler spectrum, maximum frequency				

Table B.1: SUI-II channel profile

the training symbol, which is used to initialise the FEQ coefficients. The FEQ coefficients are held static throughout the frame. For each new transmitted frame, a new realisation of a SUI-II channel is applied and the FEQ is updated accordingly.

Appendix C

Equalisation in FMT Modulation

A different approach to limiting the interference between subchannels in a parallel modulation scheme is to use per-subchannel filtering. One such system is known as Filtered Multitone (FMT) [26]. By relaxing orthogonality between subchannels their spectra can be designed to have much higher roll off levels in the frequency domain. The non-orthogonality will introduce Inter Symbol Interference (ISI) into the system, which has to be equalised using per-subchannel equalisation but owing to its rapid roll-off in the frequency domain, the system is subjected to low levels of Inter Channel Interference (ICI). Much of the previous work has proposed the use of Decision Feedback Equalisers (DFE) for per-subchannel equalisation. Usually the application considered is for high-speed DSLs rather than BFWA. The use of equalisation dramatically increases the complexity of the receiver. The author has investigated the use of Maximum Likelihood Sequence Estimators (MLSE) for the per-subchannel equalisation of FMT systems to gauge the performance limits for this approach. Undoubtedly, this further increases the complexity, but the author's goal is to find the practical performance limits of the system and compare it with that of a conventional OFDM systems.

The appendix is organised as follows. Section C.1 gives a brief introduction to subband systems. Since this area of research is quite diverse, this section is kept relatively short and concentrates only on the issues that relate to FMT. Section C.2 introduces the FMT modulation technique including different implementations of FMT and pointing out that the ISI caused by non-orthogonal filters is a major con-

cern. It then introduces various contributions concerning FMT, particularly ones that address wireless systems. Section C.3 shows the simulation results which concentrate upon the performance of MLSE based detection of FMT in comparison with that achieved by DFE based per-subchannel equalisation. Finally section C.4 draws some conclusions.

C.1 A Brief Introduction to Subband Systems

FMT modulation has its roots in Multirate systems for example, digital filters and Wavelet decomposition [153, 154]. This is a very rich and diverse area of research and consequently the focus will be on those areas relevant to FMT. In many applications such as audio and image coding, most of the energy in the information sequence is concentrated at low frequencies. Hence when it comes to source compression greater resolution can be given to high-energy bands if the information sequence can be separated into subbands in the frequency domain by the use of bandpass filters. Appropriate processing can then be performed separately in each band.

In an N-band decomposition with equal bandwidth filters, the subband signals will have a bandwidth approximately equal to π/N. Hence each subband signal can be subsampled by a factor of N, i.e. only one out of every N samples is retained. This process is known as *decimation* and it overcomes the problem of information growth. Since the bandpass filters are not expected to be ideal brick wall filters, the decimation process introduces aliasing. Aliasing is just one of the issues that has to be dealt with in subband coding. At the reconstruction level, the sampling rate of the processed signal has to be increased by a factor of N in order to retrieve the original signal. This process is known as *interpolation*. The term Multirate System is associated with such a system as it operates at a number of sample rates.

Figure C.1 shows a block diagram of a subband processing system. $H_0(z)$ to $H_{N-1}(z)$ represent the transfer functions of the so called decomposition or analysis filters, while $F_0(z)$ to $F_{N-1}(z)$ represent the transfer functions of the reconstruction or synthesis filters. The decimation and interpolation functions (by a factor of N) are represented by the symbols $\downarrow$N and the $\uparrow$N, respectively. The

subband signals $X_0(m)$ to $X_{N-1}(m)$ are obtained after decimating the outputs of the analysis filters. The reconstructed signal $\hat{x}(n)$ is obtained by adding together all outputs of all the synthesis filters.

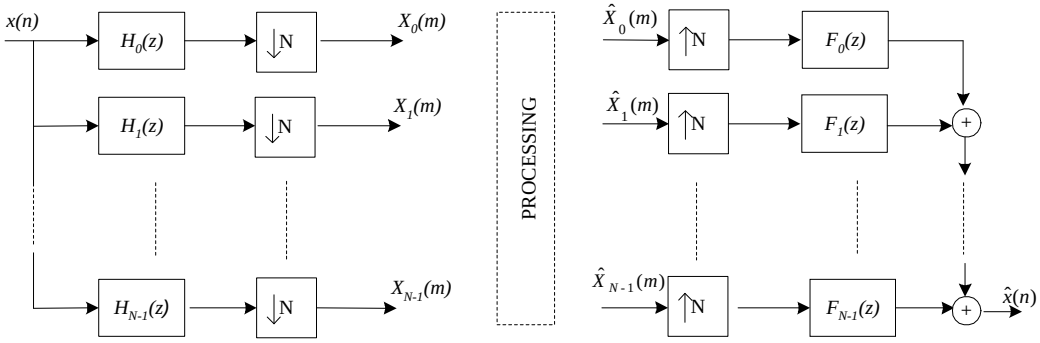

Figure C.1: Block diagram of a subband system

Ideally the subband system should have good signal reconstruction. If the subband signals are not modified during processing, the output of the synthesis filter bank should be equal to the input signal. That is $\hat{x}(n) = x(n - D)$, where D is an acceptable processing delay introduced by the filters. Hence the only modifications to the signal should be due to any processing which takes place in the subbands and not due to the filters. Such a system is known as a *perfect reconstruction* (PR) filter bank. It can be shown that the PR condition is satisfied if and only if [153]

$$\sum_{k=0}^{N-1} \sum_{m=-\infty}^{\infty} f_k(n - mN) h_k(mN - l) = \delta(n - l - D) \tag{C.1}$$

where $\delta(.)$ is the Kronecker delta function and $h_i(n)$ and $f_k(n)$ are the impulse responses of the analysis and synthesis filters, respectively. However designing realisable filters which satisfy equation (C.1) is far from a trivial task. It can be shown that if the analysis and synthesis filters are ideal bandpass filters, then the condition of (C.1) will be satisfied. Therefore by designing good bandpass Finite Impulse Response (FIR) filters, using the window approach for example, permits a close approximate to the PR condition to be made. FIR filters can be designed to have linear phase. If all channels are forced to have the same delay, then the

overall subband system will have no phase distortion, and so uncancelled aliasing leads only to amplitude distortion. Hence FIR filters are used more frequently in subband coding systems.

C.1.1 Polyphase Decomposition

Polyphase components appear very commonly in the analysis of the multirate signal processing systems. The polyphase components are formed by selecting all indices, which are identical modulo N. That is the kth polyphase component $h^k(m)$ is formed by passing the impulse response $h(n)$ though a delay z^{-k} and a $N:1$ decimator. If $H^k(z)$ is the z-transform of the kth polyphase $h^k(m)$, it can be shown that,

$$H(z) = \sum_{k=0}^{N-1} z^{-k} H^k(z^N) \, . \tag{C.2}$$

C.1.2 Transmultiplexers

Transmultiplexers were first designed in the 1970s for the conversion between the older Frequency Division Multiplex (FDM) based telephony systems to new Time Division Multiplex (TDM) based systems employing Pulse Code Modulation (PCM) [155]. TDM-to-FDM transition was done by upsampling (which created spectral images) followed by bandpass filters, which selected one of the bands. The primary concerns in transmultiplexer design are distortion and *crosstalk*. Distortion refers to any changes that are introduced by the filtering and crosstalk refers to the leakage from one channel to another. FIR filters of orders exceeding 2000 were required to reduce crosstalk to acceptable levels. However the use of polyphase network based filter banks made the implementation practical. Vetterli [156] showed that the transmultiplexer is the dual of the maximally-decimated filter bank and that crosstalk is the dual of the aliasing. This relationship allows the results applying to filter banks to be used for transmultiplexers. More specifically, the PR conditions can be used in the form of crosstalk cancellation. However sampling must be synchronised at both ends and as a result, a timing signal may have to be sent along with the transmitted signal.

C.1.3 Overlapped Basis Functions

All block transforms, such as the DFT and the Discrete Cosine Transform (DCT) with a transform matrix of size $N \times N$ are characterised by an input vector of length N. Thus if $\underline{x}$ is an input vector of length N, transformation is obtained by the applying the transformation matrix $\mathbf{A}^T$ as given by

$$\underline{X} = \mathbf{A}^T \underline{x} \tag{C.3}$$

where T here denotes complex transposition. The original signal can be obtained using

$$\underline{x} = [\mathbf{A}^T]^{-1} \underline{X} \,. \tag{C.4}$$

If $\mathbf{A}^T = \mathbf{A}^{-1}$ then $\mathbf{A}$ is an orthogonal transform. Each column of $\mathbf{A}$ is a basis function and is of size N. The N-band filter bank with each filter having a length N can also be looked at in this way. In this case, they are known as *critically sampled* or uniform filter banks. However, such restrictions will limit the frequency domain resolution and gives rise to blocking effects when applied to image coding. The Lapped Transforms [157] were introduced to overcome this problem by having the length of the basis function, L to be equal to an even integer multiple of the number of subbands. i.e. $L = 2KN$, where, K is known as the *overlap factor*.

C.1.4 Filter Bank based modulation for Communication

There has been a lot of work concerning the use of Filter Bank based Modulation (FBM) for DSL systems. Discrete Multitone (DMT) [158] has already found practical application in ADSL systems. DMT uses IFFT based modulators (as in OFDM), but employs Hermetian symmetry within the data vector of the IFFT modulator to convert the complex data symbols in to real transmitted signals. As with OFDM, the performance of DMT is limited by the high subchannel sidelobe levels.

Several schemes have adopted Cosine Modulated Filter Bank (CMFB) based orthogonal transmultiplexers [159, 160] to overcome the problem of high sidelobe levels. DMT in particular relies on Time Domain Equalisation (TEQ), to shorten

the effect of the channel impulse response (see chapter 6 for details of TEQ design). This requires channel estimation, which is based on the transmission of pilot tones and training symbols. The authors of [160, 161] proposed a modulation scheme, namely the Discrete Wavelet Multitone Modulation (DWMT), which claims to be more robust under non-ideal tap settings of the equalisers owing to the fact that the basis functions have very high spectral containment. The authors in [162] compare DFT and CMFB based filter banks. The level of ICI is shown to be lower in CMFB but at a cost of higher ISI in the unequalised received symbols. The authors in [163] use Lapped Transforms (LT) to remove narrowband interference in a DS-CDMA scheme. It is shown that LT domain interference suppression is less sensitive to narrowband jamming as compared to DFT or DCT based schemes.

C.2 Introduction to Filtered Multitone

A different approach to LT based designs has been adopted by Cherubini et al. in their definition of the Filtered Multitone (FMT) system [26, 164]. Originally the scheme was proposed for Very High-Speed Digital Subscriber Lines (VDSL), which is the next step upward in bit rate from ADSL systems. VDSL is intended to bridge the gap between the copper based technology available today and future all-fibre backbone networks. The view is that the fibre will terminate close to the subscriber and that VDSL modems will enable data rates of up to 60 Mb/s to be achieved to users located within a few thousand feet of the termination point. FMT uses a polyphase filter bank based scheme, but has relaxed the PR and critical sampling criteria to achieve a high stopband attenuation of the order of -60 dB. Consequently the ICI introduced in to the system is insignificant. As with DWMT, the FMT schemes does not require the use of a CP. Even though CMFB schemes such as LTs and DWMT have a greater subband attenuation than OFDM or DMT, the adjacent subchannel sidelobes cross at a level 3 dB below that of the mainlobe. To satisfy the PR condition usually entails substantial overlap of the adjacent channels. FMT on the other hand does not have that limitation. The biggest advantage of FMT is the that fewer Virtual Carriers (VC) need to be used compared with other schemes. Owing to the distortion introduced by the bandpass

filters required to prevent excessive adjacent channel interference it is usually not possible to utilise the subchannels at the edges of the frequency multiplex. These subchannel are known as Virtual Carriers (VCs). In HIPERLAN/2 12 out of 64 carriers could be used as VCs [21]. FMT requires fewer VCs compared with OFDM owing to its greater spectral containment. FMT can be defined as either a critically or a non-critically sampled system [26, 165]. In [165] the authors also show that equalisation can be achieved using per-subchannel symbol spaced or fractionally spaced DFEs. The effect of using precoding and trellis coded modulation are also investigated.

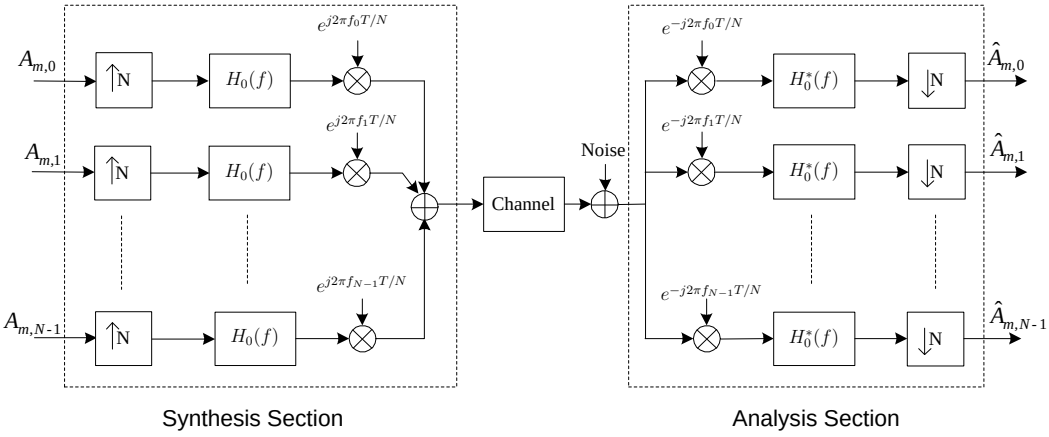

Figure C.2: Communication System using Filter Bank modulation

The critically sampled FMT system can be implemented as shown in figure C.2 [26]. Assuming there are N subbands, each symbol in a block of data is upsampled by a factor of N and then input to a *prototype* filter with a transfer function $H_0(f)$ and an impulse response $h_0(n)$. Upconversion to the appropriate subchannel frequency is then performed at the filter output. Note that the synthesis bank and the analysis banks are interchanged when compared to the subband system shown in figure C.1. Consequently, this arrangement is equivalent to the implementation of a transmultiplexer. $H_0(f)$ should be designed to be zero outside the interval $|f| \leq 1/2T$ where T is the subchannel input data rate. The analysis bank is the time reversed and conjugated version of the synthesis bank.

An example of a definition of a prototype filter is

$$H_0(f) = \begin{cases} \frac{\left|1+e^{-j2\pi fT}\right|}{\left|1+\rho e^{-j2\pi fT}\right|} & \text{if } -1/2T \leq f \leq 1/2T, \\ 0 & \text{otherwise} \end{cases} \tag{C.5}$$

where the parameter $0 \leq \rho \leq 1$ controls the spectral roll-off of the filter. The frequency responses of the first 5 subchannels are shown in figure C.3 with $N = 64$, $\rho = 0.1$ and an overlap factor, $L = 10$ [164]. Note the high spectral roll off when compared to that of the rectangular window shown in figure 3.1.

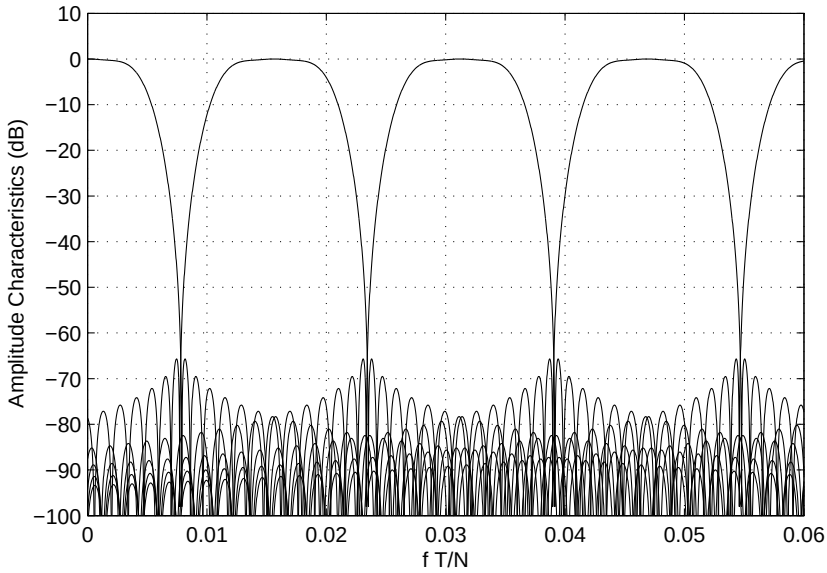

Figure C.3: Subchannel frequency responses in a FMT system

A more efficient implementation of the critically sampled filter banks shown in figure C.2 can be achieved via the IDFT/DFT combination shown in figure C.4 [166]. The upsampler, polyphase filterbank and upconverter combination is replaced by an IDFT, a polyphase filter bank and a parallel to serial converter. The analysis bank at the receiver performs the inverse functions. The polyphase transfer characteristics are represented by $H^{(i)}(f)$ and the time-reversed, conjugated polyphase filter banks, $H^{(i)*}(f)$ are used at the receiver.

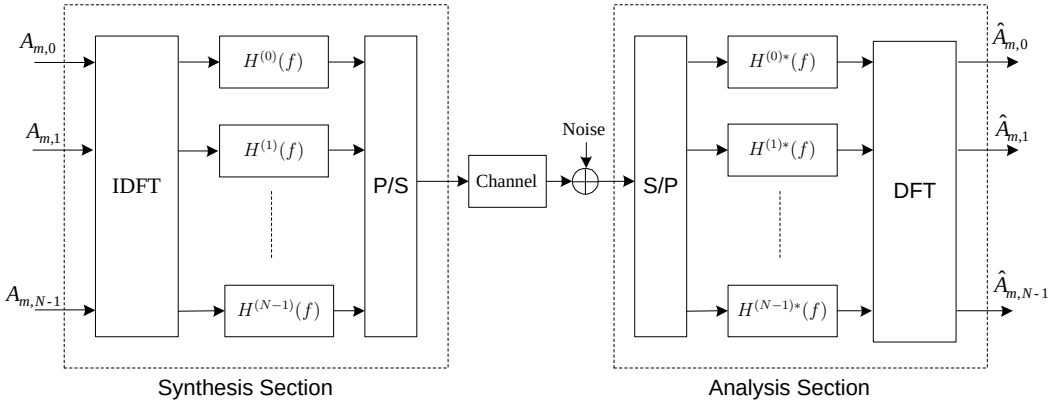

Figure C.4: Efficient implementation of a critically sampled FMT system using IDFT, DFT and polyphase filter banks

C.2.1 ISI Caused by FMT

Although FMT has negligible ICI owing to its rapid subband roll off, it introduces ISI into the system because of the loss of orthogonality. For a system with an overlap factor, $L = 10$, each polyphase branch is 10 samples long. Hence, each subchannel will have an Overall Subchannel Impulse Response (OSIR) length of 19 samples. Since the prototype is symmetric, all subchannels will be subject to the same OSIR. The OSIR of an FMT system with $N = 64$ and $L = 10$ with the prototype as defined in (C.5) is shown in figure C.5. It is important to note the high level of ISI. In all proposals regarding FMT modulation some form of equalisation is necessary to counter this subchannel ISI. This often takes the form of a Decision Feedback Equaliser (DFE). The DFE length should be of the same order as the length of the pulse that is being equalised. So, to equalise the OSIR shown in figure C.5, the symbol spaced Feedforward (FF) and Feedback (FB) filters should have a length greater than 10 symbol periods. It is evident that although increasing the overlap factor increases the subchannel decay rate, a longer DFE will be required to equalise the ISI caused by the longer OSIR.

Another more powerful but significantly more complex method of equalisation can be achieved by the use of the Maximum Likelihood Sequence Estimator (MLSE). This algorithms searches for the minimum euclidean distance

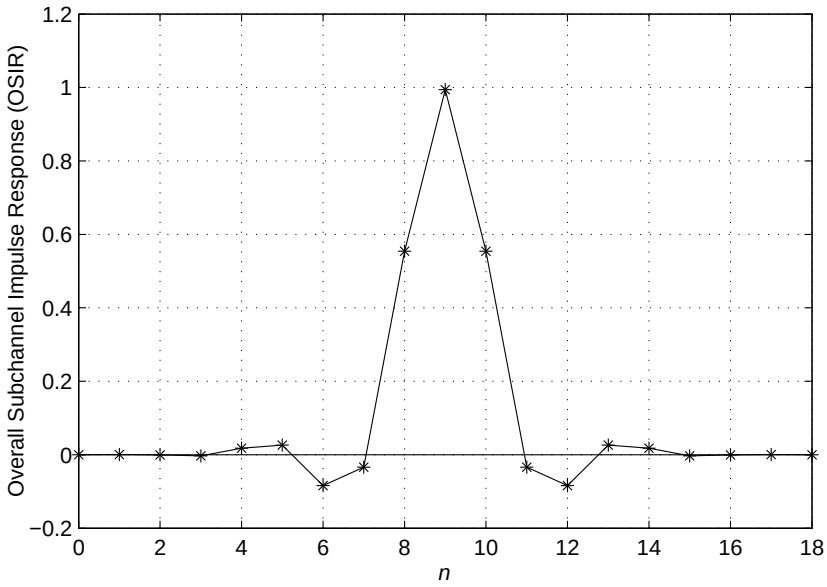

Figure C.5: Overall Subchannel Impulse Response (OSIR) of an FMT system

path through the trellis that characterises the memory of the overall impulse response [27, p.250]. If the length of the OSIR is given by N_o, then for a modulation which has two states there are 2^{N_o-1} states in the trellis. Also if the sequence has a length K, the total number of possible sequences is 2^K. The MLSE finds the sequence that has the highest posterior probability given the received sequence of symbols. Directly implementing the MLSE requires a prohibitive amount of memory. The number of sequences may be reduced using the Viterbi Algorithm [167] to eliminate unlikely sequences each time new data is received from the demodulator.

C.2.2 Achievable Bit Rate

In chapter 2 it was shown that theoretical channel capacity can be achieved by distributing the energy according the the 'waterpouring' algorithm. In most proposals regarding FMT, the authors have chosen a parameter known as the Achievable Bit Rate (ABR) as the criteria to compare system performance. It is based on allocating different numbers of bits to different subchannel depending on the subchannel

SNR. As given in [164], the number of bits allocated to subchannel i is given as,

$$b_i = \log_2 \left(\frac{\text{SNR}_i . \Gamma_c}{\Gamma_g} + 1 \right) \tag{C.6}$$

where SNR_i is the SNR of subchannel i, Γ_c is the assumed coding gain and Γ_g is the SNR gap between the channel capacity and the actual capacity usage of the transmission scheme. The ABR is given by

$$\text{ABR} = \sum_{i=0}^{N-1} b_i \, . \tag{C.7}$$

The use of FMT for wireless communication channels has been addressed by Benvenuto et al. [168, 169, 170]. In [168], the authors compare the performance of DMT and FMT in the presence of multipath delay spread and Phase Noise. The authors use only critically sampled FMT systems and use the ABR as the criterion of comparison. The authors in [169] propose a fixed DFE to equalise the OSIR and a one-tap equaliser to compensate the effects of the channel. The latter is equivalent to the FEQ in OFDM. However, for CIRs with long delay spreads, this assumption is no longer valid. The author in [171] proposes a fixed DFE computed offline in combination with a short adaptive linear equaliser with a few number of taps to be used for channels with long multipath delay spreads. In [170] the authors propose three different per-subchannel equalisation methods to counter the combined effects of the CIR and the OSIR. The first type described is known as the Decision Feedback Multichannel Equaliser (DFME), which calculates the DFE coefficients on a per-subchannel basis. The second is a Post DFT Simplified DFE (postDFME). If the assumption is made that the Channel Transfer Function (CTF) is constant over the subchannel, the channel effects can be equalised by an array of one tap equalisers following the DFT. The OSIRs are then equalised separately by an array of per-subchannel DFEs. Hence the coefficients for the DFE will be the same for all subchannels. The third type described is known as a Pre DFT Simplified DFME (PreDFME). Here the polyphase analysis bank is replaced by the FF filters. Since FMT and OFDM uses different number of VCs and the CP is used only by an OFDM system, a normalised SNR is introduced for both OFDM and FMT, so that the performance may be compared realistically.

For QPSK the normalised SNRs are [170],

$$\text{SNR}_O = \frac{\sigma_A^2(N+v-V_O)}{\sigma_w^2(N-V_O)}\frac{N}{N-V_O} \tag{C.8}$$

$$\text{SNR}_F = \frac{\sigma_A^2}{\sigma_w^2}\frac{N}{N-V_O} \tag{C.9}$$

where SNR_O and SNR_F are the normalised SNRs for OFDM and FMT, σ_A^2, σ_w^2, v, V_O and V_F are the signal power, noise power, the CP length, the number of VCs used in OFDM and the number of VCs used in FMT, respectively.

As discussed previously, the channel bit allocation will be optimal for the very harsh channels that are associated with DSL systems. There is little gain to be achieved using optimum bit allocation in the BFWA scenario using the relatively benign SUI-II channel. Hence for the studies presented here BER will be used as the performance indicator rather than the ABR.

C.3 Simulation Results

Since the objective of the analysis to be presented here is to determine the limits imposed by equalisation of the OSIR, AWGN alone is introduced to the system. Figure C.6 presents the simulation results. The performance of an OFDM system has been also been included for comparison. For the DFE, a FF length of 15 and a FB length of 15 is used. Optimal DFE coefficients are obtained by sending a very long training sequence. Since the DFE lengths and the OSIR are fixed, these coefficients will be the same for each transmitted burst. Hence, these coefficients (once obtained via training) are preloaded and 2000 QPSK symbols are sent in each burst. The SNR is normalised as given in (C.8) and (C.9). Since only AWGN channels are considered, the CP length, v is set to zero. The number of VCs selected for OFDM and FMT are 10 and 2, respectively. For each value of SNR, 500 bursts are transmitted and the BER is taken as the average. Only one subchannel is equalised at a time owing to limitations in the computer memory. To reduce the complexity of the MLSE simulations, the last few samples at either end of the OSIR in figure C.5 are neglected since they are small in value. Conse-

quently, for the results presented in figure C.6, the last 3 samples and the first 3 samples are not considered and so length of the OSIR is taken to be 13 samples. In this case, the number of states in the trellis is 4096. Note that the OSIR is completely real. Although QPSK symbols are transmitted, the OSIR will affect the real and the imaginary parts of the received signal in a similar way. Hence, the received signal can be perceived as two BPSK channels. Equalisation by the MLSE is performed using two parallel equalisers that process the real and the imaginary parts of the received sequence separately in a particular subchannel. Again, only one subchannel is considered at a time owing to limitations in the simulation environment.

As can be observed in figure C.9, since there is very little ICI, the difference in BER performance between the subchannel at the edge (with subchannel index 0) and one in the middle (with subchannel index 31) is insignificant. The OFDM system shows a 2.5 dB advantage over MLSE equalisation of FMT and an advantage of 3.5 dB over FMT equalised using DFEs. However the analysis is based on AWGN channels and so the OFDM system did not have to use a CP. In a multipath channel a CP will be required and so the OFDM advantage will be reduced according to (C.8).

Figure C.7 shows the effect of reducing the number of states on the performance of the MLSE. It compares two cases of the MLSE, one when the number of states is 4096 and another where 1024 states are used. The number of samples neglected on either side of the OSIR shown previously in figure C.5 are 3 in the former case and 4 in the later case. Consequently, the length of the OSIR is assumed to be 13 samples and 11 samples, respectively. For both cases, equalisation of the 0th and the 31st subchannel is considered separately. Equalisation using an MLSE with 4096 states takes a long time and a lot of simulation resources. The results shows that the performance degradation caused when using a shorter MLSE is insignificant below a SNR of 15 dB. As shown in figure C.5 the first 4 samples on either side of the OSIR are quite small and neglecting these samples has little effect on the subchannel BER.

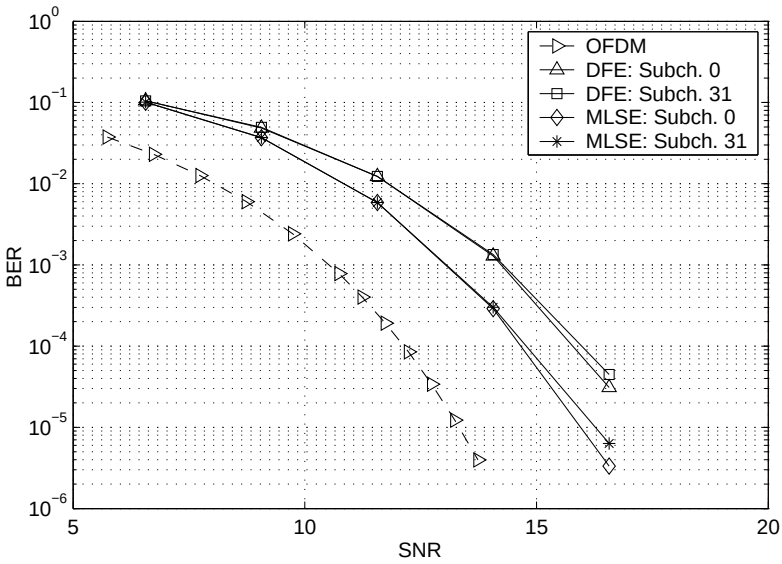

Figure C.6: The comparison of OFDM and FMT equalised by a DFE and an MLSE

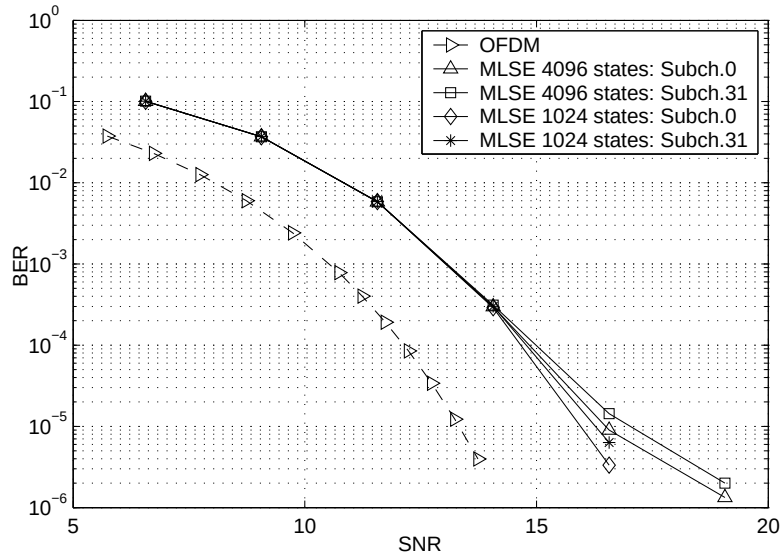

Figure C.7: The effect of MLSE length on equalisation performance

C.4 Conclusions

This appendix shows some preliminary simulation results concerning the equalisation of the OSIR in an FMT system using DFE and MLSE approaches. Subchannel error performance is worse than the conventional OFDM irrespective of the equalisation method used. However, as expected, the MLSE outperforms the DFE in all situations. Since the OSIR of the FMT system selected contains very low pre-cursor and post-cursor values, reducing the number of states in the MLSE has little effect on the subchannel BER. The real advantage of FMT lies in the use of fewer VCs and eliminating the requirement for a CP. Even though the subchannel BER is worse than OFDM in FMT, a comparison of the ABR and overall BER (utilising all the subchannels) is required to ascertain the potential performance gains.

Owing to lack of time and resources, the analysis is limited to a study of the per-subchannel BER in this work. The work presented here could be extended to accommodate systems subject to channels with multipath delay spread. In this case, the equalisation will have to take into account the CIR as well as the OSIR. The use of the CP increases the SNR penalty of OFDM systems but this effect is not included in the presented results. Further analysis could be carried out to find the total BER taking into account the VCs. However, this will require a very high level of simulation resources.

References

[1] “Broadband Stakeholder Group (BSG) - homepage.” http://www.broadbanduk.org/index.html.

[2] “Broadband Stakeholder Group (BSG) second annual report and strategic recommendations, november 2002.” http://www.broadbanduk.org/reports/BSG_Second_Annual_Report.pdf.

[3] “Broadband Stakeholder Group (BSG) wireless report, november 2002.” http://www/broadbanduk.org/reports/BSG_Second_Annual_Report-Wireless_Report.pdf.

[4] A. Norbotten, “LMDS systems and their applications,” *IEEE Communications Magazine*, pp. 150–154, June 2000.

[5] “ADSL tutorial, twisted pair access to the information highway.” http://www.adsl.com/adsl_tutorial.html.

[6] A. Dutta-Roy, “Bringing home the internet,” *IEEE Spectrum*, pp. 32–38, March 1999.

[7] J. Farserotu and R. Prasad, “A survey of future broadband multimedia satellite systems, issues and trends,” *IEEE Communications Magazine*, vol. 37, no. 10, pp. 122–126, 2000.

[8] K. W. Richardson, “UMTS overview,” *IEE Electronics and Communication Engineering Journal*, pp. 93–100, June 2000.

[9] R. van Nee, G. Awater, M. M. H. Takanashi, M. Wester, and K. Halford, "New high-rate wireless LAN standards," *IEEE Communications Magazine*, vol. 37, pp. 82–88, December 1999.

[10] "IEEE wireless local area networks - homepage." http://grouper.ieee.org/groups/802/11/.

[11] "ETSI collaborative portal." http://portal.etsi.org/portal_common/.

[12] P. S. Henry and H. Luo, "WiFi: What's next?," *IEEE Communications Magazine*, vol. 40, pp. 66–72, December 2002.

[13] J. Khun-Jush, P. Schramm, G. Malmgren, and J. Torsner, "HiperLAN2: Broadband wireless communication at 5 GHz," *IEEE Communications Magazine*, vol. 40, pp. 130–136, June 2002.

[14] P. Shelswell, "The COFDM modulation system: The heart of digital audio broadcasting," *IEE Electronics and Communication Engineering Journal*, vol. 7, pp. 127–136, June 1995.

[15] U. Reimers, "Digital video broadcasting," *IEEE Communications Magazine*, vol. 36, pp. 104–110, June 1998.

[16] A. Doufexi, S. Armour, M. Butler, A. Nix, D. Bull, J. McGeehan, and P. Karlsson, "A comparison of the HIPERLAN/2 and IEEE 802.11a wireless LAN standards," *IEEE Communications Magazine*, vol. 40, pp. 172–180, May 2002.

[17] I. Koffman and V. Roman, "Broadband wireless access solutions based on OFDM access in IEEE 802.16," *IEEE Communications Magazine*, vol. 40, pp. 96–103, April 2002.

[18] C. Ekland, R. B. Marks, K. L. Stanwood, and S. Wang, "IEEE standard 802.16: A technical overview of the WirelessMAN air interface for broadband wireless access," *IEEE Communications Magazine*, vol. 40, pp. 98–107, June 2002.

[19] K. Fazel, C. Decanis, J. Klein, G. Licitra, L. Lindh, and V. Y. Lebert, "An overview of the ETSI-BRAN HIPERACCESS physical layer air interface," in *Proceedings of the 13th IEEE International Symposium on Personal, Indoor and Mobile Radio Communications (PIMRC)*, vol. 1, pp. 49–53, 2002.

[20] H. Ochiai and H. Imai, "Performance analysis of deliberately clipped OFDM signals," *IEEE Transactions on Communications*, vol. 50, pp. 89–101, January 2002.

[21] ETSI, *Broadband Radio Access Networks (BRAN); HIPERLAN2; Physical Layer*, December 2001.

[22] D. Falconer, S. L. Ariyavisitakul, A. Benyamin-Seeyar, and B. edison, "Frequency domain equalization for single-carrier broadband wireless systems," *IEEE Communications Magazine*, vol. 40, pp. 58–66, April 2002.

[23] V. Erceg, K. V. S. Hari, *et al.*, "Channel models for fixed wireless applications," tech. rep., IEEE 802.16 Broadband Wireless Access Working Group, January 2001. Ref: IEEE 802.16.3c-01/29.

[24] M. K. A. Aziz, A. R. Nix, and P. N. Fletcher, "The impact and correction of timing error, frequency offset and phase noise in IEEE 802.11a and ETSI HiperLAN/2," in *Proceedings of the IEEE Vehicular Technology Conference*, vol. 1, pp. 214–218, May Spring, 2002.

[25] T. M. Schmidl and D. Cox, "Robust frequency and timing synchronisation for OFDM," *IEEE Transactions on Communications*, vol. 45, pp. 1613–1621, December 1997.

[26] G. Cherubini, E. Eleftheriou, S. Ölçer, and J. Cioffi, "Filter bank modulation techniques for Very high-speed Digital Subscriber Lines," *IEEE Communications Magazine*, vol. 38, pp. 98–104, May 2000.

[27] J. G. Proakis, *Digital Communication, third edition*. McGraw-Hill Book Co., 1995.

[28] R. W. Chang, "High-speed multichannel data transmission with bandlimited orthogonal signals," *Bell System Journal*, vol. 45, pp. 1775–1796, December 1966.

[29] B. R. Saltzberg, "Performance of an efficient parallel data transmission systems," *IEEE Transactions on Communication Technology*, vol. 15, pp. 805–811, December 1967.

[30] S. Weinstien and P. Ebert, "Data transmission by frequency division multiplexing using the discrete fourier transform," *IEEE Transactions in Communication Technology*, vol. COM-19, pp. 628–634, October 1971.

[31] B. Hirosaki, "An orthogonal multiplexed QAM system using the Discrete Fourier Transform," *IEEE Transactions on Communications*, vol. COM-29, July 1981.

[32] J. A. C. Bingham, "Multicarrier modulation for data transmission: An idea whose time has come," *IEEE Communications Magazine*, pp. 5–14, May 1990.

[33] C. Shannon, "The zero capacity of a noisy channel," *IEEE Transactions on Information Theory*, vol. 2, pp. 8–19, September 1956.

[34] I. Kalet, "Multitone channel," *IEEE Transactions on Communications*, vol. 37, February 1989.

[35] A. Gusmao, R. Dinis, and N. Esteves, "On frequency-domain equalization and diversity combining for broadband wireless communications," *IEEE Transactions on Communications*, vol. 51, pp. 1029–1033, July 2003.

[36] H. Witsching, T. Mayer, *et al.*, "A different look on cyclic prefix for SC/DFE," in *Proceedings of the IEEE International Symposium on Personal, Indoor and Mobile Radio Communications*, vol. 2, pp. 824–828, September 2002.

[37] A. Peled and A. Ruiz, "Frequency domain data transmission using reduced computationally complexity algorithms," in *Proceedings of IEEE Interna-*

tional Conference of Acoustics, Speech and Signal Processing, pp. 964–967, April 1980.

[38] T. Pollet, M. V. Bladel, and M. Moeneclaey, "BER sensitivity of OFDM systems to carrier frequency offsets and wiener phase noise," *IEEE Transactions on Communications*, vol. 43, pp. 191–193, February/March/April 1995.

[39] M. S. El-Tanany, Y. Wu, and L. Hazy, "Analytical modelling and simulation of phase noise interference in OFDM-based digital television terrestrial broadcasting systems," *IEEE Transactions on Broadcasting*, vol. 47, pp. 20–31, March 2001.

[40] C. Muschallik, "Influence of RF oscillators on an OFDM signal," *IEEE Transactions on Consumer Electronics*, vol. 41, pp. 592–603, August 1995.

[41] L. Hanzo, W. Webb, and T. Keller, *Single- and Multi-carrier Quadrature Amplitude Modulation*. John Wiley & Sons Ltd., 2000.

[42] E. Costa and S. Pupolin, "M-QAM-OFDM system performance in the presence of a nonlinear amplifier and phase noise," *IEEE Transactions in Communications*, vol. 50, pp. 462–472, March 2002.

[43] P. Robertson and S. Kaiser, "Analysis of the effects of phase-noise in Orthogonal Frequency Division Multiplex (OFDM) systems," in *Proceedings of the IEEE International Conference on Communications*, vol. 3, (Seattle, USA), pp. 1652–1657, June 1995.

[44] B. Stantchev and G. Fettweis, "Time-variant distortions in OFDM," *IEEE Communications Letters*, vol. 4, pp. 312–314, September 2000.

[45] "Universal Microwave Corporation - specifications control drawings for VCOs of the UMZ series." http://www.vco1.com/UMZ.html.

[46] "SANYO corp. - VCO (voltage controlled oscillator) module SM012567V." http://service.semic.sanyo.co.jp/semi/ds_pdf_e/SM012567V.pdf.

[47] H. Steendam, M. Moeneclaey, and H. Sari, "The effect of carrier phase jitter on the performance of orthogonal frequency-division multiple-access systems," *IEEE Transactions on Communications*, vol. 46, pp. 456–458, April 1998.

[48] L. Piazzzo and P. Mandarini, "Analysis of phase noise effects in OFDM modems," *IEEE Transactions in Communications*, vol. 50, pp. 1696–1705, October 2002.

[49] A. G. Armada, "Understanding the effects of phase noise in Orthogonal Frequency Division Multiplexing (OFDM)," *IEEE Transactions on Broadcasting*, vol. 47, pp. 153–159, June 2001.

[50] J. H. Stott, "The effects of phase noise in COFDM," *EBU Technical Review (No. 276)*, pp. 12–25, 1998. http://www.bbc.co.uk/rd/pubs/papers/pdffiles/jsebu276.pdf.

[51] R. Hasholzner, C. Drewes, and J. S. Hammerschmidt, "The effects of phase noise on 26 mb/s OFDMA broadband radio in the local loop systems," in *Proceedings of the International Zurich Seminar on Broadband Communications*, pp. 105–112, February 1998.

[52] A. G. Armada and M. Calvo, "Phase noise and sub-carrier spacing effects on the performance of an OFDM communication system," *IEEE Communications Letters*, vol. 2, pp. 11–13, January 1998.

[53] L. Tomba, "On the effect of wiener phase noise in OFDM," *IEEE Transactions on Communications*, vol. 46, pp. 580–583, May 1998.

[54] T. Onizawa, M. Mizoguchi, T. Sakata, and M. Morikura, "A new simple adaptive phase tracking scheme employing phase noise estimation for OFDM signals," in *Proceedings of the IEEE Vehicular Technology Conference, Spring 2002*, May 2002.

[55] K. Nikitopoulos and A. Polydoros, "Compensation schemes for phase noise and residual frequency offset in OFDM systems," in *Proceedings*

of the IEEE Global Telecommunications Conference, vol. 1, pp. 330–333, November 2001.

[56] L. Tomba and W. A. Krzymien, "A model for the analysis of timing jitter in OFDM system," in *Proceedings of IEEE International Conference on Communications*, vol. 3, pp. 1227–1231, June 1998.

[57] M. El-Tanany, Y. Wu, and L. Hazy, "OFDM uplink for interactive broadcast wireless: Analysis and simulation in the presence of carrier, clock and timing errors," *IEEE Transactions on Broadcasting*, vol. 47, pp. 3–19, March 2001.

[58] T. M. Schmidl, *Synchronization Algorithms for Wireless Data Transmission Using Orthogonal Frequency Division Multiplexing (OFDM)*. PhD thesis, Stanford University, USA, June 1997.

[59] M. Speth, D. Daecke, and H. Meyr, "Minimum overhead burst synchronization for OFDM based broadband transmission," in *Proceedings of the IEEE Global Telecommunications Conference*, vol. 5, pp. 2777–2782, November 1998.

[60] T. Pollet and M. Peeters, "Synchronization with DMT modulation," *IEEE Communications Magazine*, pp. 80–86, April 1999.

[61] M. Speth, F. Classen, and H. Meyr, "Frame synchronization of OFDM systems in frequency selective fading channels," in *Proceedings of the IEEE Vehicular Technology Conference*, vol. 3, pp. 1807–1811, May 1997.

[62] J.-J. van de Beek and M. Sandell, "ML estimation of time and frequency offset in OFDM systems," *IEEE Transactions on Signal Processing*, vol. 45, pp. 1800–1805, July 1997.

[63] T. Keller, L. Piazzo, P. Mandarini, and L. Hanzo, "Orthogonal frequency division multiplex synchronization techniques for frequency-selectivity fading channels," *IEEE Journal on Selected Areas in Communications*, vol. 19, pp. 999–1007, June 2001.

[64] D. Landström, S. K. Wilson, J.-J. van de Beek, and P. Ödling, "Symbol time offset estimation in coherent OFDM systems," in *Proceedings of the IEEE International Conference on Communication*, vol. 1, pp. 500–505, June 1999.

[65] G. Santella, "A frequency and symbol synchronization system for OFDM signals: Architecture and simulation results," *IEEE Transactions on vehicular Technology*, vol. 49, pp. 254–275, January 2000.

[66] H. Nogami and T. Nagashima, "A frequency and timing period acquisition technique for OFDM systems," in *Proceedings of the IEEE International Symposium on Personal, Indoor and Mobile Radio Communications*, pp. 1010–1015, September 1995.

[67] R. Negi and J. Cioffi, "Blind OFDM symbol synchronization in ISI channels," in *Proceedings of the IEEE Global Telecommunications Conference*, vol. 5, pp. 2812–2817, November 1998.

[68] B. Yang, K. B. Letaief, R. S. Cheng, and Z. Cao, "Timing recovery for OFDM transmission," *IEEE Journal on Selected Areas in Communications*, vol. 18, pp. 2278–2290, November 2000.

[69] A. Palin and J. Rinne, "Enhanced symbol synchronization method for OFDM systems in SFN channels," in *Proceedings of the IEEE Global Telecommunications Conference*, vol. 5, pp. 2788–2793, November 1998.

[70] E. G. Larsson and G. L. ad G. B. Giannakis, "Joint symbol timing and channel estimation for OFDM based WLANs," *IEEE Communications Letters*, vol. 5, pp. 325–327, August 2001.

[71] S. Çelebi, "Interblock interference (IBI) and time of reference (TOR) computation in OFDM systems," *IEEE Transactions on Communications*, vol. 49, pp. 1895–1900, November 2001.

[72] J. L. Seoane, S. K. Wilson, and S. Gelfand, "Analysis of intertone and interblock interference in OFDM when the length of the cyclic prefix is

shorter than the length of the impulse response of the channel," in *Proceedings of the IEEE Global Telecommunications Conference*, vol. 1, pp. 32–35, 1997.

[73] D. Kim and G. L. Stüber, "Residual ISI cancellation for OFDM with applications to HDTV broadcasting," *IEEE Journal on Selected Areas in Communications*, vol. 16, pp. 1590–1599, October 1998.

[74] T. N. Zogakis and J. M. Cioffi, "The effect of timing jitter on the performance of a discrete multitone system," *IEEE Transactions on Communications*, vol. 44, pp. 799–808, July 1996.

[75] E. Martos-Naya, J. López-Ferdinández, L. D. del Río, M. C. Aguayo-Torres, and J. T. E. Muñoz, "Optimized interpolator filters for timing error correction in DMT systems for xDSL applications," *IEEE Journal on Selected Areas in Communications*, vol. 19, pp. 2477–2485, December 2001.

[76] M. Speth, S. A. Fechtel, G. Fock, and H. Meyr, "Optimum receiver design for wireless broad-band systems using OFDM - part I," *IEEE Transactions on Communications*, vol. 47, pp. 1668–1677, November 1999.

[77] V. S. Abhayawardhana and I. J. Wassell, "Residual frequency offset correction for coherently modulated OFDM systems in wireless communications," in *Proceedings of the 55th IEEE Vehicular Technology Conference, Spring 2002*, vol. 2, pp. 777–781, 2002.

[78] H. Minn and V. K. Bhargava, "A simple and efficient timing offset estimation for OFDM systems," in *Proceedings of the 51st IEEE Vehicular Technology Conference*, vol. 1, pp. 51–55, May 2000.

[79] H. Minn, M. Zeng, and V. K. Bhargava, "On timing offset estimation for OFDM systems," *IEEE Communications Letters*, vol. 4, pp. 242–244, July 2000.

[80] A. J. Coulson, "Maximum likelihood synchronization for OFDM using a pilot symbol: Algorithms," *IEEE Journal on Selected Areas in Communications*, vol. 19, pp. 2486–2494, December 2001.

[81] A. J. Coulson, "Maximum likelihood synchronization for OFDM using a pilot symbol: Analysis," *IEEE Journal on Selected Areas in Communications*, vol. 19, pp. 2495–2503, December 2001.

[82] B. McNair, L. J. Cimini, Jr., and N. Sollenberger, "A robust timing and frequency offset estimation scheme for orthogonal frequency division multiplexing (OFDM) systems," in *Proceedings of the IEEE 49th Vehicular technology Conference*, vol. 1, pp. 690–694, May 1999.

[83] M. J. Garcia, S. Zazo, and J. M. Borrallo, "Tracking of time-frequency misalignments in 2D-pilot-symbol-aided coherent OFDM systems," in *Proceedings of the IEEE Vehicular Technology Conference (Fall)*, vol. 4, pp. 1704–1708, September 2000.

[84] K. Nikitopoulos and A. Polydoros, "Post-FFT fine frame synchronization for OFDM systems," in *Proceedings of the IST Mobile Summit*, June 2002.

[85] H. Meyr, M. Moeneclaey, and S. A. Fechtel, *Digital Communication Receivers; Synchronization Channel Estimation and Signal Processing*. John Wiley & Sons Inc., 1998.

[86] P. H. Moose, "A technique for orthogonal frequency division multiplexing frequency offset correction," *IEEE Transactions on Communications*, vol. 42, pp. 2908–2914, October 1994.

[87] M. Morelli and U. Mengali, "An improved frequency offset estimator for OFDM applications," *IEEE Communications Letters*, vol. 3, pp. 75–77, March 1999.

[88] Y. H. Kim, I. Song, S. Yoon, and S. R. Park, "An efficient frequency offset estimator for OFDM systems and its performance characteristics," *IEEE Transactions on Vehicular Technology*, vol. 50, pp. 1307–1312, September 2001.

[89] N. Lashkarian and S. Kiaei, "Class of cyclic-based estimators for frequency-offset estimation of OFDM systems," *IEEE Transactions on Communications*, vol. 48, pp. 2139–2149, December 2000.

[90] M. Garcia, O. Edfors, and J. Paez-Bprallo, "Frequency offset correction for coherent OFDM in wireless systems," *IEEE Transactions on Consumer Electronics*, vol. 47, pp. 187–193, February 2001.

[91] S. Y. Park and C. G. Kang, "Performance of pilot-assisted channel estimation for OFDM system under time-varying multi-path Rayleigh fading with frequency offset compensation," in *Proceedings of the IEEE Vehicular Technology Conference (Spring)*, vol. 2, pp. 1245–1249, 2000.

[92] J. Armstrong, "Analysis of new and existing methods of reducing intercarrier interference due to carrier frequency offset in OFDM," *IEEE Transactions on Communications*, vol. 47, pp. 365–369, March 1999.

[93] Y. Zhao and S.-G. Häggman, "Sensitivity to Doppler and carrier frequency errors in OFDM systems - the consequences and solutions," in *Proceedings of the IEEE Vehicular Technology Conference*, vol. 3, pp. 1564–1568, 1996.

[94] Y. Zhao and S.-G. Häggman, "Intercarrier interference self-cancellation scheme for OFDM mobile communication systems," *IEEE Transactions on Communications*, vol. 49, pp. 1185–1191, July 2001.

[95] U. Tureli, H. Liu, and M. D. Zoltowski, "OFDM blind carrier offset estimation: ESPRIT," *IEEE Transactions on Communications*, vol. 48, pp. 1459–1461, September 2000.

[96] V. B. Manimohan and W. J. Fitzgerald, "Blind frequency synchronisation for OFDM systems with pulse shaping," in *Proceedings of the IEEE International Conference on Communications*, pp. 178–181, June 1999.

[97] H. Bölcskei, "Blind estimation of symbol timing and carrier frequency offset in wireless OFDM systems," *IEEE Transactions in Communications*, vol. 49, pp. 988–999, June 2001.

[98] M. A. Visser, P. Zong, and Y. Bar-Ness, "A novel method for blind frequency offset correction in an OFDM system," in *Proceedings of the 9th IEEE International Symposium on Personal, Indoor and Mobile radio Communications*, vol. 2, pp. 816–820, 1998.

[99] K. Bang, N. Cho, J. Cho, H. Jun, K. Kim, H. Park, and D. Hong, "A course frequency offset estimation in an OFDM system using the concept of coherence phase bandwidth," *IEEE Transactions on Communications*, vol. 49, pp. 1320–1324, August 2001.

[100] M. Morelli, A. N. D'Andrea, and U. Mengali, "Frequency ambiguity resolution in OFDM systems," *IEEE Communications Letters*, vol. 4, pp. 134–136, April 2000.

[101] M. Gudmundson and P.-O. Anderson, "Adjacent channel interference in an OFDM system," in *Proceedings of the IEEE 46th Vehicular Technology Conference*, vol. 2, pp. 918–922, April-May 1996.

[102] Y. Li and L. J. Cimini, "Bounds on the interchannel interference of OFDM in time-varying impairments," *IEEE Transactions on Communications*, vol. 49, pp. 401–404, March 2001.

[103] K. Sathananthan and C. Tellambura, "Probability of error calculation for OFDM systems with frequency offset," *IEEE Transactions on Communications*, vol. 49, pp. 1884–1888, November 2001.

[104] Y. S. Lim and J. H. Lee, "An efficient carrier frequency offset estimation scheme for an OFDM system," in *Proceedings of the IEEE Vehicular Technology Conference (Fall)*, vol. 5, pp. 2453–2458, September 2000.

[105] W.-Y. Kuo and M. P. Fitz, "Frequency offset compensation of pilot symbol assisted modulation in frequency flat fading," *IEEE Transactions in Communications*, vol. 45, pp. 1412–1416, November 1997.

[106] O. Besson and P. Stoica, "On frequency offset estimation for flat-fading channels," *IEEE Communications Letters*, vol. 5, pp. 402–404, October 2001.

[107] H. Kobayashi, "A novel symbol frame and carrier frequency synchronization for burst mode OFDM signal," in *Proceedings of the IEEE Vehicular Technology Conference (Fall)*, vol. 3, pp. 1392–1396, September 2000.

[108] H. Kobayashi, "A novel coherent demodulation for M-QAM OFDM signal operating in the burst mode," in *Proceedings of the IEEE Vehicular Technology Conference (Fall)*, vol. 3, pp. 1387–1391, September 2000.

[109] M. Luise and R. Reggiannini, "Carrier frequency acquisition and tracking for OFDM systems," *IEEE Transactions on Communications*, vol. 44, pp. 1590–1598, November 1996.

[110] D. Falconer and F. Magee, "Adaptive channel memory truncation for maximum likelihood sequence estimation," *Bell System Technical Journal*, vol. 52, pp. 1541–1562, November 1973.

[111] J. S. Chow and J. M. Cioffi, "A cost-effective maximum likelihood receiver for multicarrier systems," in *Proceedings of IEEE International Conference on Communication*, pp. 948–952, June 1992.

[112] N. Al-Dhahir and J. M. Cioffi, "Optimum finite-length equalization for multicarrier transceivers," *IEEE Transactions on Communications*, vol. 44, pp. 56–64, January 1996.

[113] P. J. Melsa, R. C. Younce, and C. E. Rohrs, "Impulse response shortening for discrete multitone transceivers," *IEEE Transactions on Communications*, vol. 44, pp. 1662–1672, December 1996.

[114] B. Lu, L. D. Clark, G. Arslan, and B. L. Evans, "Fast time-domain equalization for discrete multitone modulation systems," in *Proceedings of the IEEE Digital Signal Processing Workshop*, 2000.

[115] I. Lee, J. S. Chow, and J. M. Cioffi, "Performance evaluation of a fast computation algorithm for the DMT in high-speed subscriber loop," *IEEE Journal on Selected Areas of Communications*, vol. 13, pp. 1564–1570, December 1995.

[116] N. Al-Dhahir and J. M. Cioffi, "Optimum finite-length equalization for multicarrier transceivers," *Proceedings of the IEEE Global Telecommunications Conference*, vol. 3, pp. 1884–1888, November 1994.

[117] N. Al-Dhahir and J. M. Cioffi, "A bandwidth-optimized reduced-complexity equalized multicarrier transceiver," *IEEE Transactions on Communications*, vol. 45, pp. 948–956, August 1997.

[118] G. Arslan, B. L. Evans, and S. Kiaei, "Optimum channel shortening for discrete multitone transceivers," in *Proceedings of the IEEE International Conference on Acoustics, Speech and Signal Processing*, vol. 5, pp. 2965–2968, 2000.

[119] G. Arslan, B. L. Evans, and S. Kiaei, "Equalization for discrete multitone transceivers to maximise bit rate," *IEEE Transactions on Signal Processing*, vol. 49, pp. 3123–3135, December 2001.

[120] W. Henkel and T. Kessler, "Maximising the channel capacity of multi-carrier transmission by suitable adaptation of the time-domain equalizer," *IEEE Transactions on Communications*, vol. 48, pp. 2000–2004, December 2000.

[121] N. Al-Dhahir and J. M. Cioffi, "A low-complexity pole-zero MMSE equalizer for ML receivers," in *Proceedings of the Allertron Conference on Communications Control and Computing*, pp. 623–632, September 1994.

[122] J. S. Chow, J. M. Cioffi, and J. A. Bingham, "Equalizer training algorithms for multicarrier modulation systems," in *Proceedings of IEEE International Conference on Communication*, pp. 761–765, May 1993.

[123] T. Pollet, M. Peetersa, M. Moonen, and L. Vandendorpe, "Equalization for DMT-based broadband modems," in *IEEE Communications Magazine*, pp. 106–113, May 2000.

[124] B. Wang and T. Adali, "Joint impulse response shortening for discrete multitone systems," in *Proceedings of the IEEE Global Telecommunications Conference*, vol. 5, pp. 2508–2512, December 1999.

[125] K. V. Acker, G. Leus, M. Moonen, O. van de Weil, and T. Pollet, "Per tone equalization for DMT receivers," in *Proceedings of IEEE Global Telecommunications Conference*, vol. 5, pp. 2311–2315, 1999.

[126] S. Armour, A. Nix, and D. Bull, "Performance analysis of a pre-FFT equalizer design for DVB-T," *IEEE Transactions on Consumer Electronics*, vol. 45, pp. 544–552, August 1999.

[127] S. Armour, A. Nix, and D. Bull, "A pre-FFT equalizer design for application to HIPERLAN/2," in *Proceedings of the IEEE Vehicular Technology Conference, (Fall)*, vol. 4, pp. 1690–1697, 2000.

[128] B. Farhang-Boroujney and M. Ding, "Design methods for time-domain equalizers in DMT transceivers," *IEEE Transactions on Communications*, vol. 49, pp. 554–562, March 2001.

[129] N. Lashkarian and S. Kiaei, "Optimum equalization of multicarrier systems: A unified geometric approach," *IEEE Transactions on Communications*, vol. 49, pp. 1762–1769, October 2001.

[130] M. V. Bladel and M. Moeneclaey, "Time-domain equalization for multicarrier communication," in *Proceedings of IEEE Global Telecommunications Conference*, pp. 167–171, November 1995.

[131] S. U. H. Qureshi, "Adaptive equalization," *IEEE Proceedings*, pp. 1349–1387, September 1985.

[132] W.-R. Wu and Y.-M. Tsuie, "An LMS-based decision feedback equalizer for IS-136 receivers," *IEEE Transactions on Vehicular Technology*, vol. 51, pp. 130–143, January 2002.

[133] C. W. Therrien, *Discrete Random Signals and Statistical Signal Processing*. Prentice-Hall Inc., 1992.

[134] R. Schober and W. H. Gerstacker, "On the distribution of zeros of mobile channels with application to GSM/EDGE," *IEEE Journal on Selected Areas in Communications*, vol. 19, pp. 1289–1299, July 2001.

[135] A. V. Oppenheim and R. W. Schafer, *Digital Signal Processing*. Prentice Hall International Editions, 1975.

[136] J. G. Proakis and D. G. Manolakis, *Digital Signal Processing, Principles, Algorithms and Applications: Third Edition*. Prentice-Hall Inc., 1996.

[137] F. Ling and J. G. Proakis, "Adaptive lattice decision-feedback equalizers - their performance and application to time-variant multipath channels," *IEEE Transactions on Communications*, vol. COM-33, pp. 348–356, April 1985.

[138] V. S. Abhayawardhana and I. J. Wassell, "Frequency scaled time domain equalization for OFDM in wireless communication," in *Proceedings of the European Wireless Conference*, vol. 2, pp. 776–780, February 2002.

[139] IEEE 802.11 Website URL: http://ieee802.org/11.

[140] C. Muschallik, "Improving an OFDM reception using an adaptive Nyquist windowing," *IEEE Transactions on Consumer Electronics*, vol. 42, pp. 259–269, August 1996.

[141] L. Wei and C. Schlegel, "Synchronization requirements for multi-user OFDM on satellite and two-path Rayleigh fading channels," *IEEE Transactions on Communications*, vol. 43, pp. 887–895, February/March/April 1995.

[142] A. Vahlin and N. Holte, "Optimal finite duration pulses for OFDM," *IEEE Transactions on Communications*, vol. 44, pp. 10–14, 1996.

[143] S. H. Muller-Weinfurtner and J. Huber, "Optimum Nyquist windowing for improved OFDM receivers," in *Proceedings of the IEEE Global Telecommunications Conference*, vol. 2, pp. 711–715, November 2000.

[144] S. H. Muller-Weinfurtner, "Optimum Nyquist windowing in OFDM receivers," *IEEE Transactions on Communications*, vol. 49, pp. 417–420, March 2001.

[145] S. Kapoor and S. Nedic, "Interference suppression in DMT receivers using windowing," in *Proceedings of the IEEE International Conference on Communications*, pp. 778–782, June 2000.

[146] Y. Lee and P. Huang, "Performance analysis of a decision feedback orthogonality restoration filter for IEEE802.11a," in *Proceedings of the IEEE Wireless Communications and Networking Conference*, March 2002.

[147] B. Yang, Z. Cao, and K. B. Letaief, "Analysis of low-complexity windowed DFT-based MMSE channel estimator for OFDM systems," *IEEE Transactions on Communications*, vol. 49, pp. 1977–1987, November 2001.

[148] N. G. Kingsbury, "E5 analogue modulation and noise course." Cambridge University Engineering Department, 2000.

[149] K. Pahlavan and A. H. Levesque, *Wireless Information Networks*. New York: J. Wiley & Sons, 1995.

[150] R. Steele, *Mobile Radio Communications*. Pentech Press, 1994.

[151] T. S. Rappaport, *Wireless Communications*. Prentice-Hall, 1996.

[152] J. W. Porter and J. A. Thweatt, "Microwave propagation characteristics in the MMDS frequency band," in *Proceedings of the IEEE International Conference on Communications (ICC)*, vol. 3, pp. 1578–1582, 2000.

[153] P. P. Vaidyanathan, *Multirate Systems and Filter Banks*. Prentice Hall, 1993.

[154] G. Strang and T. Nguyen, *Wavelets and Filter Banks*. Wellesley-Cambridge Press, 1997.

[155] A. N. Akansu and M. J. Medley, eds., *Wavelet, Subband and Block Transforms in Communication and Multimedia*. Kluwer Academic Publishers, 1999.

[156] M. Vitterli, "Perfect transmultiplexers," in *Proceedings of the IEEE International Conference on Acoustics, Speech and Signal Processing*, pp. 2567–2570, April 1986.

[157] H. S. Malvar, *Signal Processing with Lapped Transforms*. Artech House, 1992.

[158] J. M. Cioffi, "A multicarrier primer," Tech. Rep. 91-157, ANSI T1E1.4 Committee Contribution, 1992.

[159] G. W. Worell, "Emerging applications of multirate signal processing and wavelets in digital communication," *Proceedings of the IEEE - Special Issue on Wavelets*, vol. 84, pp. 586–603, April 1996.

[160] S. D. Sandberg and M. A. Tzannes, "Overlapped discrete multitone modulation for high speed copper wire communication," *IEEE Journal on Selected Areas in Communications*, vol. 13, pp. 1571–1585, December 1995.

[161] M. A. Tzannes, M. C. Tzannes, J. G. Proakis, and P. N. Heller, "DMT systems, DWMT systems and digital filter banks," in *Proceedings of the IEEE International Conference on Communications*, vol. 1, pp. 311–315, May 1994.

[162] A. D. Rizos, J. G. Proakis, and T. Q. Nguyen, "Comparison of DFT and cosine modulated filter banks in multicarrier modulation," in *Proceedings of the IEEE Global Telecommunications Conference*, vol. 2, pp. 687–691, November 1994.

[163] M. J. Medley, G. J. Saulnier, and P. K. Das, "Narrow-band interference excision in spread spectrum systems using lapped transforms," *IEEE Transactions on Communications*, vol. 45, November 1997.

[164] G. Cherubini, E. Eleftheriou, and S. Ölçer, "Filtered multitone modulation for VDSL," in *Proceedings of the IEEE Global Telecommunications Conference*, pp. 1139–1144, December 1999.

[165] G. Cherubini, E. Eleftheriou, and S. Ölçer, "Filtered multitone modulation for Very high-speed Digital Subscriber Lines," *IEEE Journal on Selected Areas in Communication*, vol. 20, pp. 1016–1028, June 2002.

[166] M. G. Bellenger, G. Bonnerot, and M. Coudreuse, "Digital filtering by polyphase networks: Application to sample-rate alteration and filter banks," *IEEE Transactions on Acoustics, Speech and Signal Processing*, vol. ASSP-24, pp. 109–114, April 1976.

[167] G. D. F. Jr., "The Viterbi algorithm (invited paper)," *Proceedings of the IEEE*, vol. 61, pp. 268–278, March 1973.

[168] N. Benvenuto, G. Chrubini, and L. Tomba, "Achievable bit rates of DMT and FMT systems in the presence of phase noise and multipath," in *Proceeding of the IEEE Vehicular Technology Conference*, vol. 3, pp. 2108–2112, 2000.

[169] N. Benvenuto, S. Tomasin, and L. Tomba, "Receiver architectures for FMT broadband wireless systems," in *Proceeding of the IEEE Vehicular Technology Conference*, vol. 1, pp. 643–647, May 2001.

[170] N. Benvenuto, S. Tomasin, and L. Tomba, "Equalization methods in OFDM and FMT systems for broadband wireless communication," *IEEE Transactions on Communications*, vol. 50, pp. 1413–1418, September 2002.

[171] I. Berenguer, "Filtered multitone (FMT) modulation for broadband fixed wireless systems," Master's thesis, University of Cambridge, August 2002.